

UNIVERSITÀ DEGLI STUDI DI PAVIA

FACOLTÀ DI INGEGNERIA

DIPARTIMENTO DI INGEGNERIA CIVILE E ARCHITETTURA

Degree of Doctor in Philosophy

ANALYSIS AND SIMULATION OF ADDITIVE  
MANUFACTURING PROCESSES

Analisi e Simulazione di processi di stampa additiva

— PHD THESIS —

Supervisor: Professor  
**FERDINANDO AURICCHIO**  
Co - supervisor: Professor:  
**SIMONE MORGANTI**

Author:  
**ALBERTO CATTENONE**  
**UIN 439747**

---

Academic year 2017/2018

*Life is on the wire, the rest is just waiting*  
*(Mike McDermott - Rounders)*



# Abstract

In the last years Additive Manufacturing (AM) or 3D printing has conquered a relevant role among the newest enabling technologies of the fourth industrial revolution. 3D printing allows to realize parts made of different materials without any geometrical constraint. This characteristic is unique in the world of industrial production and it has renewed the classical concept of mechanical design allowing to produce the optimized components reducing the weight and maximizing the stiffness. Moreover, additive manufacturing allows to reduce production waste and energy consumption.

Most diffused Additive Manufacturing technologies are Powder Bed Fusion (PBF) and Fused Deposition Modeling (FDM). The first technology is based on the powder bed technology, in which the powder (metal or ceramics) are spread on the building plate and sintered through a heat source. The second one, instead, employs a fused filament (generally plastic) which is deposited through an extruder on the building plate. The cooling process of the fused filaments and the consequent bonding among the fibers, give rise to the solid component. These technologies allow to realize optimized components merging the last scientific findings with the uniqueness of the artisan productions. The possibility to realize customized components with a high rate of technology without a real production chain make 3D printing one of the main performers of the fourth industrial revolution. Nevertheless a lot 3D printing technologies are already patented, the usage of 3D printing is not diffused on large scale yet, and the processes itself are affected by some difficulties given by the complexity of the physical phenomena. The practical experience suggest that a correct setting of printing process parameters allow to improve the results of the print; although, at now, the experimentation process is very expensive due to the high costs of the materials. A solution to avoid this inconvenience is the possibility to simulate the printing process to predict the effects of printing parameters variation on final components shape.

In the present thesis we will focus on the simulation of 3D printing processes. The dissemination is organized in two parts: the former is dedicated to Powder Bed Fusion, the latter to Fused Deposition Modeling. For both the technologies we propose a wide ranging discussion on the mechanical properties of the used materials and on the physical problems of the specific technology. We analyze in detail the simulation approaches present in literature and, for each technology, we have developed an appropriate computational method.

The simulation approaches for Powder Bed Fusion can be distinguished according to the scale level of the simulation. Powder level simulations are focused on the study of the interaction between the laser beam and the powder and on the study of the thermo-dynamic evolution of the melt pool. From a literature review it emerged that the only computational method able to simulate these aspects of Powder Bed Fusion is the Lattice Boltzmann method.

Once derived the Boltzmann equation from the kinetic theory of gases and after having explained its close relationship with the Navier-Stokes-Fourier equations, we have derived the Lattice Boltzmann method and we have used it to solve some interesting thermo-fluid dynamic problems strictly related to the powder bed technology. Finally, we have developed a finite element method (FEM) based on sequential element activation to simulate powder layer deposition and the interaction between the heat source and the powder. With this approach we have investigated the influence of the printing parameters on a microscopic titan domain; then we have used this method to simulate a real component.

The second part of this thesis is dedicated to the simulation of the Fused Deposition Modeling. In this case we have developed a FEM method based on the sequential element activation to simulate the deposition of the fused filament following the instructions contained in the GCode file used for the printing process. With this approach we have simulated the printing of two plastic components and we have compared the numerical results with experimental measurements obtained through a high precision laser scanner.

# Sommario

Negli ultimi anni la manifattura additiva, o stampa 3D, si è ritagliata un ruolo di rilievo tra le nuove tecnologie abilitanti della quarta rivoluzione industriale. La stampa 3D consente di realizzare oggetti di vario materiale senza alcun vincolo geometrico. Questa caratteristica, unica nell'ambito delle produzioni industriali, ha rivoluzionato il concetto classico di progettazione meccanica permettendo di progettare l'oggetto in maniera ottimizzata, riducendone la massa o massimizzandone la rigidezza. Inoltre, la manifattura additiva consente di ridurre al minimo gli scarti di lavorazione e il consumo di energia.

Le tecnologie additive maggiormente diffuse sono la Powder Bed Fusion (PBF) e il Fused Deposition Modeling (FDM). La prima è basata sulla tecnologia a letto di polvere, in cui le polveri (metalliche o ceramiche) vengono dapprima stese sul piano di costruzione strato per strato e, in seguito, sinterizzate in maniera selettiva. La seconda invece utilizza un filamento fuso (tipicamente plastico) depositato, tramite un estrusore, sul piatto di costruzione. Il raffreddamento dei filamenti fusi e il conseguente bonding tra le fibre, danno vita al componente solido. Queste due tecnologie consentono di realizzare componenti ottimizzati e personalizzati coniugando gli ultimi ritrovati scientifici e tecnici con l'unicità tipica delle produzioni artigianali. Proprio la possibilità di realizzare componenti specifici ad alta tecnologia senza la necessità di realizzare una vera e propria catena produttiva, rendono la stampa 3D uno degli attori principali della quarta rivoluzione industriale. Nonostante molti tecnologie di stampa siano già patentate, l'utilizzo della stampa 3D non è ancora diffusa su larga scala e i processi stessi sono interessati da alcune difficoltà dovute alle complessità dei fenomeni fisici interessati. L'esperienza pratica suggerisce come un corretto settaggio dei parametri di stampa permette di migliorare i risultati finali delle stampe; tuttavia, in questa fase, la sperimentazione è molto onerosa in termini economici per via del costo dei materiali. Una soluzione per ovviare a questo inconveniente è rappresentata dalla possibilità di simulare il processo di stampa e predire gli effetti dei parametri di stampa sui componenti finali.

Nella presente tesi ci occuperemo della simulazione dei processi di stampa 3D. La dissertazione è organizzata in due parti: la prima dedicata al Powder Bed Fusion e la seconda dedicata al Fused Deposition Modeling. Per entrambe le tecnologie proponiamo un excursus ad ampio raggio focalizzato sulle caratteristiche meccaniche dei materiali utilizzati e sui problemi fisici coinvolti nei processi. I fenomeni fisici sono analizzati in dettaglio insieme con le metodologie di simulazione presenti in letteratura. In seguito, per ogni tecnologia abbiamo sviluppato un metodo di simulazione appropriato.

Nel caso della Powder Bed Fusion il problema della simulazione del processo può essere affrontato a livello particellare o a livello del componente. Le simulazioni particellari si focalizzano sullo studio dell'interazione tra il laser e le polveri microscopiche e sullo studio

dell'evoluzione termofluido dinamica della pozza di fusione. Da ricerche di letteratura è emerso che l'unico metodo computazionale capace di simulare questi processi con risultati apprezzabili è il Lattice Boltzmann Method, basato sulla discretizzazione dell'equazione di Boltzmann. Dopo aver derivato l'equazione di Boltzmann della teoria cinetica dei gas e aver spiegato il suo legame con le equazioni di Navier-Stokes-Fourier, abbiamo derivato il Lattice Boltzmann Method e lo abbiamo impiegato per risolvere alcuni interessanti problemi termo-fluido dinamici strettamente correlati alla fusione a letto di polvere. In secondo luogo, abbiamo sviluppato un metodo ad elementi finiti (FEM), basato sull'attivazione sequenziale degli elementi per simulare la deposizione degli strati di polvere e il passaggio della fonte di calore. Con questo metodo abbiamo studiato l'influenza dei parametri di stampa sulla stampa di una parte microscopica di titanio; in seguito utilizzando una soluzione approssimata, abbiamo sfruttato il metodo per simulare un componente di grandezza reale.

La seconda parte di questa tesi è dedicata alla simulazione del processo di stampa Fused Deposition Modeling. In questo caso, abbiamo sviluppato un metodo FEM basato sull'attivazione sequenziale degli elementi per simulare la deposizione del filamento fuso seguendo le istruzioni contenute nel Gcode utilizzato per la stampa. Con questo approccio abbiamo simulato la stampa di due modelli plastici differenti per geometria e abbiamo confrontato i risultati ottenuti con misure sperimentali effettuate con un laser scanner 3D ad alta precisione.

# Contents

<b>List of Tables</b>	<b>IX</b>
<b>List of Figures</b>	<b>XVI</b>
<b>1 Additive Manufacturing, an overview</b>	<b>1</b>
1.1 Additive Manufacturing processes . . . . .	4
1.2 Aim of the thesis . . . . .	6
1.3 Organization of the dissertation . . . . .	7
<b>2 Powder Bed Fusion</b>	<b>9</b>
2.1 Process parameters of Powder Bed Fusion printers . . . . .	10
2.2 Powder for Powder Bed Fusion . . . . .	11
2.3 Physical aspects of Powder Bed Fusion . . . . .	19
2.3.1 Heat source . . . . .	20
2.3.2 Heat interaction with metal powder bed . . . . .	21
2.3.3 Solid-liquid phase change . . . . .	24
2.3.4 Powder bed generation . . . . .	27
2.3.5 Melting process and melt pool dynamics . . . . .	28
2.3.6 Porosity . . . . .	36
2.3.7 Surface roughness . . . . .	37
2.3.8 Residual stresses and cracking problems . . . . .	38
2.4 Numerical simulations of Powder Bed Fusion . . . . .	41
2.4.1 Powder level simulations . . . . .	41
2.4.2 Continuum level simulations . . . . .	44
2.4.3 Multi scale approaches . . . . .	46
2.4.4 Commercial Codes for Additive Manufacturing Simulations . . . . .	48
2.5 Conclusions . . . . .	49
<b>3 The Lattice Boltzmann Method</b>	<b>51</b>
3.1 The Kinetic Theory of Gases . . . . .	51
3.2 The Boltzmann Equation . . . . .	56
3.2.1 A more physical interpretation of the Boltzmann Equation . . . . .	59
3.2.2 Solution of the Boltzmann Equation . . . . .	60
3.2.3 The stationary solution: Maxwellian distributions . . . . .	62
3.3 Boltzmann Equation: a Bridge from the Micro- to the Macroscopic description	66

3.3.1	The Boltzmann Equation and the Conservation Equations . . . . .	68
3.3.2	The Bhatnagar-Gross-Krook approximation of the collision operator . .	69
3.3.3	The perturbation method and the Linearized Boltzmann equation . . .	70
3.3.4	The dimensionless Boltzmann equation . . . . .	72
3.3.5	From Boltzmann equation to Navier-Stokes equations: the Chapman-Enskog expansion . . . . .	73
3.3.6	Higher-order Chapman-Enskog expansion: Burnett and Super-Burnett equations . . . . .	76
3.3.7	Considerations about the Navier-Stokes equations and Boltzmann equation . . . . .	77
3.3.8	Final overview on the Boltzmann equation and its applications . . . . .	77
3.4	From the Boltzmann Equation to the Lattice Boltzmann Method . . . . .	79
3.4.1	Brief chronology of the Lattice Boltzmann method . . . . .	79
3.4.2	From the Boltzmann Equation to the Lattice Boltzmann Equation . . .	80
3.4.3	The integration in the momentum space . . . . .	81
3.4.4	Velocity and equilibrium distribution discretization . . . . .	83
3.5	The lattice Boltzmann method and the conservation equations . . . . .	86
3.5.1	From lattice Boltzmann equation to Navier-Stokes equations . . . . .	86
3.5.2	From lattice Boltzmann equation to Energy conservation equation . . .	89
3.6	Final considerations about the Boltzmann Equation and the lattice Boltzmann method . . . . .	92
3.6.1	Why use the lattice Boltzmann method for Powder Bed Fusion simulation	93
3.6.2	Conclusions . . . . .	94
<b>4</b>	<b>Applications of the Lattice Boltzmann method</b>	<b>96</b>
4.1	Single phase flows . . . . .	96
4.2	Thermal Lattice Boltzmann method . . . . .	100
4.3	Multiphase flows . . . . .	105
4.3.1	Thermal multiphase flows . . . . .	109
4.4	Free surface flows . . . . .	110
4.5	Phase change . . . . .	116
4.6	Conclusion and perspectives . . . . .	119
<b>5</b>	<b>Finite Element Simulation of Powder Bed Fusion</b>	<b>121</b>
5.1	Simulation approach . . . . .	121
5.1.1	Roller_Motion event series and sequential element activation . . . . .	123
5.1.2	Laser_path event series and laser scan strategy . . . . .	125
5.1.3	Roller_motion & Laser_path files generation . . . . .	126
5.1.4	General simulation framework . . . . .	128
5.1.5	Thermal analysis . . . . .	129
5.1.6	Mechanical analysis . . . . .	131
5.1.7	Material properties . . . . .	132
5.2	Simulation results . . . . .	134
5.2.1	Fine mesh simulations . . . . .	134
5.2.2	Coarse mesh simulations . . . . .	142

<b>6</b>	<b>Fused Deposition Modeling</b>	<b>146</b>
6.1	Process parameters of Fused Deposition Modeling printers . . . . .	147
6.2	Polymers used in Fused Deposition Modeling . . . . .	147
6.3	Physical aspects of Fused Deposition Modeling . . . . .	152
6.3.1	Heat conduction-convection-radiation . . . . .	152
6.3.2	Phase Change . . . . .	153
6.3.3	Bonding . . . . .	154
6.3.4	Adhesion . . . . .	155
6.4	Numerical Simulation of Fused Deposition Modeling . . . . .	157
6.4.1	Filament level simulations . . . . .	157
6.4.2	Part level simulations . . . . .	159
<b>7</b>	<b>Finite element simulation of Fused Deposition Modeling</b>	<b>160</b>
7.0.1	Sequential element activation . . . . .	160
7.0.2	Thermal analysis . . . . .	163
7.0.3	Mechanical analysis and material properties . . . . .	163
7.0.4	Part detachment procedure . . . . .	167
7.0.5	Simulated geometries . . . . .	167
7.0.6	Sensitivity analysis on simulation parameters . . . . .	169
7.0.7	Validation . . . . .	170
7.1	Results and discussion	
	171	
7.1.1	Sensitivity analysis on simulation parameters . . . . .	171
7.1.2	Validation . . . . .	176
7.1.3	Planar spring . . . . .	176
7.1.4	Bridge model . . . . .	181
7.2	Conclusions . . . . .	185
7.3	Limitations . . . . .	186
<b>8</b>	<b>Final remarks</b>	<b>187</b>
	<b>Bibliography</b>	<b>189</b>

# List of Tables

1.1	Additive Manufacturing processes. In light blue AM technologies analyzed in this thesis. . . . .	5
2.1	Mechanical properties of a AlSi <sub>12</sub> 3D printed part before and after stress relief. . . . .	12
2.2	Mechanical properties of a 316L steel 3D printed part after stress relief and after full anneal. . . . .	12
2.3	Mechanical properties of a TiGr23 3D printed part after stress relief and after isostatic pressure treatment. . . . .	13
2.4	Mechanical properties of a CoCrF75 3D printed part after anneal and after isostatic pressure treatment. . . . .	13
2.5	Mechanical properties of a Ni718 3D printed part at the end of printing process and after stress relief. . . . .	14
4.1	Contact angle between the droplet and the bottom wall. . . . .	109
5.1	Scheme of the input file for the sequential element activation. Roller ON/OFF is a bit function which states if the marching rectangle starts to move (1) or it is stopped (0). . . . .	124
5.2	Scheme of the input file for the heat source movement. . . . .	125
5.3	Thermal properties of Ti6Al4V powder with increasing temperature. . . . .	132
5.4	Thermal properties of Ti6Al4V powder with increasing temperature. . . . .	132
5.5	Thermal properties of Ti6Al4V solid alloy with increasing temperature. . . . .	133
5.6	Mechanical properties of Ti6Al4V solid alloy with increasing temperature. . . . .	133
5.7	Adopted simulation parameters for the fine mesh analyses of the parallelepiped geometry. . . . .	135
6.1	Mechanical properties of a commercial ABS filament. . . . .	148
6.2	Mechanical properties of a commercial PC filament. . . . .	148
6.3	Mechanical properties of a commercial PLA filament. . . . .	149
6.4	Mechanical properties of a commercial ULTEM filament. . . . .	149
6.5	Mechanical properties of a commercial PEEK filament. . . . .	149
7.1	Scheme of the input file for the sequential element activation. X, Y, Z are the coordinates of the filament centerline at time T. Extruded filament area represents the cross-sectional area of the extruded filament, which drops to zero in correspondence of the <i>travel movements</i> . . . . .	161



7.2	Mechanical and thermal properties of the commercial ABS filament at the ambient temperature . . . . .	164
7.3	Printing process parameters adopted for the planar spring and bridge model . .	168
7.4	Time steps adopted for the planar spring simulation . . . . .	169
7.5	Meshing strategies adopted for the planar spring simulation. In red, the meshing strategies consistent only with the filament height. In blue, the meshing strategies fully consistent with filament dimensions . . . . .	169
7.6	Constitutive models adopted for the considered ABS filament. For each constitutive model we remark the temperature dependence of the physical and the mechanical properties. $T_a$ represents the ambient temperature . . . . .	170
7.7	Experimental and numerical values of Z axis displacements on the planar spring test points. The errors are calculated between the average of the experimental results $u_z^m$ and simulation results $u_z^h$ (measured in $\mu m$ ) . . . . .	180
7.8	Experimental and numerical measurements of Z axis displacements on bridge model test points. The errors are calculated between the experimental results $u_z$ and simulation results $u_z^h$ (measured in $\mu m$ ) . . . . .	185

# List of Figures

1.1	Time-line history of AM technology. . . . .	1
1.2	Principal fields of application of 3d printing [Cotteleer and Joyce, 2014] . . . .	2
1.3	Growth rate of AM in the years 2016-2018 and estimated growth rate for the four-year period 2018-2022 [Wohlers Associates, 2017] . . . . .	3
1.4	Growth rate of photo-polymers and laser-sintered polymers sales market in different time periods [Wohlers Associates, 2017]. . . . .	3
1.5	Growth rate of metal powder sales market [Wohlers Associates, 2017]. . . . .	3
1.6	General working principle of a 3D printing machine . . . . .	4
1.7	Example of 3D printed functional parts produced with SLM technology. The .	6
1.8	Examples of 3D printed FDM parts. a) and b) Metallic parts realized with SLM. c) and d) Plastic parts realized with FDM. . . . .	6
2.1	Working principle of a generic Powder Bed Fusion printer. . . . .	9
2.2	Stress strain curves obtained trough tensile tests on AlSi <sub>12</sub> specimens realized with different energy density [Siddique et al., 2015]. . . . .	14
2.3	Stress strain curves obtained trough tensile tests on AlSi <sub>12</sub> specimens realized with different manufacturing technology [Prashanth et al., 2014]. . . . .	15
2.4	Stress strain curves obtained trough tensile tests on AlSi <sub>12</sub> SLMed parts annealed at different temperatures (a). Variation of mechanical properties with the annealing temperature on SLMed and casted parts [Prashanth et al., 2014].	15
2.5	Variation of the relative density with increasing energy density on a femoral SLMed component realized with CoCrMo [Song et al., 2014]. . . . .	16
2.6	Stress-strain curves of CoCrMo parts produced with SLM printing process adopting different process parameters (a-e) and with traditional casting process (f)[Takaichi et al., 2013]. . . . .	16
2.7	Stress-strain curves of CoCrMo parts produced SLM printing process adopting different process parameters (a-e). Stress-strain curve of a CoCrMo part realized with a traditional casting process [Vrancken et al., 2012]. . . . .	17
2.8	Stress-strain curves of Ti6Al4V parts produced with SLM printing process, with different built orientations. (a) Tensile tests results at the end of the printing process; (b) tensile tests results after heat treatment [Simonelli et al., 2014]. . .	18
2.9	Variation of the relative density with the energy density on Ni718 parts produced via SLM [Jia and Gu, 2014]. . . . .	18

2.10	Tensile test results on SLMed Ni718 parts at the end of the printing process and after different heat treatments processes (SA and HSA) [Zhang et al., 2015].	19
2.11	Physical phenomena rising during a Selective Laser Melting process. In light blu the principal physical aspects; in black the secondary physical effects. . . .	20
2.12	Typical Gaussian distribution of a laser or an electron beam. . . . .	21
2.13	Variation of the absorptance with the temperature [Prokhorov, 2018]. . . . .	22
2.14	Enthalpy variation on temperature during isothermal (a) and non-isothermal (b) phase change processes [Sani, 2017]. . . . .	24
2.15	Front tracking phase change approach [Sani, 2017]. . . . .	25
2.16	Fixed domain phase change approach [Sani, 2017]. . . . .	26
2.17	Powder packing with different powder size [Shi and Zhang, 2006]. . . . .	28
2.18	Equilibrium contact angle in wetting on a smooth surface. . . . .	29
2.19	Liquid droplet wetting on rough surface after the solid-liquid phase change. Coupled thermo-fluid dynamic simulation carried out using the free surface lattice Boltzmann method [Scharowsky et al., 2012]. . . . .	31
2.20	Example of <i>Rayleigh instability</i> on fluid water cylinder parallel to gravity direction.	32
2.21	Simulation of capillary rise and depression in pipes of different size, performed with a free surface lattice Boltzmann-method [Attar and Körner, 2009]. . . . .	33
2.22	Example of Gibbs-Marangoni effect rising due to the temperature gradient between the melt pool zones. . . . .	33
2.23	Experimental results of weight loss in 308 (1) and 309 (2) stainless steel obtained with a special long time extended welding process [Block-Bolten and Eagar, 1984].	34
2.24	On the left: bubble growing from a heated surface. On the right: velocity field after bubble detaching from the heated surface. . . . .	35
2.25	Effect of hatch spacing on part porosity [Aboulkhair et al., 2014]. . . . .	36
2.26	Surface profile/roughness of a surface inclined of 65 °C [Strano et al., 2013]. . .	37
2.27	Surface roughness obtained with a hatch spacing of 500 $\mu m$ [Jamshidinia and Kovacevic, 2014]. . . . .	38
2.28	Example of part detachment from the building plate due to residual stresses. .	38
2.29	Example of crack in 3D printed part induced by residual stresses accumulation.	39
2.30	On the left: vertical displacements before and after support removal, evaluated with a thermo mechanical finite element model. On the right: experimental results after support cutting [Papadakis et al., 2014]. . . . .	40
2.31	Distortion prediction in SLM part obtained with a coupled analytical - FEM model [Afazov et al., 2017]. . . . .	40
2.32	Simulation of wall construction using a free surface multi distribution lattice Boltzmann method [Körner et al., 2013]. . . . .	42
2.33	3D simulation of EBM in a stochastic powder bed distribution [Ammer et al., 2014a]. . . . .	42
2.34	Influence of the energy density and scan speed on the local porosity in a 3D domain of multiple powder layers [Markl et al., 2016]. . . . .	43
2.35	Effect of laser power and scan velocity change [King et al., 2015]. . . . .	44

2.36	Finite element simulation SLM process of a single layer of powder which is treated as a continuum domain. Simulation approach includes the heat source modeling and the base plate [Hussein et al., 2013]. . . . .	45
2.37	Comparison between the predicted part distortions and the experimental measurements of a cantilever beam produced with SLM [Li et al., 2017]. . . . .	46
2.38	Comparison between the predicted part distortions and the experimental measurements of a plate beam produced with SLM and simulated with a multi scale simulation. [Li et al., 2016a]. . . . .	47
2.39	Predicted and experimentally measured vertical residual stresses on a SLMed part simulated with a multi scale approach and with different numbers of macro layers [Li et al., 2018]. . . . .	48
3.1	Incoming and outgoing velocity difference between colliding particles. . . . .	54
3.2	Probability of collision between particles. . . . .	54
3.3	Height of the cylinder before and after collision of the two particles. . . . .	55
3.4	From Newton equation to Navier-Stokes-Fourier equations: basic steps. . . . .	78
3.5	LB schemes in two and three dimensions. On the left, the bi-dimensional D2Q9 model with its 9 velocities. On the right, the three-dimensional D3Q19 scheme with its 19 velocities. . . . .	83
3.6	From the Boltzmann equation to the lattice Boltzmann method: basic steps. . .	93
4.1	LBGK algorithm. The scheme consist of two loops. A main loop over time and a secondary loop over lattice cells. The bounce back rule is adopted for no-slip boundaries and the <i>Zou-He</i> model [Zou and He, 1997] is used to impose constant velocity on the top boundary. . . . .	97
4.2	LDC problem performed with different $Re$ numbers. The normalized horizontal and vertical velocity components in the middle of the domain are compared with the solution proposed by Ghia et al. [1982], showing a good agreement for the considered Reynolds number. . . . .	99
4.3	TLB algorithm, based on the multi-distribution approach. DFs represents the distributions of the fluid-dynamic problem; GFs represents the distributions for the thermo-dynamic problem. The bounce back rule is adopted to impose no-slip boundary conditions. Dirichlet boundary [Liu et al., 2010] conditions have been implemented to impose fixed temperature on the upper and the bottom sides of the domain. . . . .	104
4.4	Steady state solution of the Rayleigh-Benard convection obtained with $Pr = 1$ and varying $Ra$ numbers. . . . .	104
4.5	Variation of the $Nu$ number in fuction of the $Ra$ number. The results are compared with the solution proposed by Clever and Busse [1974]. . . . .	105
4.6	Pseudopotential LB algorithm, based on Shan and Chen [1993] model. The bounce back rule is used for no-slip boundaries. The Redlich-Kwong EOS is adopted to describe the state of matter and He and Doolen [2002] formulation is used to describe the pseudopotential function. . . . .	108

4.7	Droplet wetting on a smooth surface performed using the multiphase Shan and Chen [1993] LB scheme, using the R-K EOS. Different contact angles obtained by varying the solid wall density $\rho_w$ . . . . .	108
4.8	Droplet wetting on a smooth surface performed using the multiphase Shan and Chen [1993] LB scheme, using the R-K EOS. . . . .	109
4.9	Droplet wetting on a smooth surface performed using the multiphase Shan and Chen [1993] LB scheme, using the R-K EOS. Temperature difference is imposed between bottom and top wall. . . . .	110
4.10	Example of cell initialization and procedure to calculate the liquid fraction on the interface cells. . . . .	111
4.11	Mass exchange process among an interface cell and the neighboring liquid and interface cells. . . . .	112
4.12	Example streaming process on an interface cell. Black arrows represent the known distribution functions incoming from liquid cells. Red arrows represent the reconstructed distribution functions coming from neighboring interface and empty cells. . . . .	113
4.13	Contact angle in dynamic conditions. . . . .	114
4.14	Free surface LB algorithm, based on [Thürey et al., 2005] model. Mass exchange is calculated only for interface and fluid neighboring cells. Classic bounce back scheme is adopted to simulate no slip boundaries. . . . .	115
4.15	Dynamic wetting of a droplet on a smooth surface. . . . .	116
4.16	Solid-Liquid phase-change . . . . .	118
4.17	Solid-Liquid phase-change LB algorithm, based on Shan and Chen [1993] model. The bounce back rule is used for no-slip boundaries. The Redlich-Kwong EOS is adopted to describe the state of matter and the He and Doolen [2002] formulation is used to describe the pseudopotential function. . . . .	119
5.1	Example of the Abaqus code necessary to define the input data for the SLM simulation. . . . .	122
5.2	Example of a simple cubic component used to explain the sequential activation procedure. . . . .	124
5.3	Example of sequential element activation on a simple geometry. . . . .	125
5.4	Example of an idealized scan strategy starting at the end of the deposition process (Figure 5.3 (d)). . . . .	126
5.5	Example of a G-code file rielaborated with our Matlab script to generate the input files for SLM printing process simulation. . . . .	127
5.6	<i>Roller.inp</i> and <i>Laser.inp</i> input files rielaborated from the G-Code (Figure 5.5) by means of the Matlab code. . . . .	128
5.7	General framework adopted for SLM process simulation. . . . .	128
5.8	Laser beam: Gaussian distribution model. . . . .	130
5.9	Parallelepiped part: a) geometry, b) meshing strategy. . . . .	134
5.10	Simulation scheme adopted for the parallelepiped model. . . . .	134
5.11	Temperature and residual stress distribution obtained with different laser powers. . . . .	136
5.12	Temperature and residual stress distribution obtained with different spot radius. . . . .	136

5.13	Temperature evolution in a specific point of the domain (P), with different laser power and spot. . . . .	137
5.14	Temperature and residual stress distribution obtained with different scan overlaps among adjacent scan lines. . . . .	138
5.15	Temperature evolution in a specific point of the domain (P), with different overlap ratio. . . . .	139
5.16	Temperature and residual stress distribution obtained with different scan velocities. . . . .	140
5.17	Temperature and residual stress distribution obtained with different building plate temperatures temperatures. . . . .	141
5.18	Temperature and residual stress distribution obtained with different chamber temperatures. . . . .	141
5.19	Bridge like model. . . . .	142
5.20	Adopted laser paths for the pillars and deck of the bridge (schematic). . . . .	143
5.21	Temperature field distribution at the end of the printing process (a) and after the cooling process (b). . . . .	143
5.22	Stress field distribution at the end of the printing process (a) and after the cooling process (b). . . . .	144
5.23	Constraints adopted to simulate support structures during the printing process (a) and during the part detachment process (b). . . . .	144
5.24	Stress field distribution at the end of the cooling process (a) and after the detachment process (b). . . . .	145
5.25	Z-axis displacement field at the end of the cooling process (a) and after the detachment process (b). . . . .	145
6.1	Working scheme of a generic Fused Deposition Modeling printer. . . . .	146
6.2	Tensile (a) and shear (b) stress-strain curves of FDMed PC parts produced with different raster orientations [Cantrell et al., 2017]. . . . .	150
6.3	Ultimate tensile stress variation with the total part thickness. Different layer thickness are considered [Rankouhi et al., 2016]. . . . .	150
6.4	Tensile stress (a) and compressive stress (b) strain curves of FDMed ABS parts at different cryogenic temperatures [Weiss et al., 2015]. . . . .	151
6.5	Stress strain curves obtained trough tensile tests on FDMed ULTEM parts produced with different build orientations [Bagsik et al., 2010]. . . . .	151
6.6	Physical phenomena rising during the Fused Deposition Modeling process. In light blue the principal physical effects; in black the secondary physical effects. . . . .	152
6.7	On the left, the melting process typical of crystalline polymers; on the right, the glass transition process typical of amorphous polymers. . . . .	154
6.8	Intra-layer bonding in FDM printing process (rielaborated from [Gurralla and Regalla, 2014]). . . . .	155
6.9	Inter-layer bonding in FDM printing process (rielaborated from [Gurralla and Regalla, 2014]). . . . .	155
6.10	Variation of the radius deck in isothermal (a) and in non-isothermal (b) conditions [Bellehumeur et al., 2004]. . . . .	156

6.11	Part detachment from the building plate during FDM printing process. Detachment occurs due to the not enough adhesion force. . . . .	156
6.12	Variation of the adhesion force with extrusion temperature (a), build plate temperature (b) and build plate fabric type (c) [Sanatgar et al., 2017]. . . . .	157
6.13	Neck radius variation with time during the bonding process between two FDMed deposited filaments [Gurralla and Regalla, 2014]. . . . .	158
6.14	Temperature evolution between bounded filaments deposited at different extrusion temperatures (a) 215°C, (b) 295°C, and (c) 375°C [Xia et al., 2017]. . . . .	158
6.15	Real FDMed part distortions compared with simulation predictions. Every specimen has been realized with different printing parameter [Zhang and Chou, 2008]. . . . .	159
7.1	Overall framework of the FDM printing process. In the central part, the virtual calculation of the GCode file from a 3D CAD model of the component. On the left, the physical printing process; on the right, the simulation process. The GCode information are used both to perform the physical printing and the simulation of the part . . . . .	161
7.2	Sequence of standard instructions contained in a GCode file realized with KISSlicer	161
7.3	Element activation process. The extruded filament section (cyan ellipse) is substituted by the circumscribed <i>marching</i> rectangle (blue rectangle). The rectangle moves following the filament centerline (red line). When the center of an element (green point) falls into the volume described by the marching rectangle, then the element is activated (green element). Gray points correspond to the centroids of the non-activated elements (gray elements) . . . . .	162
7.4	Variation of thermal conductivity and specific heat with temperature in the commercial ABS filament. [Rheology Testing And Consultancy, 2004]. $T_g$ represents the glass transition temperature . . . . .	165
7.5	Variation of the Young's modulus with the temperature in the commercial ABS filament Song et al. [2012]. $T_g$ represents the glass transition temperature . . .	165
7.6	Variation of the tensile yield stress with the temperature in the commercial ABS filament Richeton et al. [2006]; Armillotta et al. [2018]. $T_g$ represents the glass transition temperature and $m$ represents the slope of the linear part . . .	166
7.7	Geometry of the planar spring (a) and bridge model (b) . . . . .	168
7.8	Layout of the printed parts with respect to the building plate; (a) planar spring, (b) bridge. . . . .	168
7.9	Test points for the evaluation of the error between simulation results and experimental measurements . . . . .	170
7.10	Results of the thermal and the mechanical analysis obtained with the smallest ( $\Delta t_1$ ) and the largest ( $\Delta t_9$ ) time steps. The time step choice has a significant influence on the element activation temperature, while it has less influence on the mechanical analyses results . . . . .	171
7.11	(a): decreasing of the activation temperature with increasing time steps. (b): Von Mises stress ( $\sigma_{vm}$ ) and stress tensor components ( $\sigma_{ij}$ ) variation with time step. . . . .	172

7.12	Computational times variation (CPU time) with the time step. A significant increase in computational times is observed, in particular, for the mechanical analysis when $\Delta t$ is lower than 1 s. . . . .	173
7.13	Adopted meshing strategies for the planar spring simulation, according to Tab. 7.5 . . . . .	173
7.14	Temperature and Von Mises stress distribution obtained varying the meshing strategy. Significantly different activation temperature is observed for meshing strategies M-1 and M-3/5. Local modifications of the stress path can be observed at the corners of the model, between meshing strategies M-1 and M-3/5	174
7.15	Computational times variation (CPU time) with increasing number of elements. We appreciate a linear behavior of the computational times both for the thermal and the mechanical analysis . . . . .	175
7.16	Von Mises stress at the end of the printing process obtained varying the constitutive model. (a,b): yielding surface is not defined. (c): yielding surface is not dependent on the temperature. (d): yielding surface is dependent on the temperature. More details about the constitutive models are specified in Table 6	176
7.17	Planar spring model after the detachment from the building plate. Warpage effect is appreciable at the corners of the component . . . . .	177
7.18	Experimental measurements of the vertical displacements of the upper surface of the planar spring. Four different samples have been considered . . . . .	177
7.19	In blue, the points that remain attached to the building plate at the end of the cooling process. In red, the points detached from the building plate at the end of the cooling process . . . . .	178
7.20	Von Mises stress at significant time instants of the simulation. Residual stresses increase during the cooling process due to the shrinking effect. Residual stresses are, finally, relaxed after the constraints removal . . . . .	179
7.21	Z axis displacements at significant time instants of the simulation. Displacements at the end of both printing and cooling process are of an order of magnitude lower than the displacements after part detachment . . . . .	180
7.22	Bridge model before and after the supports removal. A warpage effect is clearly evident on the upper surface of the model after support removal . . . . .	182
7.23	Experimental measurements of the bridge model. (a): XZ surface of the model; (b) detail of the upper surface of the model . . . . .	182
7.24	Von Mises stress at significant time instants of the simulation. Residual stresses increase during the cooling process due to the shrinking effect. Residual stresses are, finally, relaxed after the constraints removal . . . . .	183
7.25	Z axis displacements at significant time instants of the simulation. A shrinking effect is detected during the cooling process and the indentation between the external pillars and the deck of the bridge is evident in the simulation . . . . .	183
7.26	Detail of the indentation between the top of the external pillars and the deck of the bridge. The simulation is able to predict this anomalous effect . . . . .	184
7.27	X axis and Z axis displacements of the XZ surface of the bridge . . . . .	184



# Chapter 1

## Additive Manufacturing, an overview

Additive manufacturing (AM) technology (also indicated as 3D printing) is defined by the American Society for Testing and Materials (ASTM) as *the process of joining materials to make objects from 3D model data, usually layer upon layer, as opposed to subtractive manufacturing methodologies, such as traditional machining* [ASTM, 2012].

Although AM is a quite new technology, since 1984, when the first stereolithographic 3D printer was produced, a lot of new processes and new applications have been proposed. In Figure 1.1 we show a brief time-line history of AM including the main innovations proposed by various companies among the years.

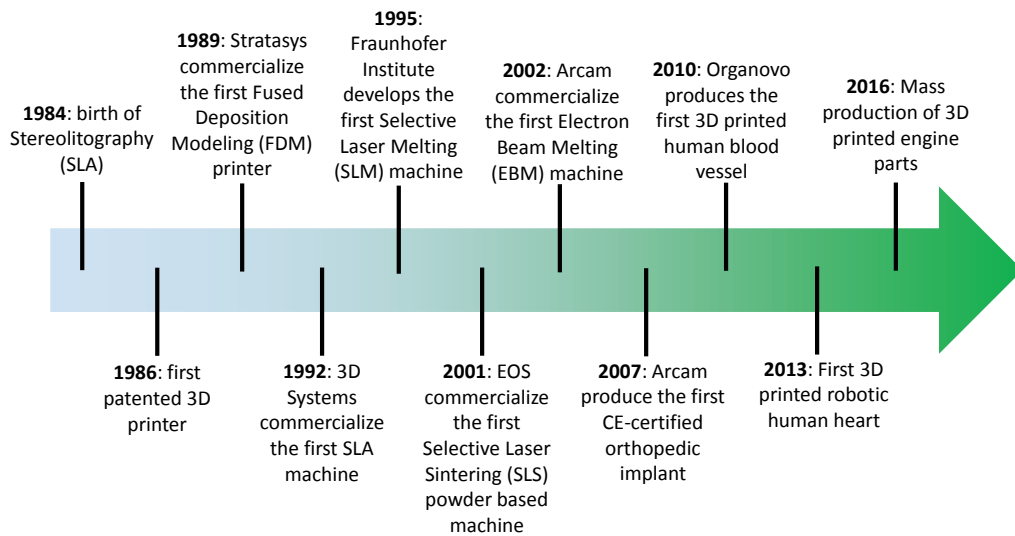


Figure 1.1: Time-line history of AM technology.

In a very first time, AM was used with the only purpose to create a single prototype of the desired component and then move to a massive production thanks to the traditional production chain. In the beginning, the main disadvantage of AM was the high production costs that discouraged a massive usage of 3D printing in industrial contests [Lipson and Kurman, 2013]. Although, thanks to the new studies and the new discovered solutions, in recent years, 3D printing has become cheaper and economically sustainable to a great number of industries.

For this reason, AM is one of the most important *enabling technologies* of the 4<sup>th</sup> industrial revolution [Economist, 2016].

The great innovation of AM is the capability to conjugate the detail precision and the specificity of the handmade production with the massive production of the industrial processes. In particular the principal characteristics of AM are:

- *possibility to manage very complex shapes*, like, for example, lattice structures, impossible to produce with milling processes and casting optimized components [Mueller, 2012];
- *possibility to produce components without assembling procedures*, since the production process is continuous and the part is produced in one shot;
- *no needs of components stocking*, since the part is directly produced using the desired material;
- *the reduced waste of material* in comparison with classic milling process [Atzeni and Salmi, 2012];
- *a very low consumption of energy* in front of the traditional processes. According to this, AM can be viewed as a green technology [Ahn et al., 2013].

Nowadays 3D printing is used for a wide range of industrial applications; in particular Cotteleer and Joyce [2014] (Figure 1.2) underlined that AM is adopted for the production of mechanical parts and consumer products, but it is successfully applied also for the production of biomedical implants [Auricchio and Marconi, 2016].

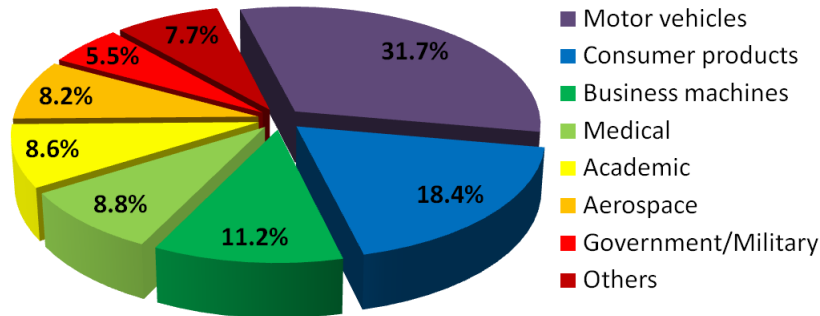


Figure 1.2: Principal fields of application of 3d printing [Cotteleer and Joyce, 2014]

The increasing interest of the industries in AM technologies is confirmed by the flux of money that is actually invested in the 3D printing supply chain. In Figure 1.3 we show the growth rate of AM in the years 2016-2018 and the estimated growth rate for the four-year period 2018-2022 [Wohlers Associates, 2017]. From 2016 to 2022 it has been estimated a worldwide growth of AM from 6.1 up to 26.2 billion \$. United States of America have almost a half of all the industrial AM machines (46.3 %), followed by Israel (26.2 %) and Europe (18.8%).

A significant growth has been appreciated, in last years, also in AM material market. In figure 1.4 we show a 15-year history of photo-polymers sales for AM and a 8-year history of laser-sintered polymers sales.

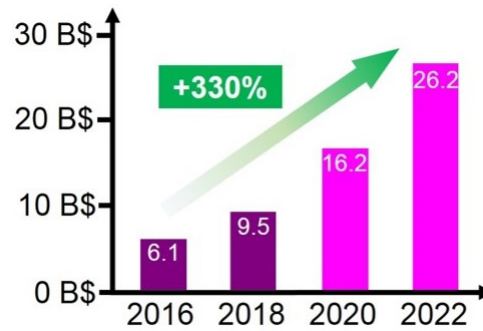


Figure 1.3: Growth rate of AM in the years 2016-2018 and estimated growth rate for the four-year period 2018-2022 [Wohlers Associates, 2017]

We appreciate how, in both cases, there has been a significant sales growth especially in the past six years meaning that the production of parts through AM is on constant growing.

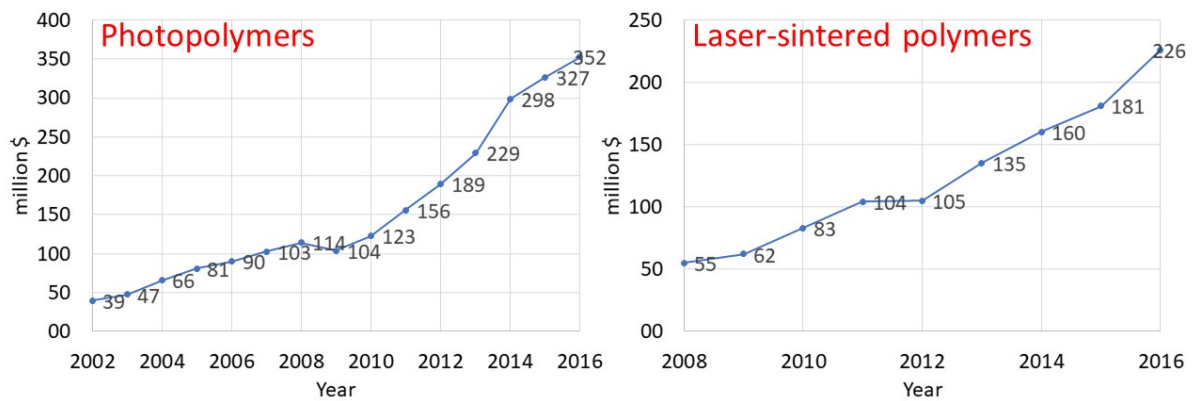


Figure 1.4: Growth rate of photo-polymers and laser-sintered polymers sales market in different time periods [Wohlers Associates, 2017].

A significant growth rate is appreciated also in metal powder market (Figure 1.5). In particular between 2014 and 2016 the sales of AM powders almost tripled.

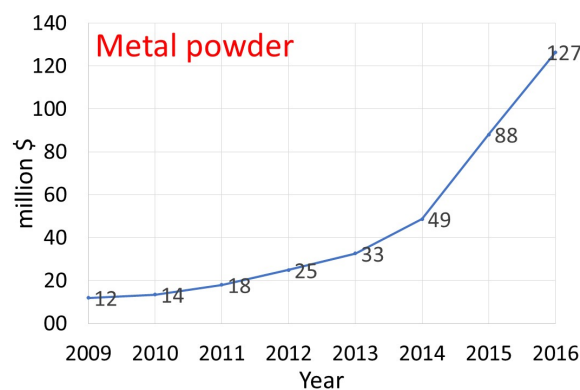


Figure 1.5: Growth rate of metal powder sales market [Wohlers Associates, 2017].

This data show that AM industry is in constant growth and support the prevision of a global economic impact of AM up to 550 billion \$/year in 2025 [Economist, 2016].

Accordingly, we can conclude that AM is going to assume much more importance in various industrial sectors; moreover all the economical predictions indicate that AM will increase its economic impact in the following years.

## 1.1 Additive Manufacturing processes

The working principle of a generic 3D printing process is detailed in Figure 1.6.

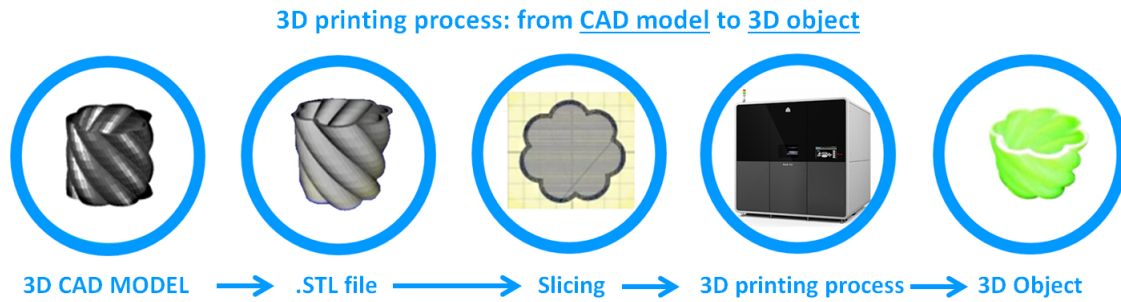


Figure 1.6: General working principle of a 3D printing machine

We start from a CAD file with the geometry of the desired component; from the CAD file we generate a triangular mesh of the external surface which is saved in the stereolithographic (STL) file. The STL file is used by a specific slicing software to virtually *slice* the model and to define all the informations needed to perform the printing process. The slicing process consists in dividing the object into horizontal layers, then for each layer the printing path is defined. Those informations are collected into a procedural file, called GCODE file which manages the printing. Finally the object is ready to be printed with the desired technology and material. The GCODE file format varies according to the specific AM technology and contains also the instructions to manage the environmental variables like the chamber and the build plate temperature, the ventilation power, etc.

Using the GCODE file, the printing process is performed and the desired object is generated. Then a controlled cooling process is performed before the part can be detached from the building plate. In case of metal 3D printing, in many cases, specific heat treatment post processing are also performed before part detaching from the building plate.

AM technologies are usually distinguished according to the adopted supply and the way the material is aggregated. Actually the most diffused AM technologies are the Powder Bed Fusion (PBF) and the Fused Deposition Modeling (FDM). In PBF powder layers are deposited on a building plate and the powder are selectively melted by a heat source following a predefined path. This technology is commonly used to produce complex shape metallic parts used in various structural applications, for example in mechanical and biomedical fields. In FDM, instead, a semi-molten plastic filament is deposited layer by layer on a building plate. In a very first time this technology was adopted only to produce non structural parts, but just prototypes. In the last years, thanks to the development of new and better performing materials, it has been adopted also to produce functional parts.

In Table 1.1 [Rombouts, 2006] we list for each technology the most significant process parameters and the processed materials for each technology.

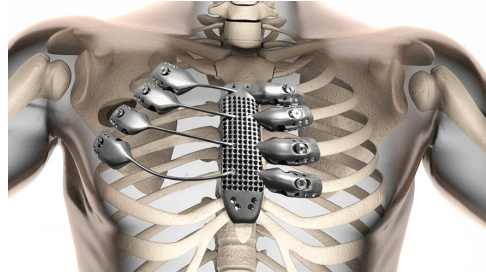
<i>Supply</i>	<i>Process</i>	<i>Lay-out</i>	<i>Layer Creation Technique</i>	<i>Phase Change</i>	<i>Materials</i>
<b>L I Q U I D</b>	<b>Stereo-lithography</b>	Liquid resin in a vat	Liquid layer deposition	Photo-polymerization	Acrylates, epoxies, filled
	<b>Fused Deposition Modeling</b>	Material melted in a nozzle	Continuous extrusion and deposition	Solidification by cooling	Polymer, wax, polymers, metals
	<b>Ink jet printing</b>	Droplets of molten material	Drop on demand deposition	Solidification by cooling	Polymers, wax
<b>P O W D E R</b>	<b>Three-dimensional printing</b>	Binder and powder in bed	Layer of powder and drop on demand deposition	No phase change	Ceramics, metals, polymers with binder
	<b>Powder Bed Fusion</b>	Powder in bed	Layer of powder	Melting and resolidification	Metals with binder, metals, ceramics
	<b>Laser cladding</b>	Powder delivery through nozzle	Continuous injection of powder	Laser melting and solidification by cooling	Metals
<b>S O L I D</b>	<b>Laminated object manufacturing</b>	Feeding, cutting and binding of sheets	Deposition of sheet material	No phase change	Polymer (foam), composites, metals, ceramics
<b>G A S</b>	<b>Selective laser chemical vapor deposition</b>	Gas flow in laser	Condensation of gas	Forming solid material from gas by chemical reaction	Metals, ceramics

Table 1.1: Additive Manufacturing processes. In light blue AM technologies analyzed in this thesis.

In figure 1.7 we show two examples of parts produced with SLM: a bike frame (a) and an artificial sternum (b). The bike frame is an example of optimized mechanical component which allows consistent material savings without decreasing the strength and the stiffness of the final part. Even if it could be (maybe) possible to produce this part with traditional machining, it would require a large amount of working time for the milling procedure and a consistent waste of material. The artificial sternum, as well as human prosthesis in general, represents an example of tailor made production, which is one of the peculiarities of additive processes. With AM in fact it is possible to produce directly patient specific prosthesis without needing of post processing operations.



(a) Bike frame



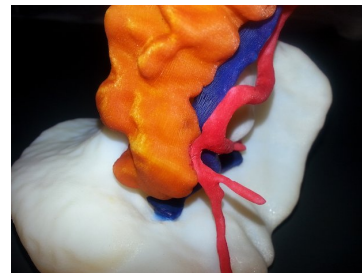
(b) Artificial sternum and ribs

Figure 1.7: Example of 3D printed functional parts produced with SLM technology. The

In figure 1.8 we show two examples of parts produced with SLM: a sprocket (a) and a human organ (b). The sprocket is a functional part that is usually produced with traditional machining, although with AM it is possible to produce only few components for specific applications without needing a production chain. The human organ, instead represents one of the most interesting applications of FDM: the reproduction of patient-specific human organs useful for the preparation of the surgery [Auricchio and Marconi, 2016].



(a) Sprockets



(b) Human organ

Figure 1.8: Examples of 3D printed FDM parts. a) and b) Metallic parts realized with SLM. c) and d) Plastic parts realized with FDM.

## 1.2 Aim of the thesis

In previous sections we have described the potential of AM technology in the fourth industrial revolution, although what has slowed down a massive diffusion of AM until now are the

relative high production costs, both in terms of AM machines and materials. Moreover, it is clear that the quality of AM parts is strictly connected to the adopted printing parameters, therefore studying the influence of those parameters is mandatory to respect the geometrical and mechanical production constraints. Since the costs of AM technologies and materials (especially metal powder) are still high, investigating the influence of printing parameters only by experimental tests is not sustainable. In this respect, developing numerical tools able to predict process failures like part distortions or fractures helps to improve the printing process allowing consistent costs savings.

In the last years the great challenge in AM industry was to develop computational tools able to simulate AM processes in reasonable time and using reasonable computational efforts.

The aim of this doctoral thesis is to analyze in detail two of the most diffused AM technologies, Selective Laser Melting (SLM) and Fused Deposition Modeling (FDM), and to develop numerical tools to simulate these processes at different scale levels.

SLM is a very complex multi-physic process which involves several phenomena including thermo-fluid dynamics and phase change. In this thesis we investigate the Lattice Boltzmann method (LBM), which is, at the author knowledge, the only method able to predict the melt pool evolution and the micro-scale characteristics of SLMed parts. We also set up a finite element method (FEM), based on sequential element activation, which is used to simulate the material deposition on the building plate and to investigate the effects of several printing parameters on temperature and residual stress distributions on a small portion of domain; moreover with FEM we simulate the production of an entire SLM part evaluating residual stress field and part displacements.

In the second part of this doctoral thesis we investigate the FDM printing process. We set up a finite element method based on sequential element activation to simulate the printing process of FDM components following exactly the informations contained in real GCode files. Two simple benchmarks are simulated and the predicted displacements are validated through comparison with experimental tests.

Nevertheless the discussed limits, the proposed simulation approaches are able to give consistent results both in SLM and FDM part distortion prediction.

### 1.3 Organization of the dissertation

The dissertation is organized as follows:

- *Chapter 2: Powder Bed Fusion.* In this chapter we describe the physical aspects of PBF and for each aspect we propose a literature review of both experimental investigations and simulation techniques. Moreover in a specific section we focus on the characteristics of the powder used in PBF and on the comparison of mechanical characteristics of traditional machined and PBFed parts. Finally we describe the principal simulation approaches underlying strengths and weaknesses for each of them;
- *Chapter 3: The Lattice Boltzmann method.* In this chapter starting from the kinetic theory of gases, we derive the Boltzmann equation and we demonstrate how this equation is an alternative way to describe at the micro-mesoscopic scale the thermo-fluid dynamic problem which is classically described at the macro-scale by the Navier-Stokes equations.

Then we derive the lattice Boltzmann method and we prove that is mathematically consistent to solve the Boltzmann equation;

- *Chapter 4*: Applications of the Lattice Boltzmann method. In this chapter we apply the Lattice Boltzmann method to solve some simple thermo-fluid dynamic problems. For each problem we show the adopted algorithm and we validate the results through a comparison with literature results and reference solutions.
- *Chapter 5*: Finite element simulation of Powder Bed Fusion. In this chapter we adopt the finite element method to set up a sequential element activation scheme to simulate the powder bed deposition and the heat source interaction with powder. We use this method to investigate the effects of several process parameters on thermal and residual stress distribution on a very small portion of domain. Finally with an homogenization approach we simulate the entire SLM process of a small component;
- *Chapter 6*: Fusion Deposition Modeling. In this chapter we describe the physical aspects of FDM and for each aspect we propose a literature review of both experimental investigations and simulation techniques. Moreover, in a specific section we focus on the characteristics of the plastic filaments used in FDM and on the comparison of mechanical characteristics of traditional prototyped and FDMed parts. Finally we describe the principal simulation approaches underlying strengths and weaknesses for each of them;
- *Chapter 7*: Finite element simulation of Fused Deposition Modeling. In this chapter we adopt the finite element method to set up a sequential element activation scheme to simulate the filament deposition in FDM. With this approach we simulate the printing process of two FDM parts using the informations contained in the GCode file; we validate the results through a comparison with experimental test.
- *Chapter 8*: Conclusions, final considerations, perspectives and on-going works.



## Chapter 2

# Powder Bed Fusion

The Powder Bed Fusion (PBF) is a group of AM technologies used to realize metallic or ceramic parts starting from a bed of powder lying on an horizontal plate. Figure 2.1 shows the working principle of a PBF machine.

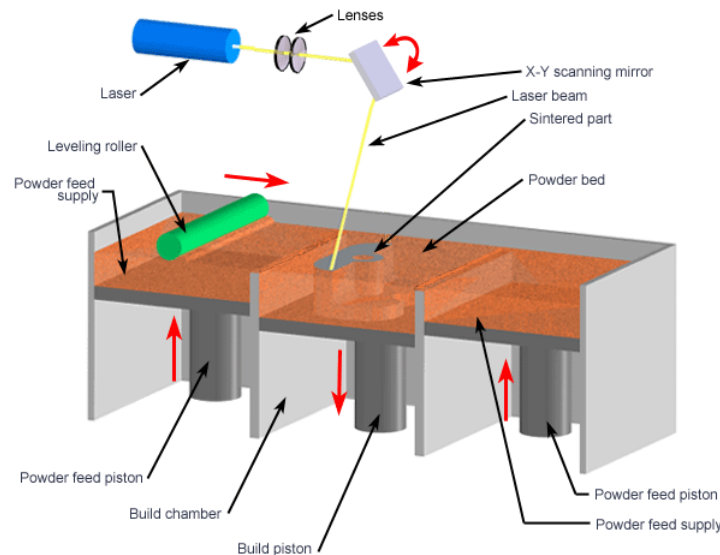


Figure 2.1: Working principle of a generic Powder Bed Fusion printer.

The PBF printing process can be summarized in the following steps:

- I. **Powder feed supply:** the powder is moved from a storage tank next to the building plate. In the example shown in Figure 2.1 the feed system consists of a moving piston, but various feeding solution are available on the market;
- II. **Preheating:** the powder are preheated to a fixed temperature, according to the selected process and the considered material;
- III. **Powder deposition:** the powder is transported on the building plate. The leveling roller moves the powder on the building plate so to obtain a layer of the desired thickness;

- IV. **Melting process:** a heat source is used to selectively melt the powder following the path defined during the the slicing process (see Figure 1.6 in Section 1);
- V. **Plate movement:** the building plate is moved down and the process restarts from point II until the final shape of the component is obtained;
- VI. **Powder removal:** at the end of the printing process the exceeding powder is stored in the tank and can be used for another print;
- VII. **Part removal:** once the part reaches the ambient temperature it is possible to remove it from the building plate;

PBF technologies can be distinguished by the adopted heat source: the Selective Laser Melting uses a YAG or CO<sub>2</sub> laser beam [S.Bremen et al., 2012], while the Electron Beam Melting (EBM) adopts an electron gun to melt the powder Murr et al. [2012]. In general a SLM machine needs a preheat treatment of the powder with a specific system, while in EBM the preheating is realized with the electron gun. On the other hand, EBM processes are performed in a vacuum chamber preventing the usage of non electrical conductive materials. Another PBF process is the Selective Laser Sintering (SLS) which differs from SLM because the powder are sintered and not completely melted [Agarwala et al., 1995].

## 2.1 Process parameters of Powder Bed Fusion printers

From 1995, when the SLM process was proposed for the first time at the Fraunhofer Institute at Aachen (Germany), a lot of companies producing PBF 3D printers born. There are several brands producing SLM or SLS machine, for example: 3DSYSTEMS, STRATASYS, EOS, RENISHAW etc., but there is just one company, Arcam, producing EBM printers.

The most important characteristics of PBF printers are listed below:

- **Heat power:** the power of the heat source is the principal parameter characterizing a PBF machine. Laser beam can vary from 100 to 1000 W, instead the electron gun can reach a 3000 W power. High heat power is suggested to melt materials with a high melting temperature (e.g. Ti6Al4V), but, in general, a 200 - 400 W heat source is enough to melt a wide range of metals (Steel, Aluminum, Nickel etc.);
- **Laser spot:** in SLM machines the laser spot can be fixed or variable. In general the range of laser spot varies from 50 to 500  $\mu\text{m}$ . Increasing the laser spot can speed up the printing process but at the same time the produced surface energy decreases inhibiting, in some cases, the complete melting of the powder;
- **Number of heat sources:** commonly, PBF machines adopt one heat source, but in the last years some companies developed machines with 2 or 4 heat sources. If the heat sources can work simultaneously the total process time can be significantly reduced;
- **Laser wavelength:** in SLM machines the laser beam, in most of cases has a fixed wavelength of 1070 nm and, with this setup, it is not possible to melt some type of powder (e.g. copper). Although there are some machines which adopt variable wavelength laser beams to treat a larger range of materials;

- **Scan velocity:** the scan velocity is a variable parameter depending on the consumer choice. With high scan velocities, keeping constant any other parameter (laser power, spot and wavelength), it is possible to speed up the printing process but at the same time, the specific surface power decreases triggering a partial powder melting;
- **Working volume:** it is a fixed characteristic of any 3D printer. It depends on the chamber volume and on the range of heat source movement on the building plate. An higher chamber volume allows the construction of bigger components, but at the same time involves a higher consumption of the inert gas filling the chamber;
- **Layer thickness:** the layer thickness is a variable parameter ranging, in most of cases from 20 to 200  $\mu m$ . A higher layer thickness speeds up the printing process but at the same time it may trigger problems to melt the deeper powder;
- **Materials:** the range of the materials that it is possible to treat with a specific machine depends, principally, from the laser characteristics. The possibility to work with a larger range of materials increases the versatility of a machine;
- **Resolution accuracy:** the resolution accuracy is a very sensitive parameter depending on laser characteristics, material and layer thickness. In general it can range from 1 to 50  $\mu m$ . A high accuracy is mandatory to achieve better results terms of surface roughness and in highly detailed parts;
- **Build envelope capacity:** it ranges, in most of cases, from 5 to 50  $cm^3/h$  and it is inversely proportional to the resolution accuracy and directly proportional to the scan velocity. It is possible to increase the printed volume rate renouncing to the geometry precision of the part and admitting the possibility of partial powder melting;
- **Multiple material:** in most of cases a PBF printer dose not allow a material change without a deep cleaning of the chamber and the feeding tank: this operation takes from 4 to 6 hours. Although there are some machines that allows a rapid change between different powder type by adopting two feeding tanks and physically dividing the building plate. On the other hand this solution decreases the physical space for the model construction;
- **Inert gas consumption:** in SLM machines, the printing process is performed in an isolated chamber filled of an inert gas, in general Argon. The gas consumption can range from 30 to 300  $l/h$ ; in addition at the start of the printing process the chamber needs to be filled of inert gas: bigger working volumes imply a higher quantity of inert gas;

In summary, we can state that most of the process parameters are related one to another and there is not an objective way to valuate the printer performances, but the optimal solution depends in any case on the characteristics of the component we have to print.

## 2.2 Powder for Powder Bed Fusion

In the last years, many types of powder have been used to produce PBFed parts and many experimentation have been conducted to characterize the mechanical behavior of the parts.

The most common powder adopted for PBF are:

- **Aluminum alloys:** e.g. AlSi<sub>12</sub> and AlSi<sub>10</sub> used to produce mechanical components for aerospace and automotive industry. It's main features are the high ratio between strength and weight and the good thermal properties that make it suitable for the realization of parts like heat exchangers. The mechanical properties of a 3D printed part produced with aluminum alloy AlSi<sub>12</sub> are listed in Table 2.1. Data distributed by 3DSystems®;

<i>Mechanical Property</i>	End of printing process	After stress relief
—	[MPa]	[MPa]
Young's Modulus	$70 \cdot 10^3 \pm 5$	$65 \cdot 10^3 \pm 5$
Ultimate strength	$470 \pm 30$	$340 \pm 30$
Yield Strength	$290 \pm 20$	$220 \pm 20$
Elongation at break	$8 \pm 2$	$10 \pm 2$

Table 2.1: Mechanical properties of a AlSi<sub>12</sub> 3D printed part before and after stress relief.

- **Stainless Steel alloys:** e.g. 316L, with a very low carbon rate, suitable for mechanical applications in aggressive environment, it grants good mechanical properties at room temperature and also at cryogenic temperatures; 17-4PH, used for various mechanical applications, it shows good mechanical properties at temperatures up to 300°C, it is suitable also for applications in slightly aggressive environment. The mechanical properties of a 3D printed part produced with stainless steel alloy 316L are listed in Table 2.2. Data distributed by 3DSystems®;

<i>Mechanical Property</i>	After stress relief	After full anneal
—	[MPa]	[MPa]
Young's Modulus	$180 \cdot 10^3 \pm 15$	$180 \cdot 10^3 \pm 5$
Ultimate strength	$660 \pm 20$	$610 \pm 30$
Yield Strength	$530 \pm 20$	$370 \pm 30$
Elongation at break	$39 \pm 5$	$51 \pm 5$

Table 2.2: Mechanical properties of a 316L steel 3D printed part after stress relief and after full anneal.

- **Titanium based alloys:** e.g Ti6Al4V with different rate of iron and oxygen contents. Composites with low contents of oxygen (TiGr23) increase the ductility of the part, but are accompanied with a slight reduction of the strength. They are used in biomedical applications like surgical implants and orthodontic appliances, which require a good fatigue strength. Composites with a higher content of oxygen increase the strength of

the part, slightly reducing the ductility. They are used for medical tools and devices in general. The mechanical properties of a 3D printed part produced with titanium alloy TiGr23 are listed in Table 2.3. Data distributed by 3DSystems®;

<i>Mechanical Property</i>	After stress relief	After isostatic pressure treatment
—	[MPa]	[MPa]
Young's Modulus	$118 \cdot 10^3 \pm 4$	$115 \pm 8$
Ultimate strength	$1160 \pm 20$	$980 \pm 30$
Yield Strength	$1060 \pm 30$	$890 \pm 50$
Elongation at break	$10 \pm 2$	$14 \pm 2$

Table 2.3: Mechanical properties of a TiGr23 3D printed part after stress relief and after isostatic pressure treatment.

- **Chromium based alloys:** e.g. CoCrF75 that allows to obtain parts with very high strength and hardness, particularly indicated for wear and part that requires high mechanical performances at high temperatures, furthermore this material forms a protective film around the part that prevents corrosive effects. Another Chromium alloy is the CoCr which allows to obtain parts with a good elasticity and a high corrosion resistance. It is suitable to produce parts that operate with high temperatures and in aggressive environment. The mechanical properties of a 3D printed part produced with chromium alloy CoCrF75 are listed in Table 2.4. Data distributed by 3DSystems®;

<i>Mechanical Property</i>	After anneal	After isostatic pressure treatment
—	[MPa]	[MPa]
Young's Modulus	$225 \cdot 10^3 \pm 5$	$225 \pm 5$
Ultimate strength	$1030 \pm 70$	$1020 \pm 70$
Yield Strength	$540 \pm 30$	$510 \pm 30$
Elongation at break	$29 \pm 6$	$29 \pm 6$

Table 2.4: Mechanical properties of a CoCrF75 3D printed part after anneal and after isostatic pressure treatment.

- **Nichel based alloys:** e.g. Ni625 which is widely used in mechanic, aerospace and chemical industry for its high strength and the very high corrosion resistance. Ni718 is characterized by the presence of small fraction of Mo that allow to obtain a good fatigue resistance in manufactured parts and good mechanical properties at very temperatures (up to  $700^\circ\text{C}$ ). Moreover Ni625 and Ni718 show excellent cryogenic properties, therefore this alloy is often used to produce parts that work in extreme conditions and aggressive environments. The mechanical properties of a 3D printed part produced with niche based alloy Ni718 are listed in Table 2.5. Data distributed by 3DSystems®;

<i>Mechanical Property</i>	End of printing process	After stress relief
—	[MPa]	[MPa]
Young's Modulus	—	—
Ultimate strength	$930 \pm 20$	$1020 \pm 70$
Yield Strength	$660 \pm 20$	$850 \pm 30$
Elongation at break	$36 \pm 2$	$31 \pm 2$

Table 2.5: Mechanical properties of a Ni718 3D printed part at the end of printing process and after stress relief.

The above mentioned properties must be considered with caution because they refers to parts produced via 3D printing with non specified process parameters. However in literature, several studies have been proposed aiming to characterize the dependence of the mechanical properties on process parameters and to compare the characteristic of 3D printed parts with the characteristics of traditionally manufactured parts.

Siddique et al. [2015] studied the influence of SLM process parameters on AlSi<sub>12</sub> parts; in particular they have investigated the micro-structure and the mechanical properties of SLMed components. In Figure 2.2, stress strain curves obtained trough tensile tests on specimens realized with different energy density are represented [Siddique et al., 2015]. The energy density is given by the ratio between the laser energy and the laser spot. We can appreciate, in particular, how, with a higher energy density the ultimate tensile strength and the elongation at break significantly increase. Finally we can observe that the ductility of part realized with high energy density is higher than the ductility of parts realized with low energy density.

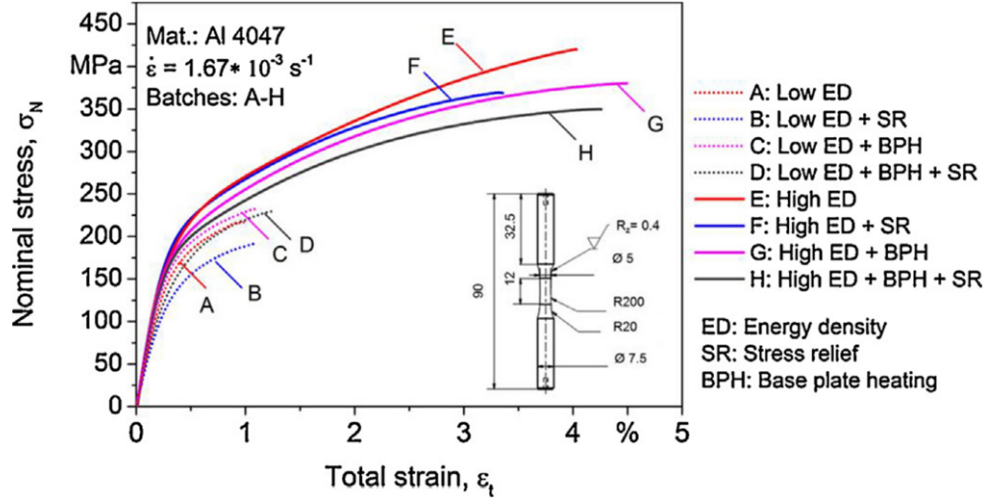


Figure 2.2: Stress strain curves obtained trough tensile tests on AlSi<sub>12</sub> specimens realized with different energy density [Siddique et al., 2015].

Prashanth et al. [2014] investigated the stress strain curves of AlSi<sub>12</sub> parts produced with SLM and with casting processes. Figure 2.3 shows the true-stress/true-strain curves obtained

with different manufacturing process. The part produced with SLM shows a higher ultimate tensile stress and a lower elongation at break than the part produced with a classic manufacturing process.

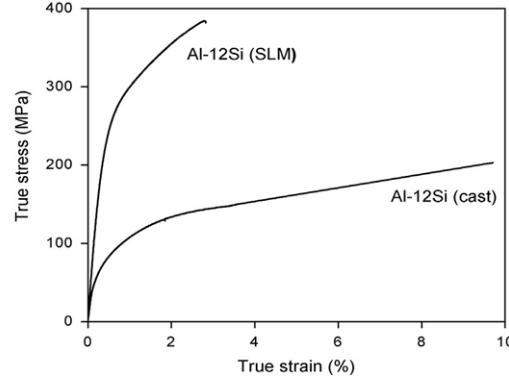


Figure 2.3: Stress strain curves obtained trough tensile tests on  $\text{AlSi}_{12}$  specimens realized with different manufacturing technology [Prashanth et al., 2014].

Furthermore, they also investigated the effects of the heat treatment on the part produced with SLM. The results, proposed in Figure 2.4 (a), show the stress-strain curves obtained with heat treatments performed at different temperatures; in Figure 2.4 (b), yield strength, tensile strength and fracture strain obtained with different annealing temperatures are displaced for both parts produced with SLM and casting process. We can observe how the heat treatment reduces the strength of the both SLMed and casted parts, while the fracture strain (i.e., the elongation at break) is significantly increased after the heat treatment.

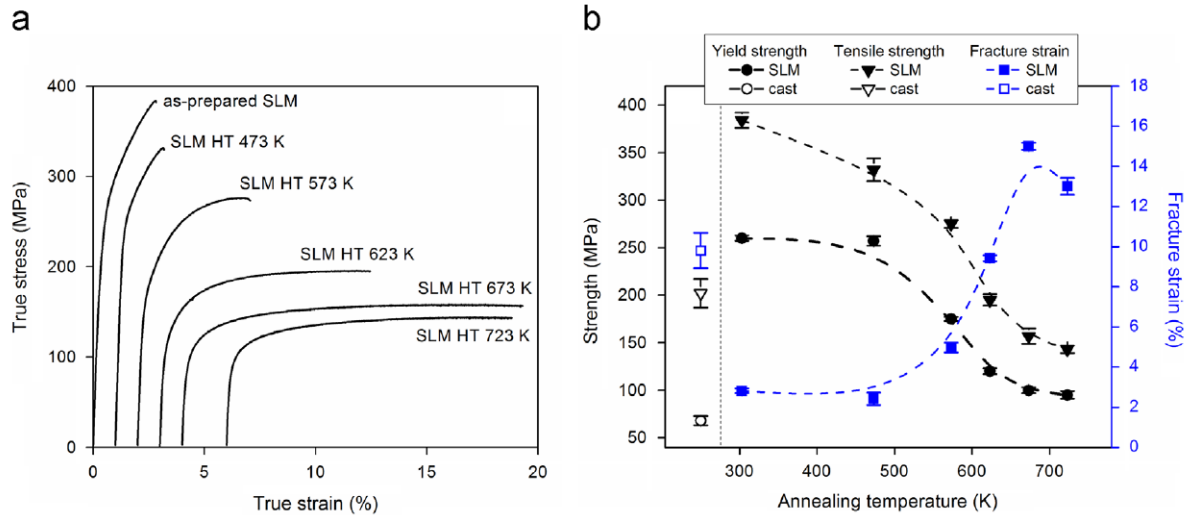


Figure 2.4: Stress strain curves obtained trough tensile tests on  $\text{AlSi}_{12}$  SLMed parts annealed at different temperatures (a). Variation of mechanical properties with the annealing temperature on SLMed and casted parts [Prashanth et al., 2014].

Song et al. [2014] studied the effects of printing parameters on a SLMed femoral component produced with CoCrMo. In particular they experimented the effects of various combinations

of laser power and scan velocity on the relative density of the part. They concluded that the energy rate assuring the highest energy density is around 0.35 J/s (see Fig. 2.5 from Song et al. [2014]).

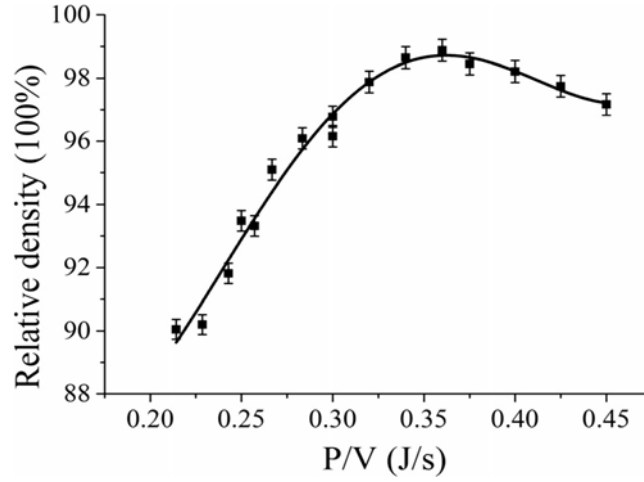


Figure 2.5: Variation of the relative density with increasing energy density on a femoral SLMed component realized with CoCrMo [Song et al., 2014].

Takaichi et al. [2013] studied the mechanical properties of CoCrMo parts produced with SLM printing process. In particular they investigated the effects of several laser power and laser spot combinations on the results of uniaxial tensile tests.

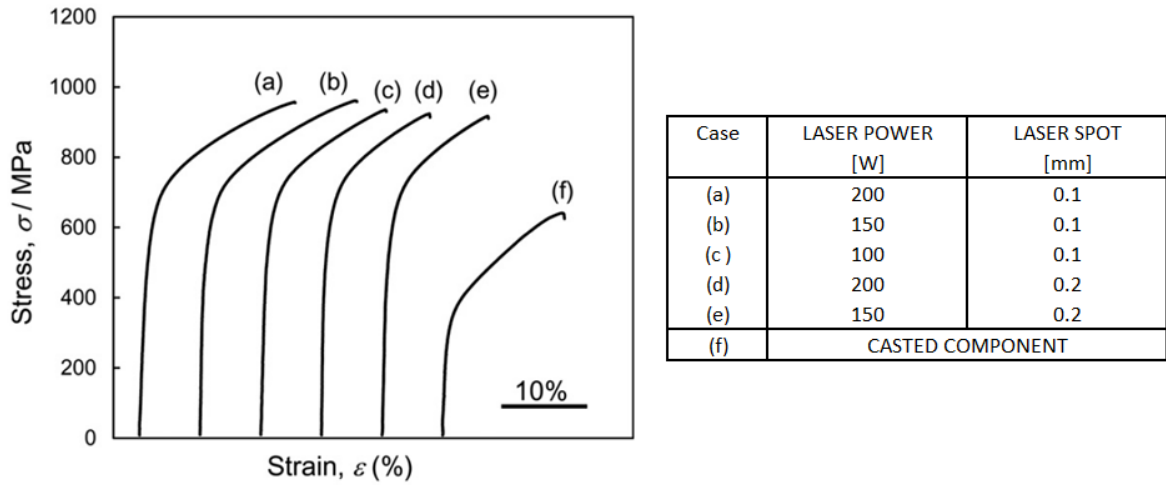


Figure 2.6: Stress-strain curves of CoCrMo parts produced with SLM printing process adopting different process parameters (a-e) and with traditional casting process (f)[Takaichi et al., 2013].

The results shown in Figure 2.6 reveal a very similar behavior of the stress-strain curves realized with various combinations of laser power and laser spot (a)-(e). Nevertheless, we can observe that the specimens realized with the highest energy densities (a,b) show higher ductility in comparison with the specimens realized with lower energy density. Finally, com-



paring the results of the SLMed specimens with the stress-strain curve of a casted component (f), we can appreciate how the SLMed specimens reveal a higher tensile strength with every combination of parameters; moreover, the specimens realized with the highest energy density (a,b) have an elongation at break very similar to the casted component. In conclusion, we can state that, according to the proposed results, the SLM parts have better mechanical properties than the part realized with a traditional manufacturing process.

Vrancken et al. [2012] studied the micro structural and the mechanical properties of Ti6Al4V parts realized with SLM printing process and they underlined the importance of the heat treatment, in order to improve the mechanical properties of SLMed components. In Figure 2.7 we can observe the stress-strain curves of parts realized with SLM, compared with the stress-strain curves of parts produced with a reference Ti6Al4V material.

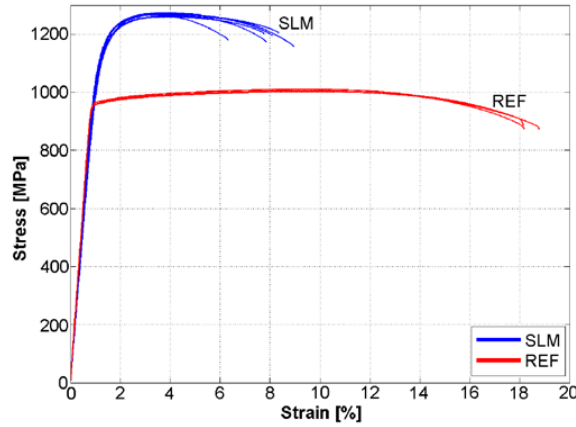


Figure 2.7: Stress-strain curves of CoCrMo parts produced SLM printing process adopting different process parameters (a-e). Stress-strain curve of a CoCrMo part realized with a traditional casting process [Vrancken et al., 2012].

We can observe that the specimens have a very similar Young's Modulus. The results of the tensile test, reveals that the SLMed parts have a higher yield stress, although they have a significant lower elongation at break, in comparison with the parts produced with a reference material.

The authors also investigated the effects of the heat treatment on the yield stress and the fracture strain of SLMed and casted parts. The heat treatment consistently reduces the fracture strain on SLMed parts, while the opposite effect is detected on casted parts. The heat treatment has almost no influence on the yield stress on SLMed parts, while the yield stress is consistently reduced after heat treatment on the casted parts.

Another very interesting study on Ti6Al4V parts produced with SLM printing process, has been proposed by Simonelli et al. [2014] who studied the influence of part orientation, during the printing, on the final mechanical properties. They concluded that the ductility of the parts is strongly influenced by the orientation; moreover, the directionality of the microstructure influences cracks formation. Figure 2.8 shows the results of tensile tests conducted on specimens built with different orientations. The specimens are analyzed at the end of the printing process (a) and after heat treatment (b). The results show a high ductility difference among specimens

realized with different orientation.

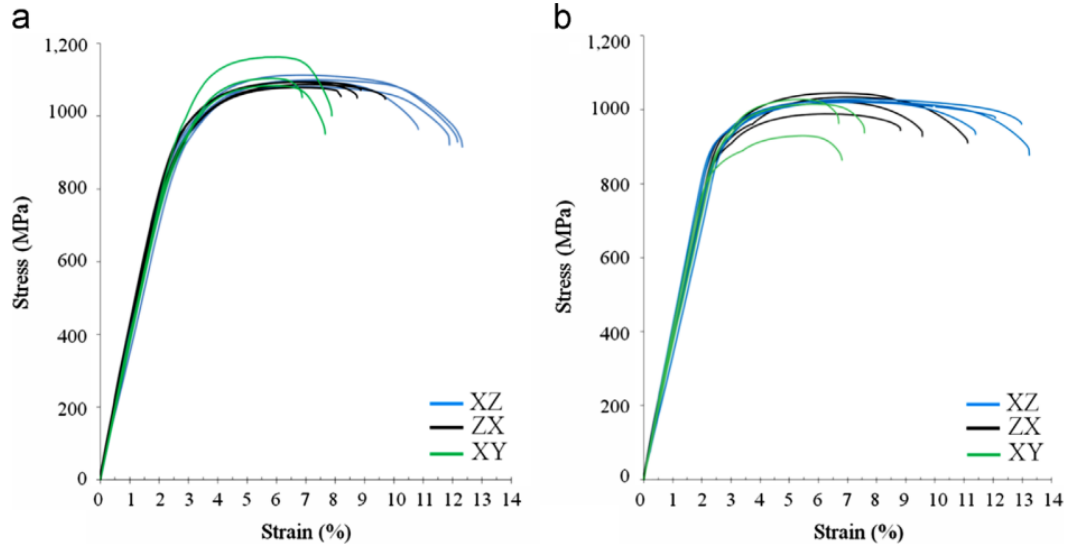


Figure 2.8: Stress-strain curves of Ti6Al4V parts produced with SLM printing process, with different built orientations. (a) Tensile tests results at the end of the printing process; (b) tensile tests results after heat treatment [Simonelli et al., 2014].

Jia and Gu [2014] studied the micro-structural properties of Ni718 parts produced via SLM. They studied the effects of the laser energy density on the relative density of the parts. They concluded that increasing the energy density allows to obtain a higher density of the part.

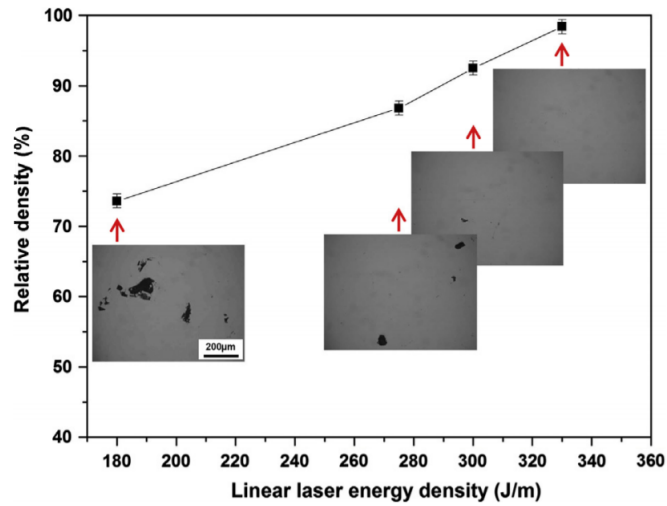


Figure 2.9: Variation of the relative density with the energy density on Ni718 parts produced via SLM [Jia and Gu, 2014].

Zhang et al. [2015] analyzed the mechanical properties of Ni718 parts produced via SLM;

moreover they investigated the effects of different heat treatments on the produced parts. The results shown in Figure 2.10 reveal a different effect of the heat treatment in comparison with the other alloys previously analyzed.

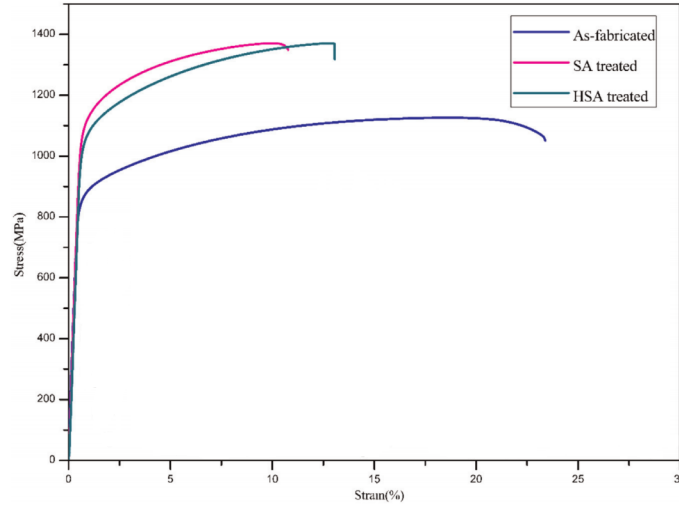


Figure 2.10: Tensile test results on SLMed Ni718 parts at the end of the printing process and after different heat treatments processes (SA and HSA) [Zhang et al., 2015].

In this case, in fact, both the SA and the HSA heat treatment produce an increasing of the yield strength but, also, a consistent decreasing of the elongation at break; therefore the heat treatment significantly reduces the ductility of the part.

Wang et al. [2012] investigated the microstructure of Ni718 parts produced via SLM. They underline that the micro-hardness of the specimens is, basically, directional independent. Furthermore they focus on the importance of the heat treatment in order to obtain the best mechanical properties. In specific they detect an average micro-hardness of 365 Hv in SLMed parts and of 470 Hv on heat treated SLMed parts.

## 2.3 Physical aspects of Powder Bed Fusion

From a physical point of view the Powder Bed Fusion (PBF) is a very complex process which involves several thermo-fluid dynamic phenomena. When the heat source scans the powder layer, very high thermal gradients rise leading the powder to the melting point. The melted powder gives rise to the so-called *melting pool* which moves among the solid particles reaching the equilibrium state and exchanging heat both with the solid particles and with the surrounding environment. When the melt pool temperature drops down, the fused material solidifies. This double phase change and the melt pool evolution are the most complex aspects in PBF processes as detailed in Kruth et al. [2007]. Figure 2.11 shows the most important aspects influencing the melt pool evolution:

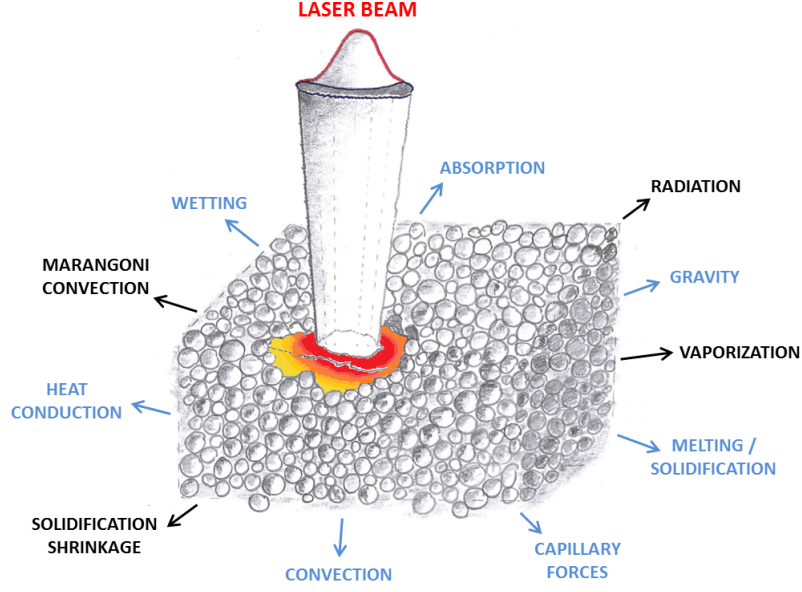


Figure 2.11: Physical phenomena rising during a Selective Laser Melting process. In light blu the principal physical aspects; in black the secondary physical effects.

where we have indicated with light blue the most important phenomena and aspects, while in black are listed the secondary ones.

The dynamics of the melt pool has a great impact on the porosity and on the surface roughness of the final part [Yadroitsev et al., 2010] furthermore, the fast cooling process may trigger a segregation between melted and solidified powder [Thijs et al., 2010]. Finally, high temperature gradients lead to the formation of residual stresses, which could significantly affect the mechanical properties of the component [Mercelis and Kruth, 2006].

In the following sections we will discuss in detail the principal and the secondary aspects acting in the PBF process.

### 2.3.1 Heat source

The heat source is a very important aspect in PBF processes, in fact the intensity of the energy distribution produced by a laser or an electron beam is fundamental in order to achieve a full melting of the powder.

The energy surface distribution of a beam, in general can be represented by a Gaussian distribution [Andrews and Phillips, 2005]:

$$I(\mathbf{x}, t) = \frac{P}{\sqrt{2\pi}\sigma} \exp\left(-\frac{(\mathbf{x} - \mathbf{v}t)^2}{2\sigma^2}\right) \quad (2.1)$$

where  $I$  is the power density in a generic point  $\mathbf{x} = \{x, y\}$  of the heated surface at time  $t$ ;  $\mathbf{v} = \{v_x, v_y\}$  is the velocity of the beam on the building plate,  $P$  is the power of the beam and  $\sigma$  is the standard deviation of the beam. The power of the beam is given by [Ammer et al., 2014a]:

$$P = V \cdot I \quad (2.2)$$

where  $V$  is the voltage and  $I$  is the current. Figure 2.12 shows the typical beam Gaussian distribution:

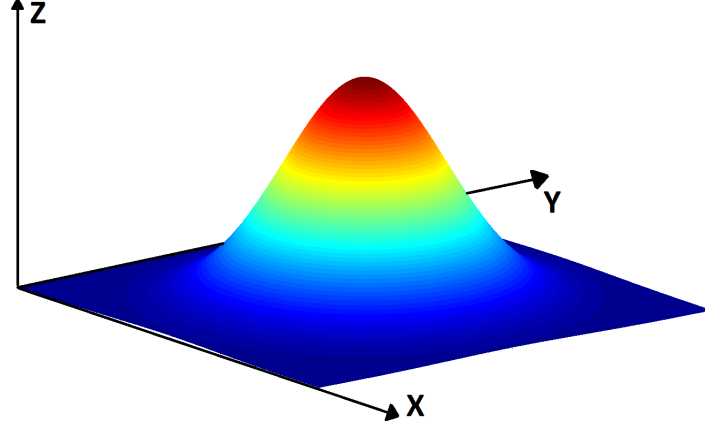


Figure 2.12: Typical Gaussian distribution of a laser or an electron beam.

The characteristics of the Gaussian distribution describe the laser setup; in particular the beam power  $P$  influences the maximum intensity of the Gaussian distribution, and the beam spot influences the standard deviation of the energy distribution.

### 2.3.2 Heat interaction with metal powder bed

When the powder bed is heated by a laser or an electron beam, the beam energy is converted in thermal energy by the absorption phenomena [Markl and Körner, 2016]. The heat conduction in absorption phenomena is governed by the following equation:

$$\rho \frac{\partial(c_p T)}{\partial t} = \nabla \cdot (k \nabla T) + \alpha I(\mathbf{x}, t) \quad (2.3)$$

where:  $\mathbf{x} = \{x, y, z\}$ ,  $\rho$  is the density,  $c_p$  is the specific heat,  $k$  is the thermal conductivity and  $\alpha$  is the absorptance, i.e the fraction of the beam energy absorbed per unit of time.

The first solution to the absorption problem of a heat source in metals was proposed by Rosenthal [1941] who developed a mathematical model to describe the heat absorption during welding and applied this model to the case of a quasi-stationary heat source [Rosenthal, 1946]:

$$T(\mathbf{x}) = \frac{q}{2\pi k} \exp\left(\frac{Vx}{2\lambda}\right) K_0\left(\frac{V \cdot R}{2\lambda}\right) \quad (2.4)$$

where  $q$  is the heat source,  $\lambda$  is the thermal diffusivity,  $K_0$  is the *Bessel* function and with

$$R = \sqrt{x^2 + y^2 + z^2}$$

Eq. 2.4 is able to predict, with good approximation the temperature distribution at a large distance from the heat source, but it is not well suited to represent the energy absorption in PBF processes since it does not takes into account the latent heat and the phase change.

The first solution taking into account also the melting process was proposed by Cline and

Anthony [1977]. With an analogous model, Brockmann et al. [2003] investigated the thermal distribution generated by a laser heat source on moving thin metal foils. Kou et al. [1981] studied the effects of a moving laser beam on a semi-infinite substrate, taking into account both the effects of the latent heat and the melting/solidification process. Finally, in literature we can find a lot of works investigating the effects of laser and scanning parameters. In particular we recall: Cheng and Lin [2000] how developed an analytical model to evaluate the thermal distribution in the laser forming of metal sheets, investigating the effects of the laser spot, the scanning velocity and the sheet thickness; and Pinkerton and Li [2004], who proposed a model to estimate the melt pool dimensions with the variation of the parameters process.

### Absorptance and thermal conductivity

In Eq. 2.3 there are two parameters that play a key role the definition of the interaction between the heat source and the powders: (i) the *absorptance*  $\alpha$  and (ii) the *thermal conductivity*  $k$ .

In pure metals, the absorptance coefficient is highly dependent on the temperature as shown by Prokhorov [2018]. In Figure 2.13 we show the variation of the absorptance with the temperature for several metal alloys. The absorptance is increasing with the temperature; in particular, in correspondence of the melting point, where it amplifies of a factor of 1-2. Moreover, it has been proved that fast growing thermal gradients lead to the instability of the melt pool may triggering an anomalous increasing of the absorptance [Debroy and David, 1995].

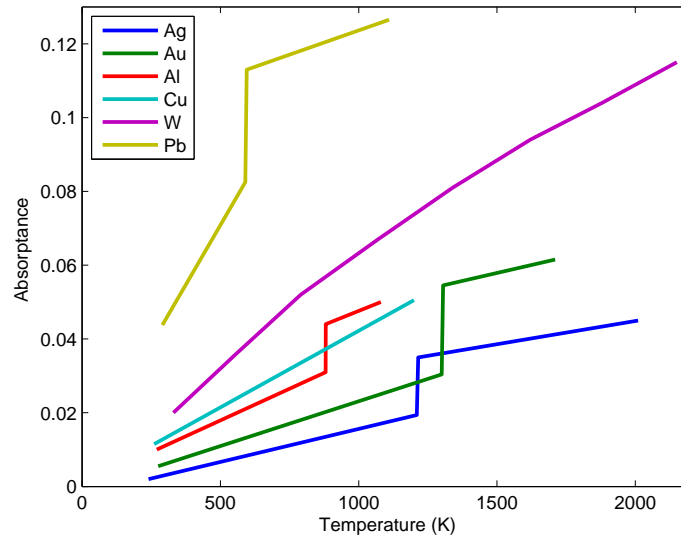


Figure 2.13: Variation of the absorptance with the temperature [Prokhorov, 2018].

The thermal conductivity  $k$  relates the heat exchanged across a surface to the perpendicular thermal gradient (*Fourier's law*). In dense materials, in general,  $k$  decreases with the temperature [Bergman et al., 2011], however, in PBF the powder bed contains a lot of pores

among the particles and almost all the parts produced with PBF processes are affected from the residual porosity  $\varphi$  [Bland and Aboulkhair, 2015]. The porosity has a significant influence on the thermal conductivity Vafai [2015]. The first model which tries to predict thermal conductivity  $k$  in a group of randomly packed perfect spheres was proposed by Maxwell [1873]:

$$\frac{k_p}{k_s} = \left( \frac{1 - 2\varphi \frac{1 - k_s/k_g}{2 + k_s/k_g}}{1 + \varphi \frac{1 - k_s/k_g}{2 + k_s/k_g}} \right) \quad (2.5)$$

with:

$$\frac{k_p}{k_s} = \frac{1 + 2\varphi}{1 - \varphi} \quad \text{for} \quad \frac{k_s}{k_g} \rightarrow \infty \quad (2.6)$$

where  $k_p$  is the thermal conductivity of the packed porous media,  $k_s$  is the thermal conductivity of the solid dense material,  $k_g$  is the thermal conductivity of the gas phase and  $\varphi$  is the ratio between the gas volume and the total volume of the domain. we remark that Eq. 2.5 is valid in the limit of low  $\varphi$ , but in PBF process the coefficient  $\varphi$  can range from 30 to 60 %. The constraint of Eq. 2.6, instead is valid for PBF processes, in fact the ratio  $k_s/k_g$  varies from 700 to 1000 which is commonly considered the infinity limit for this problem [Luikov et al., 1968]. Chiew and Glandt [1983] adapted Eq. 2.5 in order to extend the validity range from 30-60 % to  $15\% < \varphi < 85\%$ . Similar numerical methods, to valuate the thermal conductivity in regular packed powder distributions at room temperature, were proposed by Yinping and Xingang [1995] and Kou et al. [1994], however they omit to include the effects of convective and radiative flows. Although, during PBF process the high temperature gradients and the radiative effects influence the thermal conductivity. Tolochko et al. [2003] evaluated  $k$  as follows:

$$k = k_c + k_r \quad (2.7)$$

where  $k_c$  is the contact thermal conductivity and  $k_r$  is the radiative thermal conductivity which can be evaluated as follows [Zeldovich and Raizer, 2012]:

$$k_r = \frac{16LK_bT^3}{3} \quad (2.8)$$

where  $L$  is the mean photon free path between scattering events and  $K_b$  is the *Stefan-Boltzmann* constant.

### Heat absorption models

The energy absorption process has a great impact on the melting process and, in consequence, on the final quality of the PBFed part [Klassen et al., 2014]. Eq. 2.1 describes the energy distribution of a heat source on the surface of the powder bed, but it does not give any information on the variation of the energy density with depth.

In dense materials, the power density of a beam penetrating a layer of thickness  $z$  varies, in depth, according to the well-known *Beer-Lambert* law [Swinehart, 1962]:

$$\frac{dI}{dz} = -\alpha I(x, y) \quad (2.9)$$

Although, Eq. 2.9 has two strong limitations: (i) it is valid only for dense materials and (ii) it does not consider any effect of heat diffraction. In PBF process the heat is absorbed by the particle due to multiple reflections [Tolochko et al., 2000] and the thermal energy is distributed among the particles according to the density and the reflectivity [Gusarov and Kruth, 2005]. Wang et al. [2002] developed a ray tracing model to simulate the energy absorption in sparse particles distribution, and validated experimentally the results. Gusarov and Kruth [2005], instead, proposed to solve the heat radiation equation to evaluate the energy absorption in metallic powders and proposed an interesting comparison with the results obtained through the ray tracing model, showing a good agreement between the predictions of the two methods. Gusarov and Smurov [2010] developed a coupled heat radiation - heat transfer model to analyze the absorption process in SLM and to study the effects of thermal distribution on the melt pool shape. Drouin et al. [2007] set up a framework based on the Monte Carlo method able to predict the energy absorption during EBM processes. Furthermore Klassen et al. [2014] studied the energy absorption in EBM processes with a semi-empirical approach.

### 2.3.3 Solid-liquid phase change

The phase change is a very complex problem which describes the change of the state of the material. During solid-liquid phase change a certain amount of energy, referred as *latent heat*  $L_s$  is needed to win the forces that maintain the material at the solid state. The latent heat represents the enthalpy difference between solid and liquid state. In pure material, the solid-liquid phase change takes place at a fixed temperature called melting temperature  $T_m$ , in composites materials, instead, the phase change happens on a temperature interval  $T_l - T_s$ , namely, the liquid temperature and the solid temperature. The former process is called *isothermal* phase change, the latter is called *non-isothermal* phase change.

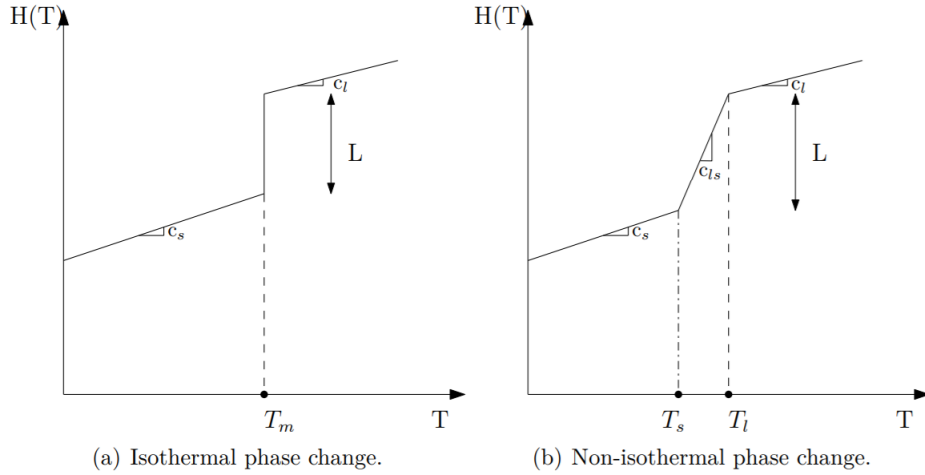


Figure 2.14: Enthalpy variation on temperature during isothermal (a) and non-isothermal (b) phase change processes [Sani, 2017].

In literature the methods adopted to describe the phase change process can be divided in three groups, according on the way they treats the boundary between the solid and the liquid part of the domain:



- Front tracking methods;
- Fixed domain methods;
- Hybrid approaches.

**Front tracking methods** divide the domain in two portions: the solid portion and the liquid portion coupled with a moving boundary describing the phase change front. This methods are very accurate since they evaluate directly the phase change front moving at every time step as well as the temperature gradient across the interface; on the other hand they are very expensive from a computational point of view and they need a starting solution.

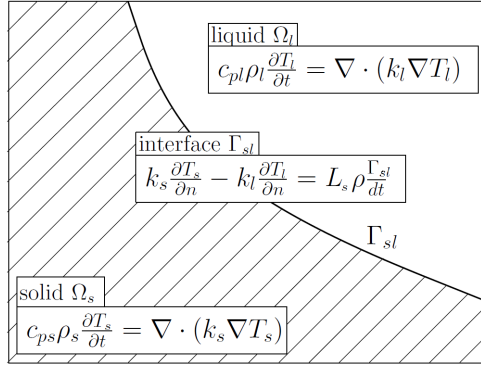


Figure 2.15: Front tracking phase change approach [Sani, 2017].

In figure 2.15, we show the equations implemented in the front tracking method. Two independent heat equations are used to describe the temperature evolution in the solid  $\Omega_s$  and the liquid  $\Omega_l$  part of the domain:

$$\begin{aligned} c_{pl}\rho_l \frac{\partial T_l}{\partial t} &= \nabla \cdot (k_l \nabla T_l) \\ c_{ps}\rho_s \frac{\partial T_s}{\partial t} &= \nabla \cdot (k_s \nabla T_s) \end{aligned} \quad (2.10)$$

where  $k_l$  and  $k_s$  are the thermal conductivities of the liquid and the solid parts, respectively and  $c_{pl}$  and  $c_{ps}$  are the specific heats of the liquid and the solid parts, respectively.

At the interface  $\Gamma_{sl}$  a specific balance condition must be satisfied; this condition, describing the thermal gradient between the solid and the liquid material, is known as *Stefan condition* and it is usually written as:

$$k_s \frac{\partial T_s}{\partial n} - k_l \frac{\partial T_l}{\partial n} = L_s \rho \frac{d\Gamma_{sl}}{dt}, \quad \mathbf{x} = \Gamma_{sl}(t) \quad (2.11)$$

where  $\Gamma_{sl}$  is the solid-liquid interface.

**Fixed domain methods** consider a single domain, governed by a single heat equation, therefore it is not necessary to impose specific conditions at the interface but the Stefan

condition is implicitly taken into account in the heat equation which is written as follows:

$$c_p \rho \frac{\partial T}{\partial t} + \rho L \frac{\partial \Gamma_{sl}}{\partial t} = \nabla \cdot (k \nabla T) \quad (2.12)$$

where  $\Gamma_{sl}$  is the solid liquid interface.

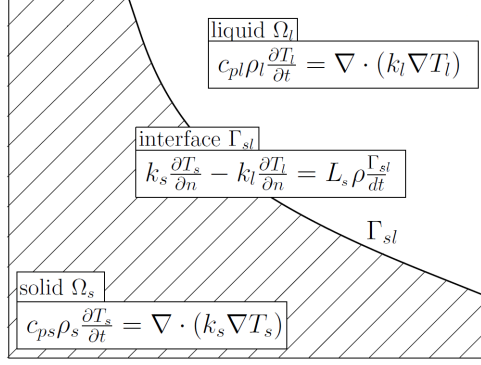


Figure 2.16: Fixed domain phase change approach [Sani, 2017].

There are three alternative methods to describe the solid liquid phase change on a fixed domain:

- Enthalpy method;
- Equivalent heat capacity method;
- Temperature transforming method.

The enthalpy method is the most common technique. It consists in writing the heat equation in terms of the enthalpy:

$$\rho \frac{\partial H}{\partial t} = \nabla \cdot (k \nabla T) \quad (2.13)$$

where the enthalpy  $H(T)$  varies with the temperature according to the selected phase change process. For example, if we consider the non-isothermal phase change, typical of metal alloys, the enthalpy is written as follows:

$$H(T) = \begin{cases} \int_{T_0}^{T_s} c_{ps}(T) dT, & T < T_s \\ \int_{T_0}^{T_s} c_{ps}(T) dT + \int_{T_s}^{T_l} \frac{\partial L_s}{\partial T} dT, & T_s \leq T \leq T_l \\ \int_{T_0}^{T_s} c_{ps}(T) dT + L_s + \int_{T_l}^T c_{pl}(T) dT, & T > T_l \end{cases} \quad (2.14)$$

Comini et al. [1974] used the enthalpy method to solve the heat conduction-convection problem with phase change in a finite element scheme. Chatterjee and Chakraborty [2005], instead, adopted the enthalpy method to describe the solid liquid phase change within a single component, single phase lattice Boltzmann method.

The equivalent heat capacity method consists in writing the heat equation in function of the specific heat:

$$\rho c_p \frac{\partial T}{\partial t} = \nabla \cdot (k \nabla T) \quad (2.15)$$

In this approach the specific heat  $c_p(T)$  varies with the temperature and the latent heat is converted into an equivalent heat capacity. Considering a non-isothermal phase change, the specific heat is given by:

$$c_p(T) = \begin{cases} c_{ps}, & T \leq T_s \\ \frac{L_s}{T_l - T_s} + \frac{c_{ps} + c_{pl}}{2}, & T_s \leq T \leq T_l \\ c_{pl}, & T > T_l \end{cases} \quad (2.16)$$

Eshraghi and Felicelli [2012] included the equivalent heat capacity model in their single-phase single component lattice Boltzmann framework to evaluate the solid liquid phase change in a representative material.

The temperature transforming method was introduced for the first time by Cao et al. [1989]. It is a kind of combination between the previous methods. The heat equation is given by:

$$\rho \frac{\partial c_p T}{\partial t} = \nabla \cdot (k \nabla T) - \rho \frac{\partial f}{\partial t} \quad (2.17)$$

where  $c_p$  is given by:

$$c_p(T) = \begin{cases} c_{ps}, & T < T_s \\ \frac{L_s}{T_l - T_s} + \frac{c_{ps} + c_{pl}}{2}, & T_s \leq T \leq T_l \\ c_{pl}, & T > T_l \end{cases} \quad (2.18)$$

and the function  $f(T)$  is given by:

$$f(T) = \begin{cases} c_{ps}(T_l - T_s), & T < T_s \\ \frac{L_s}{2} + \frac{c_{ps} + c_{pl}}{2}(T_l - T_s), & T_s \leq T \leq T_l \\ c_{pl}(T_l - T_s) + L_s, & T > T_l \end{cases} \quad (2.19)$$

We observe that, when the  $\partial f / \partial t = 0$  and  $c_p$  is independent from the position, the heat capacity model can be recovered. This method is not very diffused and in literature as been applied few times due to instability problems. D. Celentano et al. [1994] developed a finite element method to analyze phase change problems with the temperature transforming model. This approach was adopted also by Chen and Zhang [2005] who developed a finite volume scheme to analyze the phase change in selective laser sintering process.

### 2.3.4 Powder bed generation

As stressed by Wang et al. [2002] the energy absorption is dependent not only on the thermal properties of the material (conductivity and absorptance) and on the heat source, but also on the powder bed distribution. When the roller deposits the powder on the building plate, they

naturally moves reaching the stability condition; this means that the powder are not regularly displaced on the building plate. The particle position distribution can influence the absorption process promoting multiple reflection processes and causing the modification of the melted zone [Markl and Körner, 2016]. Moreover the powder distribution can influence the local porosity of the part. With this premise is clear that a correct simulation of powder distribution on the

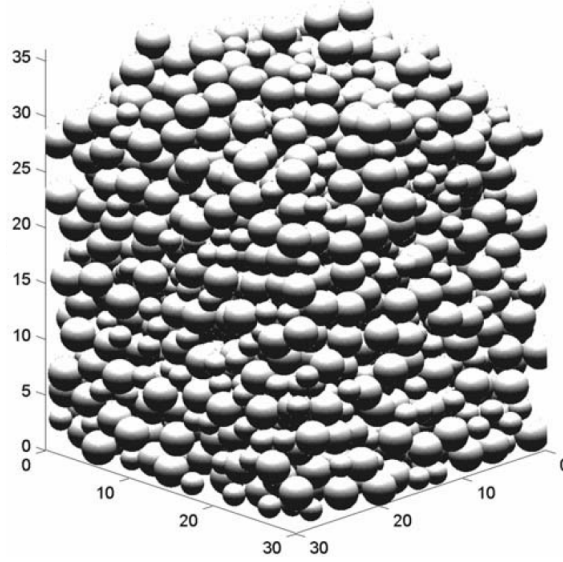


Figure 2.17: Powder packing with different powder size [Shi and Zhang, 2006].

building plate is mandatory to study correctly the melting/solidification process. In literature there are many models aiming to reproduce the powder distribution. Shi and Zhang [2006] developed a numerical model based on dropping and rolling rules to simulate the loose packing process of spherical particles moving under gravity force (Fig. 2.17). This work relies on the so-called *rain drop* model developed by [Meakin and Jullien, 1987]. The particle packing problem can be faced also with the discrete element (DE) method [Ammer et al., 2014a]. This method simplifies the packing problem neglecting cohesive and frictional forces, but it is very efficient in terms of computational times and it is able to reproduce correctly the relative density in powder bed deposition process. Finally, Zohdi [2014] developed a computational framework for additive particle deposition including inter-particle contact forces, adhesive bonding forces and electromagnetic forces which play an important rule in the interaction among very small particles ( $< 10 \mu m$ ).

### 2.3.5 Melting process and melt pool dynamics

Melting and solidification are the core of PBF processes. During the melting process the solid powder come to liquid state and moves among the other solid particles exchanging heat trough convection and conduction, furthermore part of the heat is dissipated trough the radiation with the surrounding environment. Heat exchange generates a very fast cooling effect leading to the formation of the bulk material.

The fused material is commonly known with the name of *melt pool*. The evolution of the melt pool is a typical thermo-fluid dynamic problem which is governed by the well-known

*Navier-Stokes* equations:

$$\begin{aligned}\frac{\partial \rho}{\partial t} + \nabla \cdot (\rho \mathbf{v}) &= 0 \\ \frac{\partial \mathbf{v}}{\partial t} + \mathbf{v} \cdot \nabla \mathbf{v} &= -\frac{1}{\rho} \nabla P + \nu \nabla^2 \mathbf{v} + \mathbf{g}\end{aligned}\quad (2.20)$$

and by the heat energy conservation equation:

$$\frac{\partial E}{\partial t} + \nabla \cdot (\mathbf{v} E) = \nabla \cdot (k \nabla E) + \alpha I(\mathbf{x}, t) \quad (2.21)$$

where  $\mathbf{g}$  is the gravity and  $E$  is the the thermal energy which is given by:

$$E = \int_0^T \rho C_p \Delta T + \rho \Delta H \quad (2.22)$$

Eq. 2.20 and Eq. 2.21 describe the so called *Navier-Stokes-Fourier* fluid.

The melt pool movement is principally driven by wetting, capillarity and Marangoni forces; furthermore, specially in EBM process, high power heat source can cause the partial evaporation of the powder. In the next sections we discuss in detail about this topics.

### Wetting

The wetting is the spreading behavior of a liquid on a solid surface. When a liquid comes in contact with a smooth surface, in presence of a vapor phase, at the equilibrium state, the liquid forms an angle called *contact angle* which depends on the physical and chemical properties of the liquid and the solid surface. The contact angle is described by the Young's equation [Fowkes, 1964]:

$$\cos \theta_c = \frac{\sigma_{SG} - \sigma_{SL}}{\sigma_{LG}} \quad (2.23)$$

which relates the surface tensions between the three phases: solid, liquid and gas and where  $\sigma_{sg}$ ,  $\sigma_{sl}$ ,  $\sigma_{gl}$  are the surface tension between solid-gas, solid-liquid and gas-liquid

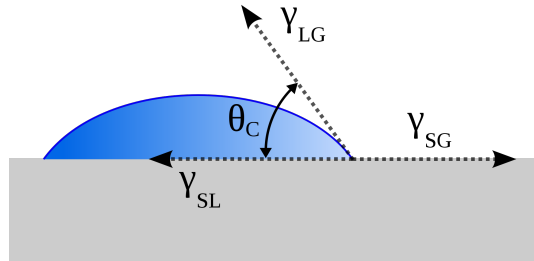


Figure 2.18: Equilibrium contact angle in wetting on a smooth surface.

Eq. 7.5 is well suited to represent the wetting on smooth and regular surfaces, but fails in describing wetting on rough surfaces and in dynamic situations. More accurate wetting models, like *Young-Duprè* model [Schrader, 1995] or *Cassie-Wenzel* model [Bormashenko et al., 2007]

allow to study the droplet spreading on rough surfaces. Furthermore Hoffman [1975] studied the wetting problem in dynamic conditions and derived that the *apparent* contact angle  $\theta_a$  in dynamic wetting is given by:

$$\theta_a = \sqrt[3]{\frac{\eta V}{C_1 \sigma_{gl}}} + \theta_c^3 \quad (2.24)$$

where *apparent* remarks the dynamic nature of the wetting angle,  $\eta$  is the dynamic viscosity,  $C_1 \approx 0.013$  is a constant of the model and  $\theta_c$  is the static wetting angle and  $V$  is the velocity of the contact line between the phases.

In melt pool dynamics, the dynamic wetting rises spontaneously and its behavior can be controlled through the *Ohnesorge* number  $O$  of the fluid:

$$O = \frac{\eta}{\sqrt{\sigma_{gl} \rho r_d}} \quad (2.25)$$

where  $r_d$  is the radius of the droplet. In specific when  $O \gg 1$  the dynamic wetting is governed by the viscous forces and when  $O \ll 1$  the dynamic wetting is governed by the inertial forces [Schiaffino and Sonin, 1997a] and the contact line velocity  $V$  can be expressed as follows:

$$\begin{aligned} V &= \frac{\sigma_{gl}}{\eta} \quad \text{with } O \gg 1 \\ V &= \sqrt{\frac{\sigma_{gl}}{\rho r_d}} \quad \text{with } O \ll 1 \end{aligned} \quad (2.26)$$

We can appreciate how the wetting angle is dependent from the dynamic viscosity  $\eta$  that in metal decreases with the temperature according to the following formula:

$$\eta = \eta_0 \exp \frac{Q}{RT} \quad (2.27)$$

where  $\eta_0$  is the viscosity at the ambient temperature,  $Q$  is the activation energy for flow and  $R$  is the universal gas constant [German, 1990].

The importance to have a good wetting behavior has been remarked by German [1984] who pointed out that in metallurgic applications a good wetting reduces the local porosity improving the mechanical properties of the component.

Several simulation frameworks have been proposed to investigate the wetting problem. Pasandideh-Fard et al. [1996] faced the simulation of a three dimensional droplet spreading on a smooth surface with the volume of fluid method. Raiskinmäki et al. [2000] used the lattice Boltzmann (LB) method to study the wetting of three dimensional droplets spreading on smooth and rough surfaces; in this work the multiphase approach developed by Shan and Chen [1993] is employed. Huang et al. [2007], using the Shan and Chen [1993] (LB) method, investigated the adhesion force between a liquid droplet and a smooth surface and developed a systematic approach to evaluate the contact angle. Attar and Körner [2009] developed a free surface lattice Boltzmann scheme, to simulate the droplet wetting problem. In this method the free surface movement is tracked with the volume of fluid approach. Moreover, Attar and Körner [2011] improved the previous framework including heat exchange, solid-liquid phase

change and wetting on rough surfaces. This method was adopted by Scharowsky et al. [2012] to simulate the powder wetting during EBM process. The results have been experimentally validated with an high speed camera monitoring the melt pool evolution during the printing process (Fig 2.19).

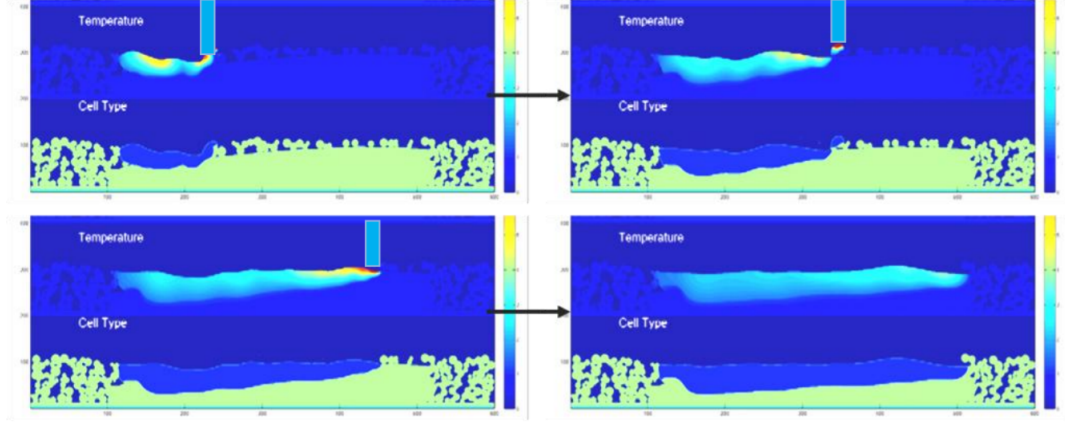


Figure 2.19: Liquid droplet wetting on rough surface after the solid-liquid phase change. Coupled thermo-fluid dynamic simulation carried out using the free surface lattice Boltzmann method [Scharowsky et al., 2012].

### Capillarity

The capillarity is the capability of a liquid to move in narrow spaces in opposition to external volume forces (e.g. gravity). Capillarity occurs due to the surface tension, generated by intermolecular forces, and the adhesion force between the fluid and the solid surfaces. During PBF process, capillarity naturally rise when the melt pool moves among the solid particles and it is often accompanied by instability problems.

The instability of liquid cylinder, free to move in space, occurs when the length of the cylinder  $L$  is greater than  $2\pi r$  and the cylinder is perturbed with a wavelength  $\lambda_r$  greater than  $2\pi r$ . When the cylinder is immersed in the gravity field, the stability condition is governed by the *Bond* ( $Bo$ ) number:

$$Bo = \frac{\rho g r}{\sigma_{lv}} \quad (2.28)$$

which expresses the ratio between the gravity forces and the surface tension. As remarked by Coriell et al. [1977], when the  $Bo$  number increases the stability limit  $L/r$  decreases, furthermore it has been proved that the liquid cylinder direction has a great impact on the stability conditions, in fact, when the filament is oriented in parallel direction to the gravity field, is less stable than when the filament is perpendicular to the gravity field [Bezdeneykh et al., 1999].

Rayleigh [1892] proposed the solution of the dynamic instability of cylinder free in space and stated that the maximal growth rate  $G_r$  (until the cylinder break) of a sinusoidal perturbation in space is given by:

$$G_r = 0.3433 \sqrt{\frac{\sigma_{lv}}{\rho r^3}} \quad (2.29)$$

and it occurs for a wavelength of  $\lambda_r = 2.8694\pi r$ . Eq. 2.29 is usually known as *Rayleigh instability* and it is valid for low viscosity fluids.



Figure 2.20: Example of *Rayleigh instability* on fluid water cylinder parallel to gravity direction.

Chandrasekar [1970] investigated the capillary instability for high viscosity fluids and pointed out that the viscosity influences the cylinder break up and the size of the generated droplets, and proposed an interesting study on the instability of liquid ferrous cylinder.

Schiaffino and Sonin [1997b] proposed an interesting study on molten liquid cylinders bounded with solid surfaces, concluding that the instability of the cylinder depends on the boundary conditions of the moving contact line. Roy and Schwartz [1999] extended the previous work to the investigation of a liquid cylinder instability on solid surfaces with various shapes, concluding that the stability limit depends on the surface geometry.

Baer et al. [2000] used the finite element method to develop a free surface scheme to simulate capillary rise near the corners of solid surfaces. Raiskinmäki et al. [2002] used the lattice Boltzmann method to simulate the capillary rise in thin pipes. Ahrenholz et al. [2008] instead adopted the multiphase Shan and Chen [1993] LB method to investigate the capillary rise in porous media. Capillary rise and depression in pipes with different diameters has been investigated also by Attar and Körner [2009] adopting a free-surface lattice Boltzmann method. Finally Ammer et al. [2014a] included the capillary effect evaluation in a complex simulation framework to simulate the thermo fluid dynamic motion of the melt pool.

Gusarov et al. [2007] applied the FV method to investigate the capillary instability in SLMed steel parts production. They studied the process with fixed laser power and varying the scan speed. They concluded that reducing the scan speed increases the stability of the melt pool. The simulation results are in accordance with experimental tests.

Zäh and Lutzmann [2010] used the finite element method to investigate the capillarity stability conditions in EBM. The authors studied the influence of different scan speeds and laser powers on the capillary instability: in particular they established a relationship between the printing parameters and the critical limit  $L/r$  which leads to melt pool fragmentation. Cheng and Chou [2013] studied the correlation between the critical limit  $L/r$  and the melt



pool area generated during an EBM process. In specific they investigated the influence of various combinations of process parameters on both the melt pool area and the instability limit.



Figure 2.21: Simulation of capillary rise and depression in pipes of different size, performed with a free surface lattice Boltzmann-method [Attar and Körner, 2009].

### Gibbs-Marangoni effect/convection

The *Gibbs-Marangoni* effect, also known as *Benard-Marangoni* convection is a thermo-capillary phenomena of fluid mass transfer between an interface due to a difference of surface tension. Keene [1988] pointed out that in liquid metal alloys, the surface tension decrease with the temperature, so during the melting process the Gibbs-Marangoni effect rise between hotter and colder zones of the melt pool.

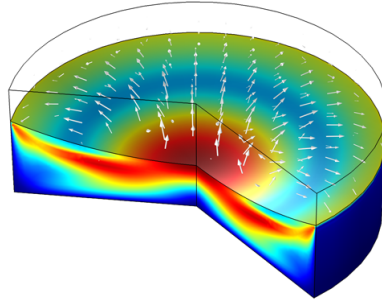


Figure 2.22: Example of Gibbs-Marangoni effect rising due to the temperature gradient between the melt pool zones.

The strength of this thermo-capillarity effect is controlled by the Marangoni number  $M_a$ :

$$M_a = \frac{\partial \sigma_{LV}}{\partial T} \frac{\partial T}{\partial s} \frac{L}{2\eta\delta} \quad (2.30)$$

where:  $\partial \sigma_{LV}/\partial T$  is the surface tension gradient,  $\partial T/\partial s$  is the surface thermal gradient,  $L$  is the characteristic length of the melt pool and  $\delta$  the thermal diffusivity.

In PBF processes the Gibbs-Marangoni convection affects both the temperature distribution in the melt pool and the melt pool shape itself [Chan et al., 1987]. Several works in literature face the problem of the Marangoni forces estimation in laser welding processes. Chan et al. [1988] demonstrated that the Marangoni convection leads to an increment of the melt

pool thickness which cannot be caught with the solution of the heat conduction equation (Eq. 2.3). Robert and Debroy [2001], instead, proposed a relationship among  $Ma$  numbers and the other non dimensional number governing a thermo-fluid dynamic problems: the Peclet's number ( $Pe$ ) and the Prandtl number ( $Pr$ ).

Qiu et al. [2015] set up a finite volume simulation to study the melt pool dynamics in SLM processes. They underlined that Marangoni forces are the main responsible of melt pool instabilities which lead to the formation of imperfections on the final part. Jamshidinia et al. [2013] developed a coupled finite element/finite volume method to investigate the melt pool dynamics, including thermo and fluid dynamics effects and the Marangoni forces estimation.

### Vaporization

Vaporization (or evaporation) can occur in PBF process when the powder bed is heated by a high power heat source. When including the liquid/vapor phase change in the thermo-fluid dynamic problem, the energy in Eq. 2.21 is given by:

$$E = \int_0^T \rho C_p \Delta T + \rho \Delta H_s + \rho \Delta H_v \quad (2.31)$$

where the latent enthalpy  $\Delta H_v(T)$  of vaporization is defined as follows:

$$\Delta H_v(T) = \begin{cases} L_v, & T > T_g, \\ L_v \cdot \frac{T - T_l}{T_g - T_l}, & T_l < T < T_g, \\ 0, & T < T_l \end{cases} \quad (2.32)$$

where  $L_v$  is the latent heat of liquid-vapor phase change,  $T_g$  is the temperature just above the vaporization point and  $T_l$  is the temperature just below the vaporization point.

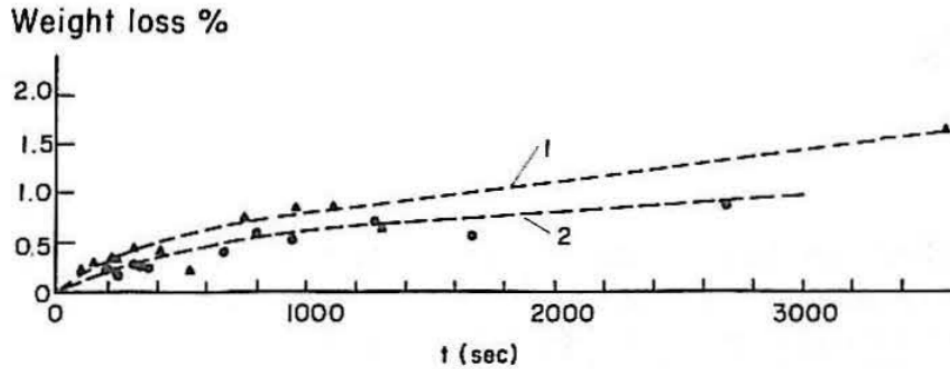


Figure 2.23: Experimental results of weight loss in 308 (1) and 309 (2) stainless steel obtained with a special long time extended welding process [Block-Bolten and Eagar, 1984].

The vaporization in PBF process can lead to the formation of a spurious pressure above the melting pool, furthermore the vapor phase can modify the heat absorption process. Boublík et al. [1973] proposed a relationship to estimate the spurious pressure in the temperature range

of the vaporization temperature  $T_v$  and the critic temperature  $T_{cr}$ :

$$P^* = P_0 \exp\left(\frac{-L_v(T - T_v)}{RTT_v}\right) \quad (2.33)$$

where  $T_v$  can be defined as  $(T_g - T_l)/2$ .

Starting from Eq. 2.33, Geiger and Poirier [1994] evaluated the evaporation rate as follows:

$$J_a = \frac{\lambda_a p_a^* C_a^5}{\rho \sqrt{2\pi M_w RT}} \quad (2.34)$$

where:  $\gamma_a$  is the activity coefficient of the component,  $p_a^*$  is the vapor pressure of the component at the current temperature,  $C_a$  is the volumetric concentration of the solute at the surface and  $M_w$  is the molar weight.

Eq. 2.33 is well suited in case of a low vaporization rate, but it is not able to predict strong vaporization behaviors. Anisimov [1996] developed the first theoretical model to predict the vaporization during laser sintering processes and studied the relation between the vacuum temperature and the evaporation rate. Knight [1979] developed a theoretical model to simulate rapid surface vaporization at the ambient temperature. Allmen and Blatter [2013] stressed the importance of the vapor pressure on the melt pool suggesting that the vapor pressure acts as a piston on the melt pool, pushing out the liquid from the pool. The authors investigate the influence of the laser spot, the liquid layer thickness and the vapor pressure on the melt pool ejection rate.

Allmen and Blatter [2013] investigated the influence of the vapor plume above the melt pool on the heat absorption rate. They underlined that the vapor cloud surrounding the melt pool modifies the incident wavefront of the heat source, furthermore when a high power heat source crosses the vapor plume, part of the vapor can condensate in sub-micro-metric droplets which can absorb, scatter and reflect a significant portion of the incident power input.

Gürtler et al. [2013] adopted the finite volume (FV) method to investigate melt pool dynamics in SLM process, including vaporization effects. Shan and Chen [1994] developed a multicomponent multiphase lattice Boltzmann scheme to simulate liquid-vapor phase transition. This method was adopted by Gong and Cheng [2012] to develop a multiphase heat transfer model with liquid-vapor phase change. The method is used to simulate bubble growing and detachment from a heated smooth surface.

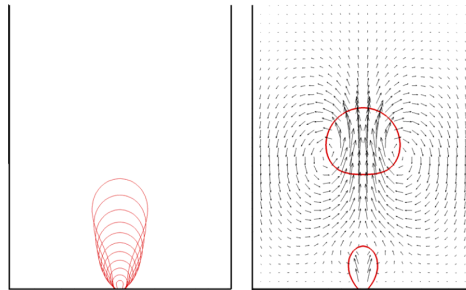


Figure 2.24: On the left: bubble growing from a heated surface. On the right: velocity field after bubble detaching from the heated surface.

Loh et al. [2015] developed a FE element method to investigate the evaporation rate in single lines of aluminum alloy realized with SLM technology with different scan speeds and laser powers. This model is able to predict the strong evaporation rate that affects the aluminum parts production; furthermore the simulation results are successfully compared to the experimental tests.

### 2.3.6 Porosity

Porosity is a big issue in PBF processes, in fact a high percentage of pores in bulk material can affect the mechanical behavior of the final component, reducing the material strength, and the fatigue resistance [Aboulkhair et al., 2014]. Porosity depends on several parameters of the printing process; in particular from: powder size and distribution, heat source power, scan velocity and scan direction [Aboulkhair et al., 2014].

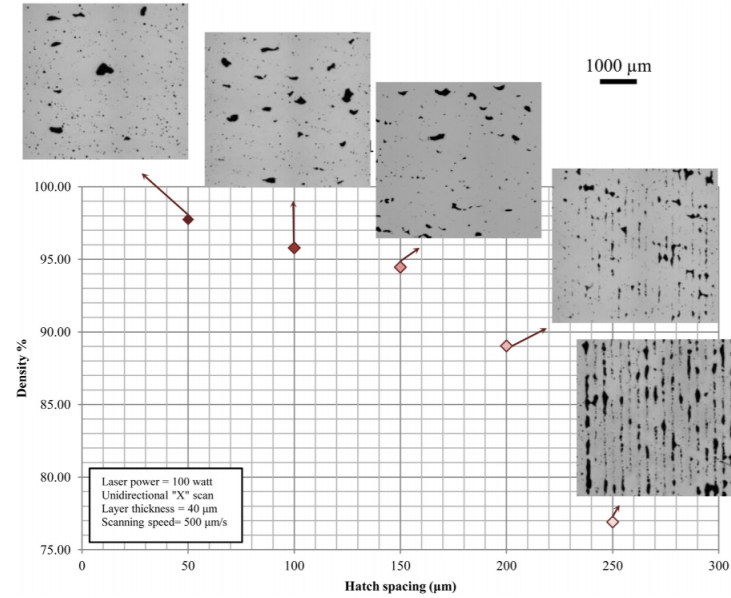


Figure 2.25: Effect of hatch spacing on part porosity [Aboulkhair et al., 2014].

From the practical experience it merges that porosity is an important problem in producing aluminum parts. One of the main causes of porosity in aluminum parts is the oxidation which can occur during the melting process on top and lateral sides of the melt pool; the contact among two oxide films generates the pores. [Louvis et al., 2011]. The oxidation of a generic metal is given by the following red-ox reaction:



Louvis et al. [2011] pointed out that in order to obtain a 100% density in SLM aluminum parts, the oxide film must be break up during the melting process. Aboulkhair et al. [2014] studied the influence of scan velocity and scan strategy on pores formation. They conclude that metallurgical pores principally rise at low scanning speeds when small gas particles are trapped into the melt pool; keyhole pores, instead rise at high scanning speeds when the rapid

cooling effect does not allow the melt pool to fill the underlying cavities. They also investigate the influence of hatch spacing in scan strategy on the resulting porosity, concluding that small hatch spacing allows to reduce part porosity, as we can appreciate in Fig. 2.27. Osakada and Shiomi [2006] stressed that high scan speeds trigger a balling effect on the top surface on the melt pool. An excessive balling effect increase the roughness of top surface, favoring keyhole pores formation.

Gürtler et al. [2013] included in their finite volume method the spurious pressure to evaluate keyhole pores formation. Bauereiß et al. [2014] adopted the lattice Boltzmann method to simulate PBF process varying the heat source power. The simulations show that with low laser power the insufficient melt pool depth and the wetting behavior give rise to a significant porosity in the part. The simulation results have been validated through experimental tests.

### 2.3.7 Surface roughness

The surface roughness is a peculiarity of parts created with PBF processes and depends on the presence of semi-molten powder on the surface of the bulk layer. In most of cases the surface roughness is an undesired effect that affects the final aspect and the mechanical properties of the parts; furthermore it is source of crack initialization [Cansizoglu et al., 2008]. In few cases, instead, the surface roughness is useful; a typical example are the mechanical implants where the surface roughness favors the contact between the mechanical part and the human bones [Rombouts et al., 2005].

The surface roughness is strongly dependent on the printing process parameters, in particular on the laser/electron beam characteristics. Gürtler et al. [2014] developed a finite volume method to investigate melt pool dynamics in SLM printing of aluminum parts and they study the effects of different powder size distributions on part porosity and surface roughness. They conclude that small size particles distribution are useful to reduce the surface roughness. Qiu et al. [2015] adopted the finite volume method to investigate melt pool dynamics in SLM parts production. The authors remark the importance of melt pool stability in order to reduce the surface roughness.

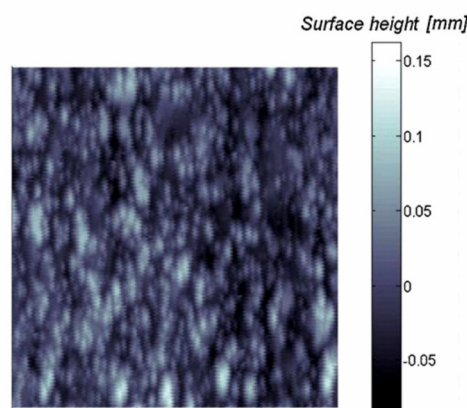


Figure 2.26: Surface profile/roughness of a surface inclined of 65 °C [Strano et al., 2013].

Strano et al. [2013] developed a mathematical model, based on experimental results, to

describe the variation of the surface roughness in function of the sloping angle.

Jamshidinia et al. [2013], instead, adopted the finite element method to investigate the effects of different hatch spacing on surface roughness in EBM. They conclude that, with the considered hatch spacings, no significant interactions between melting lines rise during the scan process, while a significant temperature difference is recovered after the cooling process. Finally they conclude that with sparser hatch spacings low temperatures on top layer surface are obtained, reducing the surface roughness. The results are validated through experimental tests [Jamshidinia and Kovacevic, 2014].

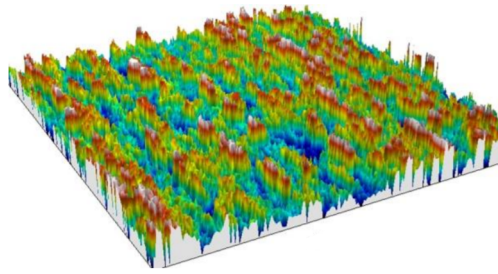


Figure 2.27: Surface roughness obtained with a hatch spacing of  $500\ \mu\text{m}$  [Jamshidinia and Kovacevic, 2014].

### 2.3.8 Residual stresses and cracking problems

During melting/solidification process high thermal gradients rise, leading to the formation of residual stresses. When the temperature increases, the material expands and the material strength decreases. The material expansion is bounded by the solid powder and once it reaches the yield stress a plastic deformation begins. When the heat source moves away from the melt pool, the melting powder starts to cool down triggering stress formation in the solidified material. Mercelis and Kruth [2006] called these stresses *residual stresses*.

Residual stress formation is strongly influenced by the temperature distribution during the printing process and by the physical constraints imposed by the support structures. In general, residual stresses can lead to high part deformations both during the printing process and after the supports removal when the residual stresses start relaxing. Fig. 2.28 shows an example of part detachment from the support structure due to the high stresses rising during the print.

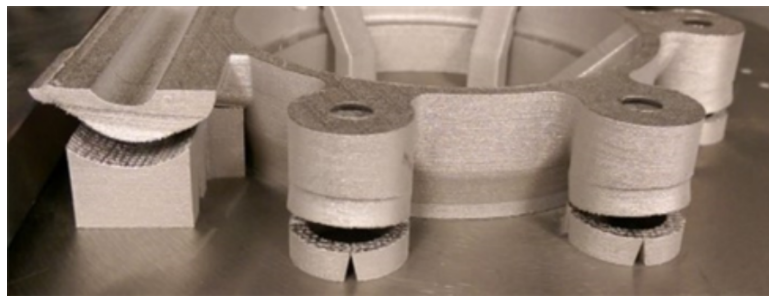


Figure 2.28: Example of part detachment from the building plate due to residual stresses.

Furthermore, when residual stresses exceed the material ultimate strength, some cracking problems can rise in the printed parts. Fig. 2.28 shows a typical example of cracks induced by residual stresses on a SLMed Stainless Steel part.

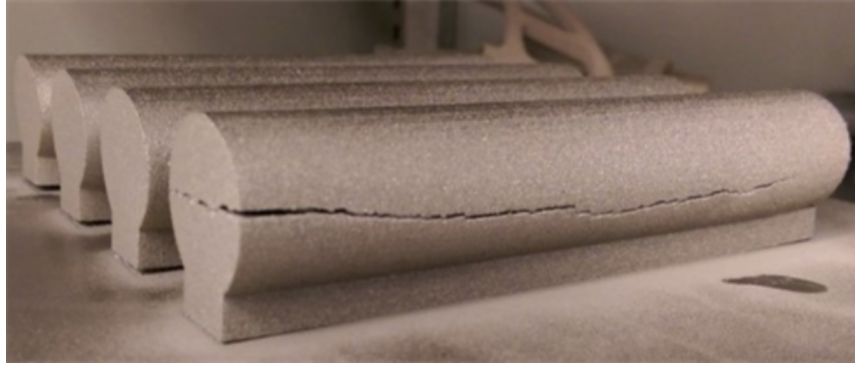


Figure 2.29: Example of crack in 3D printed part induced by residual stresses accumulation.

Mercelis and Kruth [2006] developed one of the first mathematical models to predict residual stresses in SLM parts. In this model many assumptions are taken into account: room temperature is kept constant and stresses are assumed to be constant layer by layer, but in spite of this simplifications the model is able to predict qualitatively good the residual stresses distributions.

Li et al. [2004] developed a coupled thermo mechanical finite element method, neglecting hydrodynamics effects, to investigate the dependence of residual stresses on the melt pool dynamics. Finally they relate the residual stress distributions to occurrence of the cracks detected in experimental tests. Dai and L. Shaw [2006] developed a thermo mechanical finite element method to study the SLM production of multi material dental implants of nickel and porcelain. They underlined how in multi material components the residual stresses are caused by both thermal gradients and difference between the expansion coefficients of the considered materials; in fact, because of the strong difference between the expansion coefficients of nickel and porcelain, high residual stresses arise at the interface between the two materials triggering cracks formation in the component.

Papadakis et al. [2014] investigated the residual stresses on a cantilever beam produced with SLM. They developed a uncoupled thermo mechanical finite element method, including several simplifications; the strongest ones are the homogenization of three physical layers into one layer of elements and the instantaneous application of thermal load. Nevertheless, their model is able to predict with a 25 % error the vertical part displacements.

Many other similar finite element schemes have been proposed in last years to predict residual stress distribution and parts distortions; among the other we recall the models proposed by Krol et al. [2013], Zaeh and Branner [2010] and Keller et al. [2013].

In most of those works the heat source is homogenized, the element layers correspond to several physical layers and, in some cases the scan path is not taken into account. Nevertheless, such approximations allow to predict qualitatively good stress paths and part displacements. Although, in order to predict with accuracy the stress distribution and the cracks formation it is mandatory to calculate the temperature distribution and thus to include in the calculation

the correct scan path [Seidel et al., 2014].

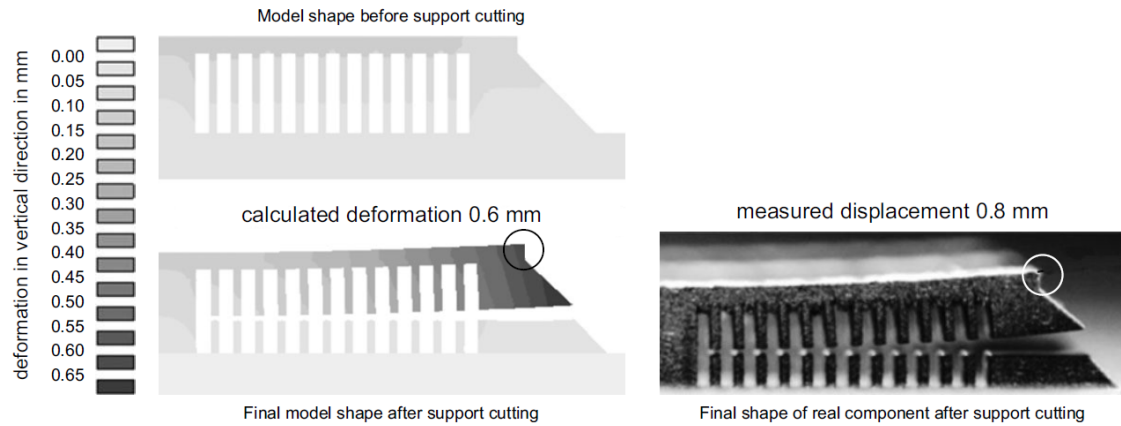


Figure 2.30: On the left: vertical displacements before and after support removal, evaluated with a thermo mechanical finite element model. On the right: experimental results after support cutting [Papadakis et al., 2014].

Li et al. [2017] developed a very accurate finite element method, to study residual stresses and part distortions in a cantilever beam produced with SLM. To reduce the computational demand they homogenize eight physical layers into one element layer, instead they follow correctly the scan path and they model the heat source.

Afazov et al. [2017] developed a coupled analytical - FEM model to predict part distortions in SLM processes. An analytical thermal model is developed to evaluate thermal functions that are then used to perform the mechanical analysis. The results are compared with experimental measurements showing a very good agreement with the experimental data. Furthermore, according to the authors, the results are obtained reducing the computational time from many days to few hours.

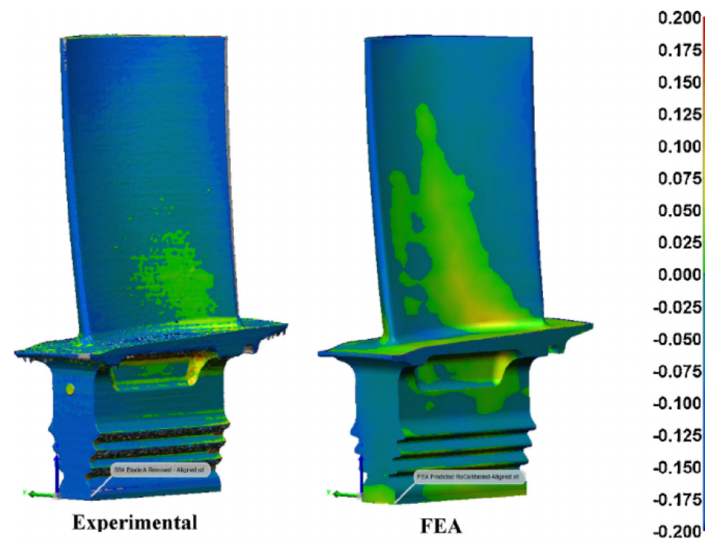


Figure 2.31: Distortion prediction in SLM part obtained with a coupled analytical - FEM model [Afazov et al., 2017].



### Cracks formation

As previously discussed a high accumulation of residual stresses can lead to cracks formation. Weisman [1976] studied hot cracks formation in welding process. From this point of view welding is very similar to SLM/EBM processes because hot cracks appear when the semi-molten material is not able to accumulate the strains induced by the shrinkage effect caused by the very fast cooling effect. The zones more subjected to hot cracking problems are the boundaries and the interfaces of the parts [Cieslak, 2002]. Furthermore it has been proved that a narrow melting-solidification temperature range reduces cracks formation. Finally Borland [1960] pointed out that the presence of gases like sulfur can favor hot cracks formation in iron-based materials.

Cieslak [2002] studied the formation of cold cracks after the solidification process. This type of cracks usually reveals after days or weeks from the part production.

Carter et al. [2014] studied the influence of the adopted laser scan strategy on the cracking behavior of nickel part produced with SLM. They proved that a *back-and-forth* scan strategy produce a more homogeneous structure characterized by regular grains which reduces the cracking occurrence.

Cracking problems can also arise from fatigue. Walker et al. [2017] evaluated fatigue cracks propagation in SLMed parts produced without heat treatment. The experiments are conducted considering different scan strategies and load magnitudes. Finally the cracks propagation is related to the porosity of the parts and the difference between the crack propagation in SLM parts and traditional manufacturing parts is investigated.

Siddique et al. [2017] investigated the effects of build plate temperature and post processing heat treatment on fatigue resistance, concluding that those parameters have a significant influence on the it. Furthermore the experimental results show that local imperfections and micro-structure can significantly increase fatigue cracks propagation.

## 2.4 Numerical simulations of Powder Bed Fusion

In previous sections we have briefly discussed about the physical aspects rising during AM processes and how they have been faced from a computational point of view. The simulation approaches can be divided in two big class according to the scale they face the problem:

- Powder level simulations
- Continuum level simulations

### 2.4.1 Powder level simulations

Powder level simulations try to solve the simulation of PBF processes at the microscopic level, typical of the powder. In general powder level simulations are adopted to investigate small portions of domain (hundreds of microns) and to study the effects of process parameters on melt pool dynamics. Furthermore they are adopted to investigate the local effects, like surface roughness and porosity, which can affect the mechanical properties of the part.

At the author knowledge, the only method which is able to solve such complicated problem is the framework proposed by Attar and Körner [2011]. This is the first model able to simulate

the solid-liquid phase change of the powder and to follow simultaneously the thermo-dynamic evolution of the melt pool. The algorithm proposed in this work is based on a free surface [Thürey et al., 2005], multi distribution [He et al., 1998] lattice Boltzmann method (LBM) and it is adopted to solve the melting/solidification problem in a 2D domain. This model is able to treat wetting, surface tension, phase-change and heat conduction-convection. They used this method to investigate melt pool evolution and balling effect during a single line scanning on a stochastic powder bed. The authors concluded that the arrangement of melt pool strongly influence balls formation and, consequently, relative density. Körner et al. [2013] used the simulation framework proposed by [Attar and Körner, 2011] to simulate the formation of a single layer of solidified material. The rain drop model is used to simulate the powder deposition. They investigated the influence of beam properties and layer thickness on the final quality of the wall. They concluded that the stochastic allocation of the powder strongly influence the wall quality, furthermore they pointed out that low scan velocities increase the final density of the part, but at the same time they increase melt pool instability and, thus, the surface roughness of the part.

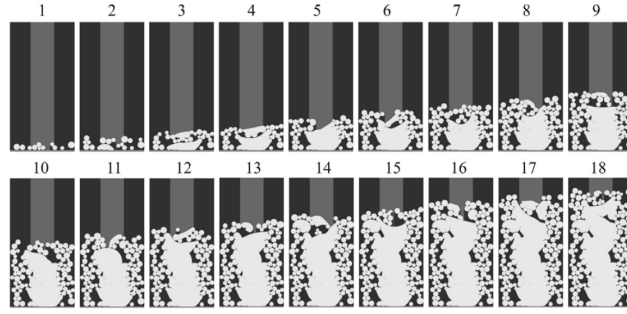


Figure 2.32: Simulation of wall construction using a free surface multi distribution lattice Boltzmann method [Körner et al., 2013].

Ammer et al. [2014a] extended this approach to three dimensions and proposed a complete simulation framework of the entire PBF process, including powder bed generation, heat source modeling and heat absorption/interaction with powder.

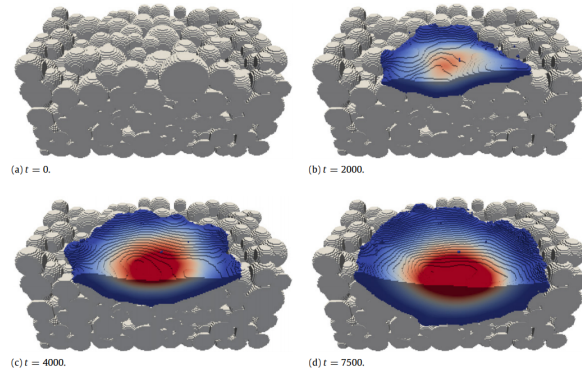


Figure 2.33: 3D simulation of EBM in a stochastic powder bed distribution [Ammer et al., 2014a].

In this method the free surface is modeled with the volume of fluid approach, which allows to evaluate the porosity as the fraction of gas trapped between the solid layer. With this method Ammer et al. [2014b] investigated a real case study which has been validated with an experimental test [Juechter et al., 2014].

A similar approach is adopted by Markl et al. [2015] to investigate the influence of process parameters on the melt pool generated by an electron beam on a single layer of powder. In this work the authors studied the influence of three process parameters on the final porosity: (i) beam power, (ii) beam spot and (iii) scan velocity. With a constant electron beam power and a constant scan velocity, the decreasing of the beam area leads to an augment of the local porosity; furthermore they show that duplicating the electron beam power, keeping constant the beam area and the scan velocities, the porosity of the part increase. This simulation approach was adopted by Markl et al. [2016] to simulate a multilayer powder bed constituted of twenty layers. The results show the presence of un-molten powder on the top of the melt pool, in particular, we notice that keeping constant the laser power and the scan velocity, the decreasing of the beam area leads to an increment of the surface roughness. In fact, higher energy density increases the instability of the melt pool, and according to Qiu et al. [2015], also the surface roughness. This simulation takes into account also the Marangoni convective flows and the evaporation.

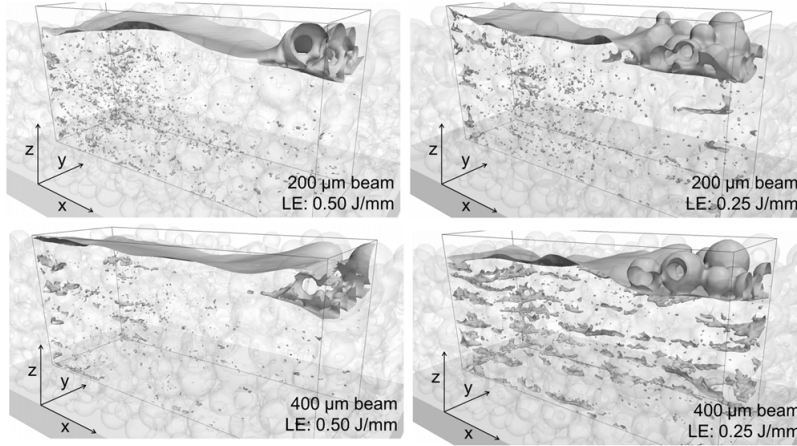


Figure 2.34: Influence of the energy density and scan speed on the local porosity in a 3D domain of multiple powder layers [Markl et al., 2016].

King et al. [2015], instead, adopted a coupled finite element/finite volume method to investigate a multilayer SLM process, although this model has some limitations: they used a continuous absorption model instead of developing a ray tracing model for heat absorption in a stochastic powder bed, moreover they do not take into account the Marangoni forces, evaporation and heat radiation. Their results show that with a higher scan speed and a higher laser power a severe balling effect occurs, due to the increasing capillary instability of the melt pool. Furthermore they investigate the effects of different scan strategies with constant laser power and scan velocity. The results show that a discontinuous track does not present a severe balling effect, but nevertheless it does not allow to avoid the fragmentation of the melt pool. In conclusion we can also notice that the results are in agreement with the

results shown by Markl et al. [2016].

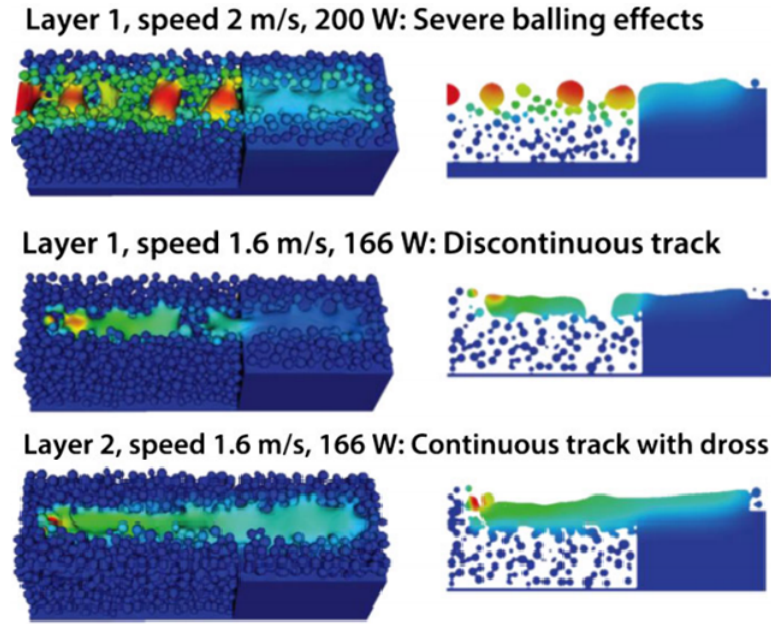


Figure 2.35: Effect of laser power and scan velocity change [King et al., 2015].

In conclusion, the powder level simulations allow to investigate with accuracy the dynamics of the melt pool and the local effects of the printing process parameters on the bulk material. Although to solve the powder level simulations, very fine computational meshes are needed. In general the element size must be of an order of magnitude lower than the powder diameter. For example let's suppose to simulate a  $1\text{mm}^3$  of domain with layers of  $40\text{ }\mu\text{m}$ ; considering a cubic element mesh of  $4\text{ }\mu\text{m}$  size we would need around 16 millions of elements. So, from a computational point of view, powder level simulations are very expensive and can be performed only with HPC computational efforts. By fact until now it is not possible to simulate at the powder level the printing process of an entire part even using supercomputers.

## 2.4.2 Continuum level simulations

Continuum level simulations are, in most of cases, used to study the PBF process at the scale of the component, in this case they can be referred as macroscopic simulations. Although, sometimes they are used also to investigate the local effects of the heat source on the powder bed. In this last case they can be considered a kind of microscopic simulation.

The main purpose of this approach is to evaluate the residual stresses rising on the component during the printing process and to evaluate the part distortions. All the macroscopic simulation approaches adopt the strong approximation to consider the powder bed as a continuous domain. Furthermore, in most of cases, they do not simulate the fluid dynamic effects, omitting the surface movement representation and neglecting wetting and surface tension effects.

The adopted meshing strategy and the time resolutions are dependent on the desired precision level of the simulation: with very fine meshes ( $\mu\text{m}$ ) and very small time steps  $\mu\text{s}$  it is

possible to study the local interaction between the heat source and the material and to follow exactly the scan strategy. Although in this case it is possible to simulate only small portions of domain ( $cm^3$ ) like in microscopic simulations, in fact in this case the typical element size is equal to the powder layer thickness.

To simulate an entire component, although, it is not possible to adopt a fine meshing strategy, but, coarser meshing strategies are needed. In general the typical element size varies between 2 and 50 times the layer height. This approach does not allow to simulate the effects of volumetric heat sources and to follow correctly the scan path, although it allows to obtain a global valuation of stress distribution and component deformations, with reasonable computational efforts.

Matsumoto et al. [2002] developed a finite element method to investigate thermal and residual stresses distribution on a single layer of powder. An uncoupled approach is adopted: first the thermal analysis is carried out, then the results of the thermal analysis are used as forcing term for the mechanical analysis. In this work the domain is assumed to be continuous and heat conduction and radiation are taken into account for the thermal analysis, while a thermo elastic constitutive model is adopted for the mechanical analysis.

Hussein et al. [2013] developed a thermo mechanical finite element method in which the scan strategy is taken into account, furthermore the heat source is modeled as a Gaussian distribution and the heat conduction with the base plate is taken into account. They conclude that the highest temperature gradient is found at the start of the printing process, while the melt pool length increases with higher scan speeds. Furthermore the authors stress the fact that the simulation is able to predict the zone that are more affected by distortions and needs particular support structures in order to obtain the desired geometry.

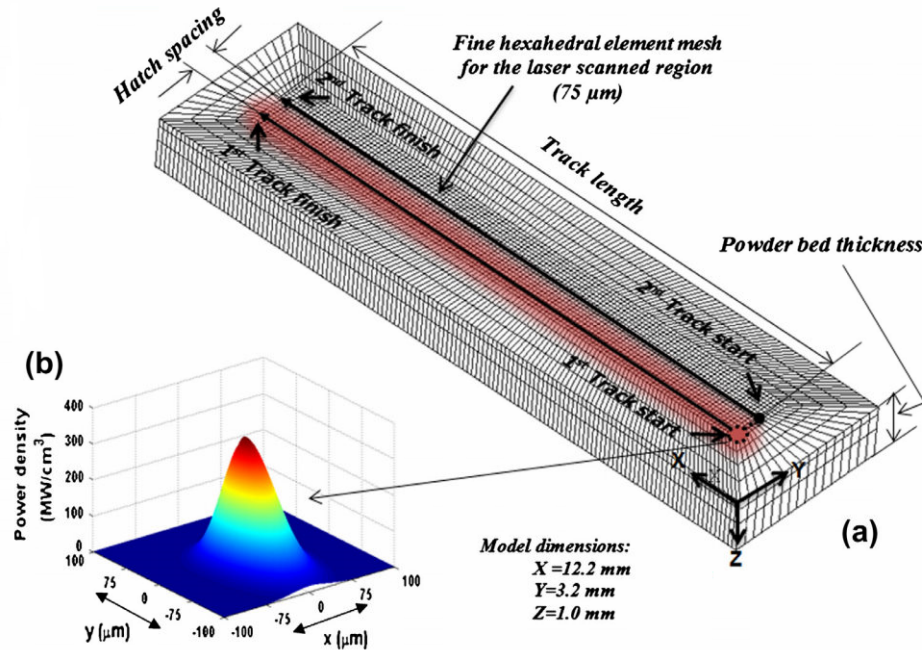


Figure 2.36: Finite element simulation SLM process of a single layer of powder which is treated as a continuum domain. Simulation approach includes the heat source modeling and the base plate [Hussein et al., 2013].

Foroozmehr et al. [2016] used the finite element method to investigate melt pool sizes during SLM process. Not only the spatial energy distribution of the laser beam, but also the beam penetration depth is taken into account. The results of the study are validated with experimental tests showing that, after a brief unstable behavior at the beginning of the first scan line, melt pool sizes stabilize and similar melt pool shapes are recovered for the subsequent scan lines.

Li et al. [2017] developed a temperature thread multi-scale model to study an equivalent body heat flux to be applied on the hatch layer and substitute the classic micro-scale heat source treatment. With this approach they reduce the computational demand allowing to simulate, layer by layer, a whole component. Finally they simulate the part detachment from the building plate and they compare the numerical distortions with the experimental results.

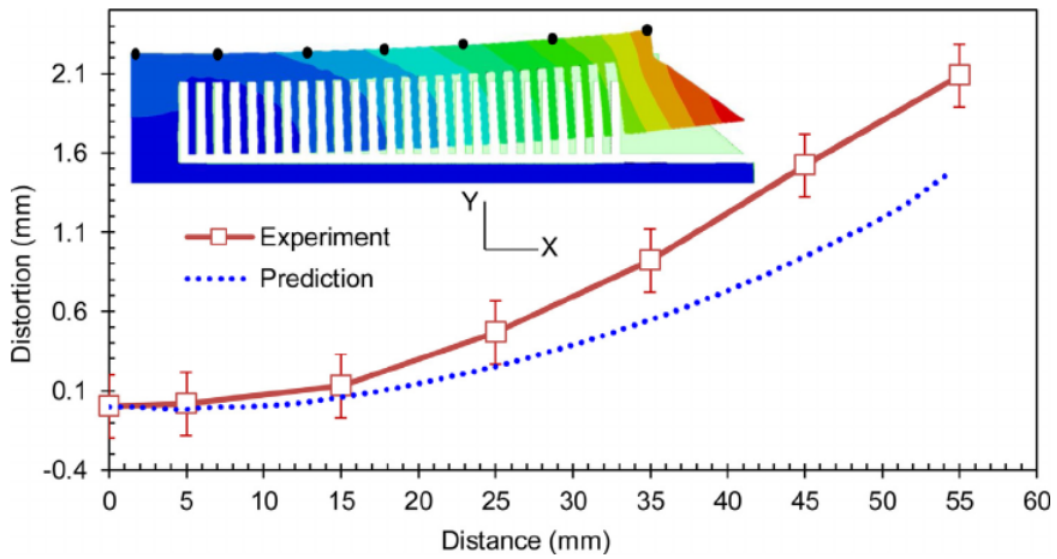


Figure 2.37: Comparison between the predicted part distortions and the experimental measurements of a cantilever beam produced with SLM [Li et al., 2017].

### 2.4.3 Multi scale approaches

Multi scale approaches aim to connect the microscopic world to the macroscopic one. In particular they try to include the information given by the powder level simulation into the microscopic simulations in order to calculate residual stresses and part distortions.

In recent years some multi scale models have been proposed; although at the state of the art is no available any multi scale model which includes the results of a powder bed analysis in a continuum scale simulation, but all the models are based on continuous approaches in which some micro-structural aspects are included in the macroscopic simulation framework.

Li et al. [2016a] developed a multi scale model, based on the finite element method, in which they integrate a micro scale laser scan model, a meso scale layer hatch model, and a macro scale part model. In the micro scale laser model the authors calculate an equivalent heat source from the energy distribution of a heat flux on scanning a layer of powder material (which is assumed to be continuous); then this equivalent heat source is included in a layer

hatch model to estimate residual stresses, and finally, the calculated residual stress field is applied to the macroscopic part, following the scan direction, in order to predict the global residual stress field. The simulation framework has been validated through the comparison with experimental data. This method is able to predict with good accuracy the part distortions with a consistent saving of computational times [Li et al., 2016b].

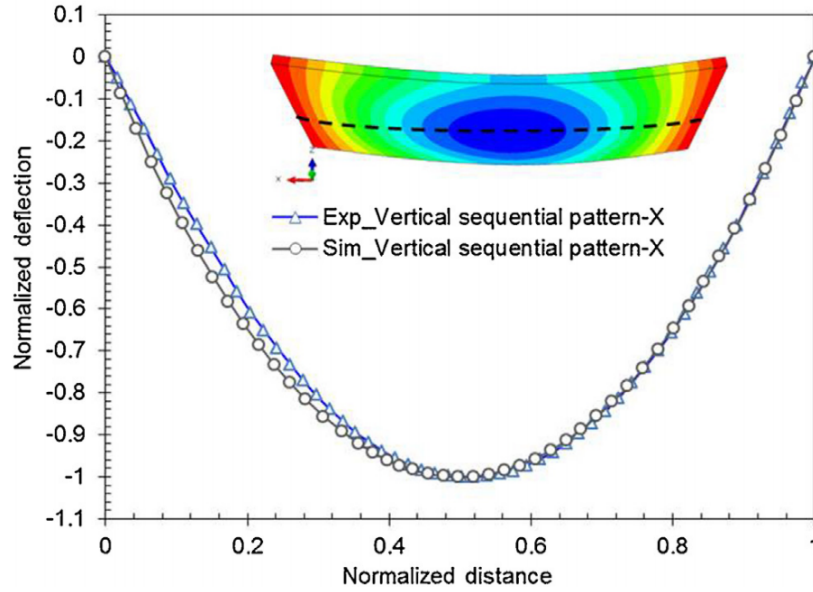


Figure 2.38: Comparison between the predicted part distortions and the experimental measurements of a plate beam produced with SLM and simulated with a multi scale simulation. [Li et al., 2016a].

Yan et al. [2015] developed a multi-scale, FEM based, approach, to simulate the electron beam interaction with the powder. The distribution of the absorbed energy is modeled using Monte Carlo simulations in front of the classical Gaussian and double ellipsoidal models. The simulation scheme is adopted to investigate the interaction between a single powder layer and the electron beam, concluding that this model is able to predict some typical phenomena, like eruption and explosion, that usually can be described only with a pure powder level simulation. Although this study is lack of an experimental validation.

Seidel and Zaeh [2018] proposed a multi scale approach in which a very accurate modeling of the heat source interaction with the powder bed is performed. The heat source absorption in the plane is estimated using the Rosenthal Equation (Eq. 2.4), while the melt pool depth is evaluated through experimental tests. The results are used to solve the temperature distribution of a single layer model; then a control volume scheme is developed to simulate the build-up of the entire part.

Li et al. [2018] pointed out that the prediction of the residual stresses in SLM parts is extremely expensive, from a computational point of view, when using a coupled thermo-mechanical FEM simulation. Moreover the authors underlined that multi-scale predictive models are necessary to reduce the computational costs and they also pointed out that scalable simulation models must be able to take into account the influence of scan strategy on residual

stresses and this is hard to obtain with a multi-layer approach in which an equivalent heat source is used. They developed a scalable predictive model based on a micro scale study of heat source interaction and meso scale hatch model where also the scan strategy is taken into account. Finally a macro scale analysis based on the concept of block layers is used to build up the part. The developed method has been used to predict the residual stresses in SLMed parts and the results have been validated with experimental measurements.

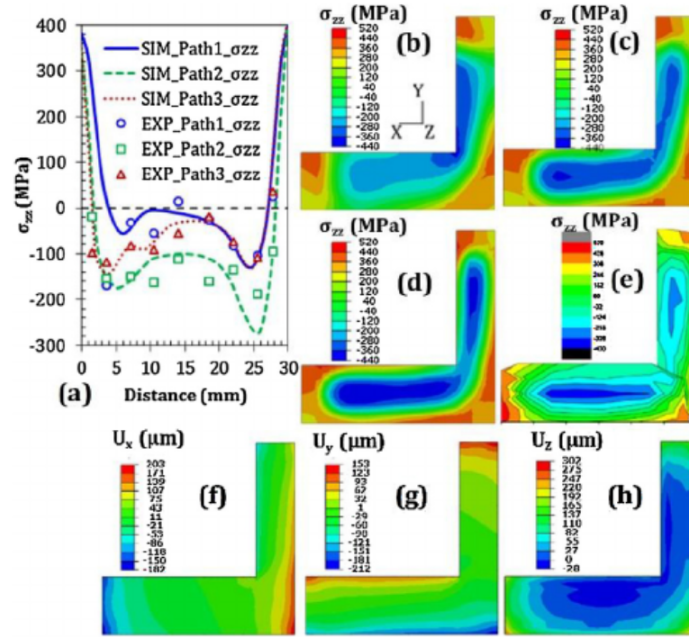


Figure 2.39: Predicted and experimentally measured vertical residual stresses on a SLMed part simulated with a multi scale approach and with different numbers of macro layers [Li et al., 2018].

#### 2.4.4 Commercial Codes for Additive Manufacturing Simulations

The continuum level simulations and the multi scale simulations of AM are based on the assumption of a continuum domain and, in general, they are performed using commercial softwares. In literature the most frequently used commercial softwares are:

- Abaqus (Simulia, USA);
- COMSOL Multiphysics (COMSOL, Inc., USA);
- ANSYS (ANSYS, Inc., USA);

Abaqus is a well know finite element code that since 2016 started the development of a tool dedicated to PBF simulations in which, two simulation approaches are proposed:

- *Microscopic* in which a very fine meshing strategy (equal or less than the layer thickness) is adopted and the heat source can be modeled to study the interaction with the powder bed, taking into account the scan strategy;



- *Macroscopic* in which a coarser meshing strategy (element layer representing several physical layers) and the heat source can be modeled to study the interaction with the powder bed, taking into account the scan strategy.

In both cases the analysis is solved using an uncoupled thermo-mechanical approach in which the results of the thermal analysis are used as forcing term in the mechanical analysis.

Next to this *classic* finite element codes, new softwares dedicated to AM simulation have been proposed in the last years. In particular we refer to:

- DIGIMAT AM (ExStream Engineering - MSC, Belgium);
- Virfac iAM (GeonX, Belgium);
- 3D Experience AM (Dassault Systemes, France);

Digimat AM is a tool developed by ExStream Engineering which allows to simulate various AM processes, including SLM and SLS. The simulation is divided in two steps:

1. A preprocessing step where several representative volume elements of material are printed, using a fully thermo-mechanical coupled analysis to identify the warpage behavior of the printed material as a function of the process parameters;
2. A structural job, where material is deposited layer-by-layer and then cooled down once the full part is built.

The warpage behavior of the representative volume is studied using the Inherent Strain Method. The software allows the definition of several printing process parameters, including the chamber temperature, the laser power, the scan spacing, the scan speed and the recoating time. Although, when the author write, the software is able to perform simulations just with a thermo-elastic constitutive model and no plastic or viscous characteristics can be taken into account. Thanks to the usage of the Inherent Strain Method and the layer-by-layer construction, the software is very fast and allows a consistent time saving in face of the classic FEM approach.

Virfac iAM is a multi-physic multi-scale software dedicated to SLM process simulation. The simulation framework is similar to the one proposed by Li et al. [2018], although at the state of the art, only the macroscopic layer-by-layer construction is available and the simulation of the build-up model is performed with the Inherent Strain Method. At the author knowledge, the micro and the meso-structural tools will use the lattice Boltzmann Method. One of the best characteristics of this software is the possibility to perform parallel computations with a super fast GPU acceleration tool. This feature allows to obtain very low computational times even on a simple desktop computer.

## 2.5 Conclusions

In this chapter, we have studied the physical effects rising in Powder Bed Fusion process and we have investigated the possible computational solutions to simulate PBF process.

PBF is a very complex process which involves several physical phenomena including wetting and phase change. In the first part of this chapter we have analyzed in detail each phenomena, focusing on the physical aspects and on the common experimental approaches; furthermore, we have proposed a brief literature review of each phenomena, focusing both on experimental studies and on computational approaches.

In the second part of this chapter we have focused on numerical simulations of Powder Bed Fusion. Simulation approaches can be divided into two big classes: powder level and continuum simulations; although in last years multiscale approaches which try to include microscale results into a macroscopic framework have been developed. We have analyzed advantages and disadvantages of each simulation approach, leaving applications of micro and macroscopic simulations to the next chapters.

## Chapter 3

# The Lattice Boltzmann Method

The Boltzmann Equation can be derived from the kinetic theory of gases (KTG). Henceforth, in the next sections, starting from the kinetic theory of gases and following step by step Boltzmann's work, we will derive the Boltzmann Equation.

### 3.1 The Kinetic Theory of Gases

In the molecular theory of matter a general volume of gases is a system with a very large number of particles moving in an irregular way. If we consider particles as mass points and assume to deal with  $N$  particles, the classical *Newton's equations*, governing the motion of the  $i$ -th particle (with  $i = 1, \dots, N$ ) can be written as:

$$\dot{\mathbf{x}}_i = \boldsymbol{\xi}_i, \quad \dot{\boldsymbol{\xi}}_i = \mathbf{F}_i \quad \rightarrow \quad \ddot{\mathbf{x}}_i = \mathbf{F}_i \quad (3.1)$$

where  $\mathbf{x}_i$  is the space position vector of the  $i$ -th particle,  $\boldsymbol{\xi}_i$  is the velocity, and  $\mathbf{F}_i$  denotes the force acting upon the  $i$ -th particle divided by the mass particle.

For a generic system of  $N$  particles, solving the time evolution problem means to know the position and the velocity  $(\mathbf{x}_i, \boldsymbol{\xi}_i)$  for each particle at each time step: this involves the resolution of  $6N$  first-order differential equations (Eq. 3.1) with  $6N$  unknowns. In order to simplify the notation it is common, and very useful, to introduce the  $6N$ -dimensional *Phase Space* with the generic element  $\mathbf{z}$  represented as follows:

$$\mathbf{z} = \begin{Bmatrix} \mathbf{X} \\ \boldsymbol{\Xi} \end{Bmatrix} \quad (3.2)$$

where  $\mathbf{X}$  is a  $3N$  dimensional space containing the  $N$  three-dimensional vectors  $\mathbf{x}_i$ , and  $\boldsymbol{\Xi}$  is a  $3N$  dimensional space containing the  $N$  three-dimensional vectors  $\boldsymbol{\xi}_i$ . It is possible to represent the time evolution of  $\mathbf{z}$  as follows:

$$\mathbf{Z} = \dot{\mathbf{z}} = \frac{d\mathbf{z}}{dt} \quad \text{with} \quad \mathbf{Z} = \begin{Bmatrix} \dot{\mathbf{X}} \\ \dot{\boldsymbol{\Xi}} \end{Bmatrix} \quad (3.3)$$

where  $\dot{\mathbf{X}}$  is a  $3N$  dimensional space containing the  $N$  three-dimensional vectors  $\boldsymbol{\xi}_i$ , and  $\dot{\boldsymbol{\Xi}}$  is a  $3N$  dimensional space containing the  $N$  three-dimensional vectors  $\mathbf{F}_i$ .

Solving such a large system is an impossible task as shown by Borel [1914]. To get over the hump, we renounce to compute the analytical solution of Eq. 3.3 and we use a probabilistic approach. In fact, it is possible to introduce a probability density function,  $P(\mathbf{z}, t)$ , representing the probability to find each particle (of the  $N$  particle system) in a certain position with a certain velocity at time  $t$ . Considering a region  $\mathbb{D}$  of the phase space, the probability to find the state  $\mathbf{z}$  inside this region is given by:

$$\text{Prob}(\mathbf{z} \in \mathbb{D}) = \int_{\mathbb{D}} P(\mathbf{z}, t) d\mathbf{z} \quad (3.4)$$

In a similar way, we can define  $P_0(\mathbf{z}) = P(\mathbf{z}, 0)$  as the probability density function representing the probability to find, at time  $t = 0$ , each particle (of the  $N$  particle system) in a certain position with a certain velocity. Under specific regularity conditions [Cercignani, 1969], we can substitute the discrete mass distribution in Eq. 3.3, with a continuous mass distribution whose density is proportional to the probability density function  $P$ . Then, applying the mass conservation principle to Eq. 3.3, we obtain:

$$\frac{dP}{dt} = \frac{\partial P}{\partial t} + \nabla \cdot (P\mathbf{Z}) = 0 \quad (3.5)$$

where  $(\nabla \cdot)$  is the classical divergence operator. Equation 3.5 is commonly known as *Liouville equation* (LE). The second addend of Eq. 3.5 can be written as follows:

$$\nabla \cdot (P\mathbf{Z}) = \mathbf{Z} \cdot (\nabla P) + P(\nabla \cdot \mathbf{Z}) \quad (3.6)$$

where the divergence of  $\mathbf{Z}$  can be written in terms of the physical variables, as following:

$$\nabla \cdot \mathbf{Z} = \sum_{i=1}^N \left( \frac{\partial}{\partial \mathbf{x}_i} \cdot \boldsymbol{\xi}_i + \frac{\partial}{\partial \boldsymbol{\xi}_i} \cdot \mathbf{F}_i \right) \quad (3.7)$$

Now, if we assume  $\mathbf{x}_i$  and  $\boldsymbol{\xi}_i$  to be independent variables and we consider the force per unit mass to be velocity independent (i.e.  $(\partial/\partial \boldsymbol{\xi}_i) \cdot \mathbf{F}_i = 0$ ), it is straightforward to write:  $\nabla \cdot \mathbf{Z} = 0$ . The second assumption is physically consistent if we assume to deal with a system of particles not immersed in a magnetic field (i.e. no Lorentz Force is acting on the particles). With those considerations, inserting Eq. 3.6 in Eq. 3.5, we can write the *Liouville's equation* in such a way:

$$\frac{\partial P}{\partial t} + \mathbf{Z} \cdot \frac{\partial P}{\partial \mathbf{z}} = 0 \quad (3.8)$$

or, in terms of the physical variables  $\mathbf{x}_i$  and  $\boldsymbol{\xi}_i$ :

$$\frac{\partial P}{\partial t} + \sum_{i=1}^N \boldsymbol{\xi}_i \cdot \frac{\partial P}{\partial \mathbf{x}_i} + \sum_{i=1}^N \mathbf{F}_i \cdot \frac{\partial P}{\partial \boldsymbol{\xi}_i} = 0 \quad (3.9)$$

Finally, if there is no force acting on the particles, we can write a simplified version of Eq. 3.9

as follows:

$$\frac{\partial P}{\partial t} + \sum_{i=1}^N \boldsymbol{\xi}_i \cdot \frac{\partial P}{\partial \mathbf{x}_i} = 0 \quad (3.10)$$

It is possible to demonstrate that Eq. 3.9 represents an alternative way to write Eq. 3.3 for a continuous system, containing, not only the informations about a given motion, but also on the motion close to the latter [Cercignani, 1969]. Another important point is that, if the initial data are given with certainty,  $P_0$  is a *Dirac Delta* function and the evolution distribution  $P$  is, likewise, a *Dirac Delta* function: in this case the center of the *Delta* function is the exact solution of the equation of motion (Eq. 3.3).

Let us consider, now, the probability density function  $P$  for a system of  $N$  particles:

$$P(\mathbf{z}, t) = P(\mathbf{x}_1, \boldsymbol{\xi}_1, \dots, \mathbf{x}_N, \boldsymbol{\xi}_N, t) \quad (3.11)$$

As stressed by Cercignani [1972], and by Boltzmann himself, it is not possible to adopt *Liouville equation* for practical purposes due to the enormous number of unknowns ( $\cong 10^{20}$ ). In order to have a more manageable equation, we need, so, to reduce the numbers of unknowns in function  $P$ .

Following Boltzmann's work, we write the evolution equation for just one particle distribution,  $P^{(1)}$ , and not for the entire system of  $N$  particles. We define  $P^{(1)}$  as the probability to find a particle with certain position and certain velocity, whatever is the state of the other particles.  $P^{(1)}$  is expressed as follows:

$$P^{(1)}(\mathbf{x}_1, \boldsymbol{\xi}_1, t) = \int_{\mathbb{C}^{N-1} \times \mathbb{R}^{3N-3}} P(\mathbf{x}_1, \boldsymbol{\xi}_1, \mathbf{x}_2, \boldsymbol{\xi}_2, \dots, \mathbf{x}_N, \boldsymbol{\xi}_N, t) d\mathbf{x}_2 d\boldsymbol{\xi}_2 \dots d\mathbf{x}_N d\boldsymbol{\xi}_N \quad (3.12)$$

where  $\mathbb{C}^{N-1}$  is the region of the physical space covered by  $N - 1$  positions of the  $N - 1$  particles.  $\mathbb{R}^{3N-3}$  is, instead, the velocity axis covered by the  $3N - 3$  velocity components of the  $N - 1$  particles. In absence of collisions,  $P^{(1)}$  must satisfy Eq. 3.10, so we can write:

$$\frac{dP^{(1)}}{dt} = \frac{\partial P^{(1)}}{\partial t} + \sum_{i=1}^N \boldsymbol{\xi}_i \cdot \frac{\partial P^{(1)}}{\partial \mathbf{x}_i} = 0 \quad (3.13)$$

In this way the problem is written in seven unknowns (three positions  $\mathbf{x}_i$ , three velocities  $\boldsymbol{\xi}_i$  and the time  $t$ ).

Accordingly, approaching the one particle problem from a probabilistic point of view is quite simple. However, as suggested by Boltzmann, the problem gets much more complex if we intend to write the dynamic of a particle considering the possibility of collision with a second particle. We assume, for simplicity, that the particles have the same dimensions (diameter  $\sigma$ ); the probability of a collision depends on the probability to find another particle at the distance of diameter from the considered one. We need, so, another probability density  $P^{(2)} = P^{(2)}(\mathbf{x}_1, \boldsymbol{\xi}_1, \mathbf{x}_2, \boldsymbol{\xi}_2, t)$  which states the probability to find particle 1 in position  $\mathbf{x}_1$  with velocity  $\boldsymbol{\xi}_1$  and particle 2 in position  $\mathbf{x}_2$  with velocity  $\boldsymbol{\xi}_2$  at time  $t$ . Similarly to  $P^{(1)}$ , we can

evaluate  $P^{(2)}$  as follows:

$$P^{(2)}(\mathbf{x}_1, \boldsymbol{\xi}_1, \mathbf{x}_2, \boldsymbol{\xi}_2, t) = \int_{\mathbb{C}^{N-2} \times \mathbb{R}^{3N-6}} P(\mathbf{x}_1, \boldsymbol{\xi}_1, \mathbf{x}_2, \boldsymbol{\xi}_2, \dots, \mathbf{x}_N, \boldsymbol{\xi}_N, t) d\mathbf{x}_3 d\boldsymbol{\xi}_3 \dots d\mathbf{x}_N d\boldsymbol{\xi}_N \quad (3.14)$$

where  $\mathbb{C}^{N-2} \times \mathbb{R}^{3N-6}$  is easily defined as an expansion of the integral domain in Eq. 3.12.

In order to define the evolution equation of this system of two particles, we have to investigate what happens during the collision between the particles. Fig 3.1 represents the collision between particle 1 and particle 2:  $\boldsymbol{\xi}'_1 - \boldsymbol{\xi}'_2$  is the difference between particle velocities coming closer before collision, while  $\boldsymbol{\xi}_1 - \boldsymbol{\xi}_2$  is the difference between particle velocities moving away after collision.

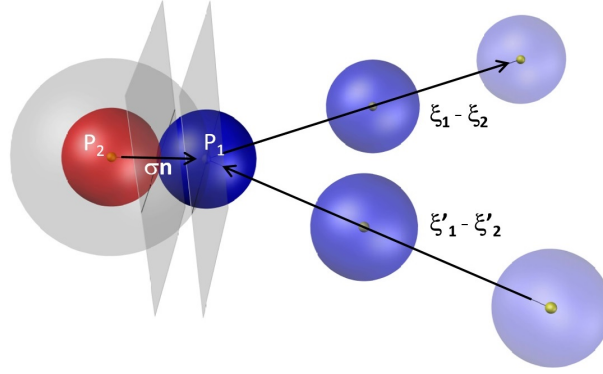


Figure 3.1: Incoming and outgoing velocity difference between colliding particles.

For sake of simplicity, we introduce the following quantities:

$$\mathbf{v} = \boldsymbol{\xi}_1 - \boldsymbol{\xi}_2 \quad \text{and} \quad \mathbf{v}' = \mathbf{v} - 2\mathbf{n}(\mathbf{n} \cdot \mathbf{v}) \quad (3.15)$$

To evaluate the effects of the collisions between the particles, we refer to Fig. 3.2. Let us consider a point,  $\mathbf{x}_1$ , on the sphere surface, we define  $\sigma\mathbf{n}$  as the vector joining the center of the sphere  $\mathbf{x}_2$  and the point  $\mathbf{x}_1$ . We consider, also, an area  $dS$  (green area around  $\mathbf{x}_1$ ) defined as  $dS = \sigma^2 d\mathbf{n}$ , where  $d\mathbf{n}$  is the area of an element on the surface of the sphere around  $\mathbf{n}$ . On  $dS$  we can construct a cylinder containing the particles hitting  $dS$  in the time  $t + dt$ . The height of that cylinder is defined as  $|\mathbf{v}_1 \cdot \mathbf{n}|dt$ .

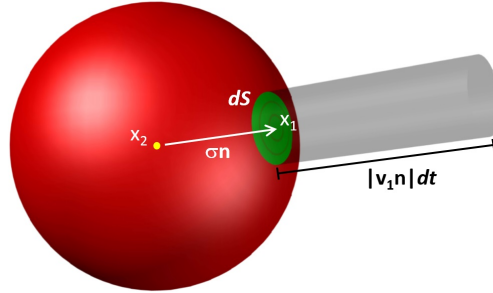


Figure 3.2: Probability of collision between particles.

We introduce the probability,  $P^c$ , of collision between the particle 1 and the particle 2 in the elements of volume:  $(\mathbf{x}_1, \mathbf{x}_1 + d\mathbf{x}_1), (\boldsymbol{\xi}_1, \boldsymbol{\xi}_1 + d\boldsymbol{\xi}_1), (\mathbf{x}_2, \mathbf{x}_2 + d\mathbf{x}_2), (\boldsymbol{\xi}_2, \boldsymbol{\xi}_2 + d\boldsymbol{\xi}_2)$ .  $P^c$  is expressed as follows:

$$P^c = P^{(2)}(\mathbf{x}_1, \mathbf{x}_2, \boldsymbol{\xi}_1, \boldsymbol{\xi}_2, t) d\mathbf{x}_1 d\boldsymbol{\xi}_1 d\boldsymbol{\xi}_2 \times \sigma^2 d\mathbf{n} |\mathbf{v}_1 \cdot \mathbf{n}| dt \quad (3.16)$$

Now, if we want to evaluate the probability of collision,  $P_f^c$ , between particle 1 and 2 when the position ( $\mathbf{x}_2$ ) and the velocity ( $\boldsymbol{\xi}_2$ ) of the particle 2 are fixed, we need to integrate Eq.3.16 on  $\boldsymbol{\xi}_1$ . During this operation it is convenient to discern between two situations as shown in Fig. 3.3. When the particles are coming closer, according to the definition of vector  $\mathbf{n}$ , the quantity  $\mathbf{v}_1 \mathbf{n}$  is negative, while, when the particles are moving away after collision  $\mathbf{v}_1 \mathbf{n}$  is positive.

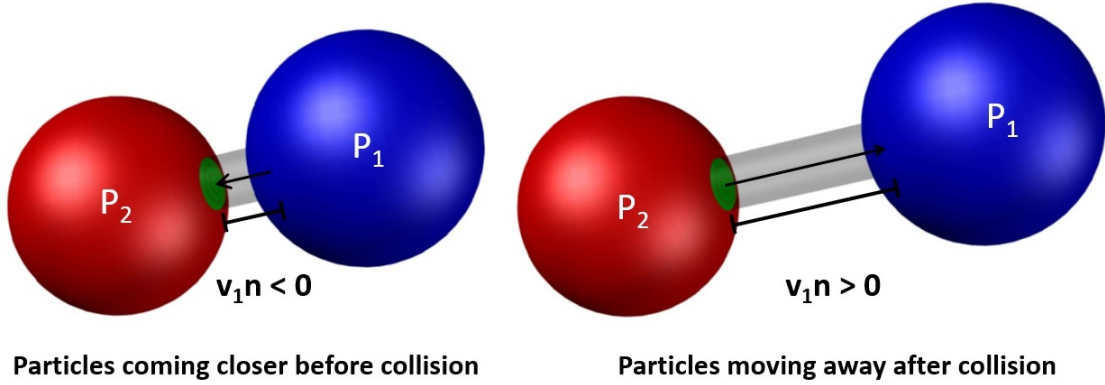


Figure 3.3: Height of the cylinder before and after collision of the two particles.

Finally, after some mathematical computations the  $P_f^c$  is expressed as:  $P_f^c = G - L$  with:

$$\begin{aligned} G &= (N-1)\sigma^2 \int_{\mathbb{R}^3} \int_{\mathbb{B}_+} P^{(2)}(\mathbf{x}_1 \boldsymbol{\xi}_1, \mathbf{x}_1 + \sigma \mathbf{n}, \boldsymbol{\xi}_2, t) |(\boldsymbol{\xi}_2 - \boldsymbol{\xi}_1) \cdot \mathbf{n}| d\boldsymbol{\xi}_1 d\mathbf{n} \\ L &= (N-1)\sigma^2 \int_{\mathbb{R}^3} \int_{\mathbb{B}_-} P^{(2)}(\mathbf{x}_1 \boldsymbol{\xi}_1, \mathbf{x}_1 + \sigma \mathbf{n}, \boldsymbol{\xi}_2, t) |(\boldsymbol{\xi}_2 - \boldsymbol{\xi}_1) \cdot \mathbf{n}| d\boldsymbol{\xi}_1 d\mathbf{n} \end{aligned} \quad (3.17)$$

where  $B_+$  is the part of domain containing the particles coming closer after collision;  $B_-$ , instead, is the part of domain containing the particles moving away after collision.  $L$  and  $G$  can be viewed, respectively, as *loss* and *earning* terms in the sense that  $L d\mathbf{x}_1 d\boldsymbol{\xi}_1 dt$  is the total number of attended particles with position between  $[\mathbf{x}_1; \mathbf{x}_1 + d\mathbf{x}_1]$  and velocity between  $[\boldsymbol{\xi}_1; \boldsymbol{\xi}_1 + d\boldsymbol{\xi}_1]$  which exit from those intervals due to collisions.  $G d\mathbf{x}_1 d\boldsymbol{\xi}_1 dt$  is the analogous number of particles entering the same intervals.

Finally, inserting Eq. 3.17 in Eq. 3.13 and considering  $P^{(2)}$  in place of  $P^{(1)}$ , we can write the evolution equation for a system of two particles including the possibility of collisions:

$$\frac{dP^{(2)}}{dt} = \frac{\partial P^{(2)}}{\partial t} + \sum_{i=1}^N \boldsymbol{\xi}_i \cdot \frac{\partial P^{(2)}}{\partial \boldsymbol{\xi}_i} = G - L \quad (3.18)$$

### 3.2 The Boltzmann Equation

As remarked by Boltzmann, Eq. 3.18 is by far to be eligible for practical purposes. In fact, the probability to find a particle  $P^{(1)}$  with certain position and velocity still involves the probability  $P^{(2)}$  (Eq. 3.17), which is very complicated to evaluate. To simplify the problem, Boltzmann introduced some hypotheses:

- The evolution equation (Eq. 3.18) is valid in the *Boltzmann-Grad* limit, namely when the number of particles  $N \rightarrow \infty$  and the diameter  $\sigma \rightarrow 0$ . Under these conditions the product  $N\sigma^2$  remains finite [Cercignani, 1972]. This hypothesis is clearly consistent, in fact, considering, for example a small domain of gas we have:  $N \cong 10^{20}$  and  $\sigma \cong 10^{-10}m$ ;
- The collision between two particles is a quite rare event [Cercignani, 1972] in fact the volume occupied by the  $N$  particles is  $N\sigma^3 \cong 10^{-10}m^3$ ;
- If the collision between two particles is a rare event, it is reasonable to consider the probability to find particle 1 in position  $\mathbf{x}_1$  with velocity  $\boldsymbol{\xi}_1$  and the probability to find particle 2 in position  $\mathbf{x}_2$  with velocity  $\boldsymbol{\xi}_2$  at time  $t$ , *stochastically independent* (i.e. the correlation coefficient between the probability density functions is 0). This hypothesis is commonly known as *Molecular Chaos* or *Stosszahlansatz*. Applying the Molecular Chaos to  $P^{(2)}$  we finally obtain:

$$P^{(2)}(\mathbf{x}_1, \boldsymbol{\xi}_1, \mathbf{x}_2, \boldsymbol{\xi}_2, t) = P^{(1)}(\mathbf{x}_1, \boldsymbol{\xi}_1, t)P^{(1)}(\mathbf{x}_2, \boldsymbol{\xi}_2, t) \quad (3.19)$$

Now, by inserting Eq. 3.19 into Eq. 3.17 and applying the *Boltzmann-Grad* limit, terms  $G$  and  $L$  can be written as follows:

$$\begin{aligned} G &= N\sigma^2 \int_{B_+} \int_{\mathbb{R}^3} P^{(1)}(\mathbf{x}_1, \boldsymbol{\xi}'_1, t)P^{(1)}(\mathbf{x}_1, \boldsymbol{\xi}'_2, t)|(\boldsymbol{\xi}_2 - \boldsymbol{\xi}_1) \cdot \mathbf{n}|d\boldsymbol{\xi}_2 d\mathbf{n} \\ L &= N\sigma^2 \int_{B_-} \int_{\mathbb{R}^3} P^{(1)}(\mathbf{x}_1, \boldsymbol{\xi}_1, t)P^{(1)}(\mathbf{x}_1, \boldsymbol{\xi}_2, t)|(\boldsymbol{\xi}_2 - \boldsymbol{\xi}_1) \cdot \mathbf{n}|d\boldsymbol{\xi}_2 d\mathbf{n} \end{aligned} \quad (3.20)$$

where  $N$  is the number of particles,  $\sigma$  is the diameter of a particle,  $\boldsymbol{\xi}'_1$  and  $\boldsymbol{\xi}'_2$  are the particle velocities before the collision and  $\boldsymbol{\xi}_1$  and  $\boldsymbol{\xi}_2$  are the velocities after collision. By inserting Eq. 3.20 in Eq. 3.18 we obtain the first formulation of the *Boltzmann Equation*:

$$\begin{aligned} \frac{\partial P^{(1)}}{\partial t} + \boldsymbol{\xi}_1 \cdot \frac{\partial P^{(1)}}{\partial \mathbf{x}_1} &= N\sigma^2 \int_B \int_{\mathbb{R}^3} [P^{(1)}(\mathbf{x}_1, \boldsymbol{\xi}'_1, t)P^{(1)}(\mathbf{x}_1, \boldsymbol{\xi}'_2, t) + \\ &\quad - P^{(1)}(\mathbf{x}_1, \boldsymbol{\xi}_1, t)P^{(1)}(\mathbf{x}_1, \boldsymbol{\xi}_2, t)]|(\boldsymbol{\xi}_2 - \boldsymbol{\xi}_1) \cdot \mathbf{n}|d\boldsymbol{\xi}_2 d\mathbf{n} \end{aligned} \quad (3.21)$$

where the left side of the Eq. 3.21 has been written in its extended formulation. Eq. 3.21 is, by fact, the evolution equation for the probability density function of one particle.

Next step of Boltzmann's work was to formulate an evolution equation for a system containing  $s$  particles. We define  $P^{(s)}$  as the probability to find particle 1 in position  $\mathbf{x}_1$  with velocity  $\boldsymbol{\xi}_1$ , particle 2 in position  $\mathbf{x}_2$  with velocity  $\boldsymbol{\xi}_2$  and particle  $s$  in position  $\mathbf{x}_s$  with velocity



$\xi_s$  at time  $t$ .  $P^{(s)}$  is expressed as follows:

$$P^{(s)}(\mathbf{x}_1, \xi_1, \mathbf{x}_2, \xi_2, \dots, \mathbf{x}_s, \xi_s, t) = \int_{\mathbb{C}^s \times \mathbb{R}^{3s}} P(\mathbf{x}_1, \xi_1, \mathbf{x}_2, \xi_2, \dots, \mathbf{x}_N, \xi_N, t) \prod_{j=s+1}^N d\mathbf{x}_j d\xi_j \quad (3.22)$$

Now, inserting Eq. 3.22 in Eq. 3.9 and integrating on variable  $\mathbf{x}_j$  ( $s+1 < j < N$ ) we found the following expression:

$$\frac{\partial P^{(s)}}{\partial t} + \sum_{i=1}^s \int_{\mathbb{C}^{N-s} \times \mathbb{R}^{3N-3s}} \xi_i \cdot \frac{\partial P}{\partial \mathbf{x}_i} \prod_{j=s+1}^N d\mathbf{x}_j d\xi_j + \sum_{k=s+1}^N \int_{\mathbb{C}^{N-s} \times \mathbb{R}^{3N-3s}} \xi_k \cdot \frac{\partial P}{\partial \mathbf{x}_k} \prod_{j=s+1}^N d\mathbf{x}_j d\xi_j = 0 \quad (3.23)$$

where  $s$  is the number of particles satisfying the condition  $|\mathbf{x}_i - \xi_i| < \sigma$  ( $i=1, \dots, N$ ,  $i \neq j$ ) and following Cercignani [1997], we separate the particles  $i < s$  from the particles  $i > s$ . Assuming  $P$  to be regular we can rewrite the second addend of Eq. 3.23 as follows:

$$\int \xi_i \cdot \frac{\partial P}{\partial \mathbf{x}_i} \prod_{j=s+1}^N d\mathbf{x}_j d\xi_j = \xi_i \cdot \frac{\partial P^{(s)}}{\partial \mathbf{x}_i} - \sum_{k=s+1}^N \int P^{(s+1)} \xi_i \cdot \mathbf{n}_{ik} d\sigma_{ik} d\xi_k \quad (3.24)$$

where  $\mathbf{n}_{ik}$  is the outgoing normal to the sphere  $|\mathbf{x}_i - \mathbf{x}_k| = \sigma$ ;  $d\sigma_{ik}$  is an infinitesimal element of that sphere and  $P^{s+1}$  is the distribution function for  $s+1$  particles with argument  $(\mathbf{x}_j, \xi_j)$  ( $j = 1, 2, \dots, s, k$ ).

The third addend of Eq. 3.23 can be rewritten by using the Gauss Lemma [Tang, 1972] as follows:

$$\begin{aligned} \int \xi_k \cdot \frac{\partial P}{\partial \mathbf{x}_k} \prod_{j=s+1}^N d\mathbf{x}_j d\xi_j &= \sum_{i=1}^s \int P^{(s+1)} \xi_k \cdot \mathbf{n}_{ik} d\sigma_{ik} d\xi_k + \\ &\sum_{i=s+1(i \neq k)}^N \int P^{(s+2)} \xi_k \cdot \mathbf{n}_{ik} d\sigma_{ik} d\xi_k d\mathbf{x}_i d\xi_i + \int P^{(s+1)} \xi_k \cdot \mathbf{n}_k dS_k d\xi_k \end{aligned} \quad (3.25)$$

where  $dS_k$  is the infinitesimal element of the boundary surface in the tridimensional subspace described by  $\mathbf{x}_k$  and  $\mathbf{n}_k$  is the outgoing normal that surface. In both Eqs. 3.24 and 3.25 we have omitted, for simplicity, the domain on the integral which is clearly the same as the one in Eq. 3.23. So, inserting Eq. 3.24 and 3.25 in Eq. 3.23 we obtain:

$$\begin{aligned} \frac{\partial P^{(s)}}{\partial t} + \sum_{i=1}^s \xi_i \cdot \frac{\partial P^{(s)}}{\partial \xi_i} &= \sum_{i=1}^s \sum_{k=s+1}^N \int P^{(s+1)} \mathbf{v}_{ik} \cdot \mathbf{n}_{ik} d\sigma_{ik} d\xi_k + \\ &\frac{1}{2} \sum_{i=s+1(i \neq k)}^N \int P^{(s+2)} \int P^{(s+2)} \mathbf{v}_{ik} \cdot \mathbf{n}_{ki} d\sigma_{ik} d\xi_k d\mathbf{x}_i d\xi_i \end{aligned} \quad (3.26)$$

where  $\mathbf{v}_{ik} = \xi_i - \xi_k$  is the relative velocity between the  $i^{th}$  and the  $k^{th}$  particle and  $\mathbf{n}_{ki} = -\mathbf{n}_{ik}$ .

It is possible to demonstrate [Cercignani et al., 2013] that the last integral in Eq. 3.26 is equal to 0 and the value of the first integral is the same whatever is the value of the  $k$  index [Cercignani, 1972], so it is common in literature to use  $*$  in place of  $k$ . After some mathematical computations [Cercignani, 1997] we can rewrite Eq. 3.26 as follows:

$$\begin{aligned} \frac{\partial P^{(s)}}{\partial t} + \sum_{i=1}^s \boldsymbol{\xi}_i \cdot \frac{\partial P^{(s)}}{\partial \mathbf{x}_i} = (N-s)\sigma^2 \sum_{i=1}^s \int_{B_+} \int_{\mathbb{R}^3} (P^{(s+1)'}) |\mathbf{v}_i \cdot \mathbf{n}_i| d\mathbf{n}_i d\boldsymbol{\xi}_* - \\ \sum_{i=1}^s \int_{B_-} \int_{\mathbb{R}^3} P^{(s+1)} |\mathbf{v}_i \cdot \mathbf{n}_i| d\mathbf{n}_i d\boldsymbol{\xi}_* \end{aligned} \quad (3.27)$$

where the apex  $'$  is used to indicate quantities before particles collision;  $\boldsymbol{\xi}_i$  and  $\boldsymbol{\xi}_*$  in  $P^{(s+1)'}$  are substituted with:

$$\boldsymbol{\xi}'_i = \boldsymbol{\xi}_i - \mathbf{n}_i(\mathbf{n}_i \cdot \mathbf{v}_i) \quad \text{and} \quad \boldsymbol{\xi}'_* = \boldsymbol{\xi}_* - \mathbf{n}_*(\mathbf{n}_* \cdot \mathbf{v}_*)$$

Finally we can turn the two integrals in Eq. 3.27 into one integral, extended to the whole domain, by changing  $\mathbf{n}_i$  in  $\mathbf{n}'_i$ . We can also suppress index  $i$  in  $\mathbf{n}_i$  by substituting  $\mathbf{x}_*$  with:

$$\mathbf{x}_* = \mathbf{x}_i - \sigma \mathbf{n}$$

Eq. 3.27 can be, so, rewritten as follows:

$$\frac{\partial P^{(s)}}{\partial t} + \sum_{i=1}^s \boldsymbol{\xi}_i \cdot \frac{\partial P^{(s)}}{\partial \mathbf{x}_i} = (N-s)\sigma^2 \sum_{i=1}^s \int_B \int_{\mathbb{R}^3} (P^{(s+1)'} - P^{(s+1)}) |\mathbf{v}_i \cdot \mathbf{n}| d\mathbf{n} d\boldsymbol{\xi}_* \quad (3.28)$$

This system of equations is commonly known as *BBGKY Hierarchy* [Bogoliubov, 1946]. Applying the Boltzmann-Grad limit it is, finally, possible to write the evolution equation for a system of  $s$  particles as follows:

$$\frac{\partial P^{(s)}}{\partial t} + \sum_{i=1}^s \boldsymbol{\xi}_i \cdot \frac{\partial P^{(s)}}{\partial \mathbf{x}_i} = N\sigma^2 \sum_{i=1}^s \int_B \int_{\mathbb{R}^3} (P^{(s+1)'} - P^{(s+1)}) |\mathbf{v}_i \cdot \mathbf{n}| d\mathbf{n} d\boldsymbol{\xi}_* \quad (3.29)$$

This system of equations is known as *Boltzmann Hierarchy*. We have two questions to answer now:

- Is this system of equations representing the evolution of a Boltzmann Gas?
- Which is the relation between the *Boltzmann Hierarchy* (Eq. 3.29) and the *Boltzmann Equation* (Eq. 3.21)?

As remarked by Cercignani [1972], the *Boltzmann Hierarchy* does not describe *a priori* the evolution of a Boltzmann Gas, in fact only under some special hypothesis on the initial data, it turns to be eligible for this purpose, as discussed by [Spohn, 1984].

If we assume the *Molecular Chaos Hypothesis* to be valid for the initial data:

$$P^{(s)}(\mathbf{x}_1, \boldsymbol{\xi}_1, \mathbf{x}_2, \boldsymbol{\xi}_2, \dots, \mathbf{x}_s, \boldsymbol{\xi}_s, 0) = \prod_{j=1}^N P^{(1)}(\mathbf{x}_s, \boldsymbol{\xi}_s, 0)$$

As remarked by Cercignani [1972],[Cercignani, 1975],[Cercignani, 1988], if the *Boltzmann Equation* is satisfied for the initial data  $P^{(1)}(\mathbf{x}_s, \boldsymbol{\xi}_s, 0)$ , then it admits at least a solution:  $P^{(1)}(\mathbf{x}_s, \boldsymbol{\xi}_s, t)$ . If this happens, a solution of the *Boltzmann Hierarchy* is corresponding at the initial data:

$$P^{(s)}(\mathbf{x}_1, \boldsymbol{\xi}_1, \mathbf{x}_2, \boldsymbol{\xi}_2, \dots, \mathbf{x}_s, \boldsymbol{\xi}_s, t) = \prod_{j=1}^N P^{(1)}(\mathbf{x}_s, \boldsymbol{\xi}_s, t)$$

so the *Molecular Chaos Hypothesis* is not in contradiction with the *Boltzmann-Grad* limit; in other words, *Molecular Chaos Hypothesis* is still valid for a system of  $s$  particles and the Boltzmann Equation is justified.

With this considerations, we can easily remove the index <sup>(1)</sup> from Eq. 3.21 and, finally write it as follows:

$$\frac{\partial P}{\partial t} + \boldsymbol{\xi} \cdot \frac{\partial P}{\partial \mathbf{x}} = N\sigma^2 \int_B \int_{\mathbb{R}^3} (P'P'_* - PP_*) |\mathbf{v} \cdot \mathbf{n}| d\mathbf{n} d\boldsymbol{\xi}_* \quad (3.30)$$

### 3.2.1 A more physical interpretation of the Boltzmann Equation

Following Boltzmann's work, we can introduce a new unknown  $f$  defined as:

$$f = NmP = MP \quad (3.31)$$

where  $N$  is the total number of particles,  $m$  is the mass of a single particle and  $M$  is the total mass of the system. By imposing the first axiom of probability we have:

$$\int_B \int_{\mathbb{R}^3} P d\mathbf{x} d\boldsymbol{\xi} = 1 \quad \rightarrow \quad \int_B \int_{\mathbb{R}^3} f d\mathbf{x} d\boldsymbol{\xi} = M \quad (3.32)$$

$P$  is a numerical density distribution, while  $f$  is a mass density distribution, so, at every time, the integral of the distribution  $f$  must recover the total mass of the system.

Introducing Eq. 3.32 into Eq. 3.30 the Boltzmann Equation can be written in its most popular form:

$$\frac{\partial f}{\partial t} + \boldsymbol{\xi} \cdot \frac{\partial f}{\partial \mathbf{x}} = Q(f, f) \quad (3.33)$$

The right-hand side of the equation is commonly known as *Collision Operator*:

$$Q(f, f) = \frac{\sigma^2}{m} \int (f'f'_* - ff_*) |\mathbf{v} \cdot \mathbf{n}| d\mathbf{n} d\boldsymbol{\xi}_* \quad (3.34)$$

where  $f_* = f(\boldsymbol{\xi}_*)$ ,  $f'_* = f(\boldsymbol{\xi}'_*)$  and  $f' = f(\boldsymbol{\xi}')$ . The form  $Q(f, f)$  is adopted to remark the quadratic form of the collision operator. For sake of generality, the Boltzmann Equation can be written including also a forcing term:

$$\frac{\partial f}{\partial t} + \boldsymbol{\xi} \cdot \frac{\partial f}{\partial \mathbf{x}} + \mathbf{F} \cdot \frac{\partial f}{\partial \boldsymbol{\xi}} = Q(f, f) \quad (3.35)$$

### 3.2.2 Solution of the Boltzmann Equation

From the mathematical point of view, the Boltzmann Equation 3.35 is an integro-partial-differential equation. It should be clear that the principal obstacle in order to solve Eq. 3.33 is the evaluation of the *Collision Operator*.

#### The Collision Invariants

Our goal is, now, to investigate some elementary properties of the collision operator  $Q(f, f)$ . We introduce a test function  $\varphi(\boldsymbol{\xi})$  and we study the integral:

$$\int_{\mathbb{R}^3} Q(f, f) \varphi(\boldsymbol{\xi}) d\boldsymbol{\xi} = \int_{\mathbb{R}^3} \int_{\mathbb{R}^3} \int_B (f' f'_* - f f_*) \varphi(\boldsymbol{\xi}) |\mathbf{v} \cdot \mathbf{n}| d\mathbf{n} d\boldsymbol{\xi} d\boldsymbol{\xi}_* \quad (3.36)$$

where  $\varphi$  and  $f$  are functions for which it is possible to change the integration order. With some mathematical manipulations [Grad, 1961] it is possible to rewrite Eq. 3.36 in three different ways:

$$\begin{aligned} \int_{\mathbb{R}^3} Q(f, f) \varphi(\boldsymbol{\xi}) d\boldsymbol{\xi} &= \frac{\sigma^2}{m} \int_{\mathbb{R}^3} \int_{\mathbb{R}^3} \int_B (f' f'_* - f f_*) \varphi(\boldsymbol{\xi}_*) |\mathbf{v} \cdot \mathbf{n}| d\mathbf{n} d\boldsymbol{\xi} d\boldsymbol{\xi}_* \\ \int_{\mathbb{R}^3} Q(f, f) \varphi(\boldsymbol{\xi}) d\boldsymbol{\xi} &= \frac{\sigma^2}{m} \int_{\mathbb{R}^3} \int_{\mathbb{R}^3} \int_B (f f_* - f' f'_*) \varphi(\boldsymbol{\xi}') |\mathbf{v} \cdot \mathbf{n}| d\mathbf{n} d\boldsymbol{\xi} d\boldsymbol{\xi}_* \\ \int_{\mathbb{R}^3} Q(f, f) \varphi(\boldsymbol{\xi}) d\boldsymbol{\xi} &= \frac{\sigma^2}{m} \int_{\mathbb{R}^3} \int_{\mathbb{R}^3} \int_B (f f_* - f' f'_*) \varphi(\boldsymbol{\xi}') |\mathbf{v} \cdot \mathbf{n}| d\mathbf{n} d\boldsymbol{\xi} d\boldsymbol{\xi}_* \end{aligned} \quad (3.37)$$

Summing Eq 3.36 with Eq. 3.37 and averaging the results we obtain:

$$\int_{\mathbb{R}^3} Q(f, f) \varphi(\boldsymbol{\xi}) d\boldsymbol{\xi} = \frac{\sigma^2}{4m} \int_{\mathbb{R}^3} \int_{\mathbb{R}^3} \int_B (f' f'_* - f f_*) (\varphi + \varphi_* - \varphi' - \varphi'_*) |\mathbf{v} \cdot \mathbf{n}| d\mathbf{n} d\boldsymbol{\xi} d\boldsymbol{\xi}_* \quad (3.38)$$

The integral of the first member gives the variation of the mean value of the function  $\varphi$  for time unit, caused by the collisions. It is very interesting to notice that, whatever is  $f$ , the integral in Eq. 3.38 is equal to zero if it is verified the following relation:

$$\varphi + \varphi_* = \varphi' + \varphi'_* \quad (3.39)$$

These functions ( $\varphi$ ) are commonly known as *Collision invariants*. The solution of Eq. 3.39 was found by Boltzmann himself, who supposed  $\varphi$  to be two times derivable gave to the collision invariants the following expression:

$$\varphi(\boldsymbol{\xi}) = a + \mathbf{b} \cdot \boldsymbol{\xi} + c |\boldsymbol{\xi}|^2 \quad (3.40)$$

where the scalars  $a$ ,  $c$  and the vector  $\mathbf{b}$  are constant. In literature many other authors tried to find different solutions of Eq. 3.39, including Grad [1961] and Carleman [1957], finally Cercignani [1990] demonstrated the analytical correctness and the uniqueness of the solution

proposed by Boltzmann. So if  $\varphi(\boldsymbol{\xi})$  has the form of Eq. 3.40 we obtain the following relation:

$$\int_{\mathbb{R}^3} Q(f, f) \varphi(\boldsymbol{\xi}) d\boldsymbol{\xi} = 0 \quad (3.41)$$

This expression states that the integral of the *Collision term* multiplied for the *Collision invariants* comes to zero for every value of distribution function  $f$ .

### Stationary solution of the Boltzmann Equation

The next step of Boltzmann's work was to study the stationary solution of the Eq. 3.35, which is given by:

$$\frac{\partial f}{\partial t} + \boldsymbol{\xi} \cdot \frac{\partial f}{\partial \mathbf{x}} + \mathbf{F} \cdot \frac{\partial f}{\partial \boldsymbol{\xi}} = 0 \quad (3.42)$$

so to prove that exist positive functions  $f$  which satisfy the following equality:

$$Q(f, f) = \frac{\sigma^2}{m} \int (f' f'_* - f f_*) |\mathbf{v} \cdot \mathbf{n}| d\mathbf{n} d\boldsymbol{\xi}_* = 0 \quad (3.43)$$

Considering Eq. 3.38, and assuming  $\varphi = \log f$ , we can write the following expression:

$$\int \log f Q(f, f) d\boldsymbol{\xi} = \frac{\sigma^2}{4m} \int (f' f'_* - f f_*) \log\left(\frac{f f_*}{f' f'_*}\right) |\mathbf{v} \cdot \mathbf{n}| d\mathbf{n} d\boldsymbol{\xi} d\boldsymbol{\xi}_* \quad (3.44)$$

With simple computations we can write Eq. 3.44 as following:

$$\int \log f Q(f, f) d\boldsymbol{\xi} = \frac{\sigma^2}{4m} \int f' f'_* (1 - K) \log K |\mathbf{v} \cdot \mathbf{n}| d\mathbf{n} d\boldsymbol{\xi} d\boldsymbol{\xi}_* \quad \text{with} \quad K = \frac{f f_*}{f' f'_*} \quad (3.45)$$

It is possible to demonstrate that for any  $K \geq 0$  it holds valid the following relation:

$$(1 - K) \log K \leq 0 \quad (3.46)$$

and thus, considering that  $f' f'_*$  is positive by definition, Eq. 3.45 can be rewritten as follows:

$$\log f Q(f, f) d\boldsymbol{\xi} \leq 0 \quad (3.47)$$

which is known as *Boltzmann inequality*. Finally, it is easy to show that Eq. 3.46 vanishes only if  $K = 1$  and thus when:

$$f f_* = f' f'_* \quad (3.48)$$

which is, just, another form to write Eq. 3.39, therefore substituting  $\varphi = \log f$  in Eq. 3.40 we obtain:

$$f(\boldsymbol{\xi}) = \exp(a + \mathbf{b} \cdot \boldsymbol{\xi} + c|\boldsymbol{\xi}|^2) \quad (3.49)$$

Eq. 3.49 has the form of a Maxwellian distribution and represents the equilibrium solution of the Boltzmann equation. Furthermore we have demonstrated that this solution is unique. We note that in order to obtain functions  $f$  integrable in all the domain, it is necessary that

$c$  is negative, furthermore, we can assume  $c = -\eta$  and  $\mathbf{b} = 2\eta\mathbf{v}$  where  $\mathbf{v}$  is another constant vector. Finally we can rewrite Eq. 3.49 as follows:

$$f(\boldsymbol{\xi}) = G \exp[-\eta + (\boldsymbol{\xi} - \mathbf{v})^2] \quad (3.50)$$

where  $G$  is a constant depending on  $a, \eta, \mathbf{v}$ . The constant vector  $\mathbf{v}$  can be viewed as a macroscopic velocity which changes the reference frame with a kind of rigid motion.

### 3.2.3 The stationary solution: Maxwellian distributions

The last step to derive the stationary solution of Boltzmann equation is to calculate the coefficients of the Maxwellian distributions (Eq. 3.49). We consider Eq. 3.35:

$$\frac{\partial f}{\partial t} + \boldsymbol{\xi} \cdot \frac{\partial f}{\partial \mathbf{x}} + \mathbf{F} \cdot \frac{\partial f}{\partial \boldsymbol{\xi}} = 0 \quad (3.51)$$

and the stationary solution (Eq. 3.49) which can be written as follows:

$$\log f = a + \mathbf{b} \cdot \boldsymbol{\xi} + c\xi^2 = a + b_l \xi_l + c\xi^2 \quad (3.52)$$

Inserting Eq. 3.52 in Eq. 3.51 we obtain:

$$\frac{\partial a}{\partial t} + \xi_l \frac{\partial b_l}{\partial t} + \xi^2 \frac{\partial c}{\partial t} + \xi_i \frac{\partial a}{\partial x_i} + \xi_i \xi_l \frac{\partial b_l}{\partial x_i} + \xi^2 \xi_i \frac{\partial c}{\partial x_i} + F_i b_i + 2c F_i \xi_i = 0 \quad (3.53)$$

and collecting the terms of the various powers of  $\xi$  we obtain:

$$\left( \frac{\partial a}{\partial t} + F_i b_i \right) + \left( \frac{\partial b_l}{\partial t} + \frac{\partial a}{\partial x_i} + 2c F_i \right) \xi_l + \left( \frac{\partial c}{\partial t} \delta_{ij} + \frac{1}{2} \left( \frac{\partial b_l}{\partial x_i} + \frac{\partial b_i}{\partial x_l} \right) \right) \xi_i \xi_l + \left( \frac{\partial c}{\partial x_i} \right) \xi^2 = 0 \quad (3.54)$$

then, we can equate the each term to zero:

$$\left( \frac{\partial a}{\partial t} + F_i b_i \right) = 0 \quad (3.55)$$

$$\left( \frac{\partial b_l}{\partial t} + \frac{\partial a}{\partial x_i} + 2c F_i \right) = 0 \quad (3.56)$$

$$\left( \frac{\partial c}{\partial t} \delta_{ij} + \frac{1}{2} \left( \frac{\partial b_l}{\partial x_i} + \frac{\partial b_i}{\partial x_l} \right) \right) = 0 \quad (3.57)$$

$$\left( \frac{\partial c}{\partial x_i} \right) = 0 \quad (3.58)$$

and finally, after some mathematical manipulation, Eq. 3.57 becomes:

$$\frac{\partial^2 b_j}{\partial x_i \partial x_l} = 0 \quad (3.59)$$

meaning that the second spatial derivatives of the term  $b_j$  are equal to zero, then  $b_j$  can be expressed as following:

$$b_j = \eta_j(t) + \beta_{ik}(t)x_k \quad (3.60)$$

Now, inserting Eq. 3.60 in Eq. 3.57, we obtain:

$$\beta_{il} = -\frac{dc}{dt}\delta_{il} + \omega_{il}(t) \quad \text{with} \quad \omega_{il} = -\omega_{li} \quad (3.61)$$

then inserting Eq. 3.60 and Eq. 3.61 in Eq. 3.56 we obtain:

$$\frac{d\eta_l}{dt} - \frac{d^2c}{dt^2}x_l + \frac{d\omega_{lk}}{dt}x_k + \frac{\partial\eta}{\partial x_l} + 2cF_l = 0 \quad (3.62)$$

and finally with some manipulations we can express the forcing term as following:

$$F_l = -\frac{1}{2c}\frac{d\omega_{lj}}{dt}x_j - \frac{\partial\phi}{\partial x_l} \quad (3.63)$$

which means that the external force is dependent on a conservative term described by the potential function  $\phi = \phi(t, \mathbf{x})$  and a non conservative term dependent on the antisymmetric tensor  $\omega_{lj}$ . Inserting Eq. 3.63 in Eq. 3.62 we obtain:

$$\eta = 2c\phi(t, \mathbf{x}) + \frac{1}{2}\frac{d^2c}{dt^2}x^2 - \frac{d\eta_l}{dt}x_l + \gamma(t) \quad (3.64)$$

where  $\gamma(t)$  is the integration constant. Now, inserting Eq. 3.64 and Eq. 3.60 in Eq. 3.55 we obtain:

$$2c\frac{\partial\phi}{\partial t} + 2\phi\frac{dc}{dt} - \frac{\partial\phi}{\partial x_i}b_i = -\frac{1}{2}\frac{d^3c}{dt^3}x^2 + \frac{d^2\eta_l}{dt^2}x_l - \frac{d\gamma}{dt} + \frac{1}{2c}\frac{d\omega_{ij}}{dt}x_jb_i \quad (3.65)$$

Considering, now, Eq. 3.63, assuming  $\phi = \phi(\mathbf{x})$ , it is easy to show that  $\omega_{lj}$  is constant and so Eq. 3.65 can be rewritten as follows:

$$2\phi\frac{dc}{dt} - \frac{\partial\phi}{\partial x_i}b_i = -\frac{1}{2}\frac{d^3c}{dt^3}x^2 + \frac{d^2\eta_l}{dt^2}x_l - \frac{d\gamma}{dt} \quad (3.66)$$

Assuming  $\phi$  to be four times differentiable in time, with some mathematical manipulations, we can rewrite Eq. 3.66 as follows:

$$\begin{aligned} & 5\frac{\partial^2\phi}{\partial x_k\partial x_m\partial x_n}\frac{dc}{dt} - \frac{\partial^3\phi}{\partial x_i\partial x_k\partial x_m}\omega_{in} - \frac{\partial^3\phi}{\partial x_i\partial x_k\partial x_l}\omega_{im} \\ & - \frac{\partial^3\phi}{\partial x_i\partial x_m\partial x_n}\omega_{ik} - \frac{\partial^4\phi}{\partial x_i\partial x_k\partial x_m\partial x_n}\left(\eta_i - \frac{dc}{dt}x_i + \omega_{il}x_l\right) = 0 \end{aligned} \quad (3.67)$$

which describes a system of ten equations in seven unknown:  $dc/dt$ ,  $\omega_{ik}$ ,  $\omega_{im}$ ,  $\omega_{in}$  and  $\alpha_i$ . Following Cercignani [1988], it is possible to show that  $\eta$  is related to  $c$  and  $\gamma$  by the following relation:

$$\eta = 2c\phi(\mathbf{x}) + \gamma \quad (3.68)$$

thus including Eq. 3.68 in Eq. 3.50, the Maxwellian distribution can be written as follows:

$$f(\boldsymbol{\xi}) = \exp(2c\phi(\mathbf{x}) + \gamma + c\phi^2) = \exp\left(\gamma - \frac{\xi^2}{2RT} - \frac{\phi(\mathbf{x})}{RT}\right) \quad (3.69)$$

with:

$$T = -\frac{1}{2Rc}$$

where  $T$  is the temperature of the system. The last issue is now to give an expression to the potential function  $\phi(\mathbf{x})$ . We consider a potential function vanishing at the third derivative defined as:

$$\phi(\mathbf{x}) = A_k x_k + \frac{1}{2} B_{km} x_k x_m \quad (3.70)$$

Then, inserting Eq. 3.70 in Eq. 3.65, we can rewrite Eq. 3.65 as follows:

$$\begin{aligned} & \left( A_i \eta_i - \frac{d\gamma}{dt} \right) + \left( 2A_i \frac{dc}{dt} - A_k \omega_{ki} - B_{ki} \eta_k - \frac{d^2 \eta_i}{dt^2} \right) x_k \\ & + \left( 2B_{km} \frac{dc}{dt} - \frac{1}{2} (B_{ki} \omega_{im} + B_{mi} \omega_{il}) + \frac{d^3 c}{2dt^3} \delta_{km} \right) x_k x_m = 0 \end{aligned} \quad (3.71)$$

so with an analogue procedure to the one adopted for Eq. 3.53, we can derive the following equalities:

$$A_i \eta_i = \frac{d\gamma}{dt} \quad (3.72)$$

$$2A_i \frac{dc}{dt} - A_k \omega_{ki} - B_{ki} \eta_k = \frac{d^2 \eta_i}{dt^2} \quad (3.73)$$

$$2B_{km} \frac{dc}{dt} - \frac{1}{2} (B_{ki} \omega_{im} + B_{mi} \omega_{il}) = -\frac{d^3 c}{2dt^3} \delta_{km} \quad (3.74)$$

Eqs. 3.72, 3.73, 3.74 represent a system of ten equations in eight unknowns:  $\eta_i$ ,  $\omega_i m$ ,  $\gamma$ ,  $c$ . This system has non trivial solution in case that  $B_{ki} = B \delta_{ki}$  is isotropic. Considering this condition, Eq. 3.74 can be written as follows:

$$2B \frac{dc}{dt} + \frac{d^3 c}{2dt^3} = 0 \quad (3.75)$$

which is a classical differential equation, with constant coefficients, whose solution is given by:

$$c = c_0 + c_1 \sin(2\sqrt{B}t) + c_2 \cos(2\sqrt{B}t) \quad (3.76)$$

where  $c_0$ ,  $c_1$ ,  $c_2$  constant coefficients. Inserting Eq. 3.75 in equation Eq. 3.73 and considering the isotropicity of  $B$  we obtain:

$$\frac{d^2 \eta_i}{dt^2} + B \eta_i = 2A_i \frac{dc}{dt} - A_k \omega_{ki} = -\frac{2A_i}{3B} \left( \frac{d^3 c}{dt^3} + B \frac{dc}{dt} \right) - A_k \omega_{ki} \quad (3.77)$$



that is a differential equation with constant coefficients, whose solution is given by:

$$\eta_i = -\frac{2A_i dc}{3Bdt} - \frac{A_k \omega_{ki}}{3} + c_3 \sin(2\sqrt{B}t) + c_4 \cos(2\sqrt{B}t) \quad (3.78)$$

where  $c_3$  and  $c_4$  are constant coefficients. Finally, Eq. 3.72 can be rewritten as follows:

$$\frac{d\gamma}{dt} = A_i \eta_i = \frac{A_i}{B} \left( -\frac{d^2 \eta_i}{dt^2} + 2A_i \frac{dc}{dt} \right) \quad (3.79)$$

which is a simple first order differential equation with constant coefficients. The solution of Eq. 3.79 is given by:

$$\gamma = -\frac{A_i}{B} \frac{d\eta_i}{dt} + \frac{2A_i A_i c}{B} + c_5 \quad (3.80)$$

In conclusion, when  $c_1 = 0$ ,  $c_2 = 0$ ,  $c_3 = 0$  and  $c_4 = 0$ , with some mathematical computations of Eqs. 3.52, 3.60, 3.64 we obtain the final expression of the Maxwellian distribution:

$$\begin{aligned} f(\boldsymbol{\xi}) &= \exp(\gamma + \boldsymbol{\eta} \cdot \boldsymbol{\xi} + \omega_{jk} x_k \xi_k + c\xi^2) \\ f(\boldsymbol{\xi}) &= \exp(\gamma) (2\pi RT)^{-\frac{3}{2}} \exp \left[ -\frac{(\boldsymbol{\xi} - \mathbf{v})^2}{2RT} \right] \end{aligned} \quad (3.81)$$

where the term  $\exp(\gamma)$  is the density. Eq. 3.81 is also known as *equilibrium distribution function* because it satisfies Eq. 3.42 and finally it can be rearranged in its most popular form:

$$f^{eq}(\boldsymbol{\xi}) = \frac{\rho}{\sqrt{(2\pi RT)^3}} \exp \left[ -\frac{(\boldsymbol{\xi} - \mathbf{v})^2}{2RT} \right] \quad (3.82)$$

### The H-theorem, the irreversibility and the second law of the thermodynamics.

The H-theorem is of basic importance in Boltzmann theory, because it states the irreversibility of the Boltzmann Equation.

To derive the H-theorem, proposed by Boltzmann [1870] itself, we introduce a new operator  $H$  which is, at the end, the integral on velocity of the quantity  $f \log f$  and is defined as follows:

$$H = \int_{\mathbb{R}^3} f \log f d\boldsymbol{\xi} \quad (3.83)$$

considering Eq. 3.33, by multiplying each side by  $f \log f$  and integrating on  $\boldsymbol{\xi}$  we can rewrite Boltzmann equation as follows:

$$\frac{\partial H}{\partial t} + \frac{\partial}{\partial \mathbf{x}} \cdot \mathbf{J} = S \quad (3.84)$$

where:

$$\begin{aligned} \mathbf{J} &= \int_{\mathbb{R}^3} \boldsymbol{\xi} f \log f d\boldsymbol{\xi} \\ S &= N\sigma^2 \int_{\mathbb{R}^3} \log f Q(f, f) d\boldsymbol{\xi} \end{aligned} \quad (3.85)$$

The *Boltzmann inequality* (Eq. 3.47) implies that  $S$  is always  $\leq 0$  and becomes equal to zero if and only if  $f$  is a Maxwellian distribution. Carleman [1933] demonstrated that the time derivative of  $H$  is never positive and it is equal to 0 if and only if  $f$  is a Maxwellian distribution. Since  $H$  is lower bounded (from the equilibrium value), it decreases until it reaches the equilibrium state where  $f$  has the form of a Maxwellian distribution, so the *Equilibrium solution* is unique.

If the solutions are spatially homogeneous (i.e.  $H$  is not depending from  $\mathbf{x}$ ), Eq. 3.84 can be rewritten as follows:

$$\frac{\partial H}{\partial t} = S \leq 0 \quad (3.86)$$

Eq. 3.86 is known as *H-Theorem* and states that  $H$  is a not increasing function in time. In other words, Eq. 3.86 shows that Boltzmann equation has the feature of the irresistibility.

From the microscopic point of view, H-Theorem can be interpreted as the likelihood of a microscopic state, in the sense that it is a measure of the information contained in  $f$  decreasing with time since the *Boltzmann Equation describes an evolution toward more likely states* [Cercignani, 1988].

From a macroscopic point of view, instead, H-theorem can be viewed as an alternative form to express the *Clausius-Duhem* inequality [Gurtin and Williams, 1966] which is, by fact, another way to express the second law of thermodynamics. Finally, according to this principle,  $H$  is related to the entropy  $S$  by the following relation:

$$\Delta H = -\frac{\Delta S}{R} \quad (3.87)$$

where  $\Delta S$  is the entropy variation,  $\Delta H$  is the variation of  $H$  function and  $R$  is the universal gas constant.

### 3.3 Boltzmann Equation: a Bridge from the Micro- to the Macroscopic description

One of the most interesting characteristics of BE is possibility to move from a microscopic to a macroscopic point of view. Now our goal is to recover macroscopic quantities from the distribution function  $f$ . In order to have a complete macroscopic description of the fluid, we need to evaluate the following quantities:

- density:  $\rho$ ;
- mass Flow:  $\rho_i$ ;
- momentum:  $\omega_i$ ;
- momentum flow:  $\Omega_{ij}$ ;
- energy density:  $\psi_{ii}$ ;
- energy flow:  $\Psi_i$ ;

Evaluating macroscopic density  $\rho$  is quite a simple task.  $\rho = \rho(\mathbf{x}, t)$  is the integral  $f$  in the one-particle phase space, so, it is straightforward to recover that:

$$\rho(\mathbf{x}, t) = \int f(\mathbf{x}, \boldsymbol{\xi}, t) d\boldsymbol{\xi} \quad (3.88)$$

The macroscopic velocity  $\mathbf{v}$  is given by the average of the molecular velocity:

$$\mathbf{v} = \frac{\int \boldsymbol{\xi} f(\mathbf{x}, \boldsymbol{\xi}, t) d\boldsymbol{\xi}}{\int f(\mathbf{x}, \boldsymbol{\xi}, t) d\boldsymbol{\xi}} \quad (3.89)$$

So considering Eq. 3.88 we can easily write also the momentum  $\omega_l$  as follows:

$$\omega_l = \rho v = \int \xi_l f d\boldsymbol{\xi} \quad (3.90)$$

To evaluate the mass flow  $\varrho_i$  we consider that every particle has its own velocity  $\boldsymbol{\xi}$ , so we can calculate the velocity deviation (usually called *peculiar velocity*) from the macroscopic velocity:

$$\mathbf{c} = \boldsymbol{\xi} - \mathbf{v} \quad (3.91)$$

By inserting Eq. 3.91 in Eq. 3.90 and considering Eq. 3.88 we write mass flow as follows:

$$\varrho_i = \int c_i f d\boldsymbol{\xi} = \int \xi_i f d\boldsymbol{\xi} - v_i \int f d\boldsymbol{\xi} = \rho v_i - \rho v_i = 0 \quad (3.92)$$

Eq. 3.92 states that the mass flow in  $i$ -th direction is equal to zero. In order to evaluate the momentum flow  $\Omega_{ij}$ , instead, we have to consider the flow of the  $i$ -th component on  $j$ -th direction:

$$\Omega_{ij} = \int \xi_i \xi_j f d\boldsymbol{\xi} \quad (3.93)$$

By applying Eq. 3.91 to Eq. 3.93 we can easily rewrite the momentum flow as follows:

$$\Omega_{ij} = \int \xi_i \xi_j f d\boldsymbol{\xi} = \rho v_i v_j + \int c_i c_j f d\boldsymbol{\xi} \quad (3.94)$$

where the momentum flow has been decomposed in a macroscopic (first addend) and a microscopic (second addend) part. The microscopic part is a hidden momentum flow caused by the random motion of the particles. It is possible to prove that the second addend of Eq. 3.94 is the only contribution to the gas stress tensor which is defined as follows [Cercignani, 1988]:

$$p_{ij} = \int c_i c_j f d\boldsymbol{\xi} \quad (3.95)$$

The evaluation of the energy density  $\psi_{ii}$  is straightforward with the application of the kinetic energy definition:

$$\psi_{ii} = \frac{1}{2} \int \xi^2 f d\boldsymbol{\xi} = \frac{1}{2} \rho v^2 + \frac{1}{2} \int c^2 f d\boldsymbol{\xi} \quad (3.96)$$

The first term of the right hand side of Eq. 3.96 represents the macroscopic kinetic energy, while the second term is known as internal energy. It is convenient to define the internal energy for mass unit  $e$ :

$$\rho e = \int c_i c_i f d\boldsymbol{\xi} \quad (3.97)$$

Looking to Eq. 3.97, it is interesting to note that  $\rho e$  is equal to the trace of  $p_{lk}$ , so the isotropic part of the stress tensor is written as follows:

$$p = \frac{2}{A} \rho e \quad (3.98)$$

Finally, applying *Boyle's Law*:  $p = \rho RT$  we can write the gas energy in following form:

$$e = \frac{A}{2} RT \quad (3.99)$$

where  $A$  is the dimension of stress tensor and assumes the values 3, 5 and 7 in case of mono- bi- or polyatomic gases. The last quantity we want to investigate is the energy flow  $\Psi_{ii}$ , defined as:

$$\Psi_i = \frac{1}{2} \int \xi_i \xi^2 f d\boldsymbol{\xi} \quad (3.100)$$

By inserting Eq. 3.91 in Eq. 3.100 and doing some manipulations we obtain:

$$\Psi_i = \frac{1}{2} \int \xi_i \xi^2 f d\boldsymbol{\xi} = v_i \left( \frac{1}{2} \rho v^2 + e \right) + v_i p_{ij} + \frac{1}{2} \int c_i c^2 f d\boldsymbol{\xi} \quad (3.101)$$

where the first addend is the energy flow caused by the macroscopic convection, the second one is the work of stress for time unit and the last addend is a *non-convective energy flow*, following Cercignani [1975] interpretation.

### 3.3.1 The Boltzmann Equation and the Conservation Equations

Let us consider, for sake of generality, Eq. 3.35, multiplying every term for  $\varphi(\boldsymbol{\xi})$ , integrating on  $\boldsymbol{\xi}$ , and considering the property of the *Collision invariants* (Eq. 3.41), we can write the following equation:

$$\frac{\partial}{\partial t} \int \varphi_k f d\boldsymbol{\xi} + \frac{\partial}{\partial x_i} \int \xi_i \varphi_k f d\boldsymbol{\xi} + F_i \int \varphi_k \frac{\partial}{\partial \xi_i} d\boldsymbol{\xi} = 0 \quad (3.102)$$

where  $k = 0, 1, 2, 3, 4$  indicates the collision invariant and  $F_i$  can be taken out from the integration operation if we assume the external force independent from the velocity. Eq. 3.102 has been written using index notation to make more clear the following computations.

In order to recover the conservation equations we need to calculate the three integrals substituting successively the five collision invariants (we omit the entire calculation). Then, considering the macroscopic quantities: density (Eq.3.88), momentum (Eq.3.90), momentum flow, (Eq.3.93), internal energy, (Eq.3.97) and energy flow, (Eq.3.101) it is possible to recover

the *Conservation Equations*:

$$\begin{aligned}\frac{\partial \rho}{\partial t} + \frac{\partial}{\partial x_i}(\rho v_i) &= 0 \\ \frac{\partial}{\partial t}(\rho v_i) + \frac{\partial}{\partial x_i}(\rho v_i v_j + p_{ij}) &= \rho F_j \\ \frac{\partial}{\partial t} \left[ \rho \left( \frac{1}{2} v^2 + e \right) \right] + \frac{\partial}{\partial x_i} \left[ \rho v_i \left( \frac{1}{2} v^2 + e \right) + p_{ij} v_j + q_i \right] &= \rho F_i v_i\end{aligned}\tag{3.103}$$

where  $q_i$  is the heat flux vector [Cercignani, 1988]. The first equation is the well known *Mass Conservation equation*. The last two equations, instead, worth a particular discussion. The terms  $p_{ij}$  and  $q_i$ , in fact need to be characterized; in other words we need to find some relations (on the basis of experiments) in order to relate  $p_{ij}$  and  $q_i$  with the physical quantities  $\rho$ ,  $\mathbf{v}$  and  $e$ . If we consider  $q_i = 0$ , no heat flux is considered and so the problem is a pure fluid dynamic problem and we can derive two different *Constitutive Models*:

- with:  $p_{ij} = p\delta_{ij}$  the *Euler fluid model* is recovered;
- with:  $p_{ij} = p\delta_{ij} - \mu \left( \frac{\partial v_i}{\partial x_j} + \frac{\partial v_j}{\partial x_i} \right) - \lambda \frac{\partial v_l}{\partial x_l} \delta_{ij}$  the *Navier-Stokes fluid model* is obtained.

Where  $\mu$  and  $\lambda$  are the viscosity coefficients. Finally if we use as heat flux model the *Fourier's Law*:

$$q_i = -k \frac{\partial T}{\partial x_i}$$

coupled with the *Navier-Stokes fluid model*, we obtain the *Navier-Stokes-Fourier fluid* (NSF), where  $k$  is the heat conduction coefficient.

It is clear that this considerations are not needed if we want to solve the *Boltzmann equation* because all the macroscopic informations are contained in distribution  $f$ . The advantage to solve the macroscopic equations in place of the Boltzmann equation is that macroscopic equations have five functions in four variables, while the BE has one function of seven unknowns.

It is important to stress the fact that those equations have been recovered by neglecting the collision operator, thanks to the property of the collision invariants. The problem of turning from a microscopic to a macroscopic representation, in non trivial situations (i.e., when the collision operator is not zero), by fact, has not been already analytically resolved.

### 3.3.2 The Bhatnagar-Gross-Krook approximation of the collision operator

The main obstacle for the resolution of the Boltzmann equation in general cases is represented by the complicated form of the collision operator  $Q(f, f)$ . To overcome this problem, the idea is to replace the collision operator  $Q(f, f)$  with an approximated form  $P(f)$  which has to verify two important conditions [Cercignani, 1997]:

- The validity of Eq. 3.41, assuring that the derivation of the macroscopic models in the stationary case is still valid:

$$\int \varphi(\boldsymbol{\xi}) P(f) d\boldsymbol{\xi} = 0\tag{3.104}$$

- The validity of the *Boltzmann inequality* (Eq. 3.47), in order to guarantee that the solution of the Boltzmann Equation is still unique and the equilibrium solution has a Maxwellian form:

$$\int \log f P(f) d\boldsymbol{\xi} \leq 0 \quad (3.105)$$

The simplest way to approximate the collision integral was proposed by Bhatnagar, Gross and Krook and it is commonly known as *BGK operator*. This operator replace the collision term with an operator which is proportional to the difference between a Maxwellian distribution  $f^m(\boldsymbol{\xi})$  and the distribution function  $f(\boldsymbol{\xi})$ :

$$P(f) = \frac{f^m(\boldsymbol{\xi}) - f(\boldsymbol{\xi})}{\Lambda} \quad (3.106)$$

where  $\Lambda$  is a contact scalar. Eq. 3.106 is known as *BGK collision term*. Inserting Eq. 3.106 in Eq. 3.104, we obtain:

$$\int \varphi_i(\boldsymbol{\xi}) f^m(\boldsymbol{\xi}) d\boldsymbol{\xi} = \int \varphi_i(\boldsymbol{\xi}) f(\boldsymbol{\xi}) d\boldsymbol{\xi} \quad (3.107)$$

which means that, independently from the position  $\mathbf{x}$  and the time  $t$ ,  $f^m(\boldsymbol{\xi})$  is equal to the density. In analogous way, inserting Eq. 3.106 in Eq. 3.105 we can rewrite Eq. 3.105 as follows:

$$\int \log f P(f) d\boldsymbol{\xi} = \frac{1}{\Lambda} \int f^m(\boldsymbol{\xi}) \left( 1 - \frac{f(\boldsymbol{\xi})}{f^m(\boldsymbol{\xi})} \right) \log \frac{f(\boldsymbol{\xi})}{f^m(\boldsymbol{\xi})} d\boldsymbol{\xi} \quad (3.108)$$

It is very interesting to notice that the *BGK collision operator*, from a mathematical point of view, is much more complicated than the classic collision operator  $Q(f, f)$ , in fact, the Maxwellian distribution  $f^m$  is defined as the following functional:

$$f^m = f^m(\mathbf{v}(f(\mathbf{x}, \boldsymbol{\xi}, t)), \rho(f(\mathbf{x}, \boldsymbol{\xi}, t)), T(f(\mathbf{x}, \boldsymbol{\xi}, t))) \quad (3.109)$$

Otherwise  $Q(f, f)$  is simply a quadratic function of  $f$ . So the natural question is: how this approximation can *simplify* the problem? In the next section we will show that using the BGK we can recover the constitutive equations for different fluid phase, and, in particular we will show how this approximation can be used to recover the Navier-Stokes equations in a general case.

### 3.3.3 The perturbation method and the Linearized Boltzmann equation

In this section we derive the *linearized Lattice Boltzmann* equation which will be used in the following section as starting point in the derivation of the constitutive equations. One of the most common strategies to linearize an equation is to apply the so called perturbation method. Here we consider the power series expansion of  $f$  in  $\varepsilon$  which is defined as follows:

$$f = \sum_{n=0}^{\infty} \varepsilon^n f_n \quad (3.110)$$

where  $n$  is the power. Applying Eq. 3.110 to the collision operator  $Q(f, f)$  we obtain:

$$f = \sum_{n=0}^{\infty} \varepsilon^n Q_n \quad (3.111)$$

where the coefficients of the power series  $Q_n$  are expressed as follows:

$$Q_n = \sum_{l=0}^n Q(f_l, f_{n-l}) \quad (3.112)$$

In literature many perturbation methods have been proposed among the years; most of this are based on the initial assumption that the zero-th term of the power expansion  $f_0$  must represent a Maxwellian distribution  $f^m$ . It follows that:

$$Q(f_0, f_0) = 0 \quad (3.113)$$

Furthermore, we can write Eq. 3.110 as follows:

$$f = f_0 + \sum_{n=1}^{\infty} \varepsilon^n f_n \quad (3.114)$$

thus, Eq. 3.112 can be rewritten as follows:

$$Q_n = 2Q(f_0, f_n) + \sum_{l=1}^{n-1} Q(f_l, f_{n-l}) \quad (3.115)$$

where the first term of Eq. 3.115 can be viewed as a *linear operator*, since the zero-th term  $f_0$  acts on the  $n$ -th term  $f_n$  of the expansion. It is common to rewrite Eq. 3.115 considering the following relations:

$$f_n = f_0 h_n \quad \text{and} \quad f_0 S_n = \sum_{l=1}^{n-1} Q(f_l, f_{n-l}) \quad (3.116)$$

where the unknowns turn from  $f_n$  to  $h_n$ . Applying the relations 3.116 to Eq. 3.115 we obtain:

$$Q_n = 2Q(f_0, f^{eq} h_n) + f^{eq} S_n \quad (3.117)$$

In conclusion, considering the new operator  $Jh_n = 2Q(f_0, f_0 h_n)/f_0$ , we can write Eq. 3.117 as follows:

$$Q_n = f_0 Jh_n + f_0 S_n \quad (3.118)$$

which is commonly known as *linearized collision operator*. Applying, now Eqs. 3.110, 3.115 to Eq. 3.33 we can rewrite the Boltzmann equation as follows:

$$\varepsilon^0 \left( \frac{\partial f_0}{\partial t} + \boldsymbol{\xi} \cdot \frac{\partial f_0}{\partial \mathbf{x}} \right) + \sum_{n=1}^{\infty} \varepsilon^n \left( \frac{\partial f_n}{\partial t} + \boldsymbol{\xi} \cdot \frac{\partial f_n}{\partial \mathbf{x}} \right) = \varepsilon^0 Q(f_0, f_n) + \sum_{n=1}^{\infty} \varepsilon^n \sum_{l=1}^{n-1} Q(f_l, f_{n-l}) \quad (3.119)$$

then, with simple computations we split Eq. 3.119 into two equations: the first describing the equilibrium state and the second describing little deviations from the equilibrium state:

$$\begin{aligned}\frac{\partial f_0}{\partial t} + \boldsymbol{\xi} \cdot \frac{\partial f_0}{\partial \mathbf{x}} &= Q(f^{eq}, f^{eq}) = 0 \\ \frac{\partial f_n}{\partial t} + \boldsymbol{\xi} \cdot \frac{\partial f_n}{\partial \mathbf{x}} &= \sum_{l=1}^{n-1} Q(f_l, f_{n-l})\end{aligned}\quad (3.120)$$

Accordingly, Introducing Eq. 3.116 in Eq. 3.120 we obtain:

$$\frac{\partial h_n}{\partial t} + \boldsymbol{\xi} \cdot \frac{\partial h_n}{\partial \mathbf{x}} = Jh_n + S_n \quad (3.121)$$

where the term  $S_n$  is defined as follows:

$$\begin{aligned}S_1 &= 0 \quad \text{for } n = 1; \\ S_n &= \frac{\sum_{l=1}^{n-1} Q(f_0 h_l, f_0 h_{n-l})}{f_0} \quad \text{for } n > 1;\end{aligned}\quad (3.122)$$

Eq. 3.121 represents a series of equation in which the difference from an equation to the previous one is given by the term  $S_n$ . Finally, considering  $n = 1$ , we obtain:

$$\frac{\partial h}{\partial t} + \boldsymbol{\xi} \cdot \frac{\partial h}{\partial \mathbf{x}} = Jh \quad (3.123)$$

where Eq. 3.123 represents the *linearized Boltzmann equation*. The main advantage of this formulation is the linear behavior of the equation, but the collision term still remains very complicated since it is already an integro-differential operator.

### 3.3.4 The dimensionless Boltzmann equation

In this section we study the order of magnitude of the terms of Boltzmann equation. We assume  $L_0$  to be the characteristic length,  $t_0$  the characteristic time,  $T_0$  the characteristic temperature and  $\rho_0$  the characteristic density of the problem. We can write the following dimensionless quantities:

$$\mathbf{x}^* = \frac{\mathbf{x}}{L_0}, \quad t^* = \frac{t}{t_0}, \quad \boldsymbol{\xi}^* = \frac{L_0}{t_0} \boldsymbol{\xi}, \quad \mathbf{F}^* = \frac{t_0^2}{L_0} \mathbf{F}, \quad f^* = \frac{L_0^3}{\rho_0 t_0^3} f \quad (3.124)$$

Thus, the Boltzmann equation (Eq. 3.35) can be rewritten in non dimensional terms, as follows:

$$\frac{\partial f^*}{\partial t^*} + \boldsymbol{\xi}^* \cdot \frac{\partial f^*}{\partial \mathbf{x}^*} + \mathbf{F}^* \cdot \frac{\partial f^*}{\partial \boldsymbol{\xi}^*} = \frac{1}{Kn} Q(f^*, f^*) \quad (3.125)$$

where  $Kn$  is the Knudsen number which describe the ratio between the mean free path of a particle  $l_f$  and characteristic length of the problem:

$$Kn = \frac{l_f}{L_0} \quad (3.126)$$



In a certain sense the Knudsen number describes the state of aggregation of the molecules, in fact, when  $Kn \rightarrow \infty$  the particles are free to move, i.e the gas is very rarefied, otherwise when  $Kn \rightarrow 0$  the gas is very dense similar in liquid state. Finally when  $Kn$  is a finite number we talk of transient state. In this thesis we focus on  $Kn \rightarrow 0$ , i.e. on very dense fluids which are basically at the liquid state.

### 3.3.5 From Boltzmann equation to Navier-Stokes equations: the Chapman-Enskog expansion

With the background delineated in the previous sections, we are now ready to describe the procedure that leads to recover the Navier-Stokes equations from the Boltzmann equation in its general configuration.

As we have shown in Section 3.3.3, to obtain a more manageable formulation of the Boltzmann equation, it is convenient to introduce some approximation, in order to linearize the equation; furthermore the classic approximation scheme relies on the perturbation method. Hilbert [1906] proposed to adopt a power series expansion of the function  $f$  and, following the procedure shown in Section 3.3.3 and assuming  $\varepsilon = Kn \rightarrow 0$ , we re-write the Boltzmann equation in function of the unknown  $h_n$ :

$$\frac{\partial f_0 h_n}{\partial t} + \boldsymbol{\xi} \cdot \frac{\partial f_0 h_n}{\partial \mathbf{x}} = J f_0 h_{n+1} + S_{n+1} \quad (3.127)$$

where  $S_{n+1}$  is defined by the Eq. and the Eq. 3.116 has been introduced.

Eq. 3.127 represent a system of equations in  $h_n$  unknowns, furthermore it can be proved [Cercignani, 1988] that the unknown  $h_n$  can be expressed as a linear combination of the five collision invariants  $\varphi(\boldsymbol{\xi})$ ; furthermore it is possible to show that the source term in the  $(n+1)$ -th step is given by:

$$\Pi_{n+1} = \frac{\frac{\partial f_0 h_n}{\partial t} + \boldsymbol{\xi} \cdot \frac{\partial f_0 h_n}{\partial \mathbf{x}} - S_{n+1}}{f_0} \quad (3.128)$$

which means that the source term is calculated using the previous step solutions. Moreover applying the orthogonality conditions [Cercignani, 2000] of the collision invariants, we can rewrite Eq. 3.127 as follows:

$$\int \varphi_k(\boldsymbol{\xi}) \left( \frac{\partial f_n}{\partial t} + \boldsymbol{\xi} \cdot \frac{\partial f_n}{\partial \mathbf{x}} \right) \boldsymbol{\xi} d\boldsymbol{\xi} = 0 \quad (3.129)$$

We observe that both  $f_n$  and  $\varphi$  are dependent on  $\boldsymbol{\xi}$ , so we can invert the order of integration and derivation and finally write Eq. 3.129 as follows:

$$\frac{\partial \rho_n^k}{\partial t} + \nabla \cdot \mathbf{j}_n^k = 0 \quad \text{with} \quad k = 0, 1, 2, 3, 4 \quad (3.130)$$

where

$$\rho_n^k = \int \varphi^k f_n d\boldsymbol{\xi} \quad \text{and} \quad \mathbf{j}_n^k = \int \boldsymbol{\xi} \varphi^k f_n d\boldsymbol{\xi} \quad (3.131)$$

Accordingly, introducing the relations derived in Section 3.3, we can write  $\rho^k$  as follows:

$$\rho^k = \begin{Bmatrix} \rho \\ \rho v_i \\ \rho(\frac{1}{2}v^2 + e) \end{Bmatrix} \quad \text{with } i = 1, 2, 3 \quad (3.132)$$

while  $\mathbf{j}^k$  can be written as follows:

$$\mathbf{j}^k = \begin{Bmatrix} \rho v_i \\ \rho v_i v_j + p_{ij} \\ \rho v_i(\frac{1}{2}v^2 + e) + p_{ij} + q_j \end{Bmatrix} \quad \text{with } i = 1, 2, 3 \quad \text{and } j = 1, 2, 3 \quad (3.133)$$

it is possible to show, with some computations, that the constitutive equations (Eqs. 3.103), can rearranged, in terms of  $\rho^k$  and  $\mathbf{j}^k$ , as follows:

$$\frac{\partial \rho^k}{\partial t} + \nabla \cdot \mathbf{j}^k = 0 \quad \text{with } k = 0, 1, 2, 3, 4 \quad (3.134)$$

We observe that Eq. 3.130 is the expansion of Eq. 3.134, so we are going to think that Eq. 3.130 represents an alternative form to write the constitutive equations. To better explain this concept, we can rewrite Eq. 3.134 as following:

$$E^k(\rho^\alpha) = S^k \quad (3.135)$$

where  $S^k$  is given by:

$$S^k = \begin{Bmatrix} 0 \\ -\frac{\partial}{\partial x_j}(p_{ij} - p\delta_{ij}) \\ -\frac{\partial}{\partial x_j}(p_i j v_j - p v_i + q_i) \end{Bmatrix} \quad (3.136)$$

and  $E^k$  is the so-called *Euler operator* which is constructed such that  $E^k(\rho^\alpha) = 0$  give the exact solution the inviscid fluid equations, called also. *Euler equations*. What Hilbert did was to expand  $\rho^\alpha$ , in Eq. 3.135, into a series of power of  $\varepsilon$  as following:

$$E^k(\rho^\alpha) = E^k(\rho_0^\alpha) + \sum_{n=1}^{\infty} \varepsilon^n E^{k\alpha}(\rho_n^\alpha) + \sum_{n=2}^{\infty} \varepsilon^n E_n^k(\rho_n^\alpha) \quad (3.137)$$

It is possible to prove [Cercignani, 1988] that the expansion of Eq. 3.137 is able to represent the inviscid fluid equations, but contains also some additive terms (last two addend of Eq. 3.137) which made it suitable to solve only certain problems imposing suitable initial data and boundary conditions. Finally we can conclude that the Hilbert expansion fails in giving valid solutions for the Boltzmann equation for given initial data and boundary value problems and, thus, it is not able to reproduce the Navier-Stokes-Fourier constitutive equations (Eq. 3.103).

A solution of this problem was provided by Chapman and Enskog who proposed [Chapman and Cowling, 1970] to expand the Boltzmann equation itself and not the solutions, like in Hilbert expansion; or in other words, to expand  $S^k$  and leave unexpanded  $\rho^\alpha$ , such that:

$$E^k(\rho^\alpha) = \sum_{n=1}^{\infty} \varepsilon^n (S_n^k) = S^k(\rho^\alpha) \quad (3.138)$$

With some computations on the space derivatives on term  $E^k$ , we can rewrite Eq. 3.138 as follows:

$$\frac{\partial \rho^\alpha}{\partial t} = D_\alpha(\rho^\beta) \quad \text{with:} \quad D_\alpha = \sum_{n=0}^{\infty} \varepsilon^n D_\alpha^{(n)} \quad (3.139)$$

where  $D_\alpha$  is a non-linear operator. Chapman and Cowling [1970] pointed out that this expansion needs to maintain the results obtained with the Hilbert expansion, i.e., that  $f$  are functionals of  $\rho^\beta$ . Applying the chain derivation rule, we can write the time derivative of  $f$  is given by:

$$\frac{\partial f}{\partial t} = \sum_{l=0}^{\infty} \frac{\partial f}{\partial (\nabla^l \rho^\beta)} \frac{\partial (\nabla^l \rho^\beta)}{\partial t} \quad (3.140)$$

and thus, we can rewrite Eq. 3.139 as following:

$$\frac{\partial}{\partial t} \nabla^l \rho^\beta = \nabla^l D_\alpha(\rho^\beta) \quad (3.141)$$

where  $\nabla^l$  denotes the  $n$ -th order spatial derivatives. Now, according with the Chapman-Enskog method, we have to expand  $f$  without expanding  $\rho^\beta$ , which means that, when  $f$  is regarded as function of  $\mathbf{x}, \boldsymbol{\xi}, t$ , it is not expanded, although, when  $f$  is regarded as functional of  $\rho^\beta$ , it is expanded in series of  $\varepsilon$ , according to Eq. 3.110. In consequence, we can expand Eq. 3.127 as follows:

$$\sum_{l=0}^{l-1} \frac{\partial^l f_0 h_{n-l}}{\partial t} + \boldsymbol{\xi} \cdot \frac{\partial f_0 h_n}{\partial t} = J f_0 h_{n+1} + S_{n+1} \quad \text{with} \quad n = 0, 1, 2, \dots \quad (3.142)$$

and of course it must hold that  $Q_0 = 0$  meaning that the  $f_0$  is a Maxwellian distribution to ensure the stationary solution. Furthermore, it must hold also the collision invariant property:

$$\int \varphi_\beta f_n d\boldsymbol{\xi} \quad (3.143)$$

Now, regarding  $f_n$  both as function of  $\boldsymbol{\xi}$  and functional of  $\rho^\beta$ , and assuming the orthogonality conditions of  $\varphi$  [Cercignani, 2000], we can rewrite Eq. 3.142 as follows:

$$\frac{\partial}{\partial t} \rho^\beta + \nabla \cdot \int \boldsymbol{\xi} \varphi_\beta f d\boldsymbol{\xi} = 0 \quad \text{with} \quad \beta = 0, 1, 2, 3, 4 \quad (3.144)$$

where  $\rho^\beta$  is left unexpanded, in the Chapman-Enskog philosophy; moreover we can approximate the integral of  $f_n$  as follows:

$$\frac{\partial \rho^\beta}{\partial t} + \nabla \cdot \int \boldsymbol{\xi} \varphi_\beta \sum_{n=0}^N \varepsilon^n f_n d\boldsymbol{\xi} = 0 \quad \text{with} \quad \beta = 0, 1, 2, 3, 4 \quad (3.145)$$

which is the final result of the Chapman-Enskog expansion.

Now, looking to Eq. 3.130 and to Eq. 3.145, we can notice that the main difference between the Hilbert expansion and the Chapman-Enskog Expansion is that in the former, higher order solutions are dependent on the previous solution, while in the latter, to obtain higher order solutions, we need to solve a completely new set of equations.

When  $n = 0$ ,  $f_0$  is a Maxwellian distribution, thus it is straightforward to see that we recover Eq. 3.136 and the contribution to the stress tensor is given by:

$$p_{ij} = p\delta_{ij} \quad (3.146)$$

In order to find the Navier-Stokes equations, instead, we have to write the solution for  $n = 1$ , thus considering the first two terms of the Chapman-Enskog Expansion. It is finally possible to show that the first two terms of the Chapman-Enskog expansion gives the following contribution to the stress and heat flux tensor [Cercignani, 1988]:

$$\begin{aligned} p_{ij} &= p\delta_{ij} - \mu \left( \frac{\partial v_i}{\partial x_j} + \frac{\partial v_j}{\partial x_i} \right) - \lambda \frac{\partial v_l}{\partial x_l} \delta_{ij} \\ q_i &= -k \frac{\partial T}{\partial x_i} \end{aligned} \quad (3.147)$$

Furthermore it is possible to show that  $\lambda = 2/3\mu$  and in consequence a Prandtl number  $Pr = 2/3$ . This results is very important, in fact it is possible to prove that both the general solution of the Boltzmann equation and the experimental tests show that for non Maxwellian molecules the Prandtl number is close to  $2/3$ .

In conclusion we have demonstrated that with a suitable expansion of certain terms of the Boltzmann equation, it is possible to recover the macroscopic description of the Navier-Stokes-Fourier viscous fluid.

### 3.3.6 Higher-order Chapman-Enskog expansion: Burnett and Super-Burnett equations

In the previous Section, we have shown that applying the Chapman-Enskog to the Boltzmann equation, it is possible to recover the Navier-Stokes-Fourier macroscopic description of a viscous fluid. Nevertheless, the Chapman-Enskog expansion has some shortcomings. In particular, we notice that if we write the solution of Eq. 3.145 for  $n > 1$ , we do not recover a more accurate description of a viscous fluid, but we recover the different equations. In specific, we know that the with  $n = 2$  we recover the so-called *Burnett equations* and with  $n = 3$  we recover the so-called *Super-Burnett equations* [Agarwal et al., 2001].

It is not object of this thesis to study the Burnett and the Super-Burnett equations. We just limit to briefly describe their applications and physical background.

Physically speaking, the Burnett and the Super-Burnett equations are used to describe micro-flows or fluid-dynamics problems at the low pressure conditions (high flights). These flows are associated to Knudsen numbers higher than 0.05, which are not precisely consistent with the assumption made in Section 3.3.5, so those equations are describing a non full dense fluid. Furthermore, many authors, including Struchtrup [2005], pointed out that those equations are very unstable, and in general the solution blows up in time.

Cercignani [1975] showed that in order to neglect higher order terms of Chapman Enskog expansion, it is possible to split the time derivative of  $f$  instead of applying the perturbation method, in this way, basically, Eq. 3.145 is truncated to the first order and only the Navier-Stokes equations are recovered.

### 3.3.7 Considerations about the Navier-Stokes equations and Boltzmann equation

In the previous sections, we have demonstrated that it is possible to derive the Navier-Stokes equations from the Boltzmann equations. In the present Section, we look to those equations, trying to give them a more physical interpretation.

First of all we rewrite the Boltzmann equation and the momentum conservation of a Navier-Stokes fluid, in their normalized formulation:

$$\begin{aligned}\frac{\partial f^*}{\partial t^*} + \boldsymbol{\xi}^* \cdot \frac{\partial f^*}{\partial \mathbf{x}^*} &= \frac{1}{Kn} Q(f^*, f^*) \\ \frac{\partial \mathbf{v}^*}{\partial t} + \mathbf{v}^* \cdot \frac{\partial \mathbf{v}^*}{\partial \mathbf{x}^*} &= \frac{1}{Re} \sum_{i=1}^3 \frac{\partial^2 \mathbf{v}_i^*}{\partial \mathbf{x}_i^{*2}} - \frac{\partial P^*}{\partial \mathbf{x}^*}\end{aligned}\tag{3.148}$$

where, in both the equations we have neglected the forcing term. The left hand side is the same for Boltzmann and Navier-Stokes equation, except for that the microscopic velocity  $\boldsymbol{\xi}^*$  is replaced by the macroscopic velocity  $\mathbf{v}^*$ . The left hand sides describe the *convection* between the particles, while the right hand sides describe the *diffusion* (or collision) among the particles. From a pure mathematical point of view, the convective term is hyperbolic, while the diffusive term is parabolic.

The Knudsen number  $Kn$  and the Reynold number  $Re$  are the two parameters which govern the non dimensional equations. It is possible to show that these non dimensional numbers are related as follows:

$$Kn = \frac{Ma}{Re}\tag{3.149}$$

where  $Ma$  is the Mach number. It is important to underline that in order to have incompressible flows,  $Ma$  must not exceed the value of 0.3.

### 3.3.8 Final overview on the Boltzmann equation and its applications

In the previous sections we have derived the Boltzmann equation starting from the Newton particles dynamic and following step by step Boltzmann's work. We have illustrated some important properties of the Boltzmann equation, like the *H – theorem* and its relation to the second law of thermodynamics. Finally we have discussed about the possibility to pass from the microscopic (particle level) to the macroscopic (continuous level) description of a fluid. Introducing some approximations (i.e., the linear collision operator and the perturbation method), we have demonstrated how it is possible to derive the Navier-Stokes-Fourier equations, starting from the Boltzmann equation.

The Boltzmann equation represents, thus a bridge between the microscopic word (Newton's law and Liouville's theorem) and the macroscopic word (Navier-Stokes-Fourier equations), in fact the Boltzmann equation conserves the essential characteristics of particle dynamics, but, at the same time the probabilistic approach allows to recover the conservation equations at the macro-scale. For this reason, in literature, it is quite common to refer to the Boltzmann equation as a *mesoscopic* approach to solve thermo-fluid-dynamic problems.

To make easier the comprehension of the discussed historical workflow, we highlight in Fig. 3.4 the fundamental equations describing the evolution of a particle system at different scale levels.

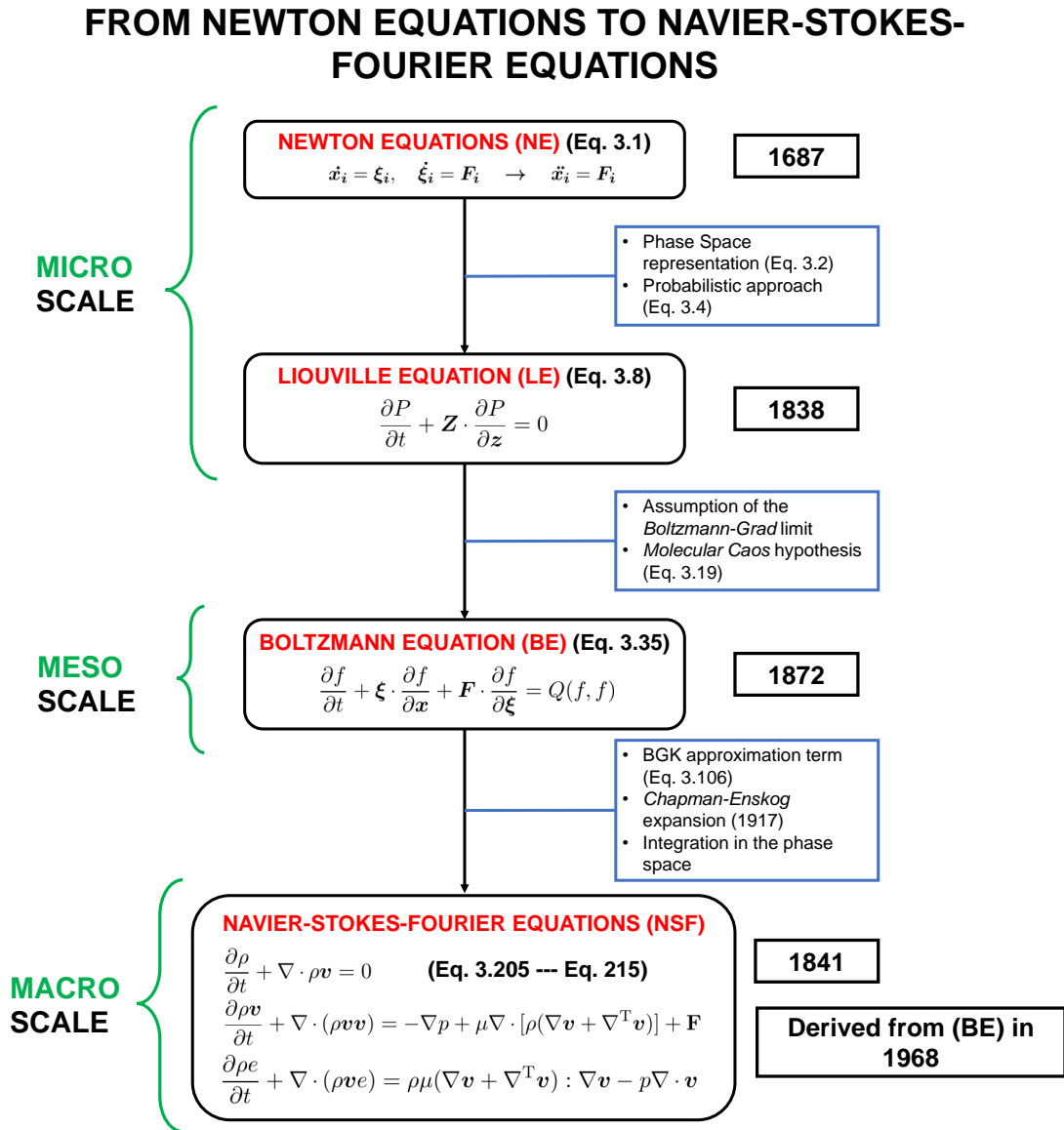


Figure 3.4: From Newton equation to Navier-Stokes-Fourier equations: basic steps.

### 3.4 From the Boltzmann Equation to the Lattice Boltzmann Method

In the previous sections, we have demonstrated that the Boltzmann equation can be successfully adopted to describe the evolution of a Navier-Stokes-Fourier fluid, thus it can be used to solve thermo-fluid dynamic problems.

The main complication in the resolution of the Boltzmann equation is represented by the complicated form of the collision operator  $Q(f, f)$ . We have shown that the analytic expression of the collision operator can be substituted by an approximated operator which is more manageable. Nevertheless, the solution of the Boltzmann equation remains still very complicated.

The first solution scheme for the Boltzmann equation was proposed by McNamara and Zanetti [1988] who developed, the so-called *Lattice Boltzmann method*. The Lattice Boltzmann method (LBM) takes its origins from the Lattice Gas Automata (LGA) method [Frisch et al., 1986]. The basic idea of LGA is that it is possible to describe the Navier-Stokes fluid on a simplified regular domain considering simplified dynamics and assuring mass and momentum conservation. LGA has been developed in the middle of seventies and then they have been used until the eighties, without a real theoretical background. The idea behind the development of LGA was to build up a computational framework easy and manageable to solve fluid dynamics problems with the available computational efforts.

The basic idea of LGA was to discretize the space with a lattice structure and to describe the fluid as an amount of particles which can move with certain velocities along fixed directions, colliding with other particles. Although, LGA showed several problems; first of all in this method the equilibrium distribution was represented by the Dyrac-Fermi distribution and not by the Maxwellian distribution, leading to a violation of the Galilean invariance [Wolf-Gladrow, 2004]. Furthermore, in LGA, the velocity is dependent on the velocity and, in general, the method suffers of instability problems.

To solve all these issues, McNamara and Zanetti [1988] proposed to substitute the Dyrac-Fermi distribution with the Maxwellian distribution, and proposed the first *Lattice Boltzmann method*.

#### 3.4.1 Brief chronology of the Lattice Boltzmann method

Nevertheless LBM is a quite new computational method, in about twenty years of life, it has been successfully applied to face different thermo-fluid dynamic problems.

At the beginning of the 90s, the LB method was tested on fluid dynamic problems with an analytical solution [McNamara and Zanetti, 1988], then Shan and Chen [1993] developed the first LB method to simulate multiphase and multicomponent flows. However, only in 1997 He and Luo [1997a] demonstrated that the LB equation can be directly derived from the BE, giving a solid theoretical background to the corresponding computational method.

In early 2000s, the LB method was used to simulate particle-fluid suspensions [Ladd and Verberg, 2001] and incompressible flows through porous media [Guo and Zhao, 2002]. Teixeira et al. [2000] and Palmer and Rector [2000] proposed two different lattice schemes to face thermal problems, while Yu et al. [2003] extended the application of LB method to incompressible flows with high Re number. Chatterjee and Chakraborty [2005] adopted the LB method to

investigate the solid-liquid phase change and Körner et al. [2005] developed a free surface LB scheme for modelling foaming. Geller et al. [2006] proposed an interesting comparison among various CFD tools, concluding that the LB method is particularly suitable to face problems with very complex geometries and boundary conditions; moreover Zheng et al. [2006] proposed a LB scheme to simulate multiphase flows with high density ratio. Attar and Körner [2011] adopted for the first time the LB method to investigate melt pool dynamics in EBM processes, including powder melting/solidification process and free surface evolution of the melt pool. Gong and Cheng [2012] used the LB method to simulate liquid-vapour phase change for high density ratio fluid mixtures; finally Huang et al. [2013] proposed an innovative LB scheme to face solid-liquid phase change problems.

From this review, it is interesting to notice that until 1997, the Lattice Boltzmann method was used without a real theoretical background, which was given right in that year by He and Luo [1997b].

The procedure to derive the *lattice Boltzmann method* from the *Boltzmann equation* can be resumed in the following steps:

- The derivation of an evolution equation discretized in time, the so-called *lattice Boltzmann equation*;
- the application of a quadrature formula to approximate the integration in momentum space;
- the calculation of a proper discrete equilibrium distribution function which allows to reproduce exactly the macroscopic quantities.

In the following section, following the work of He and Luo [1997b] we will show how LBM can be rigorously derived by the Boltzmann equation.

### 3.4.2 From the Boltzmann Equation to the Lattice Boltzmann Equation

To derive the Lattice Boltzmann equation we start from the classic formulation of the Boltzmann equation neglecting the forcing term (Eq. 3.33):

$$\frac{\partial f}{\partial t} + \boldsymbol{\xi} \cdot \frac{\partial f}{\partial \mathbf{x}} = Q(f, f) \quad (3.150)$$

now, we replace the collision term  $Q(f, f)$  with the BGK approximation and we can rewrite the Boltzmann equation as follows:

$$\frac{\partial f}{\partial t} + \boldsymbol{\xi} \cdot \frac{\partial f}{\partial \mathbf{x}} = \frac{f^{eq}(\mathbf{x}, \boldsymbol{\xi}, t) - f(\mathbf{x}, \boldsymbol{\xi}, t)}{\tau} \quad (3.151)$$

From the pure mathematical point of view, Eq. 3.151 is an ordinary difference equation (ODE). To solve Eq. 3.151, we apply the well know chain derivation rule and, thus, we rewrite Eq. 3.151 as following:

$$\frac{df}{dt} + \frac{1}{\tau} f = \frac{1}{\tau} f^{eq} \quad (3.152)$$



where the  $d$  is the total derivative operator. Eq. 3.152 is a first order differential linear equation with constant coefficients [Coddington, 2012]. The solution for this type of equations is well known and can be expressed as:

$$f(t+\delta t) = f(\mathbf{x} + \boldsymbol{\xi}\delta t, \boldsymbol{\xi}, t + \tau t) = \exp^{-\frac{\delta t}{\tau}} f(\mathbf{x}, \boldsymbol{\xi}, t) + \frac{1}{\tau} \exp^{-\frac{\delta t}{\tau}} \int_0^{\delta t} \exp^{\frac{\delta t'}{\tau}} f^{eq}(\mathbf{x} + \boldsymbol{\xi}\delta t', \boldsymbol{\xi}, t + t') dt' \quad (3.153)$$

Applying Taylor expansion around term  $\delta t = 0$  and truncating it at the first order we obtain the following equalities:

$$\exp^{-\frac{\delta t}{\tau}} = 1 - \frac{1}{\tau} \delta t + O(\delta t^2) \quad (3.154)$$

$$\frac{1}{\tau} \exp^{-\frac{\delta t}{\tau}} \int_0^{\delta t} \exp^{\frac{\delta t'}{\tau}} f^{eq}(\mathbf{x} + \boldsymbol{\xi}\delta t', \boldsymbol{\xi}, t + t') dt' = \frac{1}{\tau} f^{eq}(\mathbf{x}, \boldsymbol{\xi}, t) \delta t + O(\delta t^2) \quad (3.155)$$

Inserting the two expansions (Eqs. 3.154, 3.155) in Eq. 3.153 we obtain the final expression of the *lattice Boltzmann equation*:

$$f(\mathbf{x} + \boldsymbol{\xi}\delta t, \boldsymbol{\xi}, t + \delta t) - f(\mathbf{x}, \boldsymbol{\xi}, t) = -\frac{1}{\tau} (f(\mathbf{x}, \boldsymbol{\xi}, t) - f^{eq}(\mathbf{x}, \boldsymbol{\xi}, t)) + O(\delta t^2) \quad (3.156)$$

where  $\tau$  is called *relaxation time*.

An analogous procedure is applied to expand the equilibrium distribution function (Eq. 3.82), which can be rewritten as follows:

$$f^{eq}(\boldsymbol{\xi}) = \frac{\rho}{\sqrt{(2\pi RT)^3}} \exp\left[-\frac{\boldsymbol{\xi}^2}{2RT}\right] \exp\left[-\frac{\mathbf{v}^2}{2RT} + \frac{\boldsymbol{\xi} \cdot \mathbf{v}}{RT}\right] \quad (3.157)$$

we perform the Taylor expansion on the term  $u/\sqrt{RT}$  around  $u/\sqrt{RT} = 0$ . This procedure is usually called *low Mach number expansion* because in an ideal gas the sound speed  $c_s$  is given by:

$$c_s = \sqrt{\zeta RT} \quad (3.158)$$

where  $\zeta$  is the ratio between the isobaric and the isochoric specific heats. Thus, being the Mach number the ratio between the macroscopic velocity and the sound speed, it is proportional to  $u/\sqrt{RT}$ . Finally, applying the low Mach number expansion, we obtain the expanded formulation of the equilibrium term:

$$f^{eq}(\boldsymbol{\xi}, \mathbf{t}) = \frac{\rho}{\sqrt{(2\pi RT)^3}} \exp\left[-\frac{\boldsymbol{\xi}^2}{2RT}\right] \left[1 + \frac{\boldsymbol{\xi} \cdot \mathbf{v}}{RT} + \frac{(\boldsymbol{\xi} \cdot \mathbf{v})^2}{2(RT)^2} - \frac{\mathbf{v}^2}{2RT}\right] + O(Ma^3) \quad (3.159)$$

### 3.4.3 The integration in the momentum space

As discussed in Section 3.3, the macroscopic quantities can be recovered through the zero-th, first and second momentum of distribution functions  $f$ . Following He and Luo [1997b] procedure, to recover the lattice Boltzmann method we need to apply a quadrature formula

to solve the generic momentum:

$$M_k = \int \xi_x^l \xi_y^m \xi_z^n f(\mathbf{x}, \boldsymbol{\xi}, t) d\boldsymbol{\xi} \quad (3.160)$$

where  $k = l + m + n$ . The generic quadrature formula can be written as follows:

$$M_k = \int \xi_x^l \xi_y^m \xi_z^n f(\mathbf{x}, \boldsymbol{\xi}, t) d\boldsymbol{\xi} = \sum_{i=1}^p w_i \xi_x^l \xi_y^m \xi_z^n f(\mathbf{x}, \boldsymbol{\xi}_i, t) \quad (3.161)$$

where the velocity space  $\boldsymbol{\xi}$  is now discretized in a set of discrete velocities  $\boldsymbol{\xi}_i$ . The choice of the correct quadrature formula is of crucial importance in the discretization procedure. As pointed out by Cercignani [1975], the Chapman-Enskog expansion of the Boltzmann equation, leading to the Navier-Stokes equations, is basically an expansion of  $f$  in the first two orders  $f_0 = f^{eq}$  and  $f^1$ ; moreover He and Luo [1997b] underlined that the quadrature formula must be able to compute exactly the macroscopic quantities, so it must hold that:

$$\begin{aligned} \rho(\mathbf{x}, t) &= \int f(\mathbf{x}, \boldsymbol{\xi}, t) d\boldsymbol{\xi} = \sum_{i=1}^p w_i f(\mathbf{x}, \boldsymbol{\xi}_i, t) \\ \mathbf{v} &= \frac{\int \boldsymbol{\xi} f(\mathbf{x}, \boldsymbol{\xi}, t) d\boldsymbol{\xi}}{\rho(\mathbf{x}, t)} = \frac{\sum_{i=1}^p w_i \boldsymbol{\xi}_i f(\mathbf{x}, \boldsymbol{\xi}_i, t)}{\rho(\mathbf{x}, t)} \\ e &= \frac{\int c_j c_j f(\mathbf{x}, \boldsymbol{\xi}, t) d\boldsymbol{\xi}}{\rho(\mathbf{x}, t)} = \frac{\sum_{i=1}^p w_i c_j c_j f(\mathbf{x}, \boldsymbol{\xi}_i, t) d\boldsymbol{\xi}}{\rho(\mathbf{x}, t)} \end{aligned} \quad (3.162)$$

The problem now is: how to choose the quadrature formula? We remark that, in order to reproduce correctly the momentum, the generic quadrature formula must be such that:

$$\int \phi(\boldsymbol{\xi}) g(\mathbf{x}, \boldsymbol{\xi}, t) d\boldsymbol{\xi} = \sum_{j=1}^p w_j \phi(\boldsymbol{\xi}_j) g(\mathbf{x}, \boldsymbol{\xi}_j, t) \quad (3.163)$$

where  $\phi(\boldsymbol{\xi})$  is a generic polynomial function and  $g(\mathbf{x}, \boldsymbol{\xi}, t)$  is a generic distribution function. Thus, applying such quadrature scheme to the equilibrium distribution function (Eq. 3.159), we obtain:

$$\int \phi(\boldsymbol{\xi}) f^{eq}(\mathbf{x}, \boldsymbol{\xi}, t) d\boldsymbol{\xi} = \sum_{j=1}^p w_j \phi(\boldsymbol{\xi}_j) \frac{\rho}{\sqrt{(2\pi RT)^3}} \exp\left[-\frac{\boldsymbol{\xi}^2}{2RT}\right] \left[1 + \frac{\boldsymbol{\xi} \cdot \mathbf{v}}{RT} + \frac{(\boldsymbol{\xi} \cdot \mathbf{v})^2}{2(RT)^2} - \frac{\mathbf{v}^2}{2RT}\right] \quad (3.164)$$

From a pure mathematical point of view, Eq. 3.164 has the following form:

$$\int \exp^{-\boldsymbol{\xi}^2} \phi(\boldsymbol{\xi}) d\boldsymbol{\xi} \quad (3.165)$$

so the argument of the integral has the form of a Gaussian distribution, therefore, the integral can be computed numerically using the Gauss-Hermite quadrature formula. and, in particular, we are able to reproduce exactly integrals as proposed in Eq. 3.165.

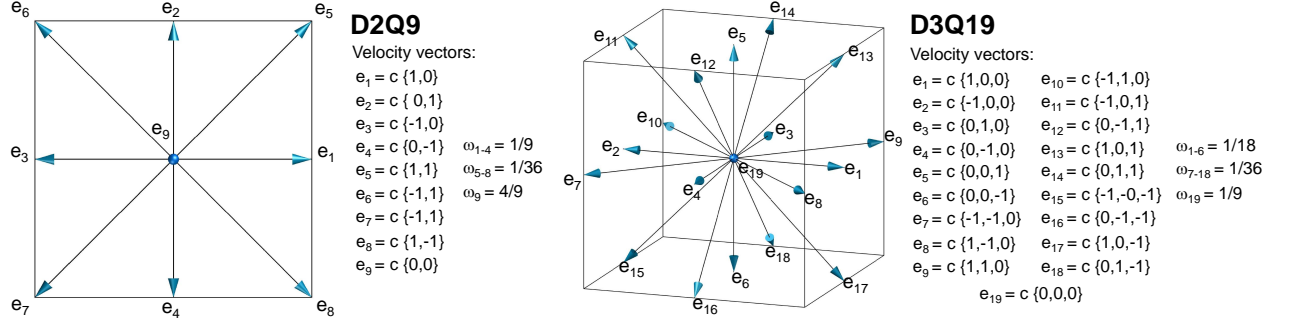


Figure 3.5: LB schemes in two and three dimensions. On the left, the bi-dimensional D2Q9 model with its 9 velocities. On the right, the three-dimensional D3Q19 scheme with its 19 velocities.

The usage of the quadrature formulas leads to discretize the velocity space. It is usual, in literature, to identify the discrete set of velocity with the denomination:  $DmQn$  where  $m$  indicates the space dimension and  $n$  indicates the number of the velocities. Classical schemes are D2Q5, D2Q9, D3Q19 and D3Q27. In Figure 3.5 we show the D2Q9 and the D3Q19 lattice schemes, which are the most adopted LBM schemes in 2D and 3D, respectively.

In the following section we will apply the Gaussian quadrature formula to derive the D2Q9 lattice scheme and the associated discrete equilibrium distribution function.

#### 3.4.4 Velocity and equilibrium distribution discretization

Let us suppose to work in a 2D space and to discretize the square lattice mesh as indicated in Figure 3.5 (left). Working in a Cartesian space, we can define the polynomial function  $\phi(\xi)$  as follows:

$$\phi(\xi)_{l,m} = \xi_x^l \xi_y^m \quad (3.166)$$

where  $\xi_x$  and  $\xi_y$  are the Cartesian components of the velocity  $\xi$ . Inserting Eq. 3.166 in Eq. 3.164 we obtain:

$$\int \phi(\xi)_{l,m} f^{eq}(\xi) d\xi = \frac{\rho}{\pi} (\sqrt{2RT})^{l+m} \left[ \left( 1 - \frac{v^2}{2RT} \right) Z_l Z_m + \frac{\sqrt{2}(v_x Z_{l+1} Z_m + v_y Z_l Z_{m+1})}{\sqrt{RT}} + \frac{v_x^2 Z_{l+2} Z_m + 2v_x v_y Z_{l+1} Z_{m+1} + v_y^2 Z_l Z_{m+2}}{RT} \right] \quad (3.167)$$

where  $Z_l$  is given by:

$$Z_l = \int_{-\infty}^{+\infty} \exp^{-\frac{\xi^2}{2RT}} \frac{\xi^l}{\sqrt{2RT}} d\xi \quad (3.168)$$

Eq. 3.168 represents the  $l$ -th order moment of the function  $\exp^{-\frac{\xi^2}{2RT}}$  that, in this contest, assumes the function of a weight function. Thus, applying the quadrature formula (Eq. 3.163)

to Eq. 3.168, we can approximate the integral as follows:

$$Z_l = \sum_{j=1}^p w_j \frac{\xi_j^l}{\sqrt{2RT}} \quad (3.169)$$

In this case, the optimal quadrature solution is obtained for  $p = 3$ . The *abscissas* of the quadrature formula are:

$$\xi_1 = -\sqrt{\frac{3}{2}} \frac{1}{\sqrt{2RT}}, \quad \xi_2 = 0, \quad \xi_3 = +\sqrt{\frac{3}{2}} \frac{1}{\sqrt{2RT}} \quad (3.170)$$

and the *weights* are:

$$w_1 = \frac{\sqrt{\pi}}{6}, \quad w_2 = \frac{2\sqrt{\pi}}{3}, \quad w_3 = \frac{\sqrt{\pi}}{6} \quad (3.171)$$

So, introducing Eqs. 3.169, 3.170, 3.171 in Eq. 3.167 we obtain:

$$\int \phi(\boldsymbol{\xi})_{l,m} f^{eq}(\boldsymbol{\xi}) d\boldsymbol{\xi} = \frac{\rho}{\pi} \sum_{l,m=1}^3 w_l w_m \phi(\boldsymbol{\xi})_{l,m} \left[ 1 + \frac{(\boldsymbol{\xi}_{l,m} \cdot \mathbf{v})}{RT} + \frac{(\boldsymbol{\xi}_{l,m} \cdot \mathbf{v})^2}{2R^2T^2} - \frac{(\mathbf{v})^2}{2RT} \right] \quad (3.172)$$

Therefore, the equilibrium distribution functions are given by:

$$f_{l,m}^{eq} = \frac{\rho w_l w_m}{\pi} \left[ 1 + \frac{(\boldsymbol{\xi}_{l,m} \cdot \mathbf{v})}{RT} + \frac{(\boldsymbol{\xi}_{l,m} \cdot \mathbf{v})^2}{2R^2T^2} - \frac{(\mathbf{v})^2}{2RT} \right] \quad (3.173)$$

where  $\boldsymbol{\xi}_{l,m}$  is the discrete set of velocities given by the quadrature formula. Then, considering the gas sound speed given by the low Mach number expansion (Eq. 3.158) and assuming  $\zeta = 1$ , we can write the lattice sound speed as following:

$$c_s = \sqrt{RT} \quad (3.174)$$

and thus rewrite Eq. 3.173 as follows:

$$f_i^{eq} = \omega_i \left[ 1 + \frac{(\mathbf{e}_i \cdot \mathbf{v})}{c_s^2} + \frac{(\mathbf{e}_i \cdot \mathbf{v})^2}{2c_s^4} - \frac{(\mathbf{v})^2}{2c_s^2} \right], \quad \text{with } i = 1, 2, \dots, 9 \quad (3.175)$$

where  $\mathbf{e}_a$  is the common name, used in literature to call the discrete set of velocities given by  $\boldsymbol{\xi}_{l,m}$  with the combination of indexes  $l = 1 : 3$  and  $m = 1 : 3$ ;  $\mathbf{e}_a$  are defined as:

$$\mathbf{e}_i = \begin{cases} e_{1,3} = (\pm 1, 0)c \\ e_{2,4} = (0, \pm 1)c \\ e_{5,6,7,8} = (\pm 1, \pm 1)c \\ e_9 = (0, 0)c \end{cases} \quad (3.176)$$

which correspond to the scheme proposed in Fig. 3.5 (left). The weights, instead, are straightforward defined as:

$$\omega_i = \frac{w_l w_m}{\pi} = \begin{cases} \omega_{1,2,3,4} = 1/9 \\ \omega_{5,6,7,8} = 1/36 \\ \omega_9 = 4/9 \end{cases} \quad (3.177)$$

The variable  $c$  can be viewed as a *speed of light* [He and Luo, 1997b] of the system and it is given by the following relation:

$$c = \sqrt{3}c_s = \sqrt{3RT} \quad (3.178)$$

Moreover, since  $c$  is by fact a scalar velocity, it can be defined as:

$$c = \frac{\delta x}{\delta t} \quad (3.179)$$

where  $\delta x$  is the lattice typical dimension and  $\delta t$  is the minimum time increment for the solution of the LBM. In literature,  $\delta x$  and  $\delta t$  are known as *lattice units*. It is also very common to assume  $\delta x = 1$  and  $\delta t = 1$ . Accordingly,  $c = 1$  and Eq. 3.178 can be rewritten as follows:

$$c_s = \frac{c}{\sqrt{3}} = \frac{1}{\sqrt{3}} \quad (3.180)$$

In consequence, Eq. 3.173 can be rewritten as follows:

$$f_i^{eq} = \omega_i \left[ 1 + \frac{3(\mathbf{e}_i \cdot \mathbf{v})}{c^2} + \frac{9(\mathbf{e}_i \cdot \mathbf{v})^2}{2c^4} - \frac{3(\mathbf{v})^2}{2c^2} \right], \quad \text{with } i = 1, 2, \dots, 9 \quad (3.181)$$

Applying the same space discretization to the Eq. 3.156, we can write the discrete lattice Boltzmann equation:

$$f_i(\mathbf{x} + \mathbf{e}_i \delta t, t + \delta t) = f_i(\mathbf{x}, t) - \frac{1}{\tau} \left[ f_i(\mathbf{x}, t) - f_i^{eq}(\mathbf{x}, t) \right] \quad \text{with } i = 1, \dots, n \quad (3.182)$$

To solve Eq. 3.182, it is usual to split the solution in two steps: the *streaming* step:

$$f_i^s(\mathbf{x} + \mathbf{e}_i \delta t, t + \delta t) = f_i(\mathbf{x}, t) \quad (3.183)$$

and the *collision* step:

$$f_i(\mathbf{x} + \mathbf{e}_i \delta t, t + \delta t) = f_i^s(\mathbf{x} + \mathbf{e}_i \delta t, t + \delta t) - \frac{1}{\tau} \left[ f_i^s(\mathbf{x} + \mathbf{e}_i \delta t, t + \delta t) - f_i^{eq}(\mathbf{x} + \mathbf{e}_i \delta t, t + \delta t) \right] \quad (3.184)$$

where the equilibrium term is given by Eq. 3.181 and the macroscopic equations are given by:

$$\begin{aligned}\rho &= \rho(\mathbf{x}, t) = \sum_{i=1}^n f_i \\ \mathbf{v} &= \mathbf{v}(\mathbf{x}, t) = \frac{1}{\rho} \sum_{i=1}^n \mathbf{e}_i f_i \\ e &= e(\mathbf{x}, t) = \frac{1}{2\rho} \sum_{i=1}^n (\mathbf{e}_i - \mathbf{v})^2 f_i\end{aligned}\tag{3.185}$$

Finally, we underline that, in order to assure the stability of the method, the macroscopic velocity  $\mathbf{v}$  must remain always below the  $c_s$ . This limit, as matter of fact, is given by the low Mach number expansion adopted to evaluate the equilibrium term.

### 3.5 The lattice Boltzmann method and the conservation equations

In the previous sections we have mathematically derived the lattice Boltzmann method from the Boltzmann equation. The natural question is: with the lattice Boltzmann method it is possible to reproduce correctly the macroscopic behavior of a thermo-dynamic fluid? In order to prove that from the lattice Boltzmann method it is possible to recover the we apply the Chapman-Enskog expansion to the discrete Boltzmann equation in order to recover the Navier-Stokes equations and the heat advection diffusion equation.

#### 3.5.1 From lattice Boltzmann equation to Navier-Stokes equations

In this section we introduce some important aspects to better characterize the lattice Boltzmann equation.

In Eq. 3.179 we have introduced the assumption  $c = 1$  which implies that LBM is characterized by a convective scaling, meaning that  $\delta t = \delta x$ . This procedure can be viewed as a kind of normalization and  $\delta t$  is related to the *Knudsen* number ( $Kn$ ). In specific, it possible to demonstrate [Kuzmin, 2010] that  $Kn = \tau$ , meaning that relaxation time is the scale parameter which governs the lattice Boltzmann equation. Accordingly, if we want to recover the conservation equations for a dense fluid, we need to perform the Chapman-Enskog expansion in the limit  $\tau \rightarrow 0$ , to be consistent with the considerations explained in Section 3.3.4.

Eq. 3.182 does not include the forcing term. External forces contribution can be taken into account as follows:

$$f_i(\mathbf{x} + \mathbf{e}_i \delta t, t + \delta t) = f_i(\mathbf{x}, t) - \frac{1}{\tau} \left[ f_i(\mathbf{x}, t) - f_i^{eq}(\mathbf{x}, t) \right] + \delta t F_i, \quad \text{with } i = 1, 2, \dots, 9 \tag{3.186}$$

where  $\delta t F_i$  is an additional term which takes into account the contribution of external forces acting on the computational domain, for example the gravitational field. The contribution of the external forces is taken into account as a external momentum, thus the macroscopic

velocity  $\mathbf{v}$  is calculated as follows:

$$\mathbf{v} = \mathbf{v}(\mathbf{x}, t) = \frac{1}{\rho} \sum_{i=1}^n \mathbf{e}_i f_i + \frac{m \mathbf{F} \delta T}{\rho} \quad (3.187)$$

where  $m$  is a constant to be determined. According to Ladd and Verberg [2001], the forcing term can be expanded in series of power as follows:

$$F_i = \omega_i \left[ A + \frac{3(\mathbf{e}_i \cdot \mathbf{B})}{c^2} + \frac{9(\mathbf{e}_i \cdot \mathbf{C})^2}{2c^4} - \frac{3(\mathbf{C})^2}{2c^2} \right], \quad \text{with } i = 1, 2, \dots, 9 \quad (3.188)$$

where  $A, \mathbf{B}, \mathbf{C}$  are constant coefficients which can be derived imposing that the moments of  $F_i$  satisfy the desired constitutive equations (in our case of study, the hydrodynamic equations). The zero-th, first, and second moments of  $F_i$  are defined as follows:

$$\begin{aligned} \sum_{i=1}^n F_i &= A \\ \sum_{i=1}^n \mathbf{e}_i F_i &= \mathbf{B} \\ \sum_{i=1}^n \mathbf{e}_i \mathbf{e}_i F_i &= \frac{\mathbf{C}^T + \mathbf{C}}{2} + \frac{c^2 \mathbf{A} \mathbf{I}}{3} \end{aligned} \quad (3.189)$$

In conclusion, we can state that in LBM the forcing term is strictly dependent on the constitutive equations we want to satisfy [Guo et al., 2002a].

### The Chapman Enskog expansion

The Chapman-Enskog expansion of the lattice Boltzmann equation (Eq. 3.186) is based on the expansion in series of powers of both the discrete distribution functions  $f_i$  and the time  $t$ :

$$\begin{aligned} f_i &= \sum_{n=1}^{\infty} \varepsilon^n f_i^{(n)} \\ t &= \sum_{n=1}^{\infty} \varepsilon^n t_{(n)} \end{aligned} \quad (3.190)$$

We observe that the series of power is dependent on the coefficient  $\varepsilon = Kn$  which tends to 0 like in the Chapman-Enskog expansion of the Boltzmann equation.

Expanding in Taylor series the right hand side of Eq. 3.186 and applying the expansion procedure to Eq. 3.186, with some mathematical computations we obtain the following

equations [Guo et al., 2002a]:

$$\begin{aligned} f_i^{(0)} &= f_i^{eq} \\ \frac{\partial f_i^{(0)}}{\partial t_{(1)}} + \mathbf{e}_i \frac{\partial f_i^{(0)}}{\partial \mathbf{x}_{(1)}} &= -\frac{1}{\tau \delta t} f_i^{(1)} + \varepsilon F_i \\ \frac{\partial f_i^{(0)}}{\partial t_{(2)}} + \left(1 - \frac{1}{2\tau}\right) \left(\frac{\partial f_i^{(1)}}{\partial t_{(1)}} + \mathbf{e}_i \frac{\partial f_i^{(1)}}{\partial \mathbf{x}_{(1)}}\right) &= -\frac{1}{\tau \delta t} f_i^{(2)} - \frac{\delta t}{2} \left(\frac{\partial \varepsilon F_i}{\partial t_{(1)}} + \mathbf{e}_i \frac{\partial \varepsilon F_i}{\partial \mathbf{x}_{(1)}}\right) \end{aligned} \quad (3.191)$$

with:

$$\frac{\partial}{\partial t} = \varepsilon \frac{\partial}{\partial t_{(1)}} + \varepsilon^2 \frac{\partial}{\partial t_{(2)}}, \quad \frac{\partial}{\partial \mathbf{x}} = \varepsilon \frac{\partial}{\partial \mathbf{x}_{(1)}} + \varepsilon^2 \frac{\partial}{\partial \mathbf{x}_{(2)}} \quad (3.192)$$

Considering the moments of the Eqs. 3.191 on  $t_1 = \varepsilon t$ , inserting Eq. 3.188, and taking into account the definition of the macroscopic quantities (Eq. 3.185), we obtain:

$$\begin{aligned} \frac{\partial \rho}{\partial t_{(1)}} + \nabla_{(1)} \cdot (\rho \mathbf{v}) &= A_{(1)} \\ \frac{\partial \rho \mathbf{v}}{\partial t_{(1)}} + \nabla_{(1)} \cdot \Pi^{(0)} &= \left(n + \frac{m}{\tau}\right) \frac{\mathbf{B}_{(1)}}{n} \end{aligned} \quad (3.193)$$

where  $n$  and  $m$  are constants to be determined given by:

$$\mathbf{A} = \varepsilon \mathbf{A}_{(1)}, \quad \mathbf{B} = \varepsilon \mathbf{B}_{(1)} \quad (3.194)$$

while  $\Pi_{\alpha\beta}^{(0)} = \sum_i \mathbf{e}_{i\alpha} \mathbf{e}_{i\beta} f_i^{(0)}$  is the zero-th order momentum flux tensor. If we assume  $A_{(1)} = 0$  and  $(n + m/\tau) = 1$  we recover the *Euler equations* which describe the dynamics of a inviscid fluid, that in the continuous case correspond to the Eqs. 3.136. This result is in accordance with the one obtained applying the Hilbert expansion to the Boltzmann equation. Moreover, the first order momentum flux can be calculated as follows:

$$\Pi_{\alpha\beta}^{(1)} = -\tau \delta t \left[ (\mathbf{v}_\alpha \mathbf{F}_{(1)\beta} + \mathbf{v}_\beta \mathbf{F}_{(1)\alpha}) + c_s^2 \rho (\nabla_{(1)\alpha} \mathbf{v}_\beta + \nabla_{(1)\beta} \mathbf{v}_\alpha) - \frac{1}{2} (\mathbf{C}_{(1)\alpha\beta} + \mathbf{C}_{(1)\beta\alpha}) \right] \quad (3.195)$$

where:  $\mathbf{F}_{(1)}$  is given by:

$$\mathbf{F} = \varepsilon \mathbf{F}_{(1)} \quad (3.196)$$

Martys et al. [1998] pointed out that if we assume  $\mathbf{C} = 2\mathbf{v}\mathbf{F}_{(1)}$ , with some computations, the momentum flux can be re-conducted to the expression of the stress tensor of the Navier-Stokes equations (Eq. 3.147):

$$\mathbf{p}_{(1)\alpha\beta} = p \delta_{\alpha\beta} - \mu (\nabla_{(1)\alpha} \mathbf{v}_\beta + \nabla_{(1)\beta} \mathbf{v}_\alpha) \quad (3.197)$$

where  $\mu$  is the kinematic viscosity and it is given by:  $\mu = c_s^2 \tau \delta t$ . However, in LBM method, the lattice discretization induces some modifications on viscosity and forcing term, so, in order to avoid instabilities, it is convenient to introduce some corrections on the viscosity definition.



We consider the second order moments of Eqs. 3.191 on  $t_2 = \varepsilon^2 t$  and we obtain:

$$\begin{aligned}\partial\rho\partial t_{(2)} &= \delta t \left( m - \frac{1}{2} \right) \nabla_{(1)} \cdot \mathbf{F}_{(1)} \\ \frac{\partial(\rho\mathbf{v})}{\partial t_{(2)}} &= \delta t \left( m - \frac{1}{2} \right) \frac{\partial\mathbf{F}_{(1)}}{\partial t_{(1)}} + \nabla_{(1)} \cdot \mathbf{p}_{(1)}\end{aligned}\tag{3.198}$$

where the stress tensor is defined as follows:

$$\begin{aligned}\mathbf{p}_{(1)\alpha\beta} &= - \left( \tau - \frac{1}{2} \right) c_s^2 \delta t \rho \left( \nabla_{(1)\alpha} \mathbf{v}_\beta + \nabla_{(1)\beta} \mathbf{v}_\alpha \right) + \\ &\delta t \left[ \left( \tau - \frac{1}{2} \right) (\mathbf{v}_\alpha \mathbf{F}_{(1)\beta} + \mathbf{v}_\beta \mathbf{F}_{(1)\alpha}) - \frac{\tau}{2} (\mathbf{C}_{(1)\alpha\beta} + \mathbf{C}_{(1)\beta\alpha}) \right]\end{aligned}\tag{3.199}$$

Looking to Eq. 3.199, we notice that it contains, basically, the Eq. 3.195 with an additional term. Those additional terms can be condensed, to recover Eq. 3.197, by assuming the following equality:

$$\mu = \left( \tau - \frac{1}{2} \right) c_s^2 \delta t, \quad \mathbf{C} = \left( 1 - \frac{1}{2\tau} \right) 2\mathbf{v}\mathbf{F}\tag{3.200}$$

Moreover, we can appreciate how, in Eqs. 3.198, space and time partial derivatives on the right hand sides cause unexpected second order effects on density and momentum distributions. In order to avoid those effects,  $m$  must be assumed equal to  $1/2$  and, in consequence, the macroscopic velocity (Eq. 3.187) can be calculated as follows:

$$\mathbf{v} = \mathbf{v}(\mathbf{x}, t) = \frac{1}{\rho} \sum_{i=1}^n \mathbf{e}_i f_i + \frac{\mathbf{F} \delta T}{2\rho}\tag{3.201}$$

where  $\mathbf{F}$  is the external forcing term. Finally the external forcing term is given by:

$$F_i = \left( 1 - \frac{1}{2\tau} \right) \omega_i \left[ \frac{3(\mathbf{e}_i - \mathbf{v})}{c^2} + \frac{9(\mathbf{e}_i \cdot \mathbf{v})}{c^4} \mathbf{e}_i \right] \cdot \mathbf{F}\tag{3.202}$$

Finally, inserting Eq. 3.201 and Eq. 3.200 in Eq. 3.193, doing some computations on the stress tensor, we can recover the Navier-Stokes equations, written as follows:

$$\begin{aligned}\frac{\partial\rho}{\partial t} + \nabla \cdot \rho\mathbf{v} &= 0 \\ \frac{\partial\rho\mathbf{v}}{\partial t} + \nabla \cdot (\rho\mathbf{v}\mathbf{v}) &= -\nabla p + \mu \nabla \cdot [\rho(\nabla\mathbf{v} + \nabla^T\mathbf{v})] + \mathbf{F}\end{aligned}\tag{3.203}$$

### 3.5.2 From lattice Boltzmann equation to Energy conservation equation

The above described procedure to derive the Navier-Stokes equations from the lattice Boltzmann equation, deals with the first two moments of the distribution functions  $f_i$ , meaning that the last of the Eqs. 3.185 is not taken into account; in fact, from the macroscopic point

of view, we have not recovered the complete description of a *Navier-Stokes-Fourier* fluid but only mass and momentum conservation equations.

In order to describe the thermal evolution of the fluid, we consider a new distribution function  $g$  defined as follows:

$$g = \frac{(\boldsymbol{\xi} - \mathbf{v})^2}{2} f \quad (3.204)$$

thus that the integral of  $g$  on the velocity space returns exactly the internal energy (Eq. 3.97). Following He et al. [1998], we can introduce Eq. 3.204 in Eq. 3.151, with some computations, we can rewrite the Boltzmann equation as follows:

$$\frac{\partial g}{\partial t} + \boldsymbol{\xi} \cdot \frac{\partial g}{\partial \boldsymbol{\xi}} = \frac{g^{eq}(\mathbf{x}, \boldsymbol{\xi}, t) - g(\mathbf{x}, \boldsymbol{\xi}, t)}{\tau_T} - f q \quad (3.205)$$

where  $f$  is the distribution function usually adopted to describe the fluid-dynamic problem, while  $q$  is defined as follows:

$$q = f(\boldsymbol{\xi} - \mathbf{v}) \cdot \left[ \frac{\partial \mathbf{v}}{\partial t} + \boldsymbol{\xi} \cdot \frac{\partial \mathbf{v}}{\partial \mathbf{x}} \right] \quad (3.206)$$

and the equilibrium distribution function  $g^{eq}(\mathbf{x}, \boldsymbol{\xi}, t)$  is given by:

$$g^{eq}(\boldsymbol{\xi}) = \frac{\rho(\boldsymbol{\xi} - \mathbf{v})}{2\sqrt{(2\pi RT)}^3} \exp \left[ -\frac{(\boldsymbol{\xi} - \mathbf{v})^2}{2RT} \right] \quad (3.207)$$

In conclusion, Eq. 3.151 and Eq. 3.205 with the associated equilibrium distributions, Eq. 3.207 and Eq. 3.82, give rise to a system of equations describing the fluid dynamic evolution of a thermal flow.

Applying to Eq. 3.205 a discretization procedure similar to the one proposed in Section 3.4.2, we can derive the discretized lattice Boltzmann equation describing the thermal evolution:

$$g_i(\mathbf{x} + \mathbf{e}_i \delta t, t + \delta t) = g_i(\mathbf{x}, t) - \frac{\delta t}{\tau_T + 0.5\delta t} \left[ g_i(\mathbf{x}, t) - g_i^{eq}(\mathbf{x}, t) \right] - \frac{\tau_T}{\tau_T + 0.5\delta t} f_i(\mathbf{x}, t) q_i(\mathbf{x}, t) \delta t$$

with  $i = 1, \dots, n$

(3.208)

and the associated discrete equilibrium term can be discretized as follows:

$$\begin{aligned} g_i^{eq} &= \rho e \omega_i \left[ \frac{3}{2} + \frac{3(\mathbf{e}_i \cdot \mathbf{v})}{2c^2} + \frac{9(\mathbf{e}_i \cdot \mathbf{v})^2}{2c^4} - \frac{3(\mathbf{v})^2}{2c^2} \right], & \text{with } i = 1, 2, \dots, 4 \\ g_i^{eq} &= \rho e \omega_i \left[ 3 + \frac{6(\mathbf{e}_i \cdot \mathbf{v})}{c^2} + \frac{9(\mathbf{e}_i \cdot \mathbf{v})^2}{2c^4} - \frac{3(\mathbf{v})^2}{2c^2} \right], & \text{with } i = 5, 6, \dots, 8 \\ g_i^{eq} &= \rho e \omega_i \left[ \frac{3(\mathbf{v})^2}{2c^2} \right], & \text{with } i = 9 \end{aligned} \quad (3.209)$$

Eq. 3.208 and Eq. 3.209 are usually referred as *thermal lattice Boltzmann method* (TLBM). For sake of completeness, we remark that this solution is not unique, in fact it is possible to adopt directly the temperature as macroscopic unknown (instead of the internal energy); furthermore, different solutions have been proposed to evaluate the equilibrium distribution functions.

### The Chapman-Enskog expansion

Like for the fluid dynamic case, also for the thermo-fluid-dynamic problem we have to demonstrate that from the thermal lattice Boltzmann method it is possible to recover the macroscopic description of a thermal fluid, i.e., the heat advection-diffusion equation.

The Chapman-Enskog expansion of the lattice Boltzmann equation (Eq. 3.208 ) is based on the expansion in series of powers of both the discrete distribution functions  $g_i$  and the time  $t$ :

$$\begin{aligned} g_i &= \sum_{n=1}^{\infty} \varepsilon^n g_i^{(n)} \\ t &= \sum_{n=1}^{\infty} \varepsilon^n t_{(n)} \end{aligned} \quad (3.210)$$

We observe that the series of power is dependent on the coefficient  $\varepsilon = Kn$  which tends to 0 like in the Chapman-Enskog expansion of the Boltzmann equation. The first order Chapman-Enskog expansion of Eq. 3.208 is given by:

$$\frac{\partial g_i^{(0)}}{\partial t_{(1)}} + \mathbf{e}_i \frac{\partial g_i^{(0)}}{\partial \mathbf{x}_{(1)}} = -\frac{1}{\tau_T} g_i^{(1)} - f_i^{(0)} q_i \quad (3.211)$$

Then, considering that  $g^{(0)} = g^{eq}$  and taking into account the definition of the distribution function  $g$  (Eq. 3.204), we can rewrite Eq. 3.211 in terms of the macroscopic quantities as follows:

$$\frac{\partial \rho e}{\partial t_{(1)}} + \nabla_{(1)} \cdot (\rho e \mathbf{v}) = -p \nabla_{(1)} \cdot \mathbf{v} \quad (3.212)$$

obtaining the *Euler energy equation* (last of the Eqs. 3.136). The second term of the right hand side of Eq. 3.212 represents the convective term and is dependent on the equilibrium term  $g^{(0)}$  which is related, by definition (Eq. 3.204) to the internal energy. The left hand side of Eq. 3.212 represents the diffusive term and is dependent on the equilibrium term  $f^{(0)}$  which is related to the pressure compression work.

Applying the second order Chapman Enskog expansion, instead, we obtain:

$$\frac{\partial g_i^{(0)}}{\partial t_{(2)}} + \frac{\partial g_i^{(1)}}{\partial t_{(1)}} + \mathbf{e}_i \frac{\partial g_i^{(1)}}{\partial \mathbf{x}_{(1)}} = -\frac{1}{\tau_T} g_i^{(2)} + \tau \left[ \frac{\partial f_i^{(0)}}{\partial t_{(1)}} + \nabla \cdot (\mathbf{e}_i f_i^{(0)}) \right] \quad (3.213)$$

Finally, inserting Eq. 3.211 in Eq. 3.213, and integrating on the velocity space, we obtain:

$$\frac{\partial \rho e}{\partial t_{(2)}} - \nabla_{(1)} \cdot (\rho k \nabla e) = \rho \mu (\nabla_{(1)} \mathbf{v} + \nabla_{(1)}^T \mathbf{v}) : \nabla_{(1)} \mathbf{v} \quad (3.214)$$

where  $k$  is the thermal conductivity. The second term of the left hand side of Eq. 3.214 represents the convective term, describing the heat convection; this term is generated from the second and the third term of the left hand side of Eq. 3.213 and it is dependent on the non equilibrium term  $g^{(1)}$  which is related, by definition (Eq. 3.204) to the internal energy. The right hand side of Eq. 3.214 represents the diffusive term, describing the heat diffusion. This contribution derives from the second term of the right hand side of Eq. 3.213 and depends on the non equilibrium term  $f^{(1)}$  which is related, by definition (Eq. 3.185) to the density.

Then combining Eq. 3.214 with Eq. 3.212, we obtain:

$$\frac{\partial \rho e}{\partial t} + \nabla \cdot (\rho \mathbf{v} e) = \rho \mu (\nabla \mathbf{v} + \nabla^T \mathbf{v}) : \nabla \mathbf{v} - p \nabla \cdot \mathbf{v} \quad (3.215)$$

Eq. 3.215 is the macroscopic energy conservation equation, thus the description of a *Navier-Stokes-Fourier* fluid is complete.

### 3.6 Final considerations about the Boltzmann Equation and the lattice Boltzmann method

In this chapter we have presented the lattice Boltzmann method which is used to solve numerically the Boltzmann equation under certain hypotheses. We have demonstrated that LBM can be analytically derived from the Boltzmann equation. Moreover we have demonstrated that the macroscopic equations governing a thermo-fluid dynamic flow (Navier-Stokes-Fourier equations) can be obtained directly from the Boltzmann equation using the Chapman-Enskog expansion. This expansion procedure has been adopted also to show that the lattice Boltzmann equation is consistent with the discrete formulation of the macroscopic description of a Navier-Stokes-Fourier fluid.

In previous sections it merged that the lattice Boltzmann method is, by fact a kinetic particle-based approach which conserves the essential information of particle dynamics, necessary to recover the conservation equations at the macroscale; in this respect, the lattice Boltzmann method, as well as the Boltzmann equation itself, represents a bridge between the micro- and the macroscopic world and therefore is usually referred as *mesoscopic*.

In Figure 3.6 we have resumed the principal results obtained in this chapter, underling the principal steps to obtain the lattice Boltzmann method. In particular we observe that, even if the first lattice Boltzmann scheme was introduced in 1988 [McNamara and Zanetti, 1988], it was mathematically demonstrated only in 1997 [He and Luo, 1997a].

## FROM BOLTZMANN EQUATION TO LATTICE BOLTZMANN METHOD

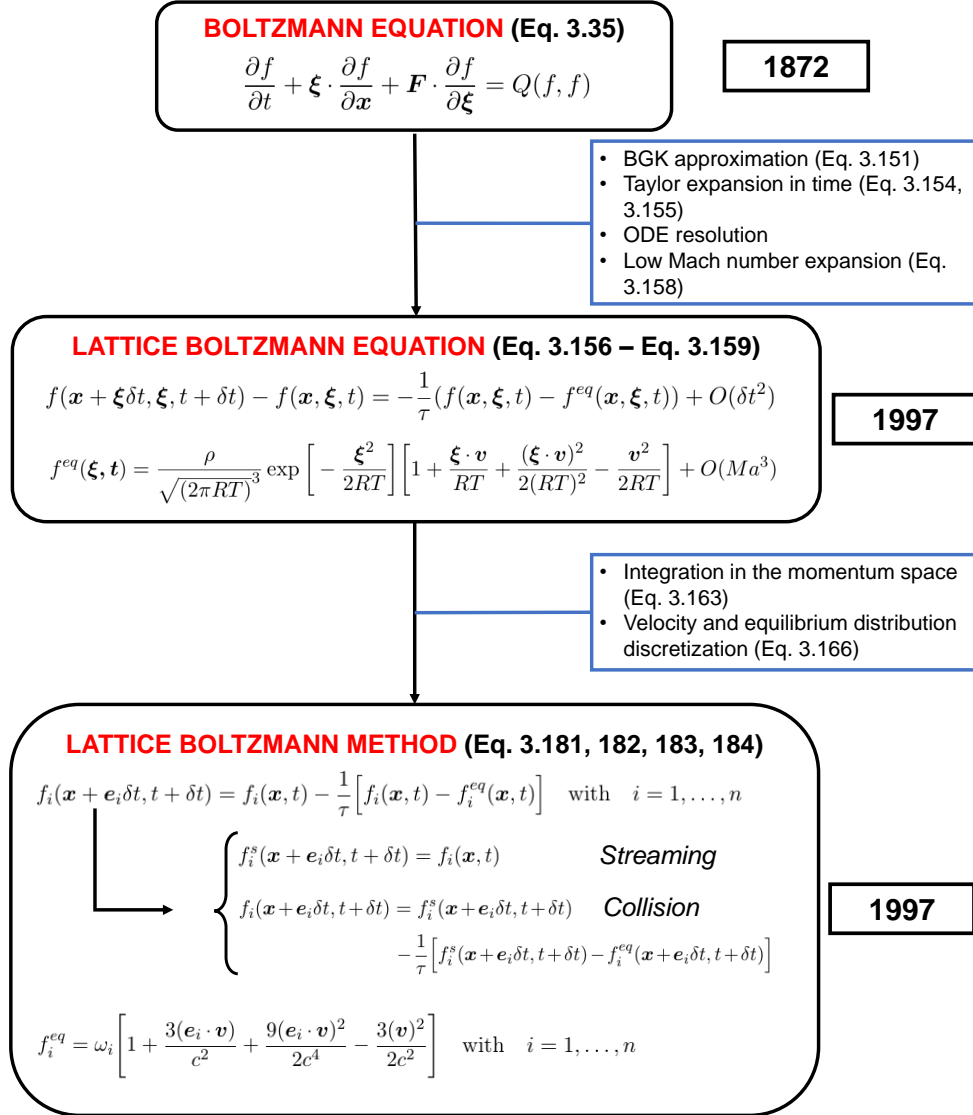


Figure 3.6: From the Boltzmann equation to the lattice Boltzmann method: basic steps.

### 3.6.1 Why use the lattice Boltzmann method for Powder Bed Fusion simulation

As discussed in Chapter 2, powder bed fusion process can be viewed as a thermo-fluid-dynamic problem. In literature, during the years several approaches have been proposed to face thermo-fluid dynamic problems.

In computational fluid dynamics (CFD) the classical methods to solve a fluid dynamic

problem can be divided according to (i) the type of grid, (ii) how the domain is discretized, (iii) how the Navier-Stokes equations are treated to face the turbulence simulation:

- Type of grid:
  - Structured grid;
  - Unstructured grid;
- Domain discretization techniques:
  - Finite volume method (FV);
  - Finite element method (FEM);
  - Finite difference method (FD);
- Turbulence resolution:
  - Direct Numerical Simulation (DNS);
  - Reynolds-averaged Navier–Stokes (RANS);
  - Large eddy simulation (LES);

This classical resolution techniques require an integration on a discrete space and in general are very expensive in terms of computational times. The lattice Boltzmann method is a full explicit method that is solved on a structured grid without needing of integration operations. Those characteristics make the lattice Boltzmann method suitable to be run on massively parallel architectures, thus it is particularly suitable for problems which require a large amount of memory, for example the simulation of powder melting in PBF. The lattice Boltzmann method has been successfully used to simulate multiphase, multicomponent and free surface flows with complex geometries thanks to the ease imposition of the boundary conditions. Those characteristics make the LBM indicated to simulated flows through porous media. This occurrence is typical of the powder bed fusion in which the melted particles move among the solid particles. Moreover, with the lattice Boltzmann method it is almost easy to incorporate the thermal treatment in the fluid description, so it is possible to manage with problems in which the fluid motion is accompanied with the heat exchange among the fluid and with the boundaries. Finally, LBM has been successfully used also to simulate phase change problems. The liquid-gas transition has been faced in many works, while, at the state of the art, only few models dealing with the solid liquid phase change are available.

### 3.6.2 Conclusions

In this chapter we have studied in detail the Lattice Boltzmann method which takes origins from the Boltzmann equation.

In the first part of the chapter, starting from the kinetic theory of gases we have derived the Boltzmann equation; then we have discussed the mathematical peculiarities of this equation, focusing on the difficult treatment of the collision term. Secondly, we have demonstrated that, applying the perturbation method, it is possible to derive, from the Boltzmann equation, the Navier-Stokes-Fourier equations.

In the second part of this chapter we have introduced the Lattice Boltzmann method, an explicit computational scheme which can be used to solve the Boltzmann equation and we have demonstrated that this approach can be used to solve the both the Navier-Stokes and the advection-diffusion equation.

In the next chapter we will use the lattice Boltzmann method to solve some simple thermo-fluid dynamic problems.

## Chapter 4

# Applications of the Lattice Boltzmann method

In this chapter we propose some examples of application of the lattice Boltzmann method. In particular we start with simple fluid and thermo dynamic problems, then we move to more complicate multiphase and free surface problems. Finally we propose an example of solid liquid phase change transition.

### 4.1 Single phase flows

In this section we focus on the LBGK method to solve single-phase flows at low  $Re$  numbers and on the corresponding algorithm, reported in Figure 4.1. In particular, we test the proposed algorithm on a reference benchmark CDF solution, i.e. the Lid-Driven-Cavity (LDC) problem, Burggraf [1966]; in this problem a square cavity is filled with fluid and a constant horizontal velocity is imposed on the upper side of the domain.

The first step of our algorithm consists in converting the dimensional quantities into lattice units. As discussed in previous chapter, the LB method relies on a discrete domain called *lattice*. Each lattice scheme is defined by a time resolution  $\Delta t$  and a space resolution  $\Delta x$  which can be defined in any set of units (e.g. SI), although in literature almost all the works are realized in *lattice units* which are a fictitious unit system scaled such that  $\Delta t = 1$  and  $\Delta x = 1$ . The conversion procedure is not unique. In this work we adopt the scheme proposed by Krüger et al. [2017] based on the *Law of Similarity* which states that two incompressible flow systems are fluid-dynamically similar if they have the same  $Re$  number and the same geometry. In single phase flow problems  $Re$  number can be expressed as follows:

$$Re = \frac{L'V'}{\nu'} = \frac{LV}{\nu} \quad (4.1)$$

where  $L'$  is the typical scale of the physical problem,  $V'$  is the typical velocity of the physical problem and  $\nu'$  is the physical viscosity. In LDC the scale of the problem is given by the cavity dimension, while  $\nu'$  is depending on the chosen fluid; furthermore from  $L'$  and  $V'$  we can easily define the typical time scale  $T' = L'/V'$ . Once defined the grid resolution  $N_x \times N_x$



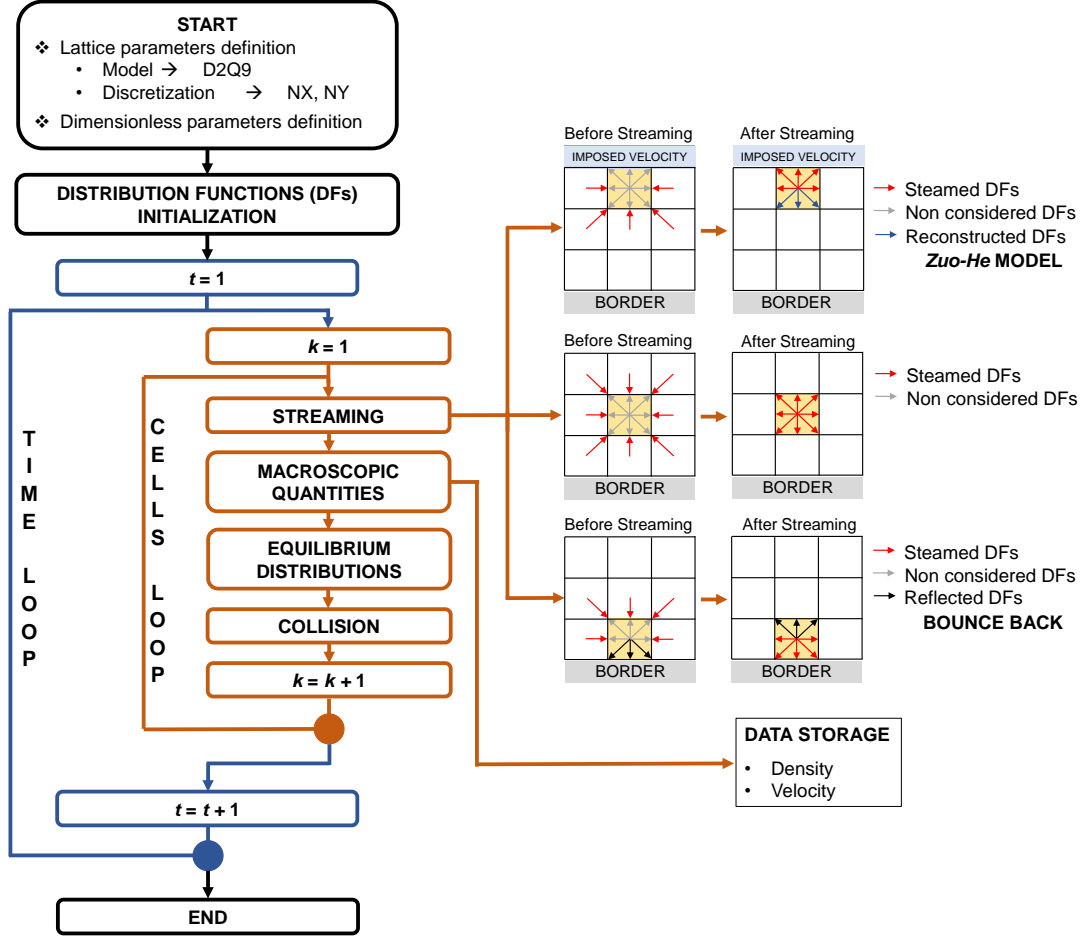


Figure 4.1: LBGK algorithm. The scheme consist of two loops. A main loop over time and a secondary loop over lattice cells. The bounce back rule is adopted for no-slip boundaries and the *Zou-He* model [Zou and He, 1997] is used to impose constant velocity on the top boundary.

we can evaluate the physical grid spacing as:

$$\Delta'_x = \frac{L'}{N_x} \quad (4.2)$$

and we can define a *conversion factor* for length as follows:

$$C_x = \frac{\Delta x'}{\Delta_x} = \frac{L'}{L} \quad (4.3)$$

from which it is simple to derive that :  $L = N_x$ . The definition of  $V$  and  $\nu$  is not straightforward because, in LB method, to avoid instability problems we must ensure that  $V < c_s$  and the relaxation time  $\tau$  is not too close to 0.5 [Krüger et al., 2017]. Once defined a proper value for

$\tau$  we can derive the kinematic lattice viscosity as follows [Frisch et al., 1986]:

$$\nu = c_s^2 \left( \tau - \frac{1}{2} \right) \quad (4.4)$$

Now, considering the physical dimensions of the viscosity we can write the following relation:

$$\frac{\nu'}{\nu} = C_\nu = \frac{C_x^2}{C_t}, \quad \rightarrow \quad C_t = \frac{C_x^2}{C_\nu} \quad (4.5)$$

where  $C_\nu$  is the viscosity conversion factor and  $C_t$  is the time conversion factor. Finally we can derive the lattice velocity  $V$  as follows:

$$V = \frac{V'}{C_V}, \quad \rightarrow \quad V = V' \frac{C_t}{C_x} \quad (4.6)$$

where  $C_V$  is the conversion factor for the velocity. Moreover, knowing  $C_t$  we can derive the physical time step as  $\Delta'_t = C_t \Delta_t$  and calculate the number of iterations needed to cover the desired time interval. If the resulting lattice velocity  $V$  is not consistent with the method constraints, as first step we try to change the relaxation time  $\tau$ , alternatively, we can change the lattice grid resolution  $N_x$ .

We notice also that the density in LB method is a pure scaling parameter, that does not affect the stability of the method, so it is possible to adopt the any desired value of  $\rho$ ; although, to be consistent with the previously assumptions, it is common to assume  $\rho = 1$ , and to define a conversion factor as follows:

$$C_\rho = \frac{\rho'}{\rho} \quad (4.7)$$

where  $\rho'$  is the physical density.

Once performed the parameters conversion, the distribution functions  $f_i$  are initialized, at the equilibrium state through Eq. 3.175 and the iterative process starts. The algorithm consists of two loops: a main loop over the time and a loop over the cells.

During the streaming step we impose the boundary conditions; in particular we implement the Dirichlet boundary conditions proposed by Zou and He [1997] to impose the fixed velocity on the upper side of the domain, while we apply the simple bounce-back scheme to perform no-slip boundaries on the other sides:

$$f_{i_r}^s(\mathbf{x} + \mathbf{e}_i \Delta t, t + \Delta t) = f_i(\mathbf{x}, t) \quad (4.8)$$

where subscript index  $i_r$  denotes the opposite direction to the considered velocity  $\mathbf{e}_i$ , such that:  $\mathbf{e}_{i_r} = -\mathbf{e}_i$ .

After the streaming step we evaluate the density  $\rho$  and the velocity  $\mathbf{v}$  through Eq.3.185, then the equilibrium distributions can be computed and finally the collision among particle distributions takes place (Eq. 3.184).

Figure 4.2 shows the simulation results of the LDC problem. We have solved the Lid Driven Cavity problem for three  $Re$  numbers:  $Re = 100$ ,  $Re = 400$  and  $Re = 1000$ . The cavity of length  $L = 1$  m is filled with water with kinematic viscosity  $\nu = 10^{-6}$  m<sup>2</sup>/s and the lattice grid dimensions are: 300 x 300.

The first three plots represent the velocity distribution ( $L^2$  norm) of the steady state solution for various  $Re$  numbers. The results have been validated through a comparison with the solution proposed by Ghia et al. [1982] which is commonly considered a reference solution for this kind of problem. The normalized horizontal and vertical velocity components ( $u$  and  $v$ -velocity) along the line of vertical and horizontal symmetry have been compared with the reference solution. We observe a good agreement between the solution obtained with the LBGK simulation and the one proposed by Ghia et al. [1982].

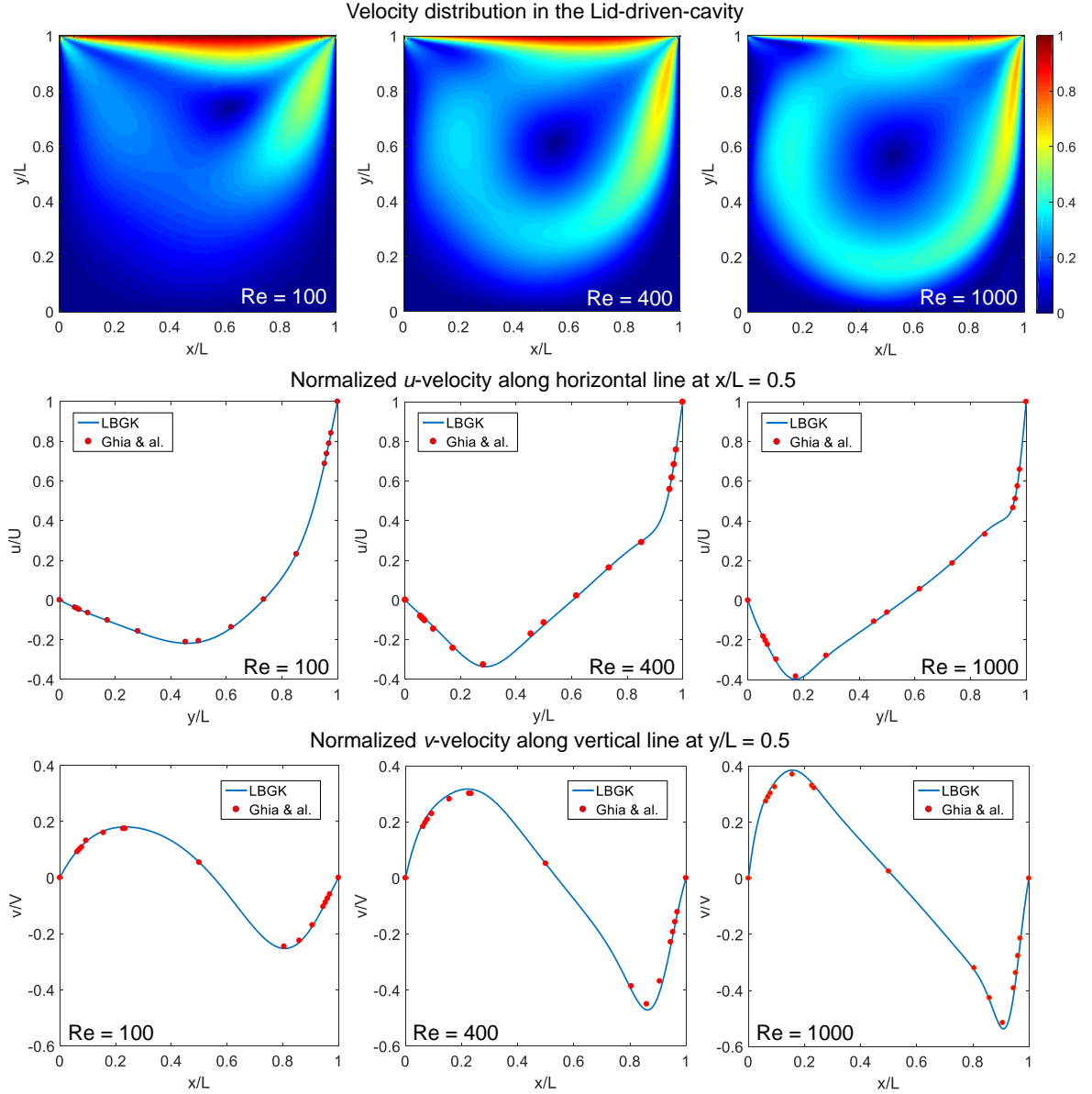


Figure 4.2: LDC problem performed with different  $Re$  numbers. The normalized horizontal and vertical velocity components in the middle of the domain are compared with the solution proposed by Ghia et al. [1982], showing a good agreement for the considered Reynolds number.

## 4.2 Thermal Lattice Boltzmann method

As above mentioned, the LB method is well suited also to describe the thermal flows. In literature, the main thermal Lattice Boltzmann (TLB) methods are the multi-distribution method [Palmer and Rector, 2000] and the multi-speed method [Teixeira et al., 2000], but the latter method was proved by McNamara et al. [1995] to suffer of instability problems.

In the following, we adopt the multi-distribution approach proposed by Guo et al. [2002b] to set up a TLB method for incompressible fluids and we test it on a conventional benchmark i.e., the Rayleigh-Benard convection. In this problem a rectangular cavity is filled with fluid and a temperature difference is applied between upper and bottom boundaries to give rise to a convective flow.

In multi-distribution approach two sets of distribution functions, namely  $f$  and  $g$ , are taken into account:  $f$  is the distribution used to study the fluid-dynamic problem, while  $g$  is adopted to study the thermo-dynamic problem. The discrete evolution equations governing a thermo-fluid dynamic problem are:

$$\begin{aligned} f_i(\mathbf{x} + \mathbf{e}_i \Delta t, t + \Delta t) &= f_i(\mathbf{x}, t) - \frac{1}{\tau} \left[ f_i(\mathbf{x}, t) - f_i^{eq}(\mathbf{x}, t) \right] \quad \text{with } i = 1, \dots, n \\ g_i(\mathbf{x} + \mathbf{e}_i \Delta t, t + \Delta t) &= g_i(\mathbf{x}, t) - \frac{1}{\tau_F} \left[ g_i(\mathbf{x}, t) - g_i^{eq}(\mathbf{x}, t) \right] \quad \text{with } i = 1, \dots, n \end{aligned} \quad (4.9)$$

where  $\tau$  and  $\tau_F$  are the relaxation times for the fluid and the thermal problem respectively. An effective numerical solution of Eq. 4.9 can be provided splitting the solution process into a *streaming* and a *collision* step.

The *streaming* step is defined as follows:

$$\begin{aligned} g_i^s(\mathbf{x} + \mathbf{e}_i \Delta t, t + \Delta t) &= g_i(\mathbf{x}, t) \\ f_i^s(\mathbf{x} + \mathbf{e}_i \Delta t, t + \Delta t) &= f_i(\mathbf{x}, t) \end{aligned} \quad (4.10)$$

where the particle distributions in position  $\mathbf{x}$  at time  $t$  are *streamed* to position  $(\mathbf{x} + \mathbf{e}_i \Delta t)$  after a time step  $\Delta t$ . At the end of the streaming, the macroscopic quantities are obtained as follows:

$$\rho = \rho(\mathbf{x}, t) = \sum_{i=1}^n f_i^s, \quad \mathbf{v} = \mathbf{v}(\mathbf{x}, t) = \frac{1}{\rho} \sum_{i=1}^n \mathbf{e}_i f_i^s, \quad T = T(\mathbf{x}, t) = \sum_{i=1}^n g_i^s(\mathbf{x}, t) \quad (4.11)$$

Henceforth the equilibrium distributions are evaluated as follows [Guo et al., 2002b]:

$$\begin{aligned} f_i^{eq} &= w_i \rho \left[ 1 + \frac{\mathbf{e}_i \cdot \mathbf{v}}{c_s^2} - \frac{\mathbf{v}^2}{2c_s^2} + \frac{(\mathbf{e}_i \cdot \mathbf{v})^2}{2c_s^4} \right] \\ g_i^{eq} &= w_i T \left[ 1 + \frac{\mathbf{e}_i \cdot \mathbf{v}}{c_s^2} \right] \end{aligned} \quad (4.12)$$

Finally, the post *collision* distribution functions are given by:

$$\begin{aligned} f_i(\mathbf{x} + \mathbf{e}_i \Delta t, t + \Delta t) &= f_i^s(\mathbf{x} + \mathbf{e}_i \Delta t, t + \Delta t) - \frac{1}{\tau} \left[ f_i^s(\mathbf{x} + \mathbf{e}_i \Delta t, t + \Delta t) - f_i^{eq}(\mathbf{x} + \mathbf{e}_i \Delta t, t + \Delta t) \right] \\ g_i(\mathbf{x} + \mathbf{e}_i \Delta t, t + \Delta t) &= g_i^s(\mathbf{x} + \mathbf{e}_i \Delta t, t + \Delta t) - \frac{1}{\tau_F} \left[ g_i^s(\mathbf{x} + \mathbf{e}_i \Delta t, t + \Delta t) - g_i^{eq}(\mathbf{x} + \mathbf{e}_i \Delta t, t + \Delta t) \right] \end{aligned} \quad (4.13)$$

The coupling between mass-momentum conservation and advection-diffusion, when considering buoyancy driven flows, can be performed by introducing the so-called *Boussinesq* approximation [Boussinesq, 1903]. This approximation states that density variations, caused by temperature gradients, are taken into account only when they are multiplied by the gravity. Considering Eq. 3.103, we can expand the body force term  $\mathbf{F}$  as:

$$\mathbf{F} = \rho \mathbf{g} \quad (4.14)$$

where  $\mathbf{g}$  denotes the gravity acceleration. Applying the *Boussinesq* approximation, we can rewrite Eq. 4.14 as follows:

$$\mathbf{F} = \rho \mathbf{g} - \rho \alpha \mathbf{g} (T - T_0) \quad (4.15)$$

where  $\alpha$  is the coefficient of thermal expansion and  $T_0$  is the average fluid temperature. The first constant term of Eq. 4.15 can be condensed into the pressure term of Eq. 3.103, so we can rewrite the NS equations as follows:

$$\begin{aligned} \nabla \cdot \mathbf{v} &= 0 \\ \frac{\partial \mathbf{v}}{\partial t} + (\mathbf{v} \cdot \nabla) \mathbf{v} - \nu \nabla^2 \mathbf{v} &= -\frac{1}{\rho} \nabla p - \alpha \mathbf{g} (T - T_0) \end{aligned} \quad (4.16)$$

The buoyancy force (Eq. 4.15) can be included in the TLB method by adding a forcing term  $F$  to Eq. 3.156:

$$f(\mathbf{x} + \boldsymbol{\xi} \Delta t, \boldsymbol{\xi}, t + \Delta t) = f(\mathbf{x}, \boldsymbol{\xi}, t) - \frac{1}{\tau} \left[ f(\mathbf{x}, \boldsymbol{\xi}, t) - f^{eq}(\mathbf{x}, \boldsymbol{\xi}, t) \right] + F \quad (4.17)$$

Henceforth, following an analogue procedure to the one proposed by He et al. [1998], we can write the discrete forcing term as follows:

$$F_i = \rho \alpha \omega_i \left[ \frac{\mathbf{e}_i \mathbf{g}}{c_s^2} \right] (T - T_0) \quad (4.18)$$

which is included in the algorithm as an addend of the right hand side of the collision process among  $f_i$  particle distributions:

$$\begin{aligned} f_i(\mathbf{x} + \mathbf{e}_i \Delta t, t + \Delta t) &= f_i^s(\mathbf{x} + \mathbf{e}_i \Delta t, t + \Delta t) - \frac{1}{\tau} \left[ f_i^s(\mathbf{x} + \mathbf{e}_i \Delta t, t + \Delta t) - f_i^{eq}(\mathbf{x} + \mathbf{e}_i \Delta t, t + \Delta t) \right] + F_i \\ g_i(\mathbf{x} + \mathbf{e}_i \Delta t, t + \Delta t) &= g_i^s(\mathbf{x} + \mathbf{e}_i \Delta t, t + \Delta t) - \frac{1}{\tau_F} \left[ g_i^s(\mathbf{x} + \mathbf{e}_i \Delta t, t + \Delta t) - g_i^{eq}(\mathbf{x} + \mathbf{e}_i \Delta t, t + \Delta t) \right] \end{aligned} \quad (4.19)$$

The adopted TLB algorithm is proposed in Figure 4.3. The conversion procedure between

real quantities and lattice quantities is similar to the one presented in Section 4.1 and it is based on two non dimensional numbers describing a convective flow: the *Prandtl* ( $Pr$ ) number and the *Rayleigh* ( $Ra$ ) number.  $Pr$  number describes the ratio between kinematic viscosity and thermal diffusivity:

$$Pr = \frac{\nu'}{k'} \quad (4.20)$$

while  $Ra$  number states if the heat is primarily transferred by conduction or convection:

$$Ra = \frac{\mathbf{g}' \alpha \Delta T' L'^3}{\nu' k'} \quad (4.21)$$

where apex  $'$  indicates the physical quantities. Combining in different manners Eq. 4.20 with Eq. 4.21 we obtain:

$$PrRa = \frac{\alpha' \Delta T' \mathbf{g}' L'^3}{k'^2} \quad \text{and} \quad \frac{Ra}{Pr} = \frac{\alpha' \Delta T' \mathbf{g}' L'^3}{\nu'^2} \quad (4.22)$$

Considering that the non dimensional groups  $PrRa$  and  $Ra/Pr$  have to remain unchanged during the conversion between physical and lattice quantities, we can write the following relations:

$$\begin{aligned} PrRa &= \frac{\alpha' \Delta T' \mathbf{g}' L'^3}{k'^2} = \frac{\alpha \Delta T \mathbf{g} L^3}{k^2} \\ \frac{Ra}{Pr} &= \frac{\alpha' \Delta T' \mathbf{g}' L'^3}{\nu'^2} = \frac{\alpha \Delta T \mathbf{g} L^3}{\nu^2} \end{aligned} \quad (4.23)$$

The conversion factor for length is defined as proposed in Section. 4.1, then following the procedure proposed by Latt [2008] we can evaluate  $\nu$  and  $k$  as follows:

$$\nu = \sqrt{\frac{Pr}{Ra}} \frac{C_t}{C_x^2} \quad \text{and} \quad \nu = \sqrt{\frac{1}{PrRa}} \frac{C_t}{C_x^2} \quad (4.24)$$

we notice that the conversion factor for temperature does not appear in Eq. 4.24, this is justified by the adimensional nature of the coefficient  $\alpha \Delta T$ . In general the choice of conversion factor for the temperature does not affect the solution since the advection-diffusion equation is linearly dependent from the temperature [Latt, 2008].

Finally, the relaxation times can be derived as follows:

$$\begin{aligned} \tau &= \frac{\nu}{c_s^2} + \frac{1}{2} \\ \tau_F &= \frac{k}{c_s^2} + \frac{1}{2} \end{aligned} \quad (4.25)$$

If the relaxation times are close to 0.5, as stressed in Section 4.1, the algorithm becomes unstable; in this case we need to modify  $C_t$ , changing the physical time step, or in second choice we can change the lattice scheme resolution.

The core of the algorithm is basically the LBGK method which is performed on  $f_i$  and  $g_i$  distributions. At the beginning of the simulation  $f_i$  and  $g_i$  distributions are initialized at the equilibrium state trough (Eq. 4.12), then at each time step a loop over all the cells is

performed.

During the streaming step we impose the boundary conditions. For the fluid-dynamic problem we adopt no-slip boundaries on the upper and the bottom sides, while periodic boundaries are adopted for left and right sides:

$$f_i^s(\mathbf{x} + S, t + \Delta t) = f_i(\mathbf{x}, t) \quad (4.26)$$

where  $S$  is the distance between the periodic boundaries of the domain. For the thermodynamic problem, we adopt periodic boundaries for left and right sides, while a fixed temperature is imposed on upper and bottom sides of the domain. The fixed temperature can be easily imposed with Dirichlet boundaries as shown in [Liu et al., 2010].

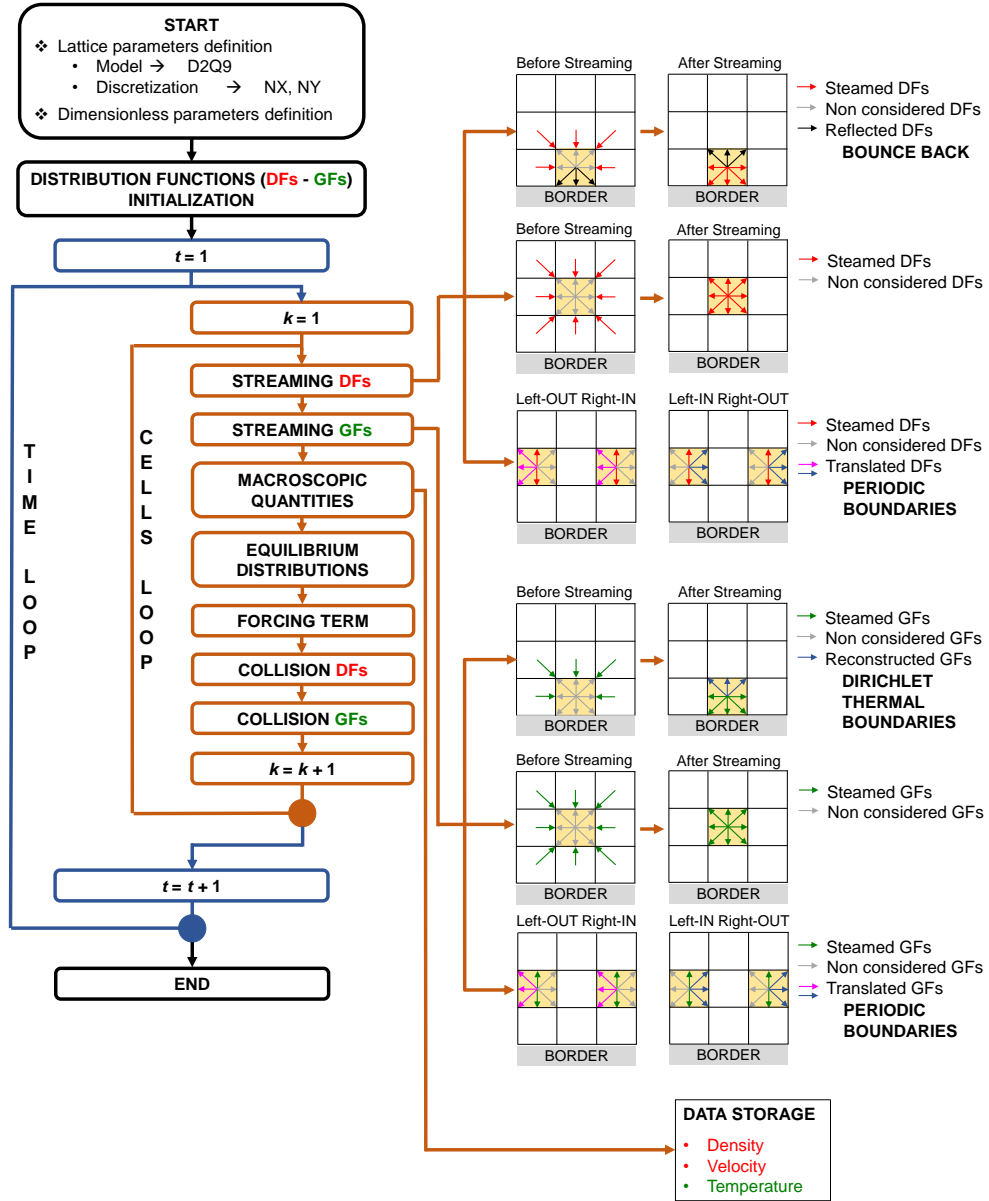


Figure 4.3: TLB algorithm, based on the multi-distribution approach. DFs represents the distributions of the fluid-dynamic problem; GFs represents the distributions for the thermo-dynamic problem. The bounce back rule is adopted to impose no-slip boundary conditions. Dirichlet boundary [Liu et al., 2010] conditions have been implemented to impose fixed temperature on the upper and the bottom sides of the domain.

Figure 4.4 shows the steady state solution of the Rayleigh-Benard convection in a 2:1 rectangular cavity. We adopt  $Pr = 1$ , which is a typical value for air or gases in general, and we study the effects of  $Ra$  numbers variation on simulation results. We consider three  $Ra$  numbers:  $Ra = 10^4$ ,  $Ra = 5 \cdot 10^4$  and  $Ra = 10^5$ . The temperature results are normalized with the formula  $(T - T_l)/\Delta T$  proposed by He et al. [1998]; the velocity results are normalized on the maximum velocity.

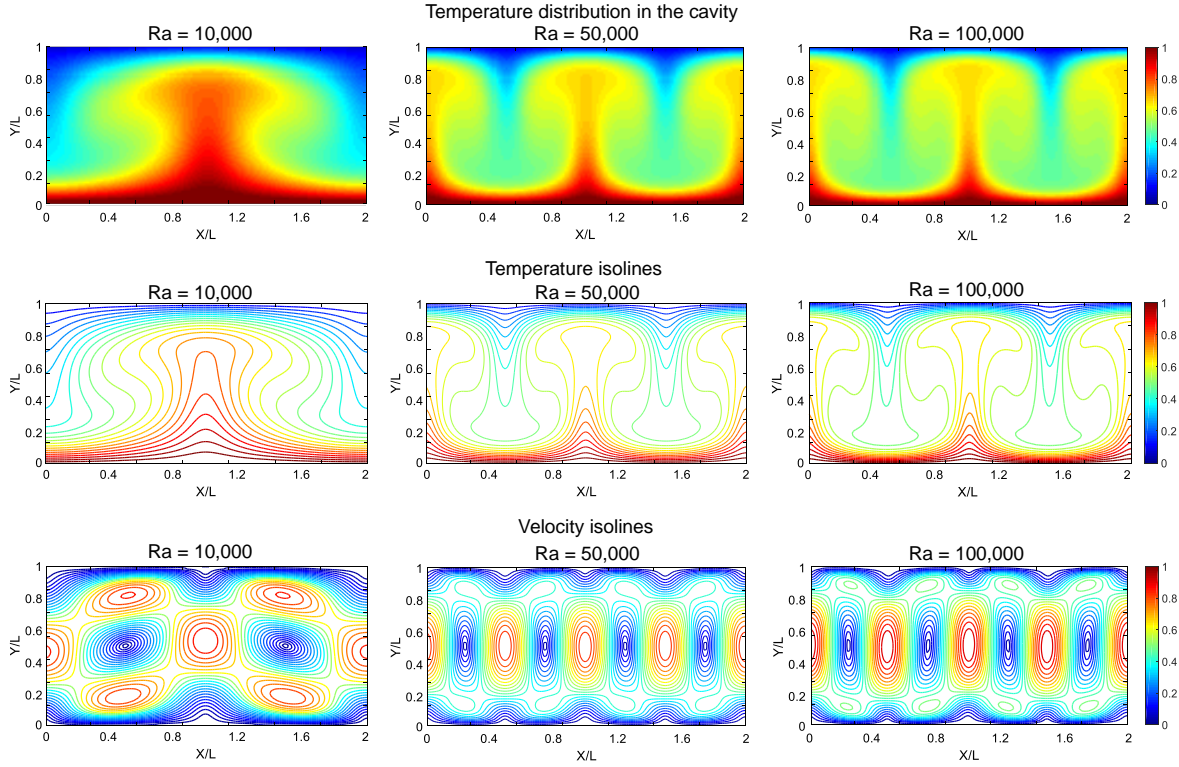


Figure 4.4: Steady state solution of the Rayleigh-Benard convection obtained with  $Pr = 1$  and varying  $Ra$  numbers.



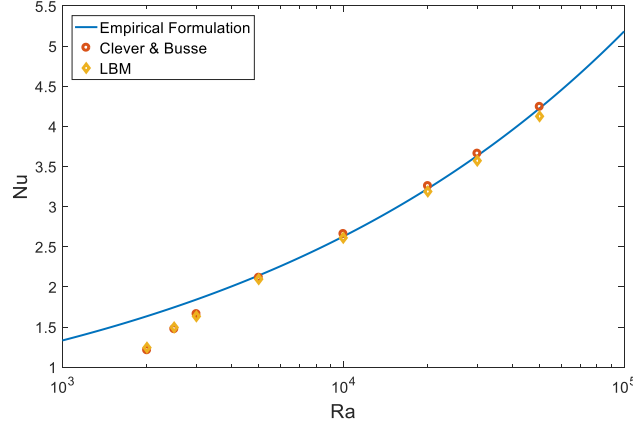


Figure 4.5: Variation of the  $Nu$  number in function of the  $Ra$  number. The results are compared with the solution proposed by Clever and Busse [1974].

We validate the results of the Rayleigh-Benard convection through a comparison with the solution proposed by Clever and Busse [1974] which is considered a reference solution for this problem. The results are expressed in terms of the Nusselt  $Nu$  number, which describes the ratio between the convective heat transfer and the conductive heat transfer. In lattice quantities  $Nu$  can be expressed as follows [Kao and Yang, 2007]:

$$Nu = 1 + \frac{\langle \mathbf{v}_y \cdot T \rangle H}{k \cdot \Delta T} \quad (4.27)$$

where  $\langle \rangle$  are the Macaulay brackets and  $H$  is the height of cavity.

### 4.3 Multiphase flows

Multiphase fluids or mixture of immiscible fluids are very interesting problems for mechanical applications, including the PBF process. In this section we present the Shan and Chen [1993] method for single component multi-phase flows. In this method a so called *pseudopotential* function  $\psi(\mathbf{x}, t)$  is introduced to simulate the interaction among neighboring particle distributions. The great innovation of Shan and Chen [1994] method consists in the possibility to simulate phase segregation without the necessity of any method to track the surface between different phases [Fyta et al., 2006].

Shan and Chen [1993] method is used to face the classical problem of a droplet wetting on a smooth surface: this problem is very interesting for several applications and it has been successfully studied by many authors; for example [Raiskinmäki et al., 2000] adopted the Shan and Chen [1993] method to simulate droplets spreading on smooth and rough surfaces.

The original Shan and Chen [1993] method is based on the LBGK method presented, except for the definition of the macroscopic velocity which is given by:

$$\mathbf{v}^{sh} = \mathbf{v} + \frac{\mathbf{F}}{2\rho} \quad (4.28)$$

where the velocity  $\mathbf{v}$  is obtained with Eq. 3.185 and  $\mathbf{F} = \mathbf{F}(\mathbf{x}, t)$  is a force acting on the fluid

which is obtained from the contribution of three type of forces [Huang et al., 2009]:

$$\mathbf{F}(\mathbf{x}, t) = \mathbf{F}_{int}(\mathbf{x}, t) + \mathbf{F}_{ads}(\mathbf{x}, t) + \mathbf{F}_{est}(\mathbf{x}, t) \quad (4.29)$$

where  $\mathbf{F}_{int}(\mathbf{x}, t)$  is the particle to particle interaction force defined as [Shan and Chen, 1994]:

$$\mathbf{F}_{int}(\mathbf{x}, t) = -G\psi(\mathbf{x}) \sum_i w_i \psi(\mathbf{x} + \mathbf{e}_i \Delta t, t) \mathbf{e}_i \quad (4.30)$$

$\mathbf{F}_{ads}(\mathbf{x}, t)$  is the adhesion force between gas or liquid phase and the solid walls, defined as follows [Benzi et al., 2006]:

$$\mathbf{F}_{ads}(\mathbf{x}, t) = -G\psi(\mathbf{x}) \sum_i w_i \psi(\rho_w) s(\mathbf{x} + \mathbf{e}_i \Delta t, t) \mathbf{e}_i \quad (4.31)$$

and  $\mathbf{F}_{est}(\mathbf{x}, t)$  is a generic forcing term. In Eqs. 4.30 and 4.31,  $G$  is a parameter that controls the strength of interaction and adhesion force,  $\psi$  is the *pseudopotential* function and  $\rho_w$  is a fictitious density assigned to the solid interfaces [Benzi et al., 2006]; finally,  $s$  is a boolean function which is equal to one if the position  $\mathbf{x} + \mathbf{e}_i \Delta t$  is employed by a solid particle, while it is equal to zero if it is employed by a fluid particle.

The definition of the *pseudopotential* function is a crucial point in the method setup; in this work we adopt the following formulation [He and Doolen, 2002]:

$$\psi(\mathbf{x}, t) = \sqrt{\frac{2(p - \rho c_s^2)}{G c_s^2}} \quad (4.32)$$

where  $p$  is the pressure evaluated with the introduction of an Equation of State (EOS). The most common EOS are [Yuan and Schaefer, 2006]:

- the Van der Waals (VdW) [der Waals, 1873] EOS, defined as follows:

$$p = \frac{\rho RT}{1 - b\rho} - a\rho^2 \quad (4.33)$$

- the Redlich-Kwong (R-K) [Redlich and Kwong, 1949] EOS, defined as follows

$$p = \frac{\rho RT}{1 - b\rho} - \frac{a\rho^2}{\sqrt{T}(1 + b\rho)} \quad (4.34)$$

- the Carnahan-Starling (C-S) [Carnahan and Starling, 1969] EOS, defined as follows:

$$p = \rho RT \frac{1 + c + c^2 - c^3}{(1 - c)^3} - a\rho^2 \quad \text{with} \quad c = \frac{b\rho}{4} \quad (4.35)$$

where  $a$  and  $b$  are the constants of the model. In Eqs. 4.33, 4.34, 4.35 the first addend of the right hand side represents the repulsive term between phases, while the second addend is the attractive term.

The algorithm adopted to face the droplet wetting problem is presented in Fig. 4.6. The

first step of our algorithm consists in the initialization of the density distribution in the domain. During the streaming step, as usual, we impose the boundary conditions. The bounce back rule is adopted to simulate non-slip boundaries on top and bottom sides of the domain, while periodic boundaries are imposed on the vertical walls.

The proposed algorithm is used to study the wetting of droplets on a smooth surface. When fluid and vapor phases come in contact with a solid wall the capillary forces leads to the thermo-dynamic equilibrium between phases. At the state of the equilibrium a typical angle between fluid phases and the solid wall is observed. This angle is usually known as contact angle and it is described by the *Young's equation*:

$$\cos(\theta^{eq}) = \frac{\sigma_{SG} - \sigma_{SL}}{\sigma_{LG}} \quad (4.36)$$

where  $\sigma$  is the surface tension between solid (S), liquid (L) and gas (G) phase. Benzi et al. [2006] showed that in Shan and Chen [1993] method the contact angle can be adjusted by changing the density of the solid wall  $\rho_w$  in Eq. 4.31.

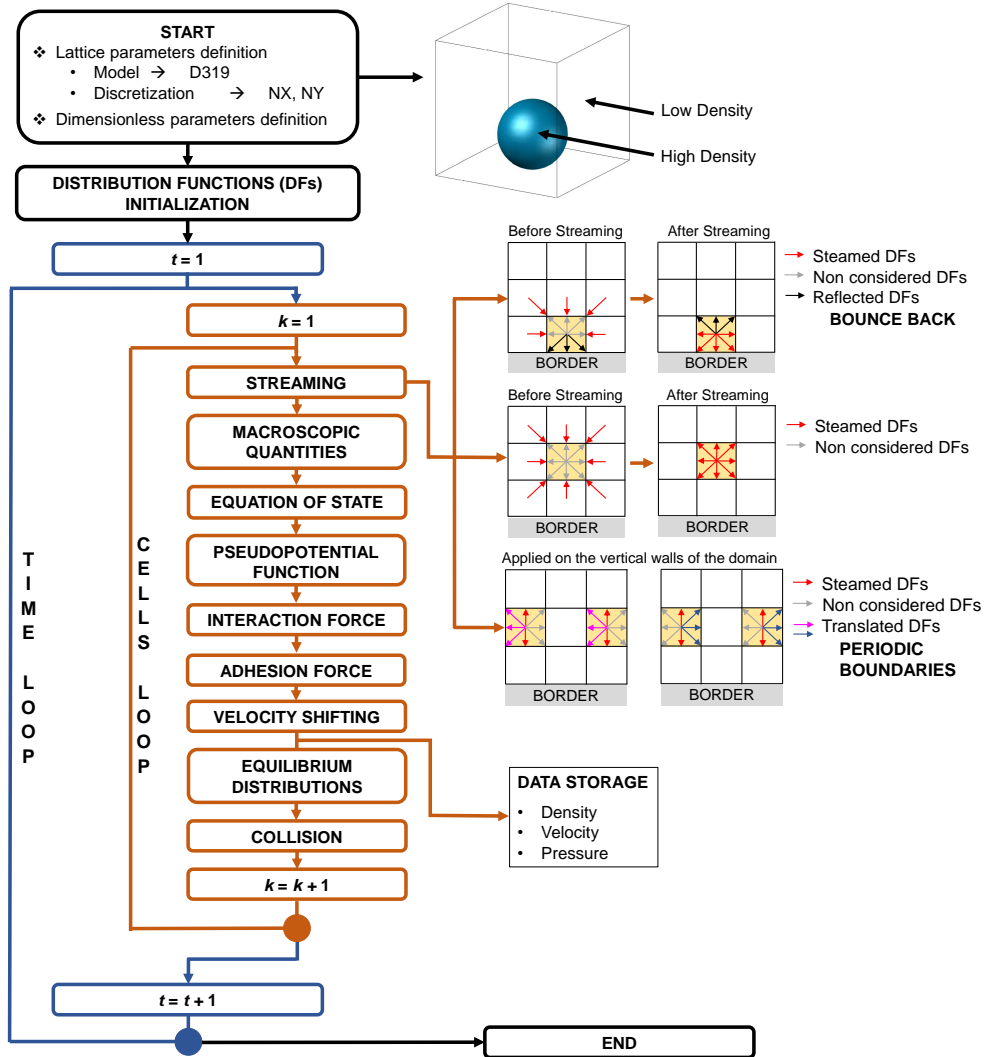


Figure 4.6: Pseudopotential LB algorithm, based on Shan and Chen [1993] model. The bounce back rule is used for no-slip boundaries. The Redlich-Kwong EOS is adopted to describe the state of matter and He and Doolen [2002] formulation is used to describe the pseudopotential function.

In Figure 4.7 an example of droplet wetting is presented. This case study has been carried out adopting the R-K EOS, with the parameters proposed by Huang et al. [2009]. Analogous parameters for the VdW and the C-S EOS have been proposed by Yuan and Schaefer [2006]. As detailed in Benzi et al. [2006], the parameter  $\rho_w$  in Eq. 4.31 can be used to vary manage the contact angle. In particular in R-K EOS when  $\rho_w$  varies between the vapor and the liquid density, the contact angle varies from  $180^\circ$  to  $0^\circ$ .

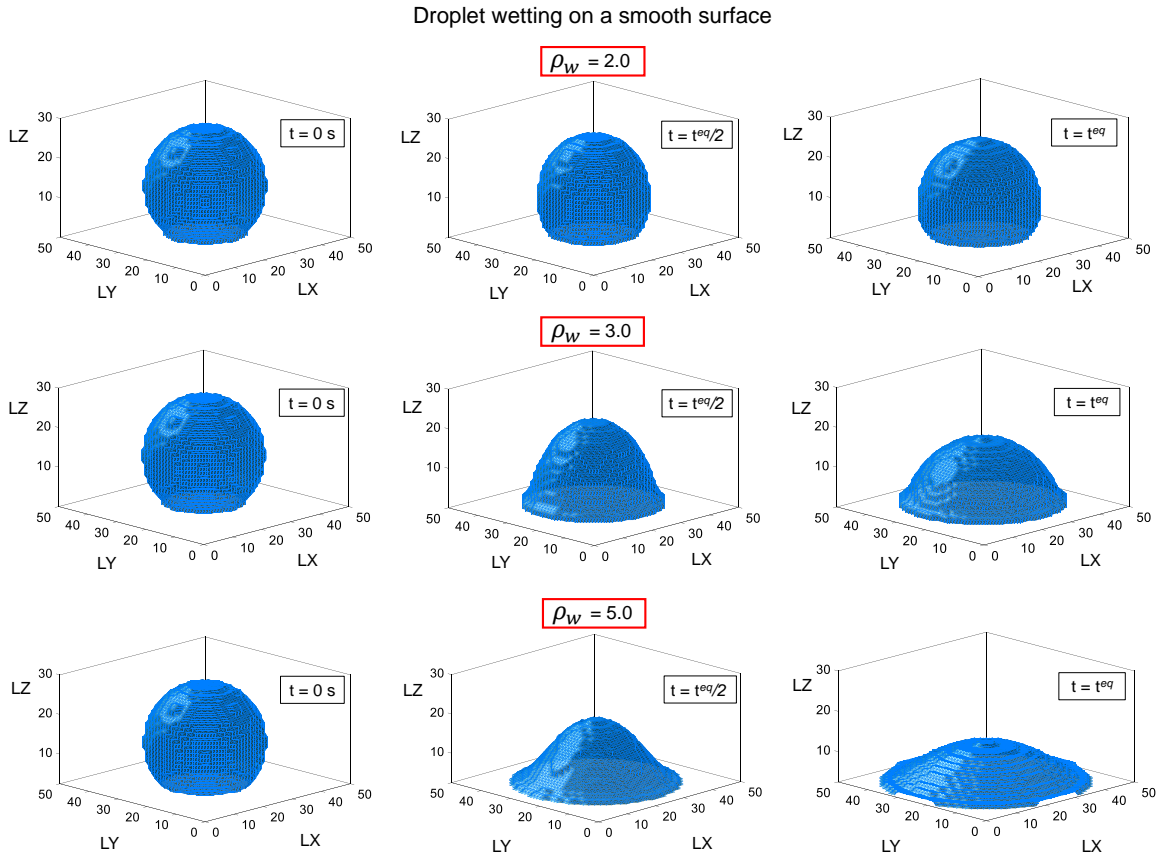


Figure 4.7: Droplet wetting on a smooth surface performed using the multiphase Shan and Chen [1993] LB scheme, using the R-K EOS. Different contact angles obtained by varying the solid wall density  $\rho_w$ .

We evaluate the equilibrium contact angle  $\theta^{eq}$  on the XZ plane; we underline that this choice does not influence anyway the results since the problem is radial symmetric. The obtained equilibrium contact angles are summarized in Table 4.1.

$\rho_w$	$\theta^{eq}$
2	153.3°
3	77.2°
5	14.6°

Table 4.1: Contact angle between the droplet and the bottom wall.

The results are very similar to the ones obtained by Huang et al. [2009] in the bi-dimensional case.

In Figure 4.8 we show an example of two droplets wetting on a smooth surface. This example has been carried out adopting the parameters proposed by Huang et al. [2009]. We can appreciate how, during the wetting process, cohesion force develops between the two droplets as well as the adhesion force of the droplets with the bottom wall.

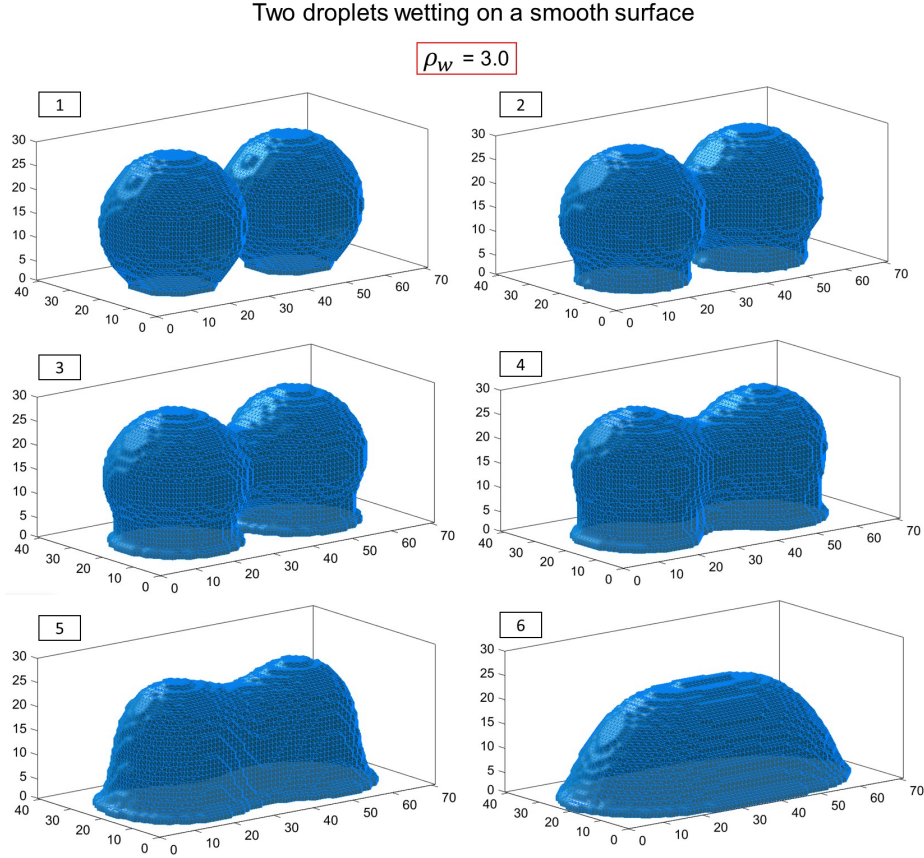


Figure 4.8: Droplet wetting on a smooth surface performed using the multiphase Shan and Chen [1993] LB scheme, using the R-K EOS.

#### 4.3.1 Thermal multiphase flows

In this section we propose an example of thermal multiphase fluid flow. The algorithm is based on the Shan and Chen [1993] *pseudopotential* lattice Boltzmann method (see Figure 4.6),

while the thermal problem has been included using the *multi-distribution* lattice Boltzmann approach proposed by Guo et al. [2002b] (see Figure 4.3).

In Figure we show an example of droplet wetting on a smooth surface. In this example we adopt the R-K EOS and the density of the bottom wall has been kept equal to 5.0. Periodic boundaries has been imposed on the vertical walls, while no-slip boundaries have been adopted on bottom and top walls. Higher temperature is imposed and maintained constant on the bottom wall. Lower temperature is imposed and maintained constant on the top wall. Periodic thermal boundaries are adopted on the vertical walls. Colored isolines represent the temperature which is normalized with the formula  $(T - T_l)/\Delta T$  proposed by He et al. [1998]. Higher temperature is equal to 100°C; lower temperature is equal to 25°C. During the wetting process we observe that higher temperature is found in correspondence of the zones of the domain with higher temperature and thermal conductivity. Furthermore we notice that the contact angle is smaller than in the case of a non-thermal flow. This result is in accordance with the experimental results shown by Ruijter et al. [1998].

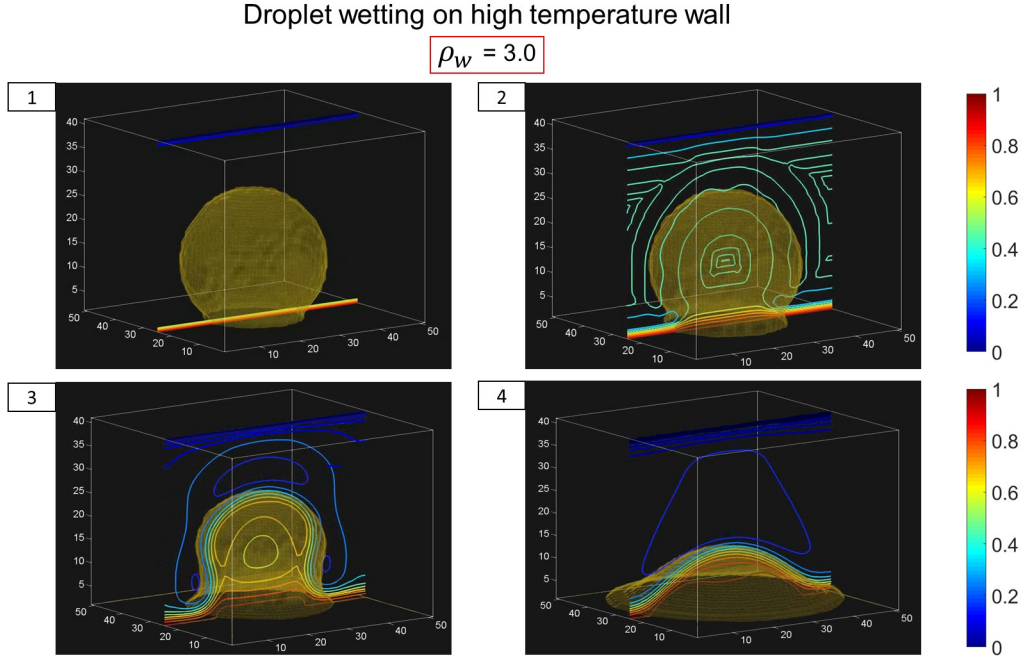


Figure 4.9: Droplet wetting on a smooth surface performed using the multiphase Shan and Chen [1993] LB scheme, using the R-K EOS. Temperature difference is imposed between bottom and top wall.

## 4.4 Free surface flows

In this section we present the LB free surface model proposed by Thürey et al. [2005]. The classical multiphase multicomponent LB methods query the computation of liquid and gas phase; in free surface LB schemes, instead, the gas phase is neglected and only the liquid phase evolution is calculated, reducing the computational costs. To simulate free surface flows, the lattice domain is divided among three parts: liquid cells, interface cells and gas

cells. Interface cells form a closed boundary around the liquid cells, so that no liquid cell is directly in contact with a gas cell. Initial density and mass are assigned to liquid and interface cells while gas cells have no mass and no density. In consequence, gas cells have no distribution functions and they are not considered during calculations. In liquid cells the mass is equal to the density, while in interface cells the mass is lower than the density. To discern liquid, interface and gas cells it is convenient to introduce a new variable called *liquid fraction* given by:

$$\epsilon(\mathbf{x}, t) = \frac{m(\mathbf{x}, t)}{\rho(\mathbf{x}, t)} \rightarrow \begin{cases} \epsilon = 1 & \rightarrow \text{Liquid cell} \\ 0 < \epsilon < 1 & \rightarrow \text{Interface cell} \\ \epsilon = 0 & \rightarrow \text{Gas cell} \end{cases} \quad (4.37)$$

where  $m(\mathbf{x}, t)$  is the mass contained in the cell at position  $\mathbf{x}$  at time  $t$  and  $\epsilon$  is the liquid fraction. Figure 4.10 shows an example of cells initialization. Both liquid and interface cells have the same density. The liquid fraction is equal to the fraction of cell filled by the liquid and it can be easily estimated by approximating the real boundary with straight adjacent lines. The precision of this procedure is dependent from the lattice mesh resolution.

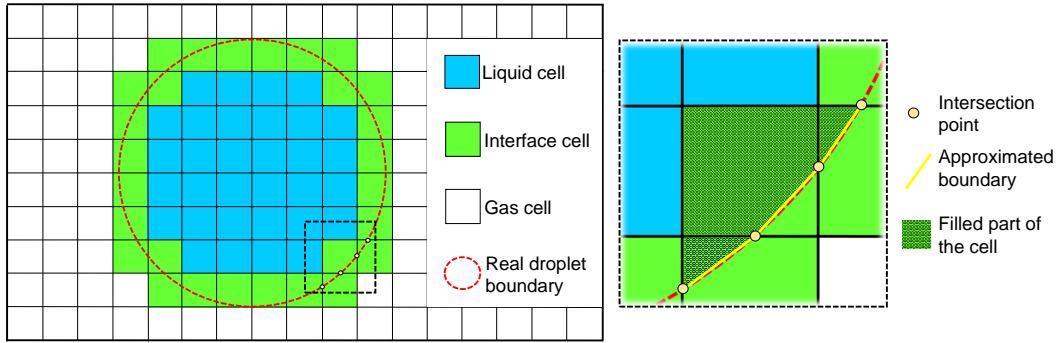


Figure 4.10: Example of cell initialization and procedure to calculate the liquid fraction on the interface cells.

The interface movement is tracked by the calculation of the mass exchange between adjacent cells, similarly to VOF (volume of fluid) method. The probability density functions correspond to a certain number of particles allocated at each cell, so the mass exchange can be performed directly at the streaming step. Only liquid and interface cells can exchange mass one to each other, no mass exchange between interface and gas cells is allowed. The mass exchange between liquid cells or between an interface and a liquid cell is basically described by the difference between in-coming and out-coming distribution functions:

$$\Delta m_i^s(\mathbf{x}, t) = f_{i_r}(\mathbf{x} - \mathbf{e}_i \Delta t, t - \Delta t) - f_i(\mathbf{x}, t - \Delta t) \quad (4.38)$$

where apex  $s$  has been used to stress the fact that mass exchange is computed while streaming step takes place. The mass exchange among two interface cells has to take into account the average fluid fraction which represents the area of fluid interface between two cells:

$$\Delta m_i^s(\mathbf{x}, t) = f_{i_r}(\mathbf{x} - \mathbf{e}_i \Delta t, t - \Delta t) - f_i(\mathbf{x}, t - \Delta t) \frac{[\epsilon(\mathbf{x} - \mathbf{e}_i \Delta t, t - \Delta t) + \epsilon(\mathbf{x}, t - \Delta t)]}{2} \quad (4.39)$$

In Figure 4.11 the mass exchange process among adjacent cells is presented in a D2Q9 lattice scheme. It is important to underline that Eqs. 4.38 and 4.40 are completely symmetric and

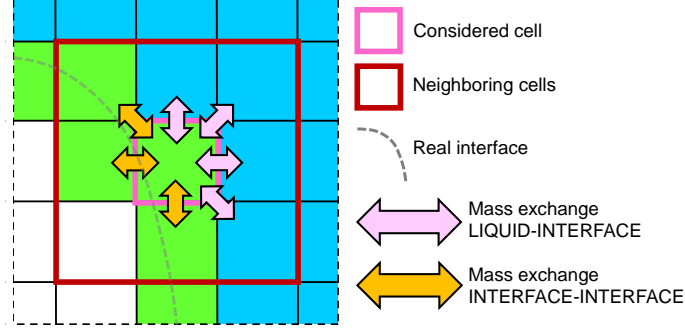


Figure 4.11: Mass exchange process among an interface cell and the neighboring liquid and interface cells.

therefore mass is automatically conserved in the whole domain:

$$m^s(\mathbf{x}, t) = m(\mathbf{x}, t - \Delta t) + \sum_i \Delta m_i^s(\mathbf{x}, t) \quad (4.40)$$

As above mentioned, Eq. 4.38 is valid for liquid/interface and liquid/liquid mass exchange, although, it is possible to simplify calculations considering that in liquid cells the mass is equal to the density and so the streaming of particle distributions among liquid cells represents the mass exchange. With this considerations it is possible to calculate only the mass exchange between liquid/interface and interface/interface cells; however it is necessary to identify the next-to-interface liquid cells.

An important relevant point in free surface flows, is how to impose boundary conditions on the interface. The streaming process between an interface and an empty cell, in fact, cannot be directly computed because in empty cells the particle distributions are not defined and they need to be reconstructed. Following the approach proposed by Körner [2008], the reconstructed distribution functions are given by:

$$f_i^s(\mathbf{x}, t) = f_{i_r}^{eq}(p^E, \mathbf{v}) + f_i^{eq}(p^E, \mathbf{v}) - f_i(\mathbf{x}, t - \Delta t) \quad (4.41)$$

where the equilibrium distributions are calculated with Eq. 4.12 and  $p^E$  is the external pressure surrounding the interface layer. The external pressure is defined as follows:

$$p^E = \frac{1}{3}\rho^E - k\sigma \quad (4.42)$$

where  $k$  is the curvature of the interface and  $\sigma$  is surface energy. Eq. 4.41 is used not only to reconstruct the distribution functions coming from the empty cells, but also to reconstruct the distribution functions coming from the directions defined by:

$$\mathbf{n} \cdot \mathbf{e}_{i_r} > 0 \quad (4.43)$$

where  $\mathbf{n}$  is the normal at the interface in the considered cell. This correction is adopted



to prevent the asymmetry rising on the interface because of the number of the unknown incoming distributions is, generally smaller than the known ones [Körner et al., 2005]. Figure 4.12 shows the streaming process on an interface cell. To state which distribution functions

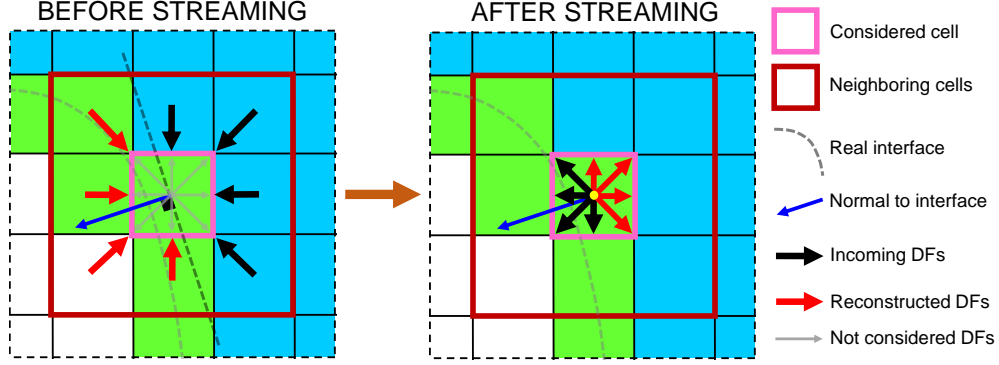


Figure 4.12: Example streaming process on an interface cell. Black arrows represent the known distribution functions incoming from liquid cells. Red arrows represent the reconstructed distribution functions coming from neighboring interface and empty cells.

need to be reconstructed it is necessary to calculate the normal in the considered interface cell. In literature there are several methods to perform the normal calculation; the simplest one is to define  $\mathbf{n}$  as a kind of average of the liquid fraction of the neighboring cells [Thürey et al., 2005]:

$$\mathbf{n}(\mathbf{x}_{k,l}) = \frac{1}{2} \begin{bmatrix} \epsilon(\mathbf{x}_{k+1,l}) - \epsilon(\mathbf{x}_{k-1,l}) \\ \epsilon(\mathbf{x}_{k,l+1}) - \epsilon(\mathbf{x}_{k,l-1}) \end{bmatrix} \quad (4.44)$$

where  $(k, l)$  are the coordinates of the considered cell. A more accurate scheme has been proposed by Thies [2005]. In this scheme, the template sphere method is adopted to evaluate both the normal at the interface and the curvature. The normal at the interface is calculated taking into account the first two layers of neighboring cells (25 cells) and can be evaluated through the following formula:

$$\begin{aligned} \tilde{\mathbf{n}}(\mathbf{x}_{k,l}) &= \sum_{s=-2}^2 \sum_{r=-2}^2 (1 - \epsilon(\mathbf{x}_{k+s,l+r})) \frac{\mathbf{x}_{k+s,l+r}}{|\mathbf{x}_{k+s,l+r}|} \\ \mathbf{n}(\mathbf{x}_{k,l}) &= \frac{\tilde{\mathbf{n}}(\mathbf{x}_{k,l})}{|\tilde{\mathbf{n}}(\mathbf{x}_{k,l})|} \end{aligned} \quad (4.45)$$

After streaming, the collision can take place for both interface and liquid cells. The inclusion of volume forces (e.g. gravity) is performed like in VOF, weighting the force with the liquid fraction:

$$f_i(\mathbf{x}, t) = f_i^s(\mathbf{x}, t) - \frac{1}{\tau} \left[ f_i^s(\mathbf{x}, t) - f_i^{eq}(\mathbf{x}, t) \right] + \epsilon(\mathbf{x}) w_i \rho(\mathbf{x}, t) \mathbf{e}_i \cdot \mathbf{g} \quad (4.46)$$

At the end of the loop over all cells, it is necessary to check if the liquid fraction of the interface

cells is still between 0 and 1; otherwise cell conversion is performed as follows:

$$\begin{aligned} \epsilon(\mathbf{x}, t) = \frac{m^s(\mathbf{x}, t)}{\rho(\mathbf{x}, t)} > 1 & \rightarrow \text{cell filled} \\ \epsilon(\mathbf{x}, t) = \frac{m^s(\mathbf{x}, t)}{\rho(\mathbf{x}, t)} < 1 & \rightarrow \text{cell emptied} \end{aligned} \quad (4.47)$$

The conversion of the cells is a very delicate step of the algorithm because it allows the interface movement and because during cells conversion the mass must be conserved and no liquid cell has to be in contact with gas cell (i.e. the interface has to be closed around the liquid cells). For definition, in liquid cells the mass must be equal to the density, while in empty cells the mass has to be equal to zero, however, normally, a mass excess rise during the conversion process. The part of mass exceeding the density in filled cells and the negative mass in emptied ones must be distributed among the surrounding interface and liquid cells. The simplest way to reallocate exceeding and negative mass is to divide it equally among the cells, but this approach can be source of instability. A more accurate solution [Thürey et al., 2005] is to redistribute the mass among surrounding cells, according to the normal direction:

$$m(\mathbf{x} + \mathbf{e}_i) = m(\mathbf{x} + \mathbf{e}_i) + m^{ex} \frac{\varphi_i}{\varphi_{total}} \quad (4.48)$$

where  $\varphi_i$  is given by:

$$\begin{aligned} \varphi_i &= \begin{cases} \mathbf{n} \cdot \mathbf{e}_i & \text{if } \mathbf{n} \cdot \mathbf{e}_i > 0 \\ 0 & \text{if } \mathbf{n} \cdot \mathbf{e}_i \leq 0 \end{cases} & \text{for filled cells} \\ \varphi_i &= \begin{cases} -\mathbf{n} \cdot \mathbf{e}_i & \text{if } \mathbf{n} \cdot \mathbf{e}_i < 0 \\ 0 & \text{if } \mathbf{n} \cdot \mathbf{e}_i \geq 0 \end{cases} & \text{for emptied cells} \end{aligned} \quad (4.49)$$

and  $\varphi_{total}$  is the sum of  $\varphi_i$ . During cells conversion, many problems may rise. More details about those topics are provided by Thürey et al. [2005] and Körner et al. [2005]. In Figure 4.15 the adopted free surface LB algorithm is presented.

With the proposed algorithm we simulate the dynamic wetting of a droplet on a smooth surface. In case of dynamic wetting, Young's equation can be rewritten as follows:

$$F_x = \sigma_{SG} - \sigma_{SL} - \sigma_{LG} \cos(\theta_{dyn}) \quad (4.50)$$

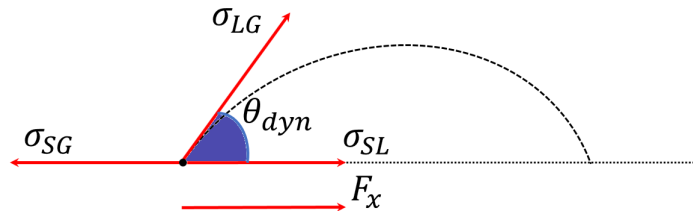


Figure 4.13: Contact angle in dynamic conditions.

Inserting Eq. 4.50 in Eq. 4.36, we obtain:

$$F_x = \sigma_{LG} \cos(\theta_{dyn}) - \sigma_{LG} \cos(\theta_{eq}) \quad (4.51)$$

meaning that force  $F_x$  vanishes when  $\theta_{dyn} = \theta_{eq}$ . In order to describe a dynamic wetting condition we need to take into account the wetting force  $F_x$ . In this work we follow the procedure proposed by Attar and Körner [2009].

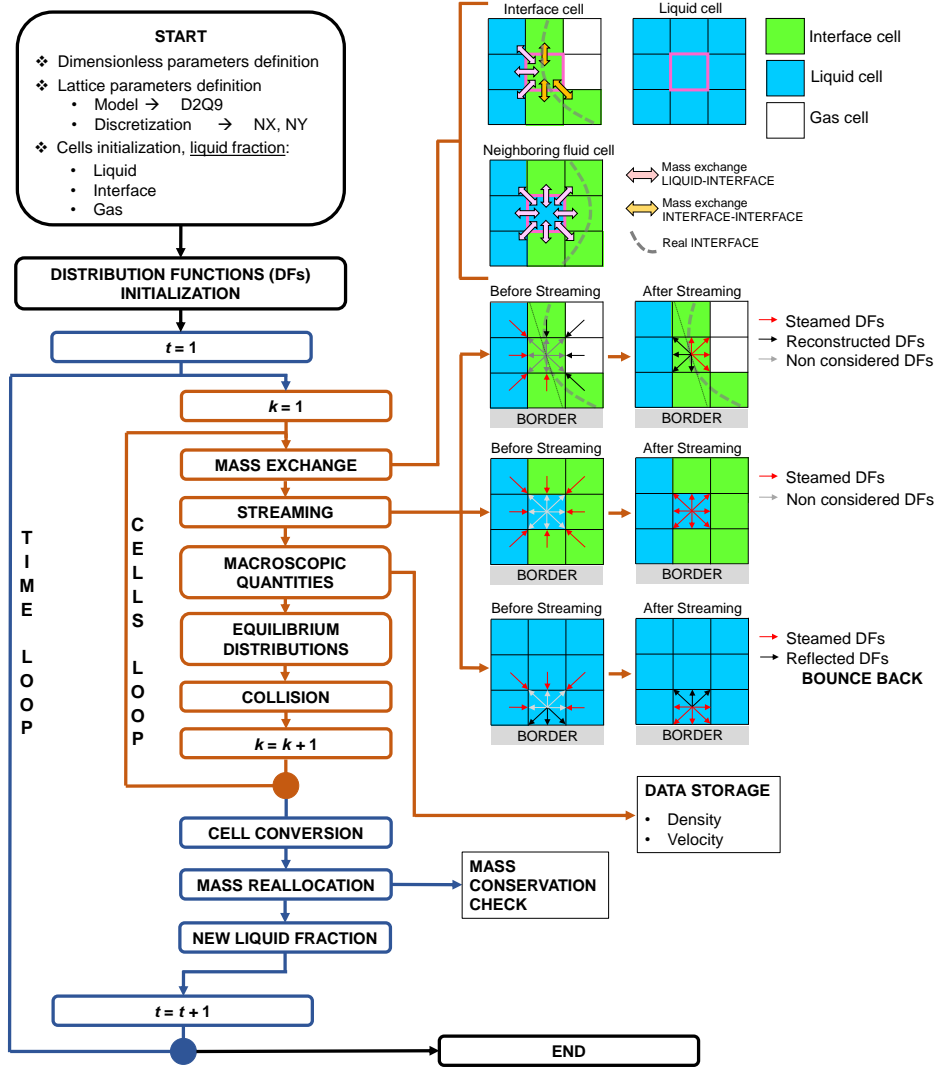


Figure 4.14: Free surface LB algorithm, based on [Thürey et al., 2005] model. Mass exchange is calculated only for interface and fluid neighboring cells. Classic bounce back scheme is adopted to simulate no slip boundaries.

In Figure we show the results of a dynamic droplet wetting on smooth surface. In this simulation gravity is considered and it is equal to  $0.00005 \text{ lu/tu}^2$  (where dimensions are expressed in lattice units); surface tension is kept equal to  $0.002 \text{ mu/tu}^2$ .

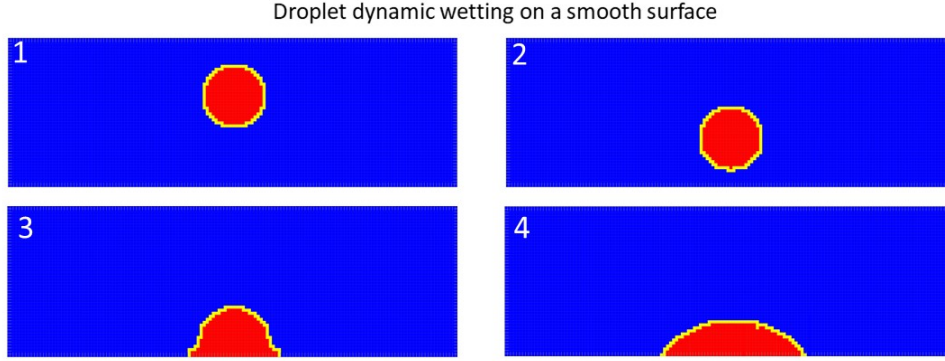


Figure 4.15: Dynamic wetting of a droplet on a smooth surface.

We can observe that the dynamic nature of the contact angle is evident during the droplet spreading on the smooth surface.

## 4.5 Phase change

A crucial point in the simulation of the PBF process is the phase change treatment. There are basically two approaches to simulate the solid-liquid phase-change: the phase-field method and the enthalpy-based method. Miller and Succi [2002] proposed a phase-field based LB method to simulate the crystal growth from the melt pool. This method uses a chemical variable to define melting and solidification of the particles. In enthalpy-based method, instead, the solid-liquid interface is traced by using the total entropy variation. Chakraborty and Chatterjee [2007] proposed an enthalpy-based LB method for solid-liquid phase change in convective flows. Because of the non linear behavior of the latent heat, the enthalpy-based LB methods need, generally, an iteration step to solve the AD equation. In this work we adopt the enthalpy-based LB model proposed by Huang et al. [2013]. This approach allows to avoid iteration steps [Chatterjee, 2009] or to solve a system of equations at each lattice cell [Eshraghi and Felicelli, 2012], to track the solid-liquid interface.

In phase change problems a heat source causes the melting of the material. The heat source can be described as follows:

$$\Phi = -\frac{\partial(\rho L_{sl}\psi)}{\partial t} \quad (4.52)$$

where  $L_{sl}$  is the latent heat of solid-liquid phase change and  $\psi$  is the liquid fraction. Advection diffusion equation can be rewritten as follows:

$$\frac{\partial(\rho H)}{\partial t} + \nabla \cdot (\rho c_p T \mathbf{v}) = \nabla \cdot (k \nabla T) \quad (4.53)$$

where  $H$  is the total enthalpy defined as:

$$H = c_p T + \psi L_{sl} \quad (4.54)$$

The phase-change LB method is a natural extension of the TLB model presented in Section

4.2; however, it is convenient to use the enthalpy in place of the temperature because the temperature is not continuously differentiable in time [Alexiades, 1992]. The change of variable is stressed by the usage of  $h_i$  in place of  $g_i$  and Eq. 4.9 is rewritten as follows:

$$h_i(\mathbf{x} + \mathbf{e}_i \Delta t, t + \Delta t) = h_i(\mathbf{x}, t) - \frac{1}{\tau_F} \left[ h_i(\mathbf{x}, t) - h_i^{eq}(\mathbf{x}, t) \right] + \Phi_i \quad i = 1, \dots, n \quad (4.55)$$

The macroscopic enthalpy of each cell is given by:

$$H = \sum_i^n h_i \quad (4.56)$$

and the equilibrium distributions are written as follows:

$$\begin{cases} h_i^{eq} = H - c_p T + w_i c_p T \left( 1 - \frac{\mathbf{v}^2}{2c_s^2} \right) & i = a_0 \\ h_i^{eq} = w_i \rho \left[ 1 + \frac{\mathbf{e}_i \cdot \mathbf{v}}{c_s^2} - \frac{\mathbf{v}^2}{2c_s^2} + \frac{(\mathbf{e}_i \cdot \mathbf{v})^2}{2c_s^4} \right] & i \neq a_0 \end{cases} \quad (4.57)$$

where  $a_0$  is the  $i$ -th direction associated to the zero velocity. The temperature is derived from the enthalpy as follows:

$$T = \begin{cases} H/c_p & T < T_s \\ T_s + \frac{H-H_s}{H_l-H_s}(T_l - T_s) & T_s \leq T \leq T_l \\ T_l + (H - H_l)/c_p & T > T_l \end{cases} \quad (4.58)$$

where  $T_s$  is the solidus temperature,  $T_l$  is the liquidus temperature,  $H_s$  and  $H_l$  are the enthalpy values related to the solid and the liquidus temperature respectively. The limit  $T_s \leq T \leq T_l$  physically means that the phase-change happens at a constant temperature  $T_m$  which is called melting temperature. With the above described procedure, the phase change can be obtained without performing any iteration step. The last obstacle to face is the description of the moving boundary. We adopt the immersed moving boundary scheme proposed by Noble and Torczynski [1998] which was verified by Strack and Cook [2007] to be accurate and computationally efficient. The solid-liquid interface is tracked with the liquid fraction. The liquid fraction varies from 0 (solid) to 1 (liquid). The lattice cells in which  $0 < \psi < 1$  represent the moving boundary. To track the boundary movement, the collision term of fluid-dynamic distributions is modified to take into account the liquid fraction:

$$f_i(\mathbf{x}, t) = f_i^s(\mathbf{x}, t) - \frac{1-B}{\tau} \left[ f_i^s(\mathbf{x}, t) - f_i^{eq}(\mathbf{x}, t) \right] + F_i + B\Omega_i \quad (4.59)$$

where  $F_i$  is the forcing term and  $B$  is defined as follows:

$$B = \frac{(1-\psi)(\tau_F - 0.5)}{\psi + \tau_F - 0.5} \quad (4.60)$$

The additive collision term  $\Omega_i$  is given by:

$$\Omega_i = f_{i_r}^s(\mathbf{x}, t) - f_i^s(\mathbf{x}, t) + f_i^{eq}(\rho, \mathbf{v}_s) - f_{i_r}^{eq}(\rho, \mathbf{v}) \quad (4.61)$$

where  $\mathbf{v}_s$  is the velocity of the solid part. A typical problem to test the phase-change problem is the melting by convection in a cavity under a constant heat flux. The algorithm adopted to solve the problem is presented in Figure 4.17. To ensure the stability of the method, for fluid and thermal boundary conditions, we adopt the non-equilibrium extrapolation scheme proposed by Zhao-Li et al. [2002]: the no-slip boundaries are decomposed into an equilibrium term and a non equilibrium term:

$$\begin{aligned} f_i^s(\mathbf{x}, t) &= f_i^{eq}(\mathbf{x}, t) + f_i^{neq}(\mathbf{x}, t) \\ h_i^s(\mathbf{x}, t) &= h_i^{eq}(\mathbf{x}, t) + h_i^{neq}(\mathbf{x}, t) \end{aligned} \quad (4.62)$$

where  $f_i^{eq}$  and  $h_i^{eq}$  distributions are derived through Eq. 4.57, while  $f_i^{neq}$  and  $h_i^{neq}$  are obtained via extrapolation from the neighboring cells [Huang et al., 2013]. In figure 4.17 the solid-liquid phase change LB algorithm is presented. The proposed algorithm is used to investigate the melting process in a square cavity. The boundary conditions of the problem are presented in Figure 4.16. A high temperature ( $T_{high}$ ) is imposed on the right side of the domain, while a low temperature ( $T_{low}$ ) is maintained on the left side of the domain. Upper and bottom sides are assumed to be adiabatic [Tang et al., 2005]. In solid-liquid phase change three non dimensional parameters are considered:  $Pr$ ,  $Ra$  and the *Stefan* ( $Ste$ ) number which is defined as follows:

$$Ste = \frac{c_p(T_{high} - T_m)}{L_{sl}} \quad (4.63)$$

where  $T_m$  is the melting temperature of the considered material. In our simulation we have adopted  $Ra = 1.0E4$ ,  $Pr = 0.01$  and  $Ste = 0.01$ . This simulation has been performed on a  $150 \times 150$  lu grid. The temperature has been normalized with the following formula:

$$T^* = \frac{T - T_m}{T_{high} - T_m} \quad (4.64)$$

where  $T_{high}$  is the imposed temperature on the left wall of the domain. In analogous manner the time can be normalized with the *Fourier* ( $Fo$ ) number which is defined as follows:

$$Fo = \frac{k \cdot t}{L_y} \quad (4.65)$$

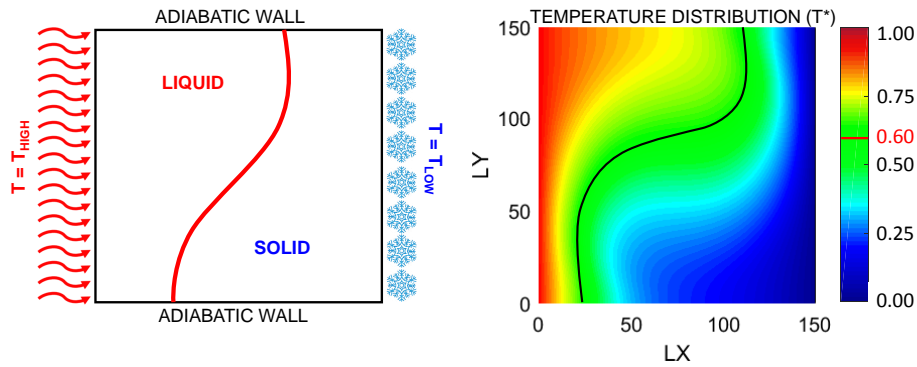


Figure 4.16: Solid-Liquid phase-change

Figure 4.16 refers to the melting process at  $Fo = 30$ .

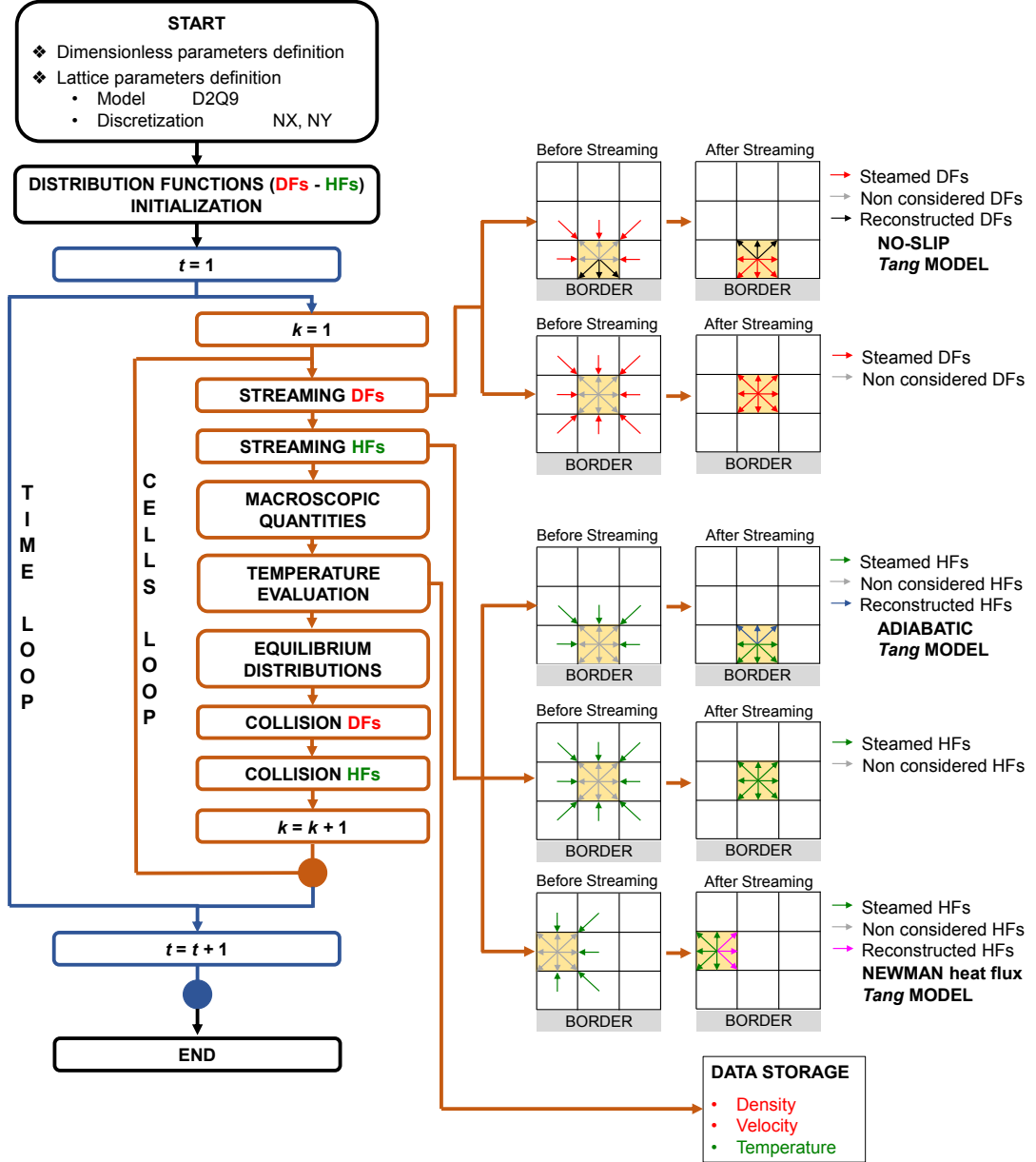


Figure 4.17: Solid-Liquid phase-change LB algorithm, based on Shan and Chen [1993] model. The bounce back rule is used for no-slip boundaries. The Redlich-Kwong EOS is adopted to describe the state of matter and the He and Doolen [2002] formulation is used to describe the pseudopotential function.

## 4.6 Conclusion and perspectives

In this section we have adopted the lattice Boltzmann method to solve some interesting thermo-fluid dynamic problems. First we have solved two classic problems, i.e., the lid driven

cavity and the Rayleigh-Benard convection, then we moved to more complicated problems such as multiphase and free-surface flows. Finally we studied the melting problem of a single component fluid. The treated problems are very interesting from AM point of view because both wetting, temperature evolution, and phase change occur during powder melting. The next step of our research will be to include the phase change algorithm within the multiphase and the free surface algorithm so to be able to simulate the thermo-fluid dynamic evolution of droplet melting in PBF process.



## Chapter 5

# Finite Element Simulation of Powder Bed Fusion

The lattice Boltzmann simulations of PBF are a very powerful instrument to investigate the melt pool evolution and the effects of the printing parameters on the stability of the melt pool and on the microscopic properties of the material. Although, as discussed in Section 2.4.2, they are not a reasonable choice in order to simulate an entire component, because they would require huge computational efforts.

To overcome this obstacle, many authors adopted the finite element method (FEM) to simulate the PBF process at different scale of analysis. Nevertheless FEM approach has the strong simplification to assume the powder bed as a continuum domain and to neglect the melt pool dynamics, it is a very good solution to simulate entire structural components; moreover, FE analysis can be adopted also to investigate the local interactions between the heat source and the powder bed.

### 5.1 Simulation approach

In this Section, using Abaqus, we develop a FE framework to simulate the PBF process at the powder and at the component scale level. As briefly mentioned in Section 2.4.4, since 2016 Abaqus started to develop a tool for SLM process simulation. This tool is in a very embryonic state, without documentation and without a graphic interface. The simulation of SLM process can be performed through an uncoupled approach: first a thermal analysis is carried out to evaluate the time evolution of the temperature field, then the results are used as input for a mechanical analysis to evaluate stress distribution and deformations. In order to respect the physical process, two basic ingredients are needed:

- Simulation of the powder bed deposition through *sequential element activation*;
- Simulation of the heat source movement on activated elements to *reproduce the laser scan path*.

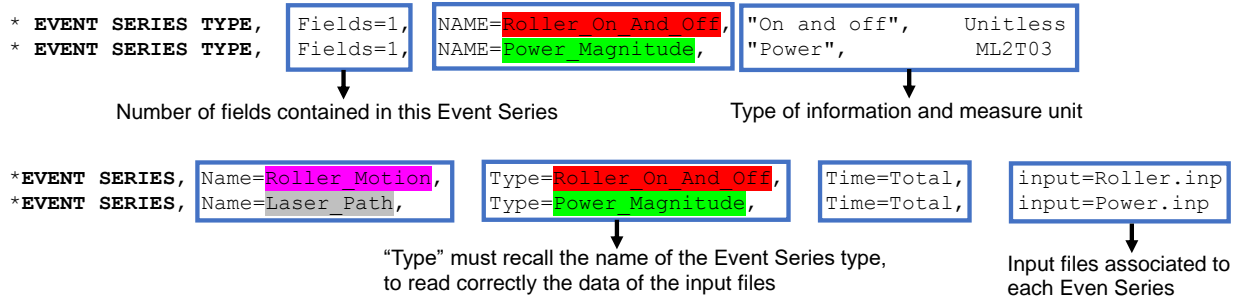
In our simulation approach, we divide the input data into three **input** groups:

- **Event Series.** In SLM we define two event series: powder deposition and laser scan simulation;

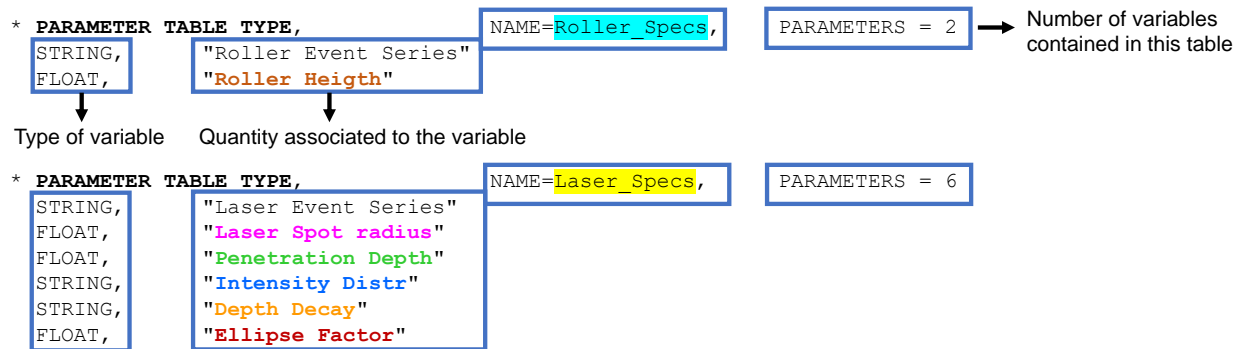
- **Parameter Table.** Here we define the needed input parameters associated to each event series;
- **Table Collection.** Here we assign the values to each previously defined parameter.

In Figure 5.1 we show the Abaqus code used to define the necessary input data.

## EVENT SERIES



## PARAMETER TABLES



## TABLES COLLECTION

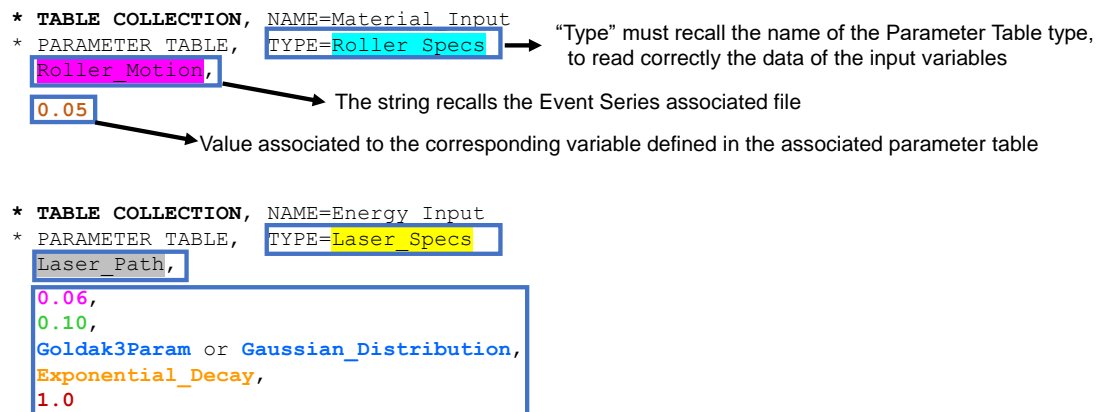


Figure 5.1: Example of the Abaqus code necessary to define the input data for the SLM simulation.

The *Event Series* reproduce the physical events during the printing process. In case of SLM, we need two event series: `Roller_Motion` in which we define the roller movements on the

building plate and we sequentially activate the elements to reproduce the powder deposition; and the `Laser_Path` in which we define the laser path of the layer of elements representing the powder layer.

The *Parameter Tables* collect all the necessary parameters to perform both the sequential element activation and the heat source interaction with the elements. We define two different tables: the former contains the variables necessary to perform the `Roller_Motion`; the latter contains all the variables needed to model the laser heat source and to simulate the `Laser_Path`.

The *Table Collection* is used to assign, to each variable contained in the parameter table, the corresponding value. The input argument can be a floating number or a string; in this last case, the string can be the name of the associated event series or a particular string to activate predefined plugin functions.

In the next sections we analyze in detail each event series following the real printing process.

### 5.1.1 Roller\_Motion event series and sequential element activation

The sequential element activation reproduces the powder deposition on the building plate. Its definition must be in accordance with the physical printing process. As shown in Figure 2.1, usually the powder is deposited on the building plate by a roller which moves along X or Y direction. In our simulation approach the roller replaced by a *marching rectangle* which moves following a predefined path. When the center of an element falls within the ideal volume covered by the marching rectangle, then the element is activated.

In order to simulate a real printing process, the typical element height must be equal (or a sub-multiple) to the powder layer height: in this case we refer to this meshing strategy as *fine*. Although, this kind of meshing strategy is not so far eligible to simulate an entire SLmed part, in fact, as discussed in Section 2.4.2, the computational costs strongly increase. In order to simulate an entire SLmed functional component, it is usual to assume the typical element height as a multiple (10 to 50 times) of the powder layer height: in this case we refer to this meshing strategy as *coarse*. The element activation process remains basically the same in both cases, but the heat source modeling is significantly different, as discussed in Section 5.1.2.

To make easier the comprehension of the element activation process, we consider a very simple benchmark of a cube with size 10 mm centered on a square building plate of size 100 mm, we aim to simulate with a *coarse* meshing strategy (Figure 5.2)

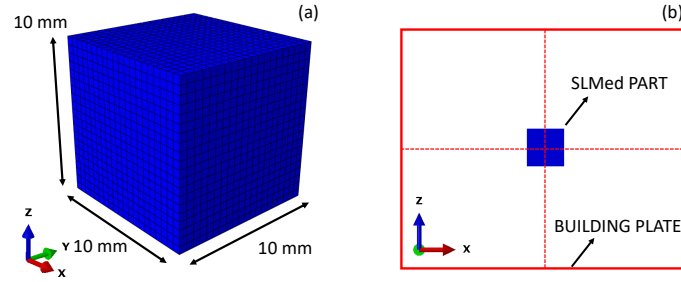


Figure 5.2: Example of a simple cubic component used to explain the sequential activation procedure.

We consider the roller moving on Y direction, moreover we assume the base of the of the marching rectangle to be infinite, while the rectangle height (roller height) is equal to the typical element height (0.5 mm). Accordingly, the *Roller.inp* file, containing the instructions to perform the sequential element activation is arranged as in Table 5.1.

T [s]	X [mm]	Y [mm]	Z [mm]	Roller ON/OFF —
0.000	0	-50	0.5	1
10.000	0	+50	0.5	0
16.394	0	-50	1.0	1
26.394	0	+50	1.0	0
...	...	...	...	...

Table 5.1: Scheme of the input file for the sequential element activation. Roller ON/OFF is a bit function which states if the marching rectangle starts to move (1) or it is stopped (0).

The sequential element activation is shown in Figure 5.3.

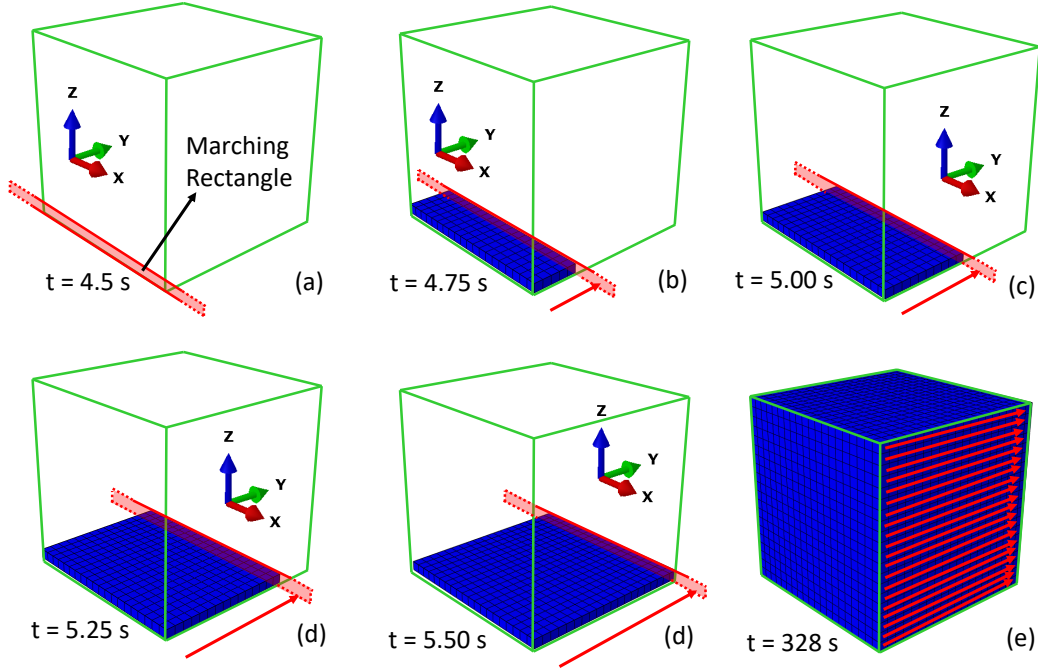


Figure 5.3: Example of sequential element activation on a simple geometry.

We observe that there is a gap between the final time instant of the first powder deposition and the beginning of the second powder deposition. During this period the laser selectively melts the powder. The laser scan simulation is performed through another event series.

### 5.1.2 Laser\_path event series and laser scan strategy

The thermal force strategy must follow exactly the real laser path. On the market there are basically two types of lasers used in for the SLM printing process: (i) pulsed lasers and (ii) continuum lasers. The former melts the powder through a series of high frequency impulses, the latter melts the powder through a continuum laser track. In our simulation, the laser path is taken into account through the input file *Laser.inp*. This file contains the coordinates of the laser heat source and the heat source power at each time step. A common sequence of instructions to manage the heat source movement is presented in Table 5.2.

T [s]	X [mm]	Y [mm]	Z [mm]	Laser Power [W]
10.001	5	5	0.25	400
10.003	4.95	5	0.25	0
10.009	4.95	4.95	0.25	400
10.014	4.90	4.95	0.25	0
...	...	...	...	...

Table 5.2: Scheme of the input file for the heat source movement.

This case simulates a pulsed laser heat source strategy, in fact the laser power is shifted in an alternate way from on to off status; this condition can be easily adapted to simulate a continuous laser heat sources. In Fig. 5.4, we show an idealized example of a simple scan strategy.

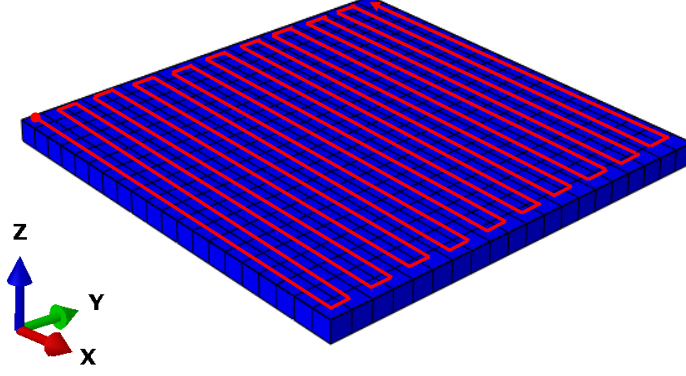


Figure 5.4: Example of an idealized scan strategy starting at the end of the deposition process (Figure 5.3 (d)).

In Section 5.1.1, we have discussed about the possibility of using a *fine* and a *coarse* meshing strategy. The adopted meshing strategy influences not only the sequential element activation, but also the *Laser.inp* file. In case of a *fine* mesh, each activated layer of elements corresponds to a physical layer of powder, therefore there is a perfect alternation of deposition and heat source movement. In case of a *coarse* mesh, instead, since a layer of elements corresponds to several layers of powder, after each deposition step we have to repeat several times the heat source movement on the deposited layer to simulate the correct number of scan paths.

### 5.1.3 Roller\_motion & Laser\_path files generation

The previous section showed that the correct definition of *Roller.inp* and *Laser.inp* files is fundamental to simulate with high fidelity the SLM process. The instructions of the real printing process are usually contained in a file referred as *G-Code*. This files contains all the informations about the laser path, but also many other informations like the chamber temperature, the building plate temperature, and all the parameters to manage the chamber inertization.

Actually, we have not at our disposal slicing softwares dedicated to SLM solutions, therefore we consider the slicing softwares commonly used for FDM printers. In this case the path contained in the G-Code file represents the filament deposition path and, for our application, we assume it to be the laser path on the powder bed. We remark that this choice is not fully consistent with the real printing process because the real laser path is typically very scattered, while the deposition process in FDM printers is more continuous.

The information needed to describe the laser path are:

- Laser position at each time step;

- Layer thickness;
- Laser power;
- Deposition process time.

The needed informations are directly extracted from the G-Code by means of a Matlab script. In correspondence of the end of each layer, a time gap is imposed to take into account the deposition process. In Figure 5.5 we show an example of the G-code file rielaborated trough our Matlab code

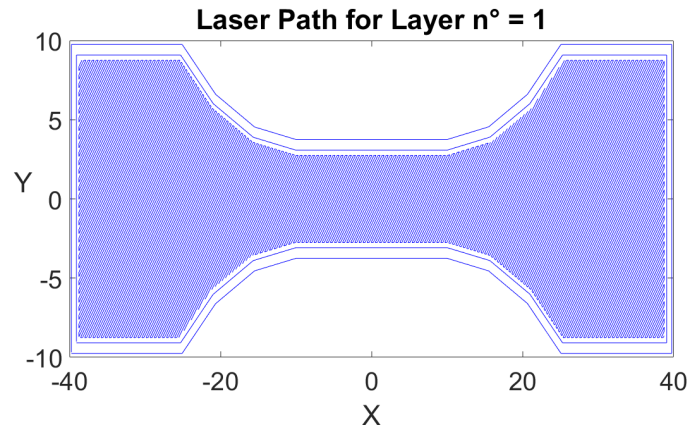


Figure 5.5: Example of a G-code file rielaborated with our Matlab script to generate the input files for SLM printing process simulation.

In Figure 5.6 we show part of the instruction of *Roller.inp* and *Laser.inp* input files generated from the rielaboration of the G-Code (Figure 5.5) by means of the Matlab file.

Roller.inp					
[T]	[X]	[Y]	[Z]	[On/Off]	
0.00000,	0.000,	-11.700,	0.040,	1	
3.00000,	0.000,	11.700,	0.040,	0	
5.54988,	0.000,	-11.700,	0.080,	1	
8.58880,	0.000,	11.700,	0.080,	0	
11.12129,	0.000,	-11.700,	0.120,	1	
14.16116,	0.000,	11.700,	0.120,	0	

Laser.inp					
[T]	[X]	[Y]	[Z]	[Power]	
3.00000,	-39.084,	-9.084,	0.040,	2.000E+05	
3.00690,	-25.292,	-9.084,	0.040,	2.000E+05	
3.00953,	-20.990,	-6.029,	0.040,	2.000E+05	
.....,	.....,	.....,	.....,	.....,	
5.54966,	38.362,	-8.754,	0.040,	2.000E+05	
5.54980,	38.633,	-8.754,	0.040,	2.000E+05	
5.54988,	38.754,	-8.633,	0.040,	0.000E+00	

Figure 5.6: *Roller.inp* and *Laser.inp* input files rielaborated from the G-Code (Figure 5.5) by means of the Matlab code.

#### 5.1.4 General simulation framework

In previous Sections we have described the working principle of Abaqus AM plugin for SLM process simulation. In this Section we explain the general simulation framework we have developed to simulated the SLM process of real components (Figure 5.7).

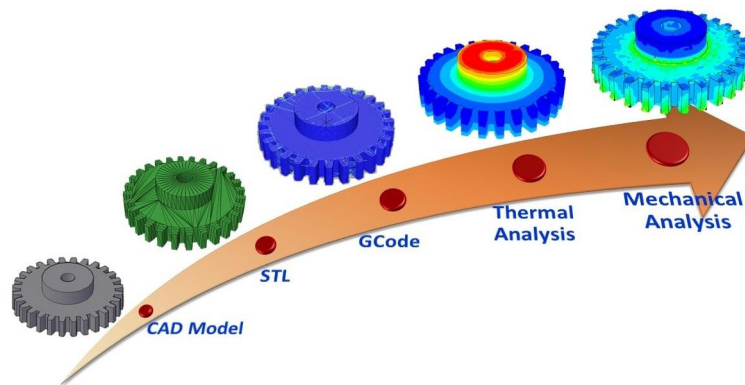


Figure 5.7: General framework adopted for SLM process simulation.

First, a model of the part is realized through a CAD software, then a triangular mesh of the external surface is generated (STL file) and used as input for the slicing software (e.g., Slic3r or KISSlicer). The G-Code file is rielaborated by means of the Matlab file; then *Roller.inp* and *Laser.inp* files are generated. Those files are used to perform the SLM process simulation of the part. The finite element simulation of SLM is splitted in two parts:



- *Thermal Analysis.* Used to evaluate the temperature field evolution during the sequential element activation and the heat source movement;
- *Mechanical Analysis.* The temperature field is used as input for the mechanical analysis and residual stress field evolution and part distortions are evaluated.

In the following Section we describe in detail the thermal and the mechanical analysis.

### 5.1.5 Thermal analysis

In SLM process the laser beam heats the powder bed exchanging heat and melting the powder; the absorbed heat is then dissipated through convection and radiation with the surrounding gas. The problem can be described by the well known heat conduction-convection equation:

$$\rho c \frac{\partial T}{\partial t} = \nabla \cdot (k \nabla T) + q \quad (5.1)$$

where  $\rho = \rho(T)$  is the material density,  $c = c(T)$  is the specific heat capacity,  $k = k(T)$  is the thermal conductivity,  $q$  is the heat source, and  $t$  is the time. The SLM printing process takes place in a chamber filled of an inert gas at constant temperature; moreover the deposited powder are usually preheated to facilitate the melting process. The initial condition of the problem is given by:

$$T(\mathbf{x}, 0) = T_p \quad \mathbf{x} \in D_p \quad (5.2a)$$

$$T(\mathbf{x}, 0) = T_c \quad \mathbf{x} \in D_c \quad (5.2b)$$

where  $\mathbf{x} = (x, y, z)$  is the position,  $D_p$  is the powder packing,  $D_c$  is the building chamber, while  $T_p$  and  $T_c$  are the powder preheating temperature and the chamber temperature, respectively. To avoid part detachments during the printing process it is usual to adopt a fixed temperature (higher than the chamber temperature) on the building plate  $D_p$ ; to simulate this occurrence we impose the following Dirichlet boundary condition:

$$T(\mathbf{x}, t) = T_p \quad \mathbf{x} \in D_p \quad (5.3)$$

where  $D_p$  is the building plate and  $T_p$  is the imposed building plate temperature. The Neumann boundary conditions of the problem are defined as follows [Schoinochoritis et al., 2017]:

$$k \frac{\partial T}{\partial n} + q_c + q_r = 0 \quad \mathbf{x} \in S(t) \quad (5.4)$$

where  $n$  is the vector normal to the surface,  $S(t)$  is the external surface (changing during element activation), while  $q_c$  and  $q_r$  are the heat fluxes due to convection and radiation, respectively, defined as:

$$q_c = h(T - T_c) \quad (5.5a)$$

$$q_r = K_b(T^4 - T_c^4)\epsilon \quad (5.5b)$$

where  $h = h(T)$  is the heat transfer coefficient,  $K_b$  represents the Stefan-Boltzmann constant, and  $\epsilon$  is the emissivity.

A very important aspect in the thermal analysis is, for sure, the laser beam modeling. In the next section we illustrate the adopted laser beam model.

### Laser beam and phase change model

The most adopted laser beam model is the Gaussian model. It assumes a symmetrical energy distribution in which the maximum irradiance is in correspondence of the center of the beam, then it vanishes in exponential way. The irradiance of a Gaussian beam is given by:

$$I(r) = I_0 \exp^{-C_c r^2} \quad (5.6)$$

where  $I_0$  is the maximum irradiance,  $C_c$  is the contraction coefficient and  $r^2 = x^2 + y^2$  is the distance of a point  $(x, y)$  from the center of the beam. The radius  $R$  of the laser beam is the distance where  $I(R) = I_0 \exp^{-2}$ ; therefore, in this case,  $C_c = 2/R^2$ . Accordingly, Eq. 5.6 can be rewritten as follows:

$$I(r) = I_0 \exp^{-\frac{2r^2}{R^2}} \quad (5.7)$$

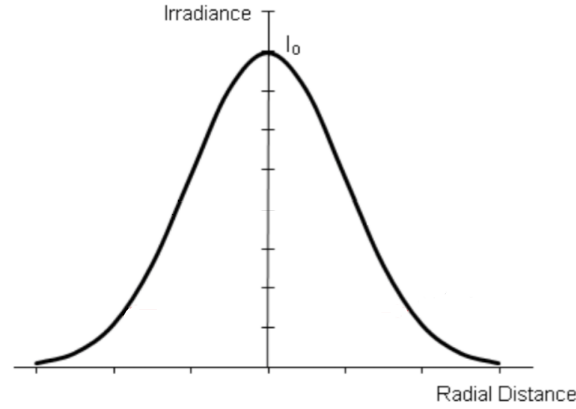


Figure 5.8: Laser beam: Gaussian distribution model.

The laser beam power is given by:

$$P = 2\pi \int_0^{+\infty} I(r) dr \quad (5.8)$$

Finally, inserting Eq. 5.7 in Eq. 5.8, we can derive the maximum irradiance in function of the laser beam power:

$$I_0 = \frac{2P}{\pi R^2} \quad (5.9)$$

and consequently, Eq. 5.7 can be rewritten as follows:

$$I(r) = \frac{2P}{\pi R^2} \exp^{-\frac{2r^2}{R^2}} \quad (5.10)$$

Eq.5.10 allows to predict the distribution of the laser power on the powder surface; although only a portion of this power is absorbed by the powder, part of the power, instead, is reflected,

as discussed in Section 2.3.2. To take into account only the absorbed laser power, Dai and L.Shaw [2005] multiplied the right hand side of Eq. 5.10 for the absorption coefficient  $\alpha$ :

$$I(r) = \frac{2P\alpha}{\pi R^2} \exp^{-\frac{2r^2}{R^2}} \quad (5.11)$$

Finally, Roberts [2012] integrated the Gaussian irradiance on the beam radius  $R$  and obtained an equivalent heat flux for Eq. 5.11:

$$q = 0.864 \frac{P\alpha}{\pi R^2} \quad (5.12)$$

Another solution for modeling the laser beam was proposed by Goldak et al. [1984] who modeled the laser beam as a Gaussian distribution over an ellipsoid with semi-axes  $a$ ,  $b$ ,  $c$  in which the maximum irradiance  $I_0$  is located in the center of the ellipse and the irradiance  $I(r)$  falls to  $0.05I_0$  in coespondence of the ellipsoidal surface. The spatial heat source of the so-called *Goldak distribution* is defined as follows:

$$q(x, y, z) = \frac{6\sqrt{6}\alpha P}{\pi\sqrt{\pi abc}} \exp^{-3\left(\frac{x^2}{a^2} + \frac{y^2}{b^2} + \frac{z^2}{c^2}\right)} \quad (5.13)$$

In this thesis we have adopted the Goldak model (Eq. 5.13) to describe the laser heat source, and we have assumed the eccentricity equal to 1.05.

The last aspect we need to treat is the solid liquid phase change in our simulation framework. In this thesis we have adopted the equivalent heat capacity model described in Section 2.3.3.

### 5.1.6 Mechanical analysis

In this work we face the simulation of parts realized with Ti6Al4V, which is a metal alloy that exhibits a typical thermo-plastic behavior. In the incremental theory of plasticity, when assuming a small strain regime, it is usual to introduce the following additive decomposition:

$$\boldsymbol{\varepsilon} = \boldsymbol{\varepsilon}^e + \boldsymbol{\varepsilon}^p + \boldsymbol{\varepsilon}^T \quad (5.14)$$

where  $\boldsymbol{\varepsilon}$  is the total strain, while  $\boldsymbol{\varepsilon}^e$ ,  $\boldsymbol{\varepsilon}^p$  and  $\boldsymbol{\varepsilon}^T$  are the elastic, plastic and thermal strain components, respectively, defined in Voigt notation as follows.

$$\begin{aligned} \boldsymbol{\varepsilon}^e &= \mathbf{D}^{-1}\boldsymbol{\sigma}, \quad \text{with} \quad \mathbf{D} = -\frac{\nu}{E}(\mathbf{1} \otimes \mathbf{1}) + \frac{1+\nu}{E}\mathbf{I} \\ \boldsymbol{\varepsilon}^p &= \lambda \boldsymbol{\sigma}^{\text{dev}} \\ \boldsymbol{\varepsilon}^T &= \alpha(T - T_0)\mathbf{1} \end{aligned} \quad (5.15)$$

where  $\boldsymbol{\sigma}$  is the stress (expressed in Voigt notation),  $E = E(T)$  is the Young's modulus,  $\nu$  is the Poisson's ratio,  $\alpha = \alpha(T)$  is the thermal expansion coefficient,  $\mathbf{I}$  is the identity,  $\mathbf{1} = \{1, 1, 1, 0, 0, 0\}^T$ , and  $\boldsymbol{\sigma}^{\text{dev}}$  represents the deviatoric part of the stress tensor:

$$\boldsymbol{\sigma}^{\text{dev}} = \boldsymbol{\sigma} - \frac{1}{3}\text{tr}(\boldsymbol{\sigma})\mathbf{1} \quad (5.16)$$

$\lambda$  is the plastic flow factor defined as follows:

$$\begin{aligned} \lambda &= 0 & \text{if } \sigma_{vm} < \sigma_p \\ \lambda &> 0 & \text{if } \sigma_{vm} > \sigma_p \end{aligned} \quad (5.17)$$

where  $\sigma_p = \sigma_p(T)$  is the yield stress and  $\sigma_{vm}$  is the effective Von Mises stress defined as follows:

$$\sigma_{vm} = \sqrt{\frac{3}{2}(\boldsymbol{\sigma}^{\text{dev}})^T \boldsymbol{\sigma}^{\text{dev}}} \quad (5.18)$$

### 5.1.7 Material properties

In this thesis we consider SLMed Ti6Al4v parts. As discussed in Section 2.2, titanium composites are indicated for medical applications due to their bio-compatibility and their good mechanical properties. The melting process significantly affects the physical and the mechanical properties of the re-solidified material.

#### Physical properties of Ti6Al4V

In Table 5.3 we show the temperature dependence of the physical properties of Ti6Al4V powder [Fu and Guo, 2014].

Temperature	<i>Density</i> [Kg/m <sup>3</sup> ]	<i>Specific Heat</i> [J/(Kg · °C)]	<i>Thermal Conductivity</i> [W/(m · °C)]
20	2652	546	0.20
100	2735	562	1.24
500	3150	641	6.43
1000	3670	651	12.91
1600	4189	750	19.40
1650	4189	759	28.30
1660	4189	831	32.10
1900	4189	831	33.50
2800	4189	831	33.50

Table 5.3: Thermal properties of Ti6Al4V powder with increasing temperature.

In Table 5.4 we report the physical properties commons to the material at powder and solid state [Fu and Guo, 2014].

<i>Solidus Temperature</i> ( $T_s$ )	1605 °C
<i>Liquidus Temperature</i> ( $T_l$ )	1650 °C
<i>Latent Heat of fusion</i> ( $L_s$ )	285 kJ/Kg

Table 5.4: Thermal properties of Ti6Al4V powder with increasing temperature.

In Table 5.5 we show the temperature dependence of the physical properties of Ti6Al4V solid alloy [Mills, 2002].

Temperature	<i>Density</i> [Kg/m <sup>3</sup> ]	<i>Specific Heat</i> [J/(Kg · °C)]	<i>Thermal Conductivity</i> [W/(m · °C)]
20	4420	546	7.00
100	4406	562	7.45
500	4350	641	12.60
1000	4282	651	19.30
1600	4198	750	27.00
1650	4189	759	28.40
1660	3920	831	33.40
1900	3750	831	34.60
2800	3138	831	34.60

Table 5.5: Thermal properties of Ti6Al4V solid alloy with increasing temperature.

The last physical parameters needed for the simulation are the emissivity  $\epsilon$  and the absorption coefficient  $\alpha$ . The measurement of the emissivity is affected by a high rate of uncertainty. In this study we assume a constant value of emissivity  $\epsilon = 0.33$  [Hagqvist et al., 2013], both for the powder and for the solid alloy. The absorption coefficient is dependent on the wavelength  $\lambda$  of the laser beam; according to Tolochko et al. [2000], with  $\lambda = 1070\mu m$  (Nd:YAG laser adopted in almost all SLM printers) the absorption coefficient of Ti6Al4V is the same for the material at the powder and at the solid state:  $\alpha = 0.77$ . Finally the heat convection coefficient (or film coefficient) is estimated equal to  $27 W/(m^2C)$ , considering a low flow rate (30 l/h) of Argon in the build chamber.

### Mechanical properties of Ti6Al4V

In Table 5.6 we show the temperature dependence of the mechanical properties of Ti6Al4V solid alloy [Mills, 2002].

Temperature	<i>Young's modulus</i> [GPa]	<i>Yield stress</i> [MPa]	<i>Expansion coefficient</i> [10 <sup>-6</sup> /°C]
25	114	1061	8.2
100	109	934	9.2
200	100	743	9.9
315	93	668	10.5
430	84	616	11.0
540	57	478	11.4
1650	0.1	1	20.1
2800	0.1	1	20.1

Table 5.6: Mechanical properties of Ti6Al4V solid alloy with increasing temperature.

## 5.2 Simulation results

In this Section we use the described simulation framework to reproduce the SLM process of simple geometry components. In the following section, we investigate the effects several printing process on thermal and residual stresses fields, using a fine meshing strategy. In Section 5.2.2, we adopt a coarse meshing strategy to simulate entire SLMed parts.

### 5.2.1 Fine mesh simulations

In Figure 5.9 we show the investigated model and the adopted meshing strategy. The model is a simple square base parallelepiped with base dimensions  $1 \times 1$  mm. The model is constituted of 2 layers of powder of  $50 \mu m$ . We adopt a cubic meshing strategy with element size equal to  $25 \mu m$ , such that the physical layer is represented of two elements in height.

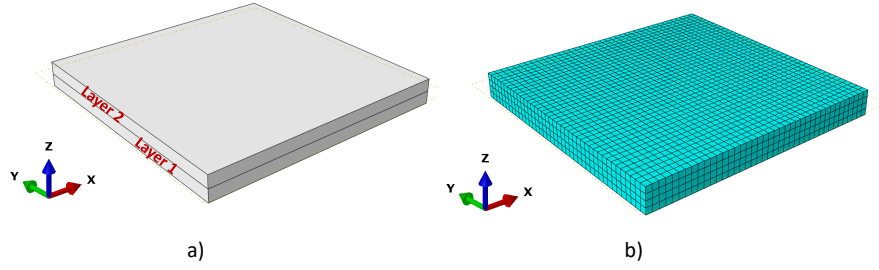


Figure 5.9: Parallelepiped part: a) geometry, b) meshing strategy.

In Fig. 5.10 we show the laser scan path used for each layer. The printing process starts with the external perimeters, then it proceeds with the infill.

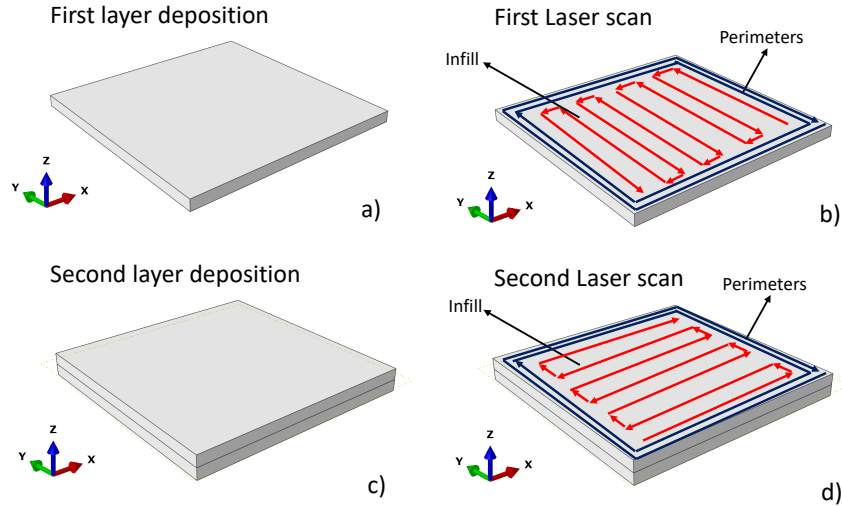


Figure 5.10: Simulation scheme adopted for the parallelepiped model.

In the following sections, we investigate the effects of (i) laser parameters, (ii) scan strategy, and (iii) printer variables on temperature and residual stress fields. In Table 5.7 we report

in detail the values of the investigated parameters, compatible with a commercial 3D metal printer.

	<i>Parameter</i>	<i>Value 1</i>	<i>Value 2</i>	<i>Value 3</i>
<b>L A S E R</b>	<b>Power</b>	100 W	200 W	400 W
	<b>Radius</b>	50 $\mu m$	75 $\mu m$	100 $\mu m$
<b>S C A N</b>	<b>Overlap</b>	20 %	50 %	80 %
	<b>Velocity</b>	2 m/s	4 m/s	6 m/s
<b>P R I N T E R</b>	<b>Build plate tempera- ture</b>	25 °C	200 °C	400 °C
	<b>Chamber tempera- ture</b>	25 °C	200 °C	400 °C

Table 5.7: Adopted simulation parameters for the fine mesh analyses of the parallelepiped geometry.

We investigate the influence of each simulation parameter, assuming for any other parameter the medium value (*Value 2*).

### Power

In Figure 5.11, we show the results of the simulation obtained varying the laser power and keeping all other parameters with *Value 2* (see Table 5.7). In particular we show the temperature distribution at an instant of the laser scan and the residual stresses at the end of the cooling process. In dark red we underline the melt pool generated by the moving heat source. We notice that with a 100 W laser heat source it is not possible to melt the powder on the external perimeters of the part because the temperature does not reach the melting temperature ( $T_m = 1625^\circ\text{C}$ ). Also the residual stress field distribution is significantly affected by the laser power. In particular we notice that with 400 W heat source the residual stresses are higher but also more homogeneous than the stresses obtained with 100 W and 200 W laser powers. This effect can be justified by that with 400 W laser power the bottom layer is partially remelted during the laser scanning of the top layer, moreover melt pool dimensions are higher than the one obtained with other laser powers, therefore, adjacent scanning lines have a higher remelting rate than with other laser powers. The partial remelting of zones of the model can be viewed as a kind of heat treatment that allows to obtain a more homogeneous cooling rate and, in consequence, a more homogeneous stress field distribution.

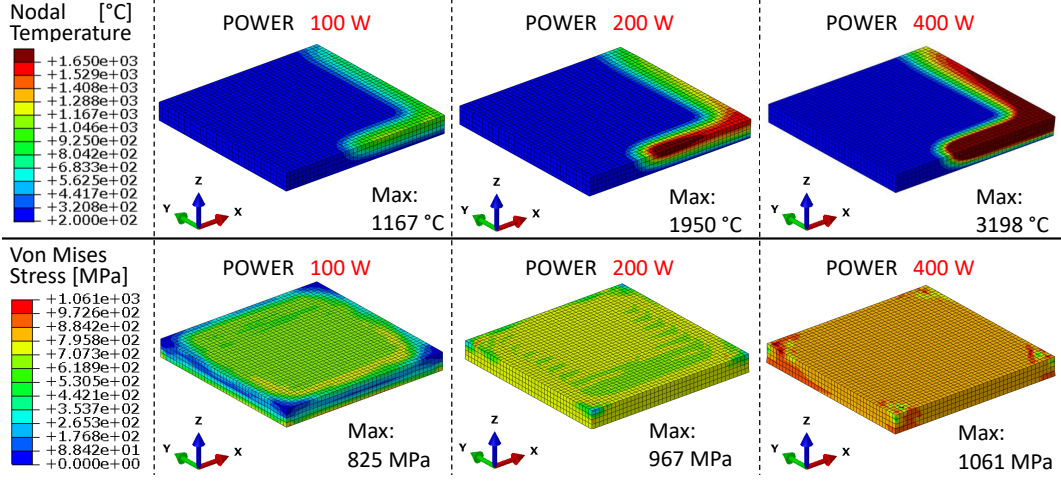


Figure 5.11: Temperature and residual stress distribution obtained with different laser powers.

### Radius

In Figure 5.12, we show the results obtained with different spot radius and keeping all other parameters with *Value 2* (see Table 5.7). In particular we show the temperature distribution at an instant of the laser scan and the residual stresses at the end of the cooling process. In dark red we underline the melt pool generated by the moving heat source. We observe that with  $100\mu m$  spot radius it is not possible to melt the powder on the external perimeters of the part because the temperature does not reach the melting temperature ( $T_m = 1625^\circ C$ ).

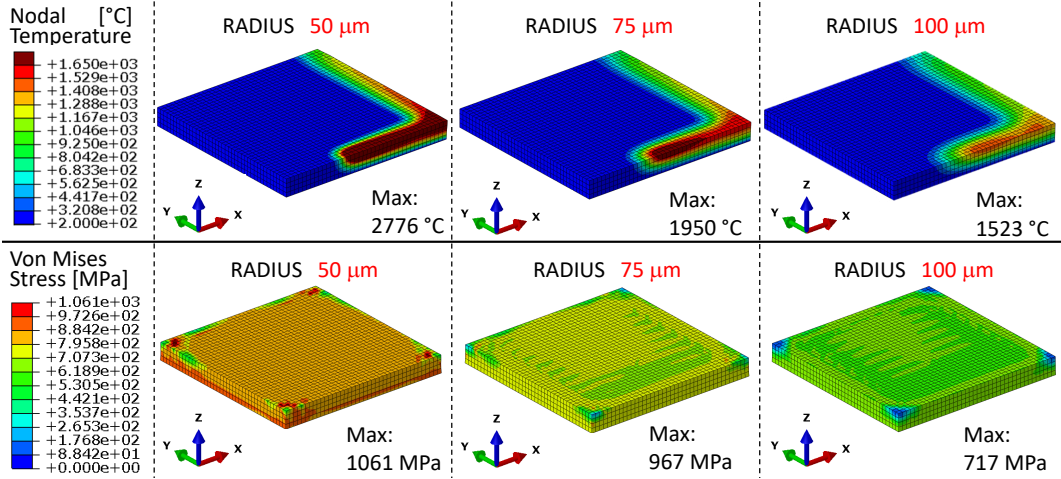


Figure 5.12: Temperature and residual stress distribution obtained with different spot radius.

Looking at residual stresses, we observe that the stress paths obtained with the following laser power and spot sets are very similar:

- 200 W — 50  $\mu m$  (Figure 5.12) and 400 W — 75  $\mu m$  (Figure 5.11)



- 200 W — 100  $\mu\text{m}$  (Figure 5.12) and 100 W — 75  $\mu\text{m}$  (Figure 5.11)

In particular in Figure 5.13 we have displaced the temperature evolution of the point P positioned in the middle of the internal infill. We observe 3 peaks in the temperature field: these peaks are given by the three next-near laser scan lines (Perimeter 1, Perimeter 2, Infill). We appreciate that, with Perimeter 1, the point P comes to liquid state only when the laser power and the laser spot are assumed to be 400 W and 75  $\mu\text{m}$  respectively, instead during the other scan lines point P is melted with both the laser parameters combinations. In this case the adopted overlap rate (50%) among the subsequent scan lines causes the subsequent remelting of the point P.

With this sets of parameters the obtained laser energy density is very similar (10 % difference) and, in consequence, also the temperature evolution of a specific point P is similar. Since residual stresses rise in consequence of the shrinkage induced by the cooling effect, we can state that residual stresses are strictly dependent of the laser energy density.

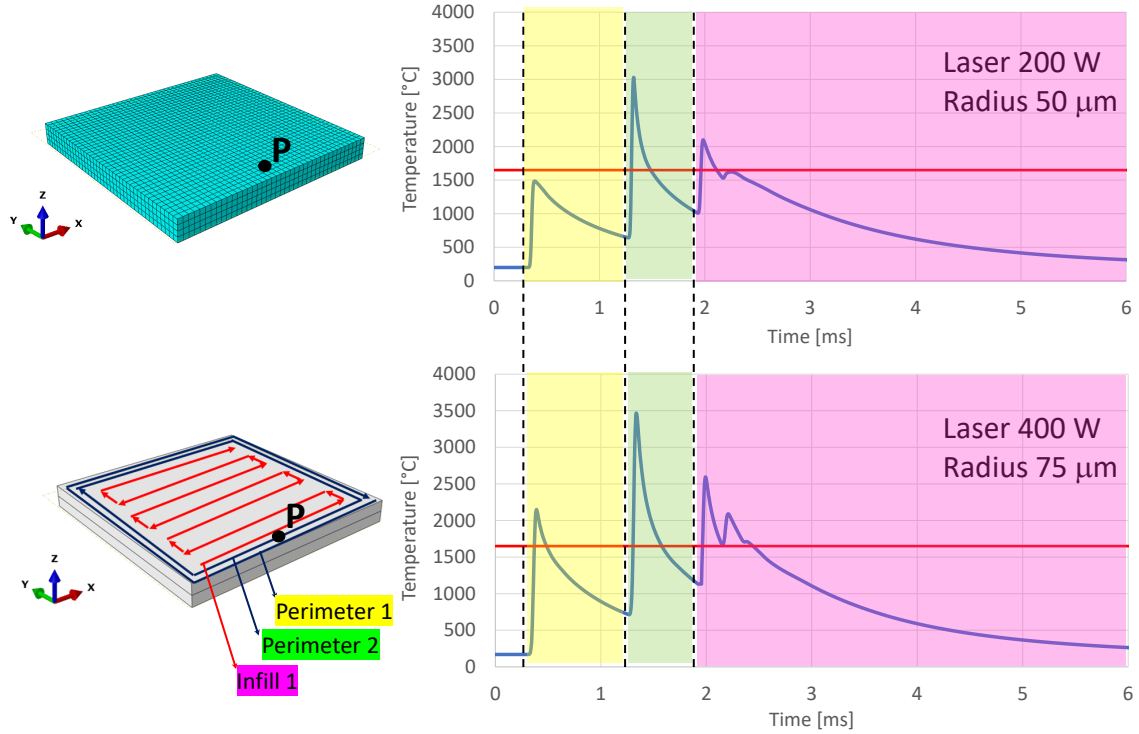


Figure 5.13: Temperature evolution in a specific point of the domain (P), with different laser power and spot.

These results allow to conclude that in order to correctly characterize the SLM process it is convenient to talk about of laser energy density and not of laser power and beam spot independently one of each other. Furthermore we have shown that the higher energy density allows to obtain a more regular residual stress field distribution.

### Overlap

In Figure 5.14, we show the results obtained with different scan velocities and keeping all other parameters with *Value 2* (see Table 5.7). In particular we show the temperature distribution at an instant of the laser scan and the residual stresses at the end of the cooling process. In dark red we underline the melt pool generated by the moving heat source. In this case, we displace the temperature distribution at the start of the infill scan path, thus to investigate the effect of the overlap between adjacent scan lines.

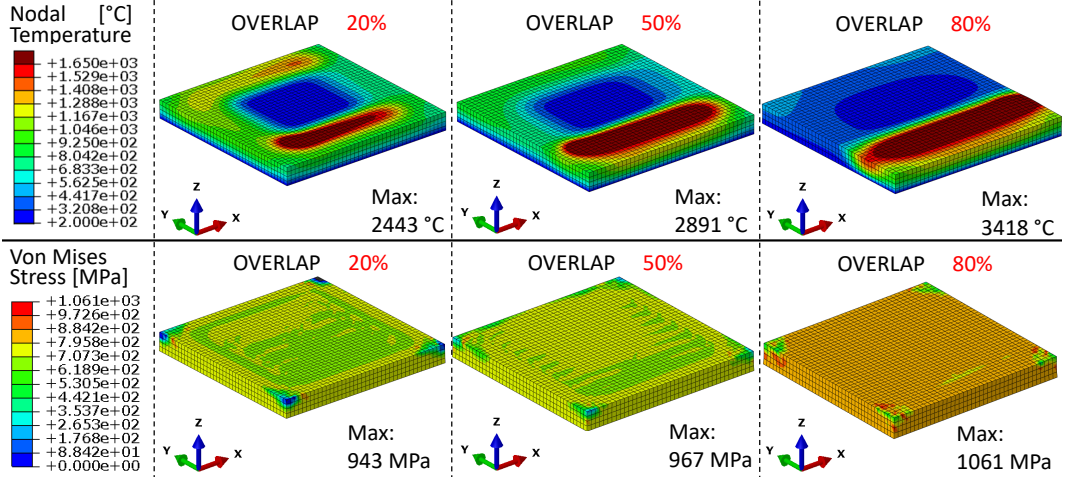


Figure 5.14: Temperature and residual stress distribution obtained with different scan overlaps among adjacent scan lines.

We observe that the overlap among adjacent scan lines significantly affects the temperature, the dimensions and the shape of the melt pool. In particular with a higher overlap we observe that melt pool dimensions increase, but at the same time, melt pool has not the typical comet's tail shape, but it is more similar to a rectangle with rounded angles. Also the melt pool temperature is significantly affected by the overlap choice and, of course, higher overlap rate leads to higher vacuum temperatures. Looking at the residual stress path distribution, we appreciate that a higher overlap allows to obtain a more regular stress distribution, but, at the same time, the values of the stresses are higher due to the higher thermal gradients rising during the melting process.

In particular, in Figure 5.15 we show the temperature evolution of point P adopting two different overlap rates. We observe that the overlap has (of course) a significant impact after the first laser scan path. With 50% overlap rate, higher temperatures are reached due to scan lines Perimeter 2 and Infill 1. Instead with a 20% overlap rate, lower temperatures are reached during the scanning process and, in specific, the melting process takes place only during the scan line Perimeter 2.

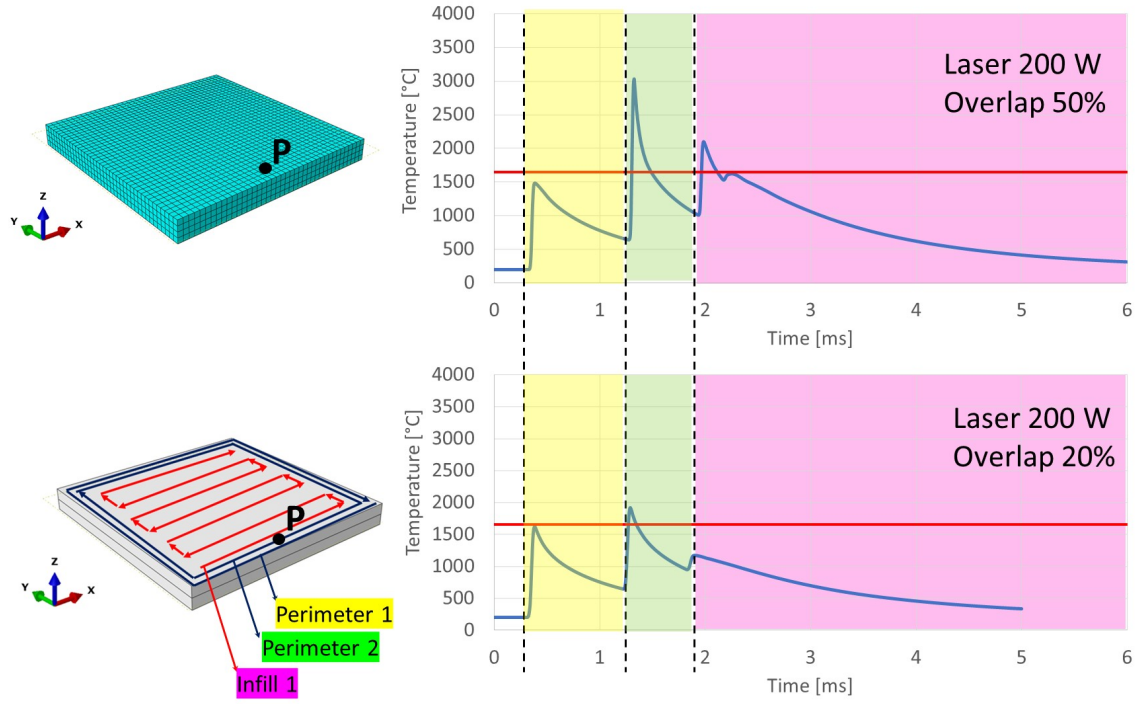


Figure 5.15: Temperature evolution in a specific point of the domain (P), with different overlap ratio.

## Velocity

In Figure 5.16, we show the results obtained with different scan velocities and keeping all other parameters with *Value 2* (see Table 5.7). In particular we show the temperature distribution at an instant of the laser scan and the residual stresses at the end of the cooling process. In dark red we underline the melt pool generated by the moving heat source. We observe that with scan velocity 6 m/s it is not possible to melt the powder on the external perimeters of the part because the temperature does not reach the melting temperature ( $T_m = 1625^\circ\text{C}$ ). Furthermore we can appreciate that reducing the scan velocity the laser heat source stands for more time on the same zone of the model and, therefore, melt pool dimensions extends.

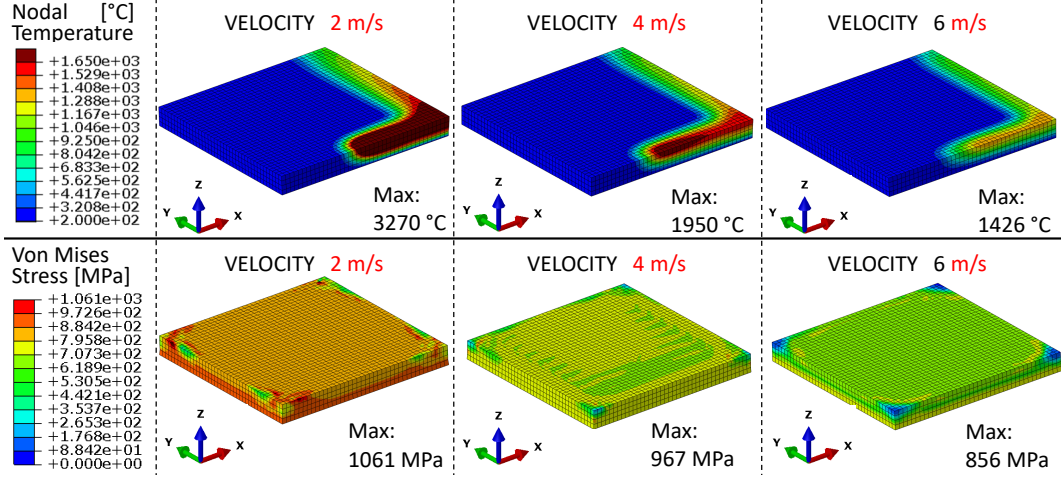


Figure 5.16: Temperature and residual stress distribution obtained with different scan velocities.

The scan velocity influences the energy rate: a lower scan velocity increases the energy rate and, in consequence, the thermal gradients generated during the melting process. We observe that higher energy rate produces higher residual stresses on the part after the cooling process. Finally we can conclude that increasing the scan velocity is a good strategy to speed up the printing process, provided that the adopted velocity is able to assure enough energy rate to perform the melting process.

### Build Plate temperature

In Figure 5.17, we show the results obtained with different building plate temperatures and keeping all other parameters with *Value 2* (see Table 5.7). In particular we show the temperature distribution at an instant of the laser scan and the residual stresses at the end of the cooling process. In dark red we underline the melt pool generated by the moving heat source. We observe that the building plate temperature has a significant impact on the temperature field results; in fact, since the part is very thin, it assumes the temperature of the building plate and it is not much influenced by the ambient temperature.

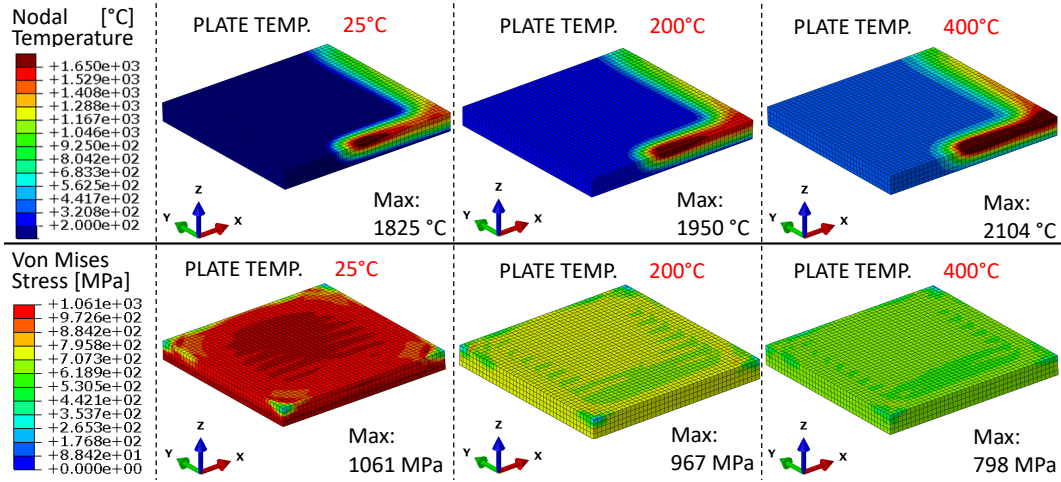


Figure 5.17: Temperature and residual stress distribution obtained with different building plate temperatures.

On the contrary, looking at residual stresses, we observe that there is significant difference among the three cases. In particular we notice that, at the end of the cooling process, the part printed with the building plate at the ambient temperature (25 °C) is almost completely yielded, while when the building plate is maintained at 400 °C, no yielding appears on the part.

### Chamber temperature

In Figure 5.18, we show the results obtained with different chamber temperatures and keeping all other parameters with *Value 2* (see Table 5.7). In particular we show the temperature distribution at an instant of the laser scan and the residual stresses at the end of the cooling process. In dark red we underline the melt pool generated by the moving heat source.

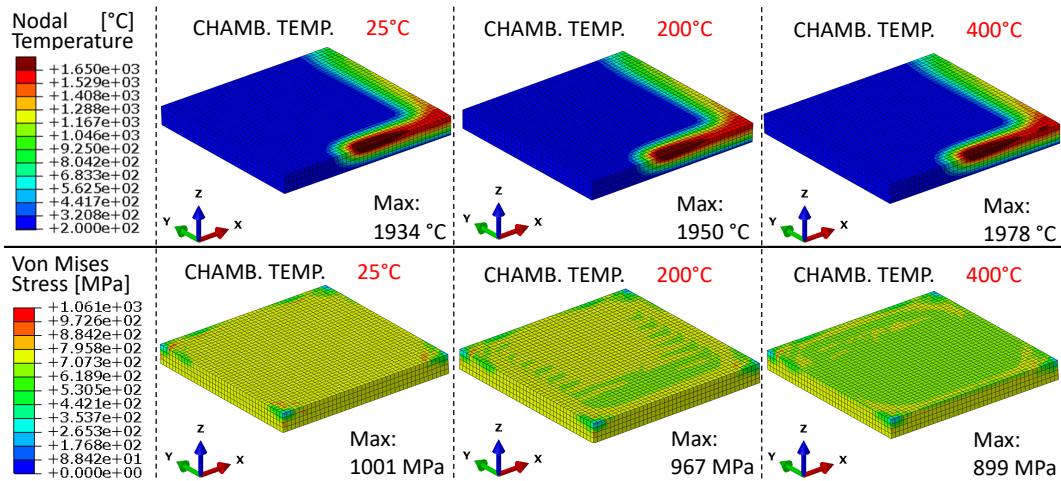


Figure 5.18: Temperature and residual stress distribution obtained with different chamber temperatures.

We observe that the ambient temperature has not a significant impact on the temperature field results; in fact, since the part is very thin, its temperature is almost equal to the building plate temperature (200 °C). Looking at the residual stresses, we observe that the stress field distributions are almost the same among the three cases. This fact is completely justified by the similar melt pool dimensions and maximum temperatures reached during the melting process.

Finally, the results obtained in this section and in the previous section, confirm that in models with a very small height (lower than 1 mm), the build plate temperature influences the residual stress field distribution much more than the chamber temperature. In particular, a high build plate temperature allows to significantly reduce residual stresses after the cooling process.

## Conclusions

In this Section we have analyzed the effects of SLM process parameters variation on the temperature and the residual stresses distribution on a small Ti6Al4V part. According to this results, we can conclude that *laser* and *scan* parameters effects must be evaluated in terms of the energy density rate dispensed during the SLM process. In general, we have demonstrated that with higher energy density rate, melt pool dimensions increase as well as melt pool temperature. This condition leads to the formation of higher residual stresses, but, also, of a more uniform stress path distribution.

On the other hand, the *printer* parameters effects must be considered in relation with the adopted geometry. In particular we have proved that in very thin geometries, residual stress after the cooling process are influenced by the build plate temperature much more than by the chamber temperature. Higher build plate and chamber temperatures allow to obtain lower values of residual stresses after the cooling process, due to the lower thermal gradients rising during the process.

### 5.2.2 Coarse mesh simulations

In Fig. 5.19 we show the investigated geometry. The model represents a simple bridge which is a classical benchmark test in AM prototyping. Bridge dimensions are typical of a part produced with a commercial AM printer. The part is produced with 100  $\mu\text{m}$  layers of Ti6Al4V powder.

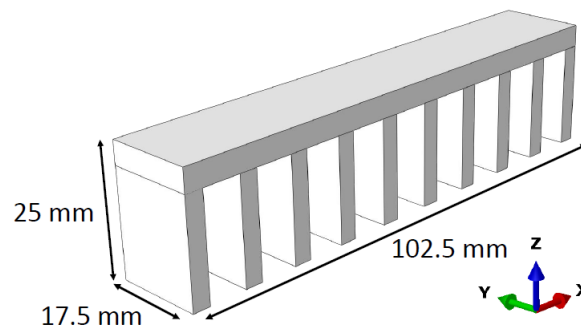


Figure 5.19: Bridge like model.



To simulate the part following correctly the printing process would mean to adopt, at least, cubic elements with size  $100\ \mu\text{m}$ . With this meshing criterion we would obtain more than 2 million elements and the computational costs would exponentially grow. For this reason we adopt a coarse meshing strategy. In specific we assume the element height equal to 0.8 mm; in such way each layer of elements represents 8 physical layers.

In Figure 5.20 we show the laser path adopted for the pillars and the deck of the bridge. We remark that the real SLS process of the bridge requires support structure among the pillars. In this example, we neglect the support structures, but we apply proper boundary conditions to simulate the clamping effect of the support structures on the bridge.

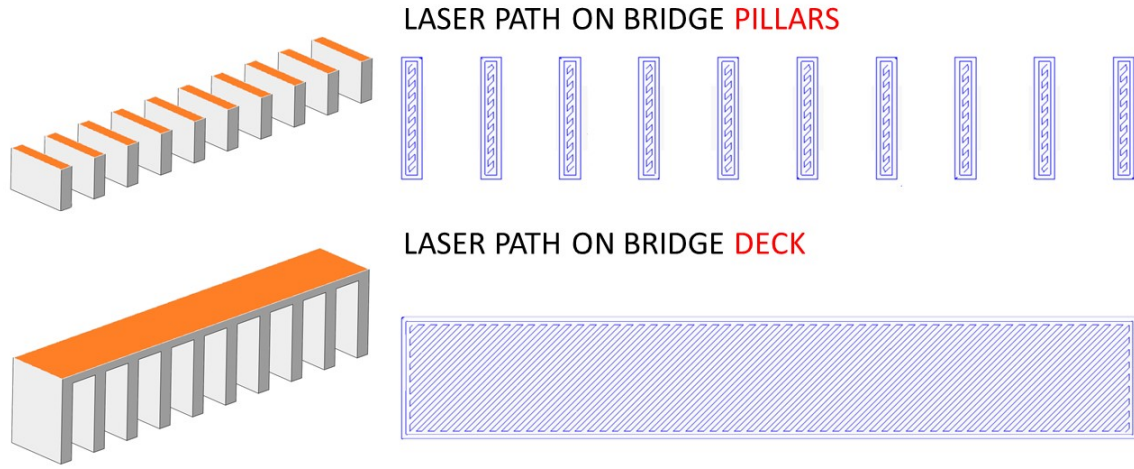


Figure 5.20: Adopted laser paths for the pillars and deck of the bridge (schematic).

In this example the laser power has been assumed equal to 400 W and the laser spot equal to  $75\ \mu\text{m}$ .

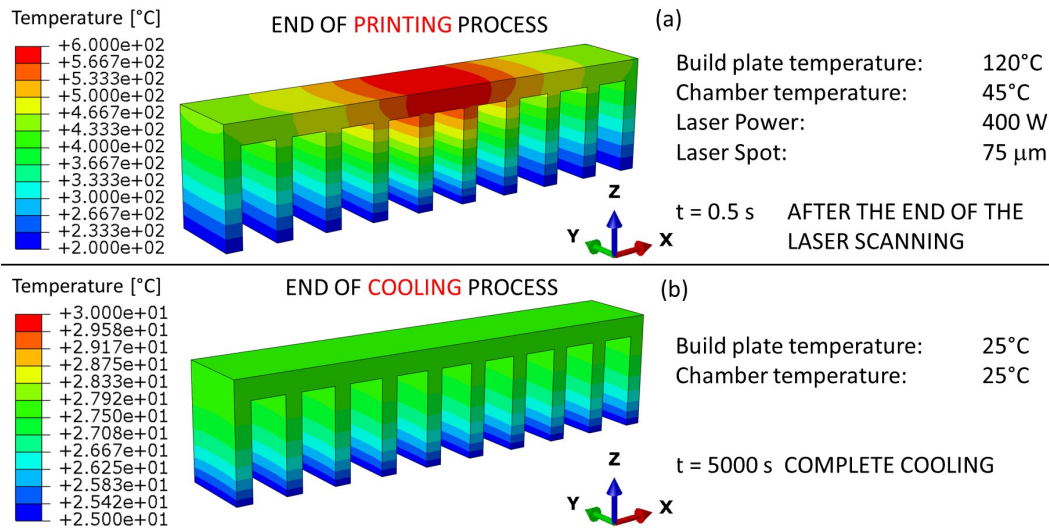


Figure 5.21: Temperature field distribution at the end of the printing process (a) and after the cooling process (b).

In Figure 5.21 we show the temperature fields at the end of the printing process (a) (0.5 s after the laser power has been shut down) and after the cooling process (b). The cooling process has been simulated adopting the cooling curve of a commercial 3D printer; in this case the part reaches the ambient temperature almost after 5000 s.

In Figure 5.22, we show the stress field at the end of the printing process (a) (0.5 s after the laser power has been shut down) and after the cooling process (b).

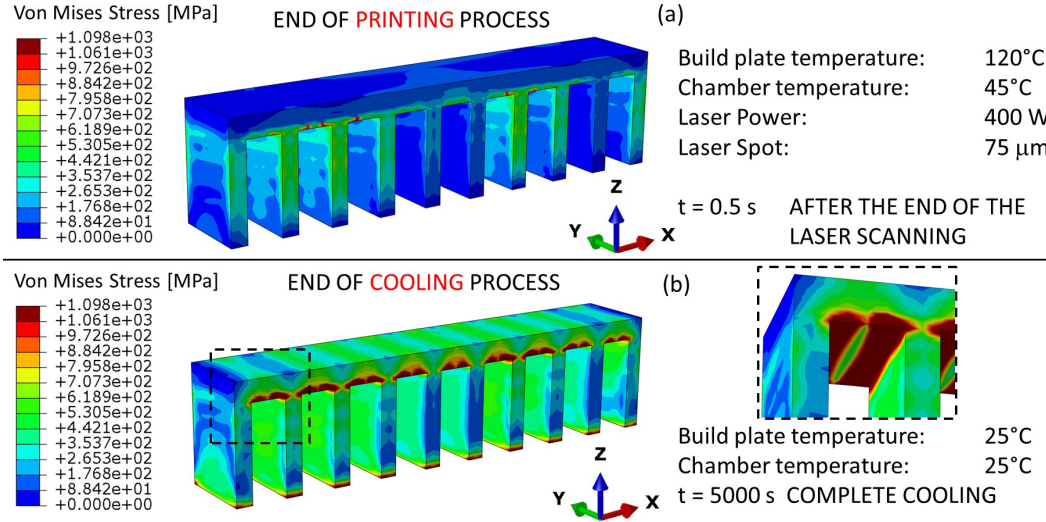


Figure 5.22: Stress field distribution at the end of the printing process (a) and after the cooling process (b).

We can appreciate how the cooling process leads to a significant increase of the residual stresses, due to the shrinkage effect. In addition, we observe that the highest residual stresses are concentrated in correspondence of the clamps imposed on the model, on the bottom of the pillars and on the bottom of the deck between the pillars.

The real detaching process of a SLMed part from the building plate is physically performed removing the support structures. In this work, since we have not simulated the support structures, we remove the constraints applied to the bridge except on the bottom of one pillar. In Figure 5.23 we show the constraints applied on the structure for the printing process simulation (a) and the constraints adopted to simulate the part detachment process (b).

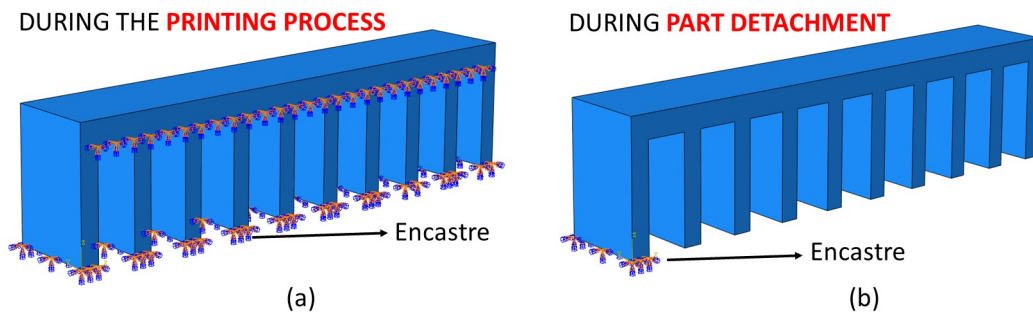


Figure 5.23: Constraints adopted to simulate support structures during the printing process (a) and during the part detachment process (b).



In Figure 5.24 we display the stress path at the end of the cooling process and after the detachment process. We observe that the maximum stress is consistently reduced after the detaching of the bridge from the building plate. The stress relief is given by the release of the elastic energy.

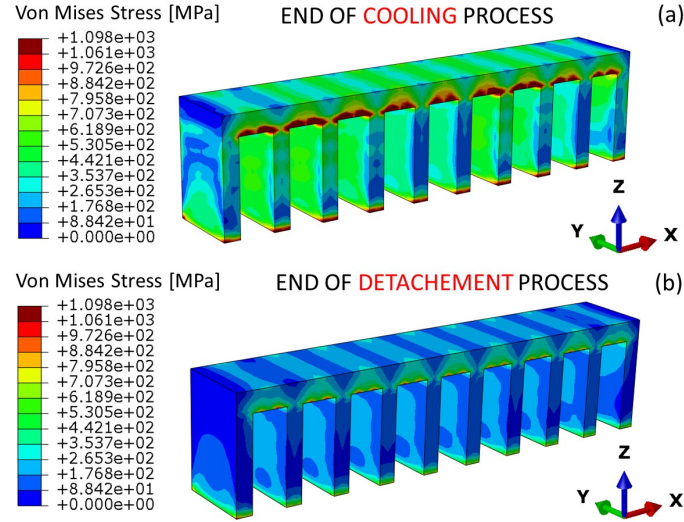


Figure 5.24: Stress field distribution at the end of the cooling process (a) and after the detachment process (b).

In Figure 5.25 we show the Z-axis displacements at the end of the cooling process and after the part detachment from the building plate.

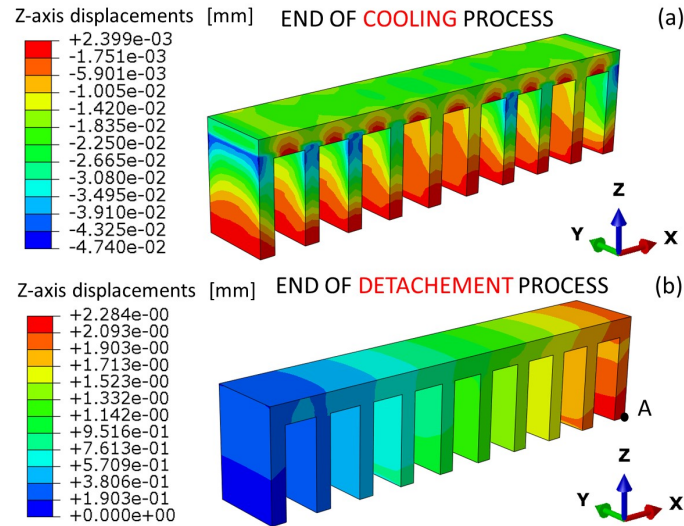


Figure 5.25: Z-axis displacement field at the end of the cooling process (a) and after the detachment process (b).

The maximum Z-axis displacement is about 2.3 mm in correspondence of point A.

## Chapter 6

# Fused Deposition Modeling

Fusion Deposition Modeling (FDM), also known as Fused filament fabrication (FFF) is a AM technology patented by Stratasy in 1992 to realized plastic parts starting from a plastic solid filament. Figure 6.1 shows the working principle of a generic FDM machine.

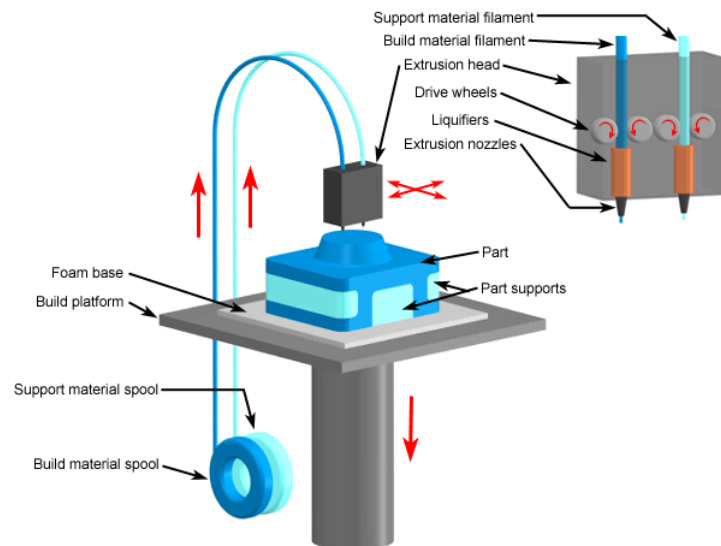


Figure 6.1: Working scheme of a generic Fused Deposition Modeling printer.

The FDM printing process can be summarized in the following steps:

- I. **Filament Supply:** a spool of filament is positioned on a particular support and the filament is inserted in the extrusion head;
- II. **Filament Extrusion:** the filament is moved by drive wheels into the nozzle, then it is heated until it reaches the semi-molten state and extruded with the desired shape and dimensions;
- III. **Filament Deposition:** the filament is deposited layer by layer on the building plate by the nozzle which moves on the building plate at a constant height;

- IV. **Nozzle Upward Movement:** when a layer is constructed, the nozzle moves upward of an height corresponding to the physical layer height and the process restarts from step III;
- V. **Part Removal:** once the part reaches the ambient temperature it is possible to remove it from the building plate.

## 6.1 Process parameters of Fused Deposition Modeling printers

FDM patent expired in 2012. From that time, a lot of companies producing FDM 3D printers born and the cost of FDM machines consistently decreased. Among the others the leading companies in this sector are: Stratasys, 3DSystems, HP. The most important characteristics of commercial FDM printers are listed below:

- **Extrusion dimensions:** common nozzles usually extrude the filament with an ellipsoidal shape. Bead height dimensions range from 0.1 to 1 mm, bead width can vary from 0.1 to 2 mm. Lower bead dimensions allow to obtain a higher detail precision during the print, although, the printing process becomes slower;
- **Maximum extruder temperature:** extrusion temperature usually ranges from 200°C to 600°C. Higher extrusion temperature allow to treat a larger range of polymers;
- **Number of the nozzles:** desktop printers have just one nozzle, professional printers, instead, adopt multiple nozzles to change material during the same printing process and allow a faster part production;
- **Working volume:** this is a fixed characteristic of each printer. A higher working volume allows to produce larger models. The dimensions can vary from 10 centimeters up to 3 or 4 meters.
- **Chamber temperature:** in desktop printers the chamber temperature is the ambient temperature, in professional 3D printers, the chamber temperature can be increased up to 150-200°C; this solution is adopted to reduce residual stresses arising during the printing process.
- **Building plate temperature:** in desktop printers the building plate temperature is kept at ambient temperature, in professional 3D printers, the building plate temperature can be increased up to 250°C; this solution is adopted to increase the adhesion force between the building plate and the part.

## 6.2 Polymers used in Fused Deposition Modeling

In the last years many types of polymers have been adopted to produce FDM parts, and many experimentations have been conducted to test parts produced with FDM.

The most common polymers adopted for in FDM printing are:

- **Acrylonitrile Butadiene Styrene (ABS)**: can be used to produce prototypes for design verification and functional performance testing. It's main features are good strength and tenacity at low temperatures, good electrical resistance and good shock resistance. The mechanical properties of a commercial ABS filament, at the ambient temperature, are listed in Table 6.1. Data are distributed by Stratasys®.

<i>Mechanical Property</i>	Value
Young's Modulus	2600-3000 [MPa]
Tensile Yield Strength	55-60 [MPa]
Flexural Modulus	1700-2200 [MPa]
Flexural Strength	65-75 [MPa]
Elongation at break	25-40% [MPa]

Table 6.1: Mechanical properties of a commercial ABS filament.

- **PolyCarbonite (PC)**: can be used for several applications in industry including: external aircraft windows, flak jackets and safety protections. It's main features are high resistance to chemically aggressive environments, good mechanical properties at high temperatures and high toughness. The mechanical properties of a commercial PC filament, at the ambient temperature, are listed in Table 6.2. Data are distributed by Stratasys®.

<i>Mechanical Property</i>	Value
Young's Modulus	1944-1958 [MPa]
Tensile Yield Strength	30-40 [MPa]
Flexural Modulus	1800-2006 [MPa]
Flexural Strength	68-89 [MPa]
Elongation at break	4.8-2.5%

Table 6.2: Mechanical properties of a commercial PC filament.

- **PolyLactic Acid (PLA)**: can be used for several applications in industry including: plastic shopping bags and part of domestic appliances, but it is suitable to produce functional components. It's main features are good tensile resistance and ease processing in injection and fused deposition modeling. The mechanical properties of a commercial PLA filament, at the ambient temperature, are listed in Table 6.3. Data are distributed by Stratasys®.

<i>Mechanical Property</i>	Value
Young's Modulus	2539-3039 [MPa]
Tensile Yield Strength	26-45 [MPa]
Flexural Modulus	2470-2930 [MPa]
Flexural Strength	45-84 [MPa]
Elongation at break	1-2.5%

Table 6.3: Mechanical properties of a commercial PLA filament.

- **ULTEM**: can be used for many applications in medical, electronic/electric, microwave, automotive, and aircraft industries. It's main features are a high tensile resistance at ambient temperature and good tensile resistance at high temperatures, high dielectric strength and stability, and a very high heat resistance. The mechanical properties of a commercial ULTEM filament, at the ambient temperature, are listed in Table 6.4. Data are distributed by Stratasys®.

<i>Mechanical Property</i>	Value
Young's Modulus	2150-2270 [MPa]
Tensile Yield Strength	47-33 [MPa]
Flexural Modulus	2050-2300 [MPa]
Flexural Strength	68-112 [MPa]
Elongation at break	2.2-5.8%

Table 6.4: Mechanical properties of a commercial ULTEM filament.

- **PolyEtherEtherKetone (PEEK)**: can be used for many applications in medical, electronic/electrical, microwave, automotive, and aircraft industries. It's main features are a high tensile resistance at ambient temperature and high ductility rate, moreover, it is resistant to aggressive environments. The mechanical properties of a commercial PEEK filament, at the ambient temperature are listed in Table 6.5. Data are distributed by Victrex®.

<i>Mechanical Property</i>	Value
Young's Modulus	4000 [MPa]
Tensile Yield Strength	98 [MPa]
Flexural Modulus	3800 [MPa]
Flexural Strength	125 [MPa]
Elongation at break	45%

Table 6.5: Mechanical properties of a commercial PEEK filament.

In literature, several studies have been proposed aiming to characterize the mechanical

properties dependence on the process parameters and to compare the characteristic of 3D printed parts with the characteristics of parts produced with traditional manufacturing.

Several studies have been conducted to estimate the mechanical properties of FDMed parts produced with different different printing parameters.

One of the most investigated parameters is the infill raster angle. Ziemian et al. [2012] investigated the effects of different raster orientations on tensile and ultimate yield strength, concluding that the maximum values are obtained with 0/90 and 45/45 raster angles, both with tensile and flexural tests. Cantrell et al. [2017] carried out analogous experiments on PC FDMed components, concluding that tensile strength is not significantly influenced by the raster orientation, while the maximum shear strength is obtained with +45/-45 raster orientation (Figure 6.2)

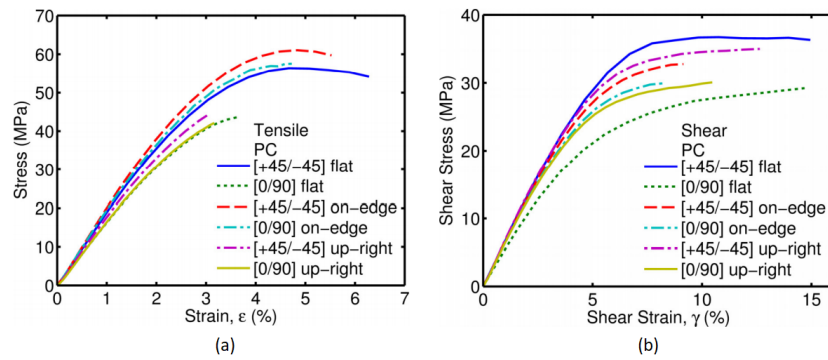


Figure 6.2: Tensile (a) and shear (b) stress-strain curves of FDMed PC parts produced with different raster orientations [Cantrell et al., 2017].

Letcher and Waytashek [2014] demonstrated that the raster orientation has a significant influence on PLA specimens response to 3-points bending test, where the 0° raster orientation allows to obtain the higher flexural strength. A similar result has been obtained by Rahman et al. [2015] for FDMed PEEK components.

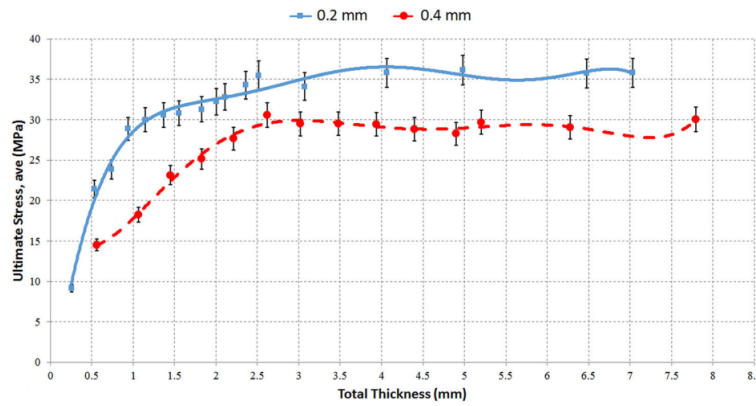


Figure 6.3: Ultimate tensile stress variation with the total part thickness. Different layer thickness are considered [Rankouhi et al., 2016].

Another parameter that have been widely investigated in literature is the layer thickness.

Rankouhi et al. [2016] proved that ABS parts produced with a layer thickness of 0.2 mm show a higher ultimate tensile strength and stiffness in comparison with parts realized with layer thickness equal to 0.4 mm (Figure 6.3).

As previously discussed, some industrial applications require good mechanical properties of plastic parts even at extreme temperatures. Many studies focused on the evaluation of the mechanical properties of FDMed parts in extreme environmental conditions. Weiss et al. [2015] conducted a very accurate study to evaluate both thermal and mechanical properties of FDMed ABS specimens at cryogenic temperatures (Figure 6.4).

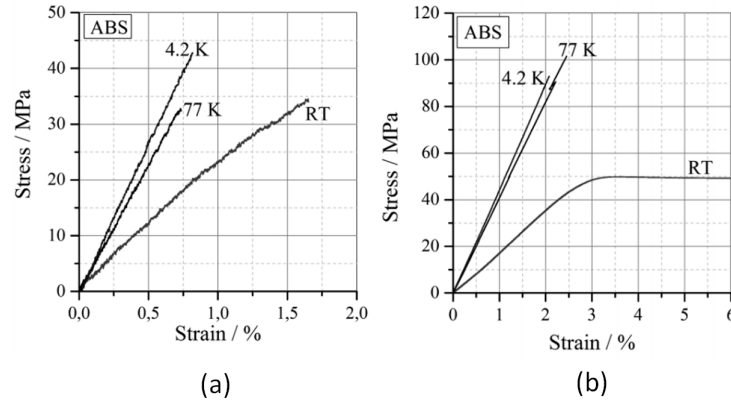


Figure 6.4: Tensile stress (a) and compressive stress (b) strain curves of FDMed ABS parts at different cryogenic temperatures [Weiss et al., 2015].

Another parameter which is often investigated in FDM printing process is the build direction of the parts. Bagsik et al. [2010] studied the stress strain curves obtained through tensile tests on FDMed ULTEM parts.

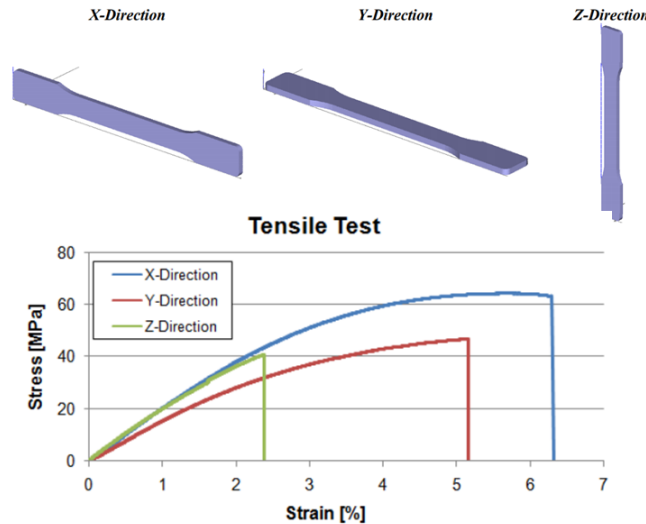


Figure 6.5: Stress strain curves obtained through tensile tests on FDMed ULTEM parts produced with different build orientations [Bagsik et al., 2010].

They concluded that the build orientation has a great impact on the mechanical properties of the part, in particular on the Young's Modulus and on the elongation at break (Figure 6.5).

### 6.3 Physical aspects of Fused Deposition Modeling

Within FDM technology, the filament is first heated to a semi-molten state and then extruded, while the nozzle moves following a predefined printing path. After deposition, the thermal energy is dissipated through conduction (within and between the filaments) as well as convection and radiation (both between the filament and the external environment). The heating and the subsequent cooling processes, leading the semi-molten filament to re-assume a solid state, are characterized by high thermal gradients inducing residual stresses on the printed component [Zein et al., 2002]. These stresses produce part distortions, either during the printing process itself and after the component removal from the building plate [Bellehumeur et al., 2004]. Figure 6.6 shows the most important aspects influencing the fused deposition modeling process:

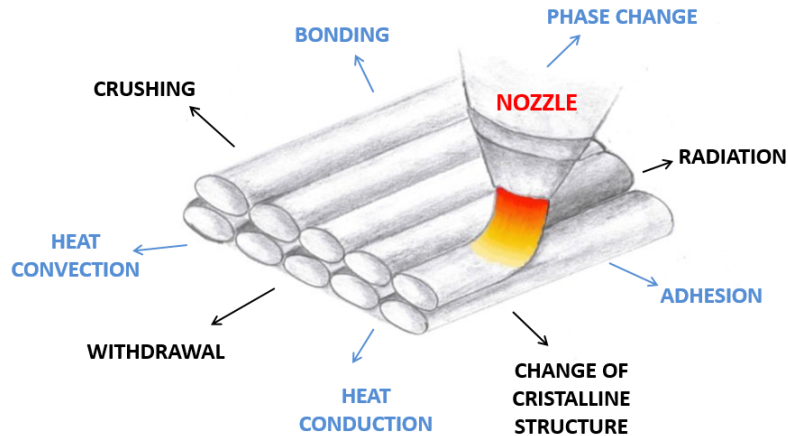


Figure 6.6: Physical phenomena rising during the Fused Deposition Modeling process. In light blue the principal physical effects; in black the secondary physical effects.

Thermal gradients strongly influence the quality of the produced parts together with other several printing parameters, like extrusion temperature, chamber temperature, nozzle velocity, and extruded filament dimensions. Most important, it has been experimentally proved that such parameters can affect not only the shape [Wittbrodt and Pearce, 2015] and the dimensions [Lieneke et al., 2016] of the printed part, but also its mechanical properties [Ziemian et al., 2012], including the yielding strength and the strain at failure [Alaimo et al., 2017].

In the following section we will describe the principal physical phenomena involved in FDM process.

#### 6.3.1 Heat conduction-convection-radiation

Differently from PBF process, in FDM the material is deposited on the building plate at a high temperature corresponding to the extrusion temperature. When the filament is extruded



it starts a cooling process which leads the filament to the solid state. During this process the filament exchanges heat through:

- **conduction** due to the temperature gradient rising inside the filament;
- **convection** between the filament and the surrounding environment;
- **radiation** of the thermal energy

Heat conduction-convection-radiation can be described by the following equation:

$$\rho c \frac{T}{t} = \nabla \cdot (k \nabla T) + q_c + q_r \quad (6.1)$$

where  $q_c$  represents the convective term and  $q_r$  represents the radiation term, which are described as follows:

$$\begin{aligned} q_c &= h(T - T_c) \\ q_r &= K_b(T^4 - T_c^4)\epsilon \end{aligned} \quad (6.2)$$

in which  $K_b$  is the Stefan-Boltzmann constant and  $\epsilon$  is the emissivity.

### 6.3.2 Phase Change

The phase change in plastic polymers is a very complicated process that is dependent on the molecular structure of the material [Tadokoro, 1979]. According to their molecular structure, plastic polymers can be divided into two classes:

- **Crystalline polymers:** characterized by a regular and periodic molecular structure at the solid state;
- **Amorphous polymers:** characterized by an irregular molecular structure at the solid state;

The degree of crystalline order, usually referred to as  $\chi$ , states if a polymer has a *crystalline* ( $\chi \approx 1$ ) or an *amorphous* ( $\chi \approx 0$ ) molecular structure. Crystalline polymers are characterized by higher density and higher stiffness than amorphous polymers; moreover, crystalline polymers can be oriented in space in order to obtain specific mechanical properties in a specific direction. This procedure gives to crystalline polymers a high rate of anisotropy.

In plastic polymers two types of phase change may occur, according to the molecular structure of the polymers:

- **Melting.** It is a typical process of crystalline polymers that occurs when, at a certain temperature, called *melting* temperature  $T_m$ , the ordered molecular chains drop into a liquid disordered state. In this process a large amount of energy is needed to win the internal forces which order the molecular structure. This process is the same that occurs in metal phase change;

- **Glass transition.** It is a typical process of amorphous polymers in which the temperature increasing simply increase the molecular disorder. This process is characterized by a typical temperature referred as *glass transition*  $T_g$ . Below the glass transition temperature, the amorphous polymers have a *glassy* behavior; over the glass transition temperature, they show a *rubbery* behavior.

In figure 6.7 we show the different phase change processes for crystalline and amorphous polymers.

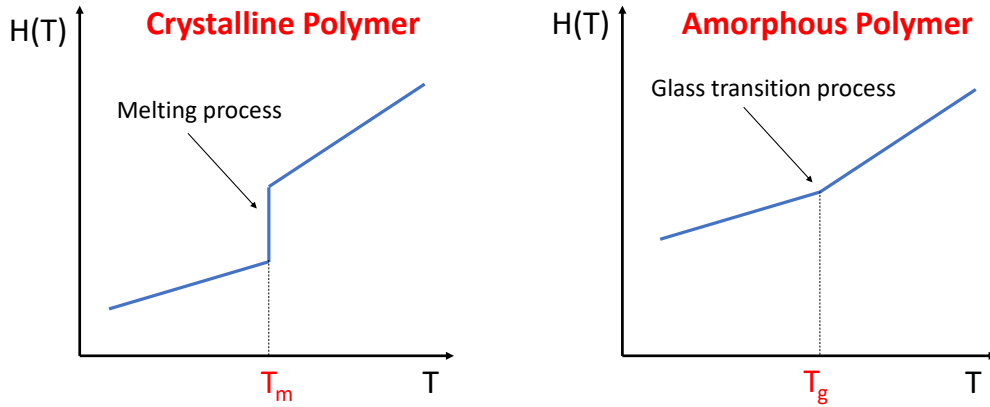


Figure 6.7: On the left, the melting process typical of crystalline polymers; on the right, the glass transition process typical of amorphous polymers.

We observe that, differently from the melting process, in glass transition process no latent heat is needed to perform the phase change.

### 6.3.3 Bonding

Bonding is the tendency of semi-molten fibers to get in contact one to each other due to the cohesion force rising between them at high temperatures. Bonding is a very important phenomenon in FDM printing process because a good bonding rate between the deposited filaments is mandatory to obtain good mechanical properties on the final parts [Gurralla and Regalla, 2014].

In FDM technology we can discern between two types of bonding:

- **Intra-layer bonding:** generated between the deposited filaments of the same layer (see Figure 6.8). The intra-layer bonding forms a typical *neck* between the bounded filaments and the resulting dimensions of the bounded filaments are smaller than the nominal ones.
- **Inter-layer bonding:** generated between subsequent deposited layers (see Figure 6.9). The inter-layer bonding forms a typical *neck* between the filaments of adjacent layers, therefore the height of a package of two layers is smaller than the nominal one.

Bellehumeur et al. [2004] pointed out that *the bonding quality among polymer filaments in the FDM process determines the integrity and mechanical properties of resultant prototypes* and they developed a Newtonian sintering model to quantitatively predict the bonding quality

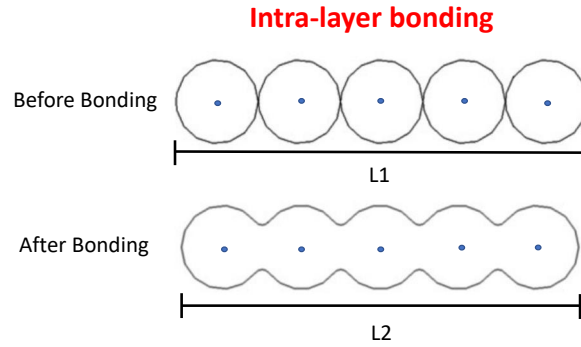


Figure 6.8: Intra-layer bonding in FDM printing process (rielaborated from [Gurralla and Regalla, 2014]).

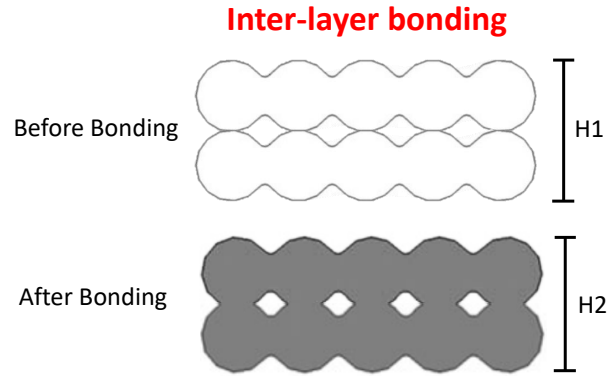


Figure 6.9: Inter-layer bonding in FDM printing process (rielaborated from [Gurralla and Regalla, 2014]).

of the part. They concluded that the bonding rate between the filaments is strongly dependent on chamber temperature and on cooling time of the deposited filaments. Figure 6.10 (a) shows the variation of neck radius with the time in isothermal conditions, obtained with different extrusion temperatures. Figure 6.10 (b) shows the variation of the neck radius with the time in non isothermal conditions. In both cases the experimental results are compared with the predictions of the Newtonian sintering model, showing a good agreement between the experimental results and the analytic model.

#### 6.3.4 Adhesion

Adhesion is a chemical-physical phenomenon rising between two chemically different materials. In FDM printing, the adhesion force origins between the building plate (which is usually made with Ultem) and the deposited filaments. The development of enough adhesion force is mandatory to maintain the part attached to the building plate. In Figure 6.11 we represent a typical case of part detachment from the building plate.

A common and well known solution to avoid part detachments from the building plate consists of increasing the build plate temperature, but, this solution can be adopted only in

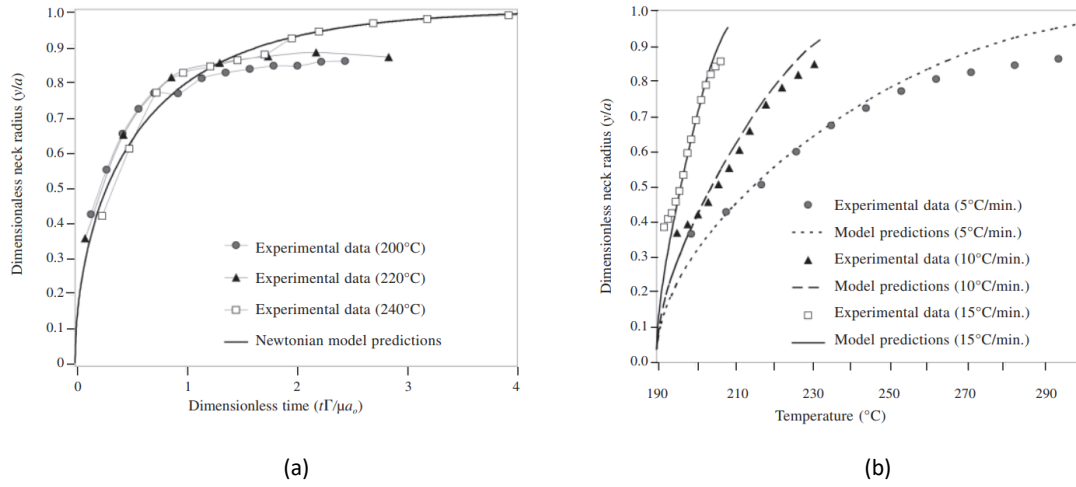


Figure 6.10: Variation of the radius deck in isothermal (a) and in non-isothermal (b) conditions [Bellehumeur et al., 2004].

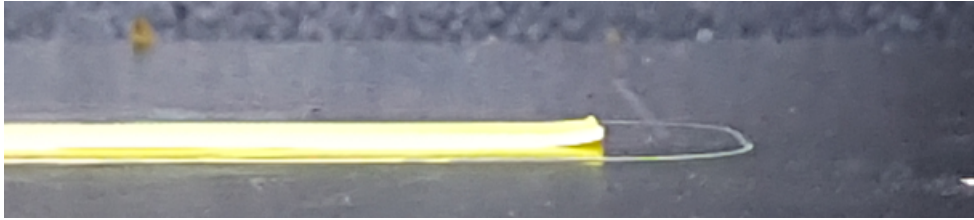


Figure 6.11: Part detachment from the building plate during FDM printing process. Detachment occurs due to the not enough adhesion force.

certain professional 3D printers. Another possible way to solve the problem is to spray special lacquers on the building plate to increase artificially the adhesion force.

In literature the adhesion in FDM process has been investigated by few authors, in particular in combination with textiles.

Pei et al. [2015] investigated the adhesion of ABS, Nylon, and PLA FDMed parts, printed directly onto textiles. Natural (cotton and wool) plastic (light polyester) textile have been considered in this study, concluding that PLA has the overall best adhesion.

A similar study was conducted by Sabantina et al. [2015] who used a high temperature after treatment to increase the adhesion force between PLA and the considered textile. This studies proposes interesting experiments with different textiles and FDM printing parameters, although they do not evaluate directly the adhesion force.

Sanatgar et al. [2017] adopted the standard SS-EN ISO11339:2010 procedure to evaluate the adhesion force of PLA and nano-composites parts during FDM printing process. They concluded that the adhesion force is highly influenced by the printing process parameters like the extrusion temperature and the build plate temperature as shown in Figure 6.12.

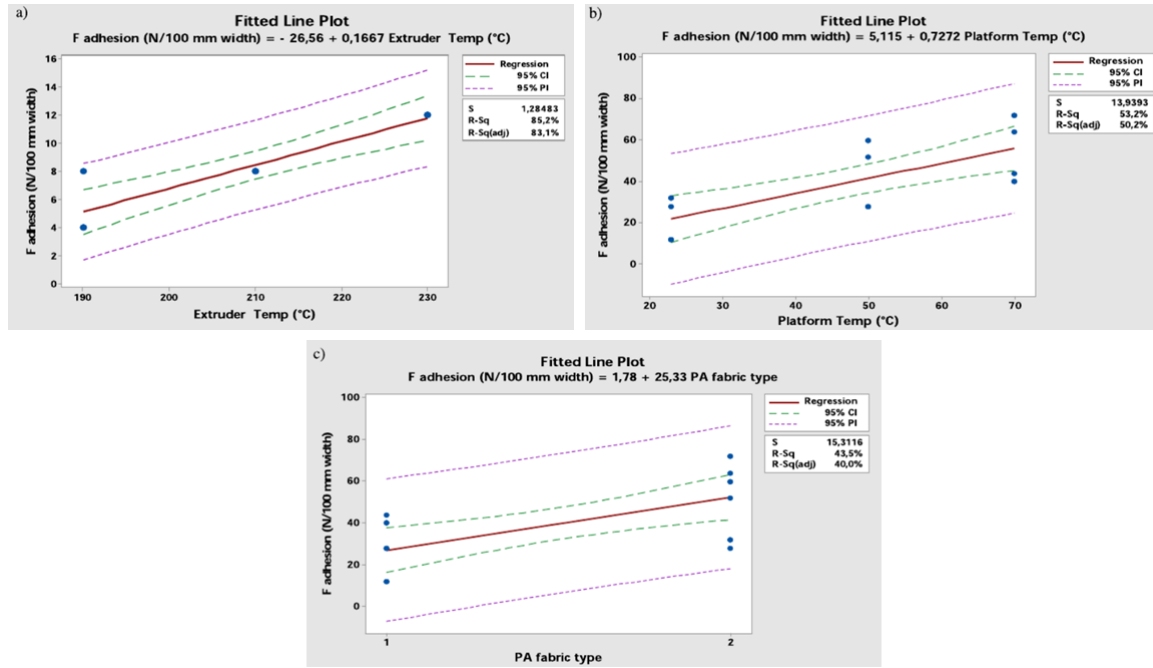


Figure 6.12: Variation of the adhesion force with extrusion temperature (a), build plate temperature (b) and build plate fabric type (c) [Sanatgar et al., 2017].

## 6.4 Numerical Simulation of Fused Deposition Modeling

The simulation approaches of FDM process can be divided into two categories:

- Filament level simulations
- Part level simulations

in the following sections we briefly describe each simulation approach.

### 6.4.1 Filament level simulations

Filament level simulations aim to predict phenomena rising at the filament level such as bonding and adhesion. As previously discussed, there are 2 types of bonding phenomena: bonding between filaments and bonding between layers.

Gurralla and Regalla [2014] proposed a mathematical model to describe the radius of the neck between two bounded filaments. The authors proved experimentally that neck sizes are time dependent and with the developed mathematical model were able to predict the evolution of the neck radius during the bonding process, as shown in Figure 6.13.

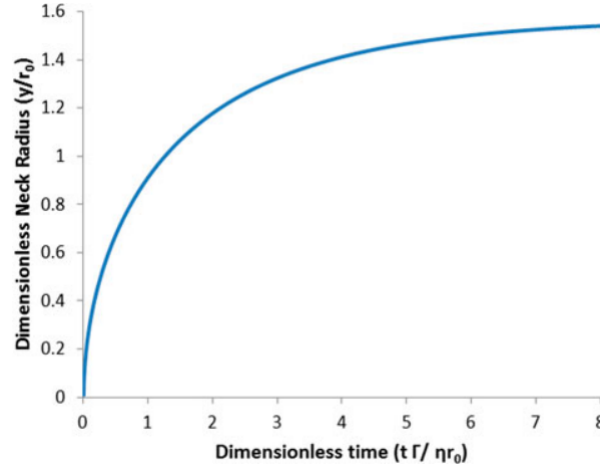


Figure 6.13: Neck radius variation with time during the bonding process between two FDMed deposited filaments [Gurralla and Regalla, 2014].

Coogan and Kazmer [2017] proposed a diffusion-controlled healing model for predicting bond strength between layers in FDM process. This model has been used to predict the bond strength in ABS specimens printed with different printing conditions and the results have been validated through experimental test.

Xia et al. [2017] adopted a mathematical model for direct multiphase flow simulations and used the finite volume method to simulate three dimensional filament deposition including bonding.

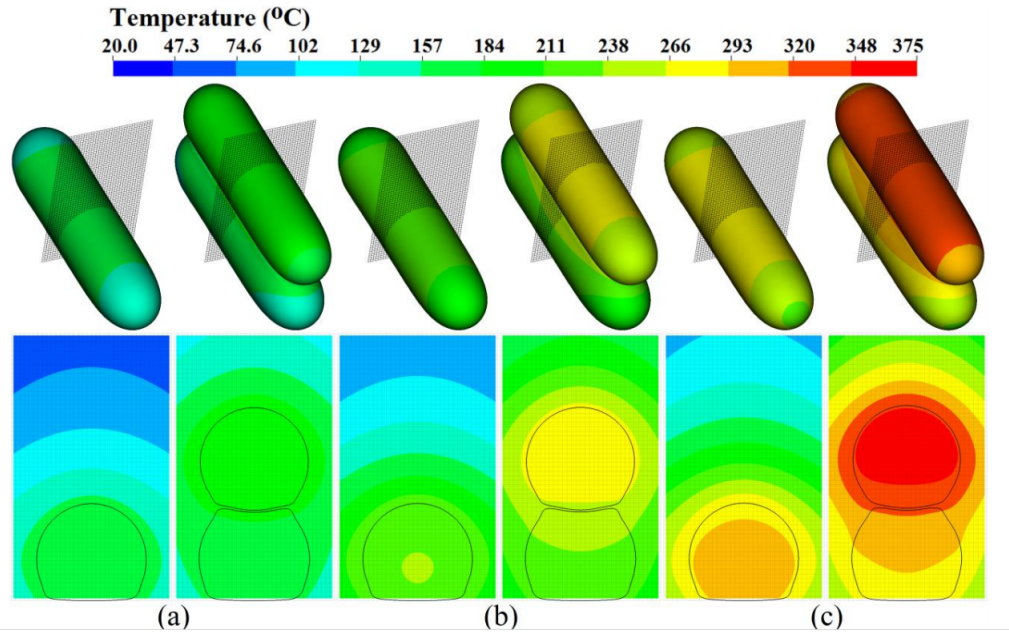


Figure 6.14: Temperature evolution between bounded filaments deposited at different extrusion temperatures (a) 215°C, (b) 295°C, and (c) 375°C [Xia et al., 2017].

The method is lack of residual stresses evaluation and has not been applied to simulate real

three dimensional components, although it considers the real shape of the deposited filament and it is able to predict with accuracy the temperature evolution within and between the filaments. Figure 6.14 shows the temperature evolution between bounded filaments deposited at different extrusion temperatures.

### 6.4.2 Part level simulations

Part level simulations aim to predict the evolution of stress and distortions field during the printing process. In particular one of the major tasks of part level simulation is to predict the distortions of the printed model from the design model, so to preventively change the printing parameters in order to avoid part distortions.

Zhang and Chou [2006] proposed the first three dimensional model to simulate FDMed components production. In this work the finite element method is adopted and a sequential element activation is performed to simulate the deposition process. This work has been followed by Zhang and Chou [2008] to simulate the FDM printing process varying layer thickness, scan speed and extrusion temperature. The results have been validated through a comparison with experimental tests showing good agreement with experimental data (see Figure 6.15).

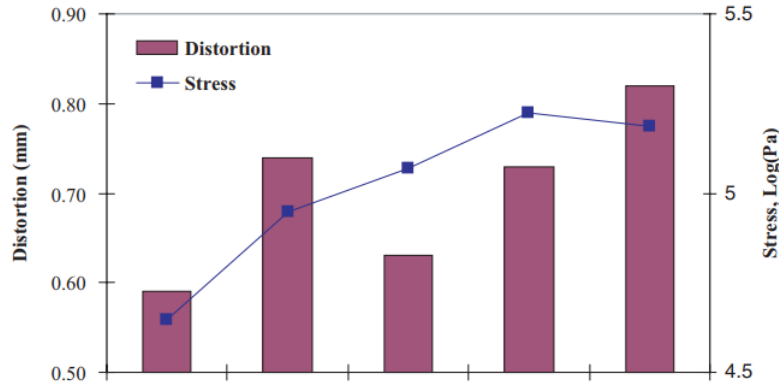


Figure 6.15: Real FDMed part distortions compared with simulation predictions. Every specimen has been realized with different printing parameter [Zhang and Chou, 2008].

In the following section we will adopt a model similar to the one proposed by Zhang and Chou [2006] to simulate real FDMed components starting from the informations contained in the G-Code file.

## Chapter 7

# Finite element simulation of Fused Deposition Modeling

In the previous chapter we have discussed about the computational approaches usually adopted for the FDM printing process simulation. Filament level simulations investigate local effects rising during the printing process. In particular they are adopted to simulate the intra and inter layer bonding and the adhesion force generated between the part and the building plate. Although, filament level simulations are very expensive in terms of computational costs and required memory and they cannot be used to simulate entire FDMed parts.

On the contrary, part level simulations are not accurate as filament level simulations are. They do not consider the real shape of the filaments and they neglect bonding and they assume a perfect adhesion between the part and building plate. Although, part level simulations have reduced computational costs and they allow to simulate entire FDMed components.

The overall framework of FDM process is shown in Fig. 7.1 (left side). First, a model of the part is realized through a CAD software, then a triangular mesh of the external surface is generated (STL file) and used as input for the slicing software (e.g., Slic3r or KISSlicer) to define all the parameters necessary to perform the printing process: the filament deposition path, the deposition velocities, the extrusion temperature, and the environmental variables. All these information are stored in a file, usually referred as GCode. This file is used both to realize the printing process and to perform the simulation of the part.

Relying on the information in the GCode, we set up a finite element analysis (FEA) in Abaqus (v. 2017 Simulia, Dassault Systemés) Courter et al. [2017] based on a sequential element activation scheme to simulate the entire printing process. The analysis is divided in two steps. A thermal analysis, solving the heat equation, is performed to evaluate the time-spatial temperature field evolution during the sequential element activation process. Subsequently, the resulting temperature field is adopted as forcing term in a mechanical analysis, used to evaluate residual stresses and part distortions (see Fig. 7.1 right side).

### 7.0.1 Sequential element activation

During the FDM printing process, the nozzle deposits a semi-molten filament following a predefined path contained in the GCode file. As an example, in Fig. 7.2 we show a sequence of standard instructions extracted from a GCode file realized with KISSlicer.



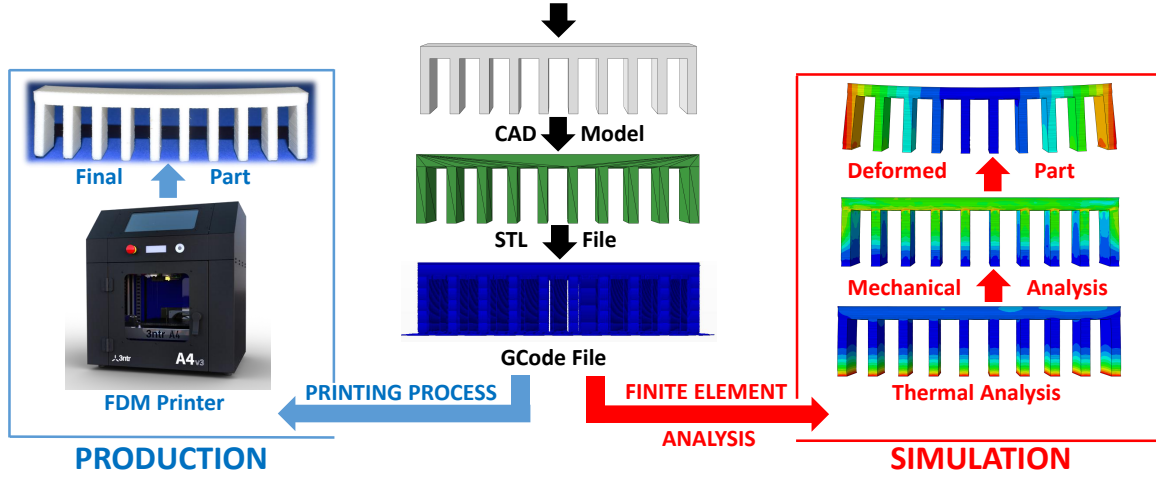


Figure 7.1: Overall framework of the FDM printing process. In the central part, the virtual calculation of the GCode file from a 3D CAD model of the component. On the left, the physical printing process; on the right, the simulation process. The GCode information are used both to perform the physical printing and the simulation of the part

```

; BEGIN_LAYER_OBJECT Z=7.40
; 'Perimeter Path', 0.6 [feed mm/s], 33.2 [head mm/s]
G1 X109.57 Y88.14 E9.0562 F9000
G1 X109.57 Y88.13 E9.0563 F1992
G1 X109.57 Y71.38 E9.3716
G1 X109.60 Y71.34 E9.3725
G1 X112.40 Y71.34 E9.4251
.. .....
```

Figure 7.2: Sequence of standard instructions contained in a GCode file realized with KISSlicer

The three necessary information, included in the GCode and needed to perform the sequential element activation, are: (i) the nozzle position, (ii) the nozzle velocity, and (iii) the cross sectional dimensions of the extruded filament.

$t$ [s]	X [mm]	Y [mm]	Z [mm]	Extruded filament area [mm <sup>2</sup> ]
1351.68	109.57	88.14	7.40	0.10
1315.69	109.57	88.13	7.40	0.10
1332.44	109.57	71.38	7.40	0.10
1332.49	109.60	71.34	7.40	0.10
1335.29	112.40	71.34	7.40	0.10
...	...	...	...	...

Table 7.1: Scheme of the input file for the sequential element activation. X, Y, Z are the coordinates of the filament centerline at time T. Extruded filament area represents the cross-sectional area of the extruded filament, which drops to zero in correspondence of the *travel movements*

We extract these information from the GCode file by means of an in-house Matlab code that directly write a suitable input file for the finite element analysis, as reported in Tab. 7.1. Columns X, Y, and Z describe the position of the centerline of the extruded filament at time  $t$ , while the last column contains the cross sectional area. The deposition path defined in the GCode file is, usually, not completely continuous, since the nozzle, in some cases, moves on the building plate without depositing material; such movements are usually referred as *travel movements*. To be fully consistent with the GCode file, during the sequential element activation, we assume the area of the filament equal to zero in correspondence of the travel movements.

The cross section of the extruded filament is typically characterized by a rectangular shape with round corners, resembling an ellipsoidal shape. For simplicity, we consider the cross section to be rectangular with dimensions equal to the ellipse axes.

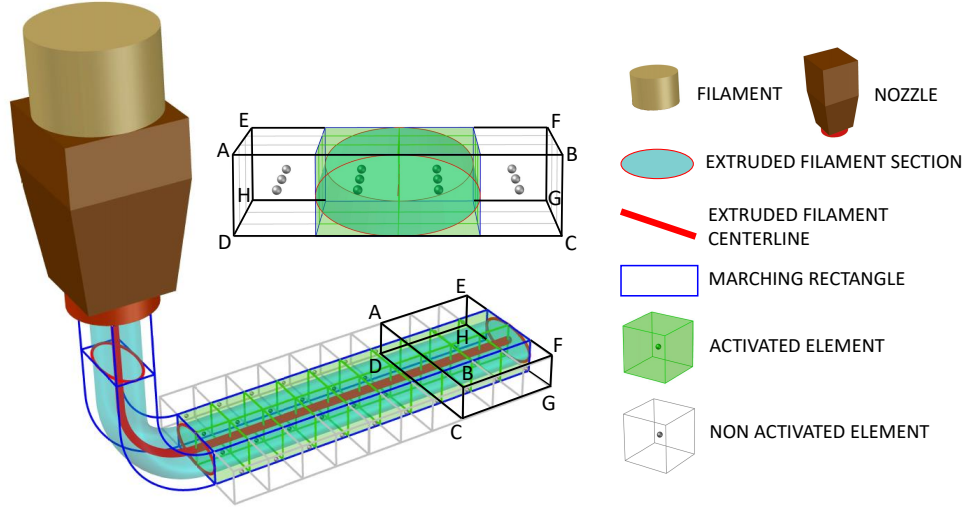


Figure 7.3: Element activation process. The extruded filament section (cyan ellipse) is substituted by the circumscribed *marching* rectangle (blue rectangle). The rectangle moves following the filament centerline (red line). When the center of an element (green point) falls into the volume described by the marching rectangle, then the element is activated (green element). Gray points correspond to the centroids of the non-activated elements (gray elements)

To realize the sequential element activation, a *marching rectangle*, representing the filament cross section, is imagined to move following the filament centerline contained in the GCode file (filament centerline coincident with marching rectangle center): if the center of an element falls within the ideal volume described by the marching rectangle, then the element is activated. Figure 7.3 shows the element activation process for a single layer of elements.

**Remark.** To respect the physics of the problem, it is necessary to adopt a meshing strategy in which the element height is equal to the height of the extruded filament (physical layer height) or to a sub-multiple of such height; furthermore it is convenient, but not mandatory, to keep the element width equal or a sub-multiple of the width of the extruded filament. With this precautions we ensure that the activated elements exactly match the dimensions of the

extruded filament. This topic will be discussed more in detail in Section 7.0.6.

### 7.0.2 Thermal analysis

During the FDM process the filament is extruded at temperature  $T_f$  and it is deposited on the building plate  $D_p$  having temperature  $T_p$ . The building chamber  $D_c$  is kept at constant temperature  $T_c$ . Due to temperature gradients, the filaments exchange thermal energy with both the previously deposited material and with the surrounding air in the chamber.

The time spatial evolution of the temperature field  $T(\mathbf{x}, t)$  is governed by the well-known heat equation Hussein et al. [2013]:

$$\rho c \dot{T} = \nabla \cdot (k \nabla T) + q \quad (7.1)$$

where  $\rho = \rho(T)$  is the material density,  $c = c(T)$  is the specific heat capacity,  $k = k(T)$  is the thermal conductivity,  $q$  is the internal heat source, and  $t$  is the time. The initial conditions of the problem are given by Schoinochoritis et al. [2017]:

$$T(\mathbf{x}, 0) = T_f \quad \mathbf{x} \in D_f \quad (7.2a)$$

where  $\mathbf{x} = (x, y, z)$  is the position,  $D_f$  is the extruded deposited material,  $D_c$  is the building chamber, while  $T_f$  and  $T_c$  are the extrusion and the chamber temperature, respectively. On the building plate  $D_p$  we impose the following Dirichlet boundary condition:

$$T(\mathbf{x}, t) = T_p \quad \mathbf{x} \in D_p \quad (7.3)$$

where  $D_p$  is the building plate and  $T_p$  is the imposed building plate temperature. The Neumann boundary conditions of the problem are defined as follows Schoinochoritis et al. [2017]:

$$k \frac{\partial T}{\partial \mathbf{n}} + q_c + q_r = 0 \quad \mathbf{x} \in S(t) \quad (7.4)$$

where  $S(t)$  is the external surface of the body (changing during element activation) and  $\mathbf{n}$  is the vector normal to the surface of the body, while  $q_c$  and  $q_r$  are the heat fluxes due to convection and radiation, respectively, defined as:

$$q_r q_c = Kh(T^4 - T_{\infty}^4)\epsilon \quad (7.5a)$$

where  $h = h(T)$  is the heat transfer coefficient,  $K_b$  represents the Stefan-Boltzmann constant, and  $\epsilon$  is the emissivity.

### 7.0.3 Mechanical analysis and material properties

In this paper we face the simulation of parts realized with a ABS filament, which is an amorphous polymer that exhibits a typical thermo-plastic behavior Tiganis et al. [2002]. In the incremental theory of plasticity, assuming a small strain regime, it is standard to introduce the following additive decomposition:

$$\boldsymbol{\varepsilon} = \boldsymbol{\varepsilon}^e + \boldsymbol{\varepsilon}^p + \boldsymbol{\varepsilon}^T \quad (7.6)$$

where  $\boldsymbol{\varepsilon}$  is the total strain, while  $\boldsymbol{\varepsilon}^e$ ,  $\boldsymbol{\varepsilon}^p$  and  $\boldsymbol{\varepsilon}^T$  are the elastic, plastic and thermal strain components, respectively, defined in Voigt notation as follows.

$$\begin{aligned}\boldsymbol{\varepsilon}^e &= \mathbf{D}^{-1}\boldsymbol{\sigma}, \quad \text{with} \quad \mathbf{D} = -\frac{\nu}{E}(\mathbf{1} \otimes \mathbf{1}) + \frac{1+\nu}{E}\mathbf{I} \\ \boldsymbol{\varepsilon}^p &= \lambda \boldsymbol{\sigma}^{\text{dev}} \\ \boldsymbol{\varepsilon}^T &= \alpha(T - T_0)\mathbf{1}\end{aligned}\tag{7.7}$$

where  $\boldsymbol{\sigma}$  is the stress (expressed in Voigt notation),  $E = E(T)$  is the Young's modulus,  $\nu$  is the Poisson's ratio,  $\alpha = \alpha(T)$  is the thermal expansion coefficient,  $\mathbf{I}$  is the identity,  $\mathbf{1} = \{1, 1, 1, 0, 0, 0\}^T$ , and  $\boldsymbol{\sigma}^{\text{dev}}$  represents the deviatoric part of the stress tensor:

$$\boldsymbol{\sigma}^{\text{dev}} = \boldsymbol{\sigma} - \frac{1}{3}\text{tr}(\boldsymbol{\sigma})\mathbf{1}\tag{7.8}$$

$\lambda$  is the plastic flow factor defined as follows:

$$\begin{aligned}\lambda &= 0 \quad \text{if} \quad \sigma_{vm} < \sigma_p \\ \lambda &> 0 \quad \text{if} \quad \sigma_{vm} > \sigma_p\end{aligned}\tag{7.9}$$

where  $\sigma_p = \sigma_p(T)$  is the yield stress and  $\sigma_{vm}$  is the effective Von Mises stress defined as follows:

$$\sigma_{vm} = \sqrt{\frac{3}{2}(\boldsymbol{\sigma}^{\text{dev}})^T \boldsymbol{\sigma}^{\text{dev}}}\tag{7.10}$$

At the ambient temperature ( $T_a = 25^\circ\text{C}$ ) the adopted material properties, correspond to a commercial ABS filament (see Table 7.2).

<i>Property</i>	<i>Value</i>	<i>Property</i>	<i>Value</i>
Density	1040 Kg/m <sup>3</sup>	Thermal expansion coefficient	$9 \cdot 10^{-5}^\circ\text{C}^{-1}$
Young modulus	1826 MPa	Specific heat	1290 J/( $^\circ\text{C} \cdot \text{Kg}$ )
Poisson ratio	0.32	Thermal conductivity	0.15 W/( $^\circ\text{C} \cdot \text{m}$ )
Yield stress	25 MPa	Glass transition temperature	95 $^\circ\text{C}$

Table 7.2: Mechanical and thermal properties of the commercial ABS filament at the ambient temperature

In amorphous polymers the glass transition temperature, usually indicated as  $T_g$ , marks the transition from the *glassy* to the *rubbery* mechanical behavior of the material. This process, usually referred as *glass transition*, is different from the *melting* process, because it does not involve a transition from a ordered to a disordered molecular structure. The melting process, typical of crystalline polymers, occurs when the ordered polymer chains fall out of their crystalline structure giving rise to a disordered liquid; instead the glass transition

process, typical of amorphous polymers, simply indicates an increasing disorder associated to the molecular structure, since at the solid state the molecular chains are not arranged in an ordered crystalline structure. Accordingly, the glass transition temperature  $T_g$  influences the thermal properties of amorphous polymers. In Fig. 7.4 we show the variation of thermal conductivity and specific heat with temperature in the commercial ABS filament.

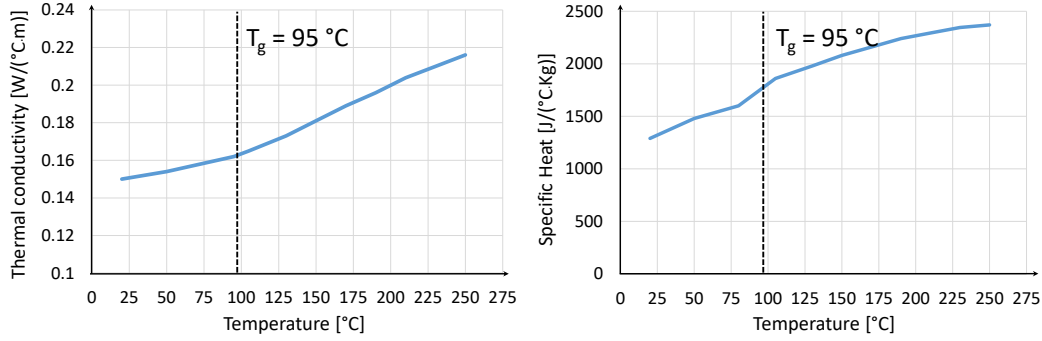


Figure 7.4: Variation of thermal conductivity and specific heat with temperature in the commercial ABS filament. [Rheology Testing And Consultancy, 2004].  $T_g$  represents the glass transition temperature

Furthermore the glass transition temperature  $T_g$  has a great impact on the mechanical properties of the ABS filament; in fact, above this temperature the Young's modulus and the yield stress drop down to values close to zero Song et al. [2012]; Armillotta et al. [2018]. Figure 7.5 shows the variation of the Young's modulus with the temperature for the considered ABS filament Song et al. [2012].

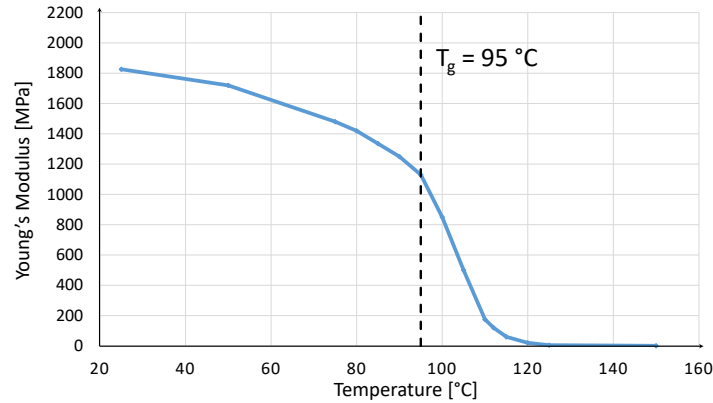


Figure 7.5: Variation of the Young's modulus with the temperature in the commercial ABS filament Song et al. [2012].  $T_g$  represents the glass transition temperature

Following Richeton et al. [2005, 2006] the variation of the yield stress in amorphous polymers can be described by the following cooperative model:

$$\left\{ \begin{array}{ll} \sigma_p = \sigma_{p0} - mT + \frac{2K_b T}{V} \sinh^{-1} \frac{\dot{\varepsilon}}{\dot{\varepsilon}_0 \exp\left(-\frac{\Delta H_B}{K_b T}\right)} & \text{for } T < T_g \\ \sigma_p = \frac{2K_b T}{V} \sinh^{-1} \frac{\dot{\varepsilon}}{\dot{\varepsilon}_0 \exp\left(-\frac{\Delta H_B}{K_b T}\right) \exp\left(\frac{c_1^g(T - T_g) \ln 10}{c_2^g + T - T_g}\right)} & \text{for } T \geq T_g \end{array} \right. \quad (7.11)$$

where  $\sigma_{p0}$  is the yield stress at the absolute zero temperature,  $V$  is an arbitrary activation volume,  $\Delta H_B$  is the activation energy,  $\varepsilon_0$  is a constant pre-exponential strain, and  $c_1^g$  and  $c_2^g$  are the coefficients of the Williams-Landel-Ferry (WLF) time-temperature superposition. Evaluating all the parameters in Eq. 7.11 is not a simple task and, in addition, no experimental data are available in literature for ABS. However, a review of the studies dealing with the yield stress temperature dependency of amorphous polymers shows that: (i) below the glass transition temperature the yield stress linearly decreases with slope  $m$  Rault [1998] and (ii) above the glass transition temperature the yield stress can be assumed almost constant with a value close to zero Armillotta et al. [2018]. Accordingly, for the considered ABS we assume a yield stress variation with temperature as shown in Fig. 7.6, where  $m = 0.24$  and  $\sigma_p = 1$  MPa Armillotta et al. [2018], for  $T > 100^\circ\text{C}$ .

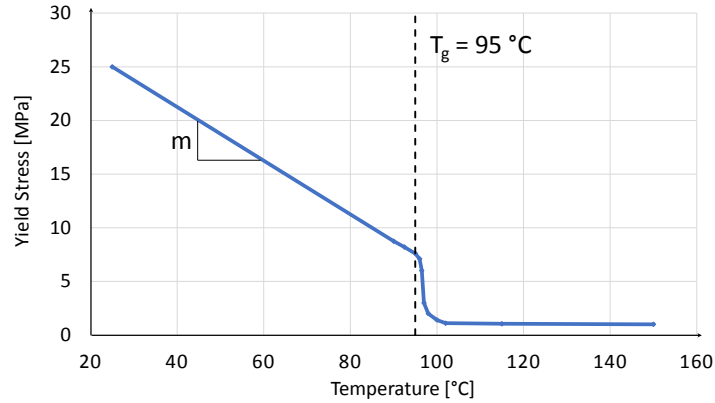


Figure 7.6: Variation of the tensile yield stress with the temperature in the commercial ABS filament Richeton et al. [2006]; Armillotta et al. [2018].  $T_g$  represents the glass transition temperature and  $m$  represents the slope of the linear part

**Remark 1:** Eq. 7.11 was proposed by Richeton et. al. Richeton et al. [2005] to describe the variation of the compressive yield stress with the temperature. However, in the present study, we assume that the same functional relation is also valid for the tensile yield stress.

**Remark 2:** The filament as-deployed can be considered homogeneous and isotropic (Rodríguez et al. [2003], Alaimo et al. [2017]) but the geometrical structure at a sub-millimeter scale, resulting from the deposition process, implies, at the macro-scale, an overall mechanical anisotropy. In particular, several works (Ning et al. [2017], Liao et al. [2018], Ryder et al. [2018]) showed that both yielding stress and Young's modulus vary with fiber orientation and filament cross-sectional dimensions. Assuming an orthotropic, transversely isotropic behavior, such a dependence with fiber orientation is usually more evident when observing yielding

stress at macro-scale (up to 30% in transverse direction compared to fiber orientation). As concerns the Young's modulus, the decrease in stiffness is usually less pronounced, resulting in variation up to 15% in transverse direction compared to fiber orientation. Such data refer to tensile tests performed on ABS unidirectional specimens at ambient temperature. To capture the 3D-printed part anisotropy, it should be used a extremely fine mesh (element dimensions much smaller than the filament cross section) able to accurately represent the microstructure. In the present work we neglected the anisotropy, but as confirmed by the obtained results, this assumption can be considered acceptable.

#### 7.0.4 Part detachment procedure

During the printing process, residual stresses arise due to the constrained progressive cooling of the body still under construction, in response to the temperature decreasing from the extrusion temperature  $T_f$  to the chamber temperature  $T_c$ . Similarly, during the cooling transient after the printing process, residual stresses increase since the temperature goes from the chamber temperature  $T_c$  to the ambient temperature  $T_a$ . Residual stresses tend to induce a warping deformation that is usually prevented by the adhesion between the part and the building plate. However, if residual stresses are high enough, they can cause part detachment, since the warp tendency is not be balanced by the adhesion force.

Accordingly, a crucial point for a complete characterization of the process is the evaluation of the adhesion force. This task can be very complicated because the adhesion force is influenced by local imperfections, impurities, and a non uniform temperature distribution of the building plate, as well as by the chemical properties and the dimensions of the filament. A widely adopted method to prevent the part detachment is to introduce, between the building plate and the part to be realized, a support structure usually referred as *raft*. Raft basically consists of 4-6 filament layers, the first of which is characterized by a filament of relatively large dimensions. Typical values of the first raft layer height and width are 0.6 and 1.8 mm, respectively. The dimensions of this layer increase the adhesion force, thus avoiding component detachment.

When a part is printed on the raft, no detachment usually occurs during the printing or the cooling process. In this case, in the proposed model we simulate the part as constrained in correspondence of the supports and, at the end of the cooling process, we remove all the constraints, allowing the part to reach its final deformed configuration.

Instead, when a part is printed without pre-printing the raft, detachments can occur, most of the times during the cooling process. In this case, neglecting the adhesion force evaluation, in the proposed model we consider the part as constrained during all the printing and the cooling process, then adopting a reverse engineering approach, we remove the constraints only in correspondence of the detachment points of the part.

#### 7.0.5 Simulated geometries

In this study we simulate the FDM printing process of two parts, shown in Fig. 7.7: a planar spring (a) and a bridge model (b). In particular we observe that the planar spring and the bridge model have comparable dimension on the XY plane, while the planar spring presents a reduced dimension along Z-axis.

The first model is printed without raft, thus the adhesion force plays an important role, while the second model is printed using support structures (needed for geometry) and raft as usually done in long printing processes ( $\geq 3$  hours).

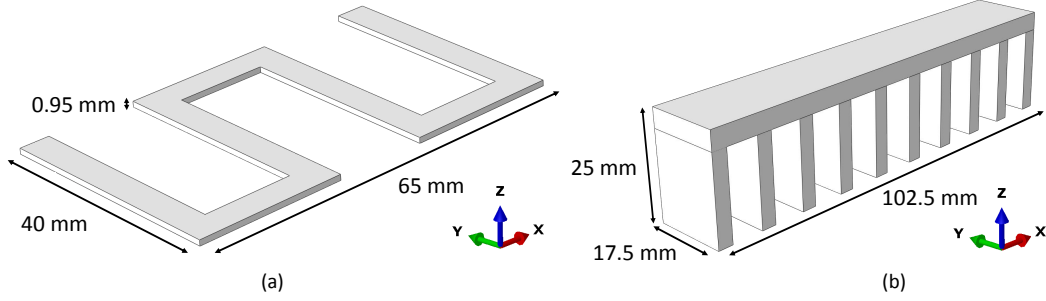


Figure 7.7: Geometry of the planar spring (a) and bridge model (b)

For sake of completeness, we report in Tab. 7.3 the adopted printing process parameters.

<i>Geometry</i>	$T_f$ [°C]	$T_p$ [°C]	$T_c$ [°C]	Infill [%]	Raft	Supports
Planar spring	240	90	45	100	No	No
Bridge	240	120	45	30	Yes	Yes

Table 7.3: Printing process parameters adopted for the planar spring and bridge model

The 3D printer used for the present study is a 3NTR A4v3 Win. The machine is equipped with three extruders, which can be heated up to 410 °C, through a ceramic heating component; a nozzle of 0.4 mm of diameter is used. The bed temperature can reach 120 °C, while the heated chamber can reach 85 °C. Figure 7.8 shows the part orientation with respect to the printing bed.

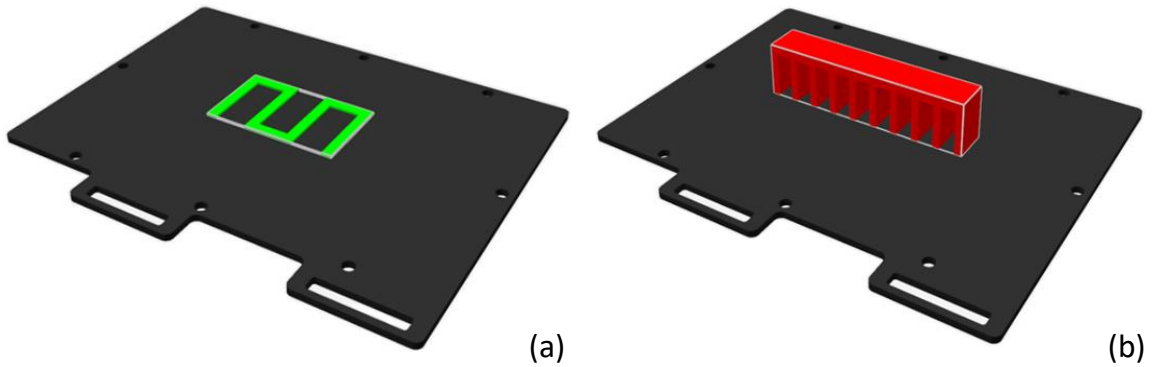


Figure 7.8: Layout of the printed parts with respect to the building plate; (a) planar spring, (b) bridge.



### 7.0.6 Sensitivity analysis on simulation parameters

The FDM numerical analyses are mainly influenced by (i) the time step  $\Delta t$ , (ii) the meshing strategy, and (iii) the adopted constitutive model. We now focus on the planar spring problem (Fig. 7.7(a)) and we investigate the influence of the parameters listed above on the simulation results, adopting the ranges discussed in the following:

1. *Time step.* The printing process has been simulated with the time steps listed in Tab. 7.4:

	$\Delta t_1$	$\Delta t_2$	$\Delta t_3$	$\Delta t_4$	$\Delta t_5$	$\Delta t_6$	$\Delta t_7$	$\Delta t_8$	$\Delta t_9$
Value [s]	8	4	2	1	0.5	0.25	0.125	0.0625	0.03125

Table 7.4: Time steps adopted for the planar spring simulation

2. *Meshing strategy.* As previously discussed, in order to correctly reproduce the printing process, it is necessary that the typical element height is equal to a sub-multiple of the filament height. Accordingly, to be fully consistent with the real process, the element width should be equal or a sub-multiple of the filament width, but in some cases this meshing strategy can lead to finite element models with a very large number of elements ( $\geq 10^6$ ), which requires very strong computational resources. For this reason we also investigate meshing strategies consistent with the height but not with the width of the deposited filament. In this work we use a square base mesh with variable height. Denoting with  $l_y$  the filament width and with  $h_y$  the filament height (i.e., the element height), we report the adopted meshing strategies in Table 7.5:

<i>Meshing strategy</i>	Height	Width
<b>M-1</b>	$h_y$	$4l_y$
<b>M-2</b>	$h_y$	$2l_y$
<b>M-3</b>	$h_y$	$l_y$
<b>M-4</b>	$h_y$	$l_y/2$
<b>M-5</b>	$h_y/2$	$l_y/2$

Table 7.5: Meshing strategies adopted for the planar spring simulation. In red, the meshing strategies consistent only with the filament height. In blue, the meshing strategies fully consistent with filament dimensions

3. *Constitutive model.* ABS properties needed for numerical simulations can be divided in two groups: (i) physical properties, including density, heat coefficient, specific heat and expansion coefficient; (ii) mechanical properties, including Young's modulus and yielding stress; all those properties are temperature dependent. We always consider the dependency of the physical properties on the temperature and we investigate the effect of neglecting, or including, also the dependency of the mechanical properties on the temperature. Accordingly, in Tab. 6 we report the combinations of the adopted constitutive models with the temperature dependence of the ABS mechanical properties.

<i>Constitutive model</i>	Physical properties	Young's modulus	Yield stress
Linear elastic - 1 (LE1)	Variable	Constant ( $T_a$ )	-
Linear elastic - 2 (LE2)	Variable	Variable (Fig. 7.5)	-
Elasto plastic - 1 (EP1)	Variable	Variable (Fig. 7.5)	Constant ( $T_a$ )
Elasto plastic - 2 (EP2)	Variable	Variable (Fig. 7.5)	Variable (Fig. 7.6)

Table 7.6: Constitutive models adopted for the considered ABS filament. For each constitutive model we remark the temperature dependence of the physical and the mechanical properties.  $T_a$  represents the ambient temperature

### 7.0.7 Validation

To validate the developed numerical framework, we compare the Z-axis displacements obtained from the simulation to the ones obtained from experimental measurements. The reference value for z-axis displacements has been assumed as the theoretical one from the CAD model. In particular, for the planar spring we consider the experimental results of four samples, while for the bridge model we consider two experimental tests, but, due to the high repeatability of the printing, we compare the numerical prediction with just one experimental measurement.

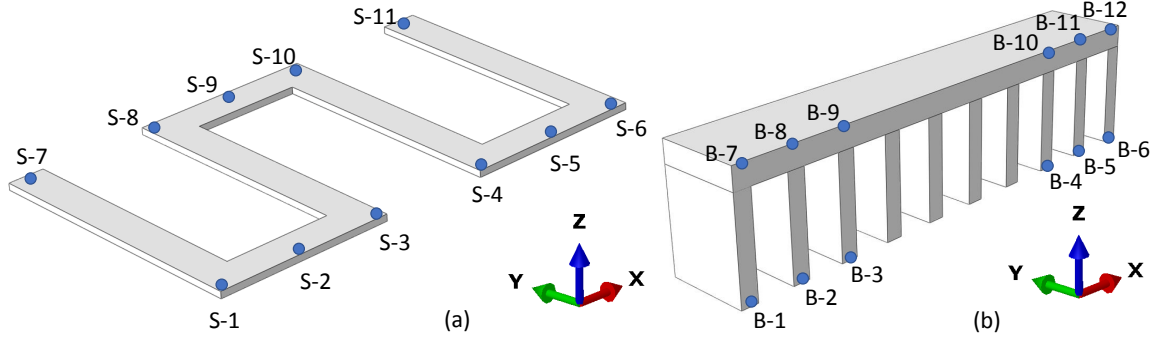


Figure 7.9: Test points for the evaluation of the error between simulation results and experimental measurements

For each model we evaluate the numerical errors in specific *test points*. Figure 7.9 shows the test points for both the planar spring (a) and the bridge model (b).

The error evaluation is slightly different between the two models. For the planar spring, in each test point, we consider the Z-axis displacements measured on each sample  $u_z^i$  and we calculate the average Z-axis displacement  $u_z^m$ . For the bridge model, instead, in each test point we consider the Z-axis displacement  $u_z$  measured on a single sample. Then, we evaluate the point-wise Z-axis displacement errors. For the planar spring we calculate the difference between the average of the experimental measurement and the simulation displacement  $u_z^m - u_z^h$ , then we estimate the relative error  $(u_z^m - u_z^h)/u_z^m$ . For the bridge model the procedure is very similar, except that  $u_z^m$  is replaced by  $u_z$ .

Finally, we estimate the global displacement error for each model calculating the coefficient

of variation  $CV$  of the obtained data:

$$CV = \frac{SD}{\mu}, \quad \text{with:} \quad SD = \sqrt{\frac{\sum_N (u_z^* - u_z^h)^2}{N}}, \quad \text{and} \quad \mu = \frac{\sum_N u_z^*}{N} \quad (7.12)$$

where  $SD$  is the standard deviation,  $\mu$  is the arithmetic mean,  $N$  is the number of the test points, and  $u_z^*$  correspond to  $u_z^m$  for the planar spring and to  $u_z$  for the bridge model.

## 7.1 Results and discussion

### 7.1.1 Sensitivity analysis on simulation parameters

In this section we show the influence of the simulation parameters on the thermal and mechanical analysis results of the planar spring model. All the simulations have been carried out on a Intel Core i7-6700 CPU 3.4 GHz machine, using 16GB of Ram and 4 CPUs.

#### Time step

We study the time step influence on simulation results considering the meshing strategy M-3 and the constitutive law EP2. Figure 7.10 shows the temperature and the Von Mises stress fields during the sequential element activation and at the end of the printing process, respectively. In particular, we show the results obtained with the largest ( $\Delta t_1$ ) and the smallest ( $\Delta t_9$ ) time steps. The element activation temperature should be equal to the extrusion temperature  $T_f$  (see Tab. 7.3). We note that the adopted time step strongly influences the activation temperature: in fact, using the time step  $\Delta t_9$ , the activation temperature is close to  $T_f$ , while with the time step  $\Delta t_1$  the activation temperature is less than  $T_f/2$ .

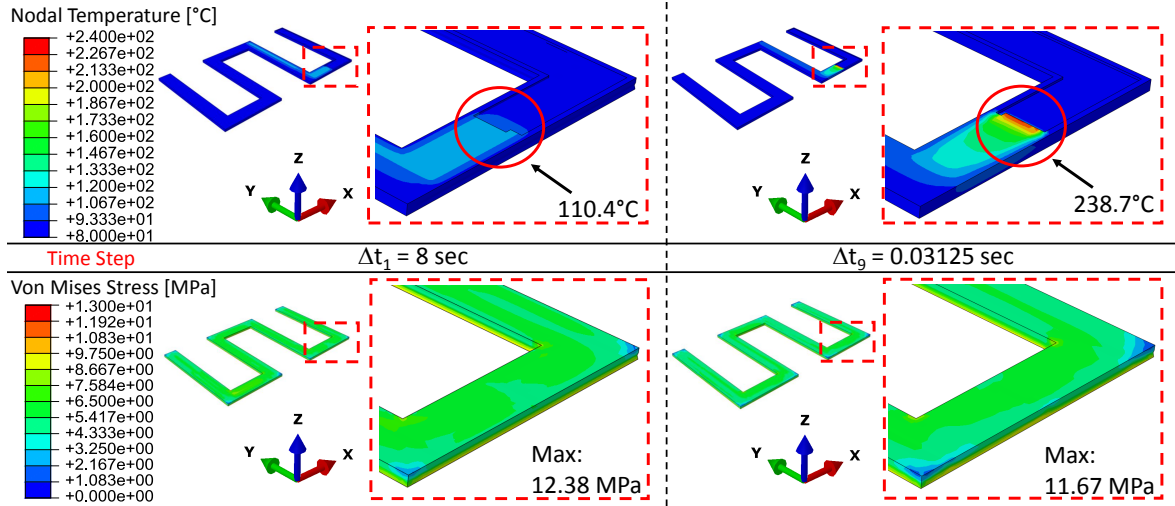


Figure 7.10: Results of the thermal and the mechanical analysis obtained with the smallest ( $\Delta t_1$ ) and the largest ( $\Delta t_9$ ) time steps. The time step choice has a significant influence on the element activation temperature, while it has less influence on the mechanical analyses results

On the contrary, looking at the residual stress results, we appreciate a low difference between the residual Von Mises stress obtained with time step  $\Delta t_1$  and with time step  $\Delta t_9$ ; in both cases the stress distribution looks almost coincident, except on the corners of the model where the time step  $\Delta t_9$  allows to predict a stress gradient that is not well predicted with the time step  $\Delta t_1$ . In Fig. 7.11 we show the detailed variation of the element activation temperature and the residual stresses for increasing time steps. The activation temperature difference is justified observing that the average cooling rate of an ABS filament, during a standard FDM printing process, is close to 25 °C/s Bellehumeur et al. [2004], thus to capture a temperature variation of 1 °C, it is necessary a time step lower than 0.04 s. Consequently, adopting higher time steps, it does not allow to correctly capture the temperature field time evolution during the deposition process.

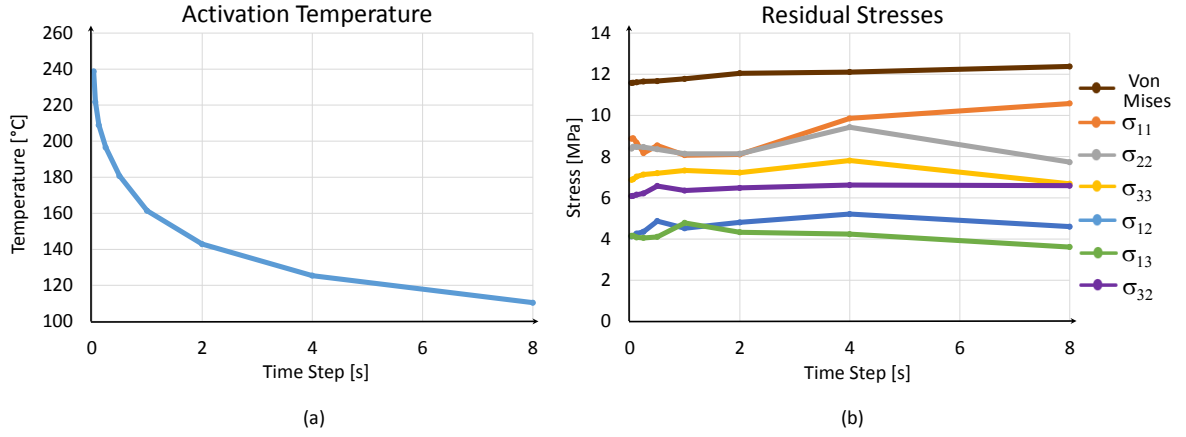


Figure 7.11: (a): decreasing of the activation temperature with increasing time steps. (b): Von Mises stress ( $\sigma_{vm}$ ) and stress tensor components ( $\sigma_{ij}$ ) variation with time step.

Finally, in Fig. 7.12 we show the dependency of the computational time on the time step for both the thermal and the mechanical analysis. We appreciate how the computational time of the mechanical analysis carried out with the time step  $\Delta t_9$  is 9 times higher than the computational time obtained with time step  $\Delta t_1$ .

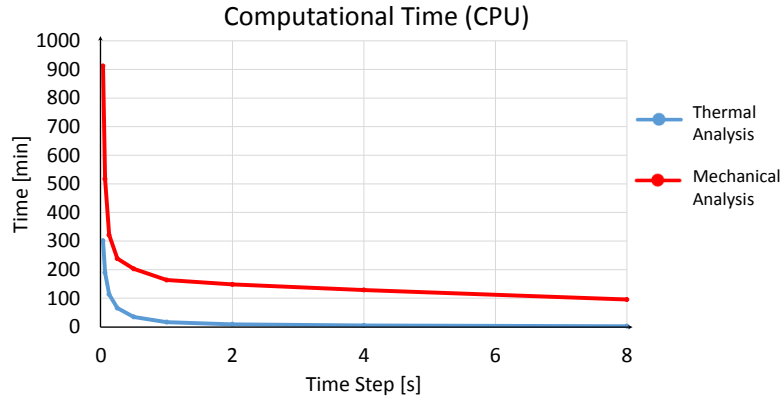


Figure 7.12: Computational times variation (CPU time) with the time step. A significant increase in computational times is observed, in particular, for the mechanical analysis when  $\Delta t$  is lower than 1 s.

According to this results, we can conclude that: (i) a small enough time step is mandatory to evaluate the temperature distribution during the printing process; (ii) the residual stress field at the end of the printing process is not significantly influenced by the adopted time step; (iii) the computational time is strongly influenced by the time step choice, in particular with regard to the mechanical analyses with time steps below  $\Delta t_4$ .

### Meshing strategy

We study the influence of the meshing strategy on simulation results with the constitutive law EP2 and with the time step  $\Delta t_5$ . Figure 7.13(a) shows the layers of the sliced model, while Figs. 7.13(b)-(f) show the adopted meshing strategies. The filament height (i.e., the layer height)  $h_y$  is equal to 0.35 mm for the first layer and to 0.2 mm for the other layers, while the filament width is equal to 0.5 mm for each layer.

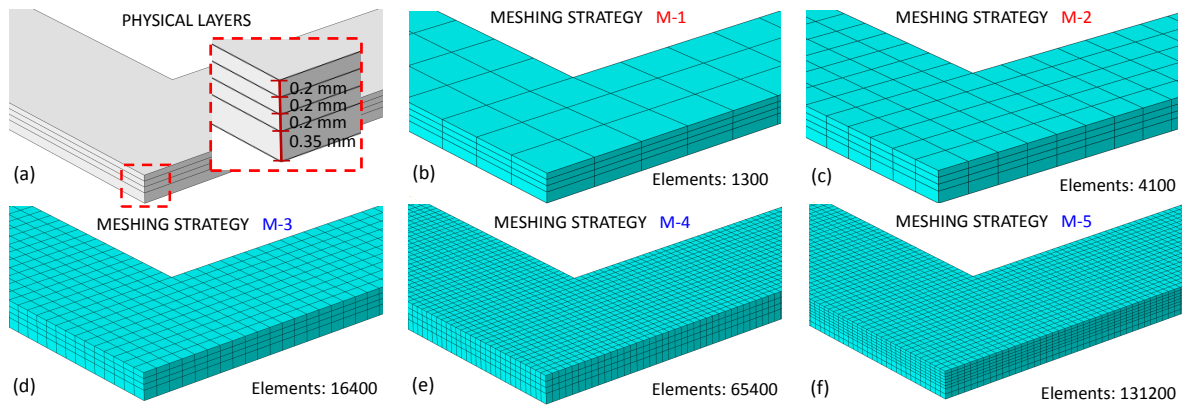


Figure 7.13: Adopted meshing strategies for the planar spring simulation, according to Tab. 7.5

In Fig. 7.14 we show the results of the thermal and the mechanical analyses obtained

with the considered meshing strategies. In particular, we show the temperature during the sequential element activation and the residual stresses at the end of the printing process. With the meshing strategies M-3 and M-5, we obtain very similar results both in terms of element activation temperature and in terms of maximum Von Mises stress; furthermore, the stress field distribution is very similar for the two cases. Meshing strategy M-1, instead, presents local modifications of the stress path in correspondence of the corners of the planar spring, in comparison with meshing strategies M-3/5. Looking, in specific, at the bottom corner of the model, we observe that the stress gradient obtained with the meshing strategy M-1 is significantly lower from the one obtained with the meshing strategies M-3 and M-5. In particular, the Von Mises stress difference between points A and B is equal to 0.67 MPa with mesh M-1, to 4.02 MPa with mesh M-3, and to 4.13 MPa with mesh M-5. This discrepancy can be justified considering that the meshing strategy M-1 has a base dimension that is four times the filament width; instead meshes M-3 and M-5 are fully consistent with filament dimensions.

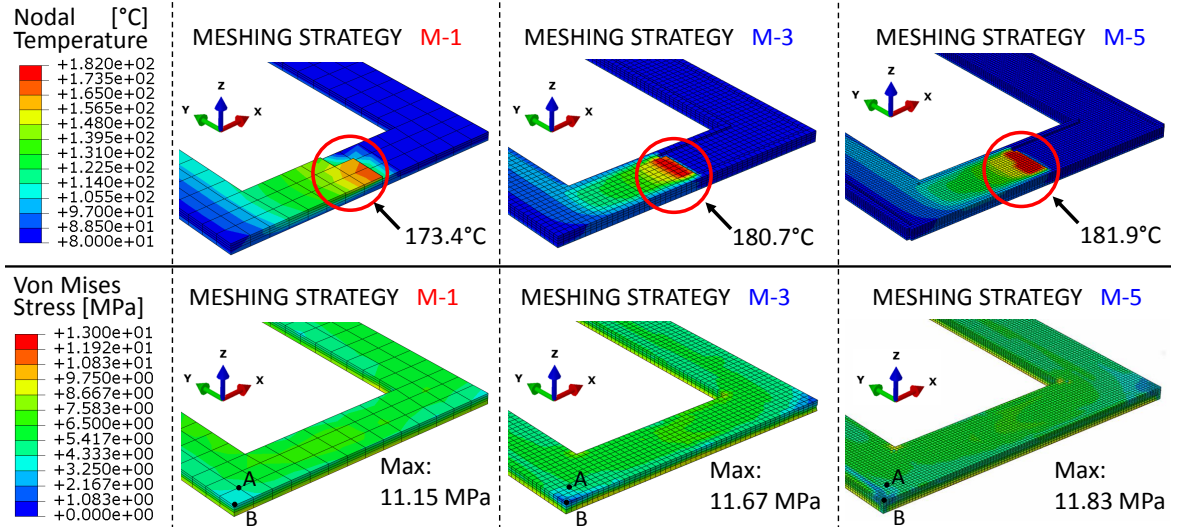


Figure 7.14: Temperature and Von Mises stress distribution obtained varying the meshing strategy. Significantly different activation temperature is observed for meshing strategies M-1 and M-3/5. Local modifications of the stress path can be observed at the corners of the model, between meshing strategies M-1 and M-3/5

Finally, in Fig. 7.15 we show the dependence of the computational times on the number of elements for both the thermal and the mechanical analyses. We observe that the computational times have almost a linear behavior while increasing the number of elements.

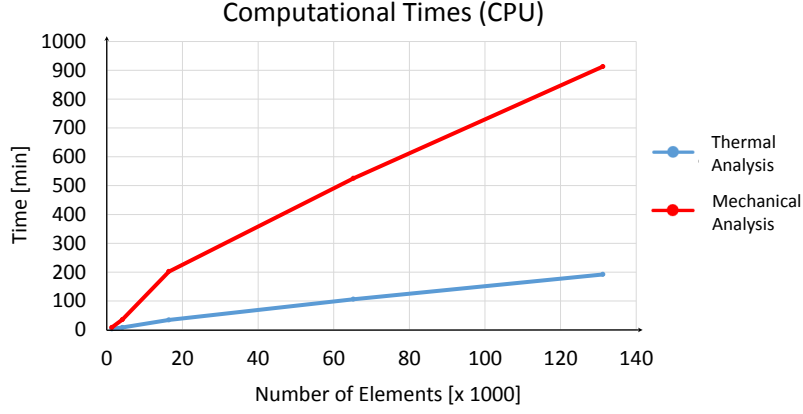


Figure 7.15: Computational times variation (CPU time) with increasing number of elements. We appreciate a linear behavior of the computational times both for the thermal and the mechanical analysis

In summary, the choice of the meshing strategy is not univocal. We have shown that a finer meshing strategy, fully consistent with the filament dimensions, allows to predict with more accuracy stress gradients, although the computational demand strongly increases. We suggest to use a finer meshing strategy for small models which require lower computational costs and in which the local effect can significantly affect the deformed shape of the part. On the other hand, in large models, where the local effects are negligible in comparison with the global dimensions of the part, we suggest to adopt a coarser meshing strategy to contain computational costs.

### Constitutive model

We study the influence of the constitutive model on simulation results with the meshing strategy M-3 and with the time step  $\Delta t_5$ . Since the adopted physical properties are the same for all the constitutive models, no variation is observed among the thermal analysis results.

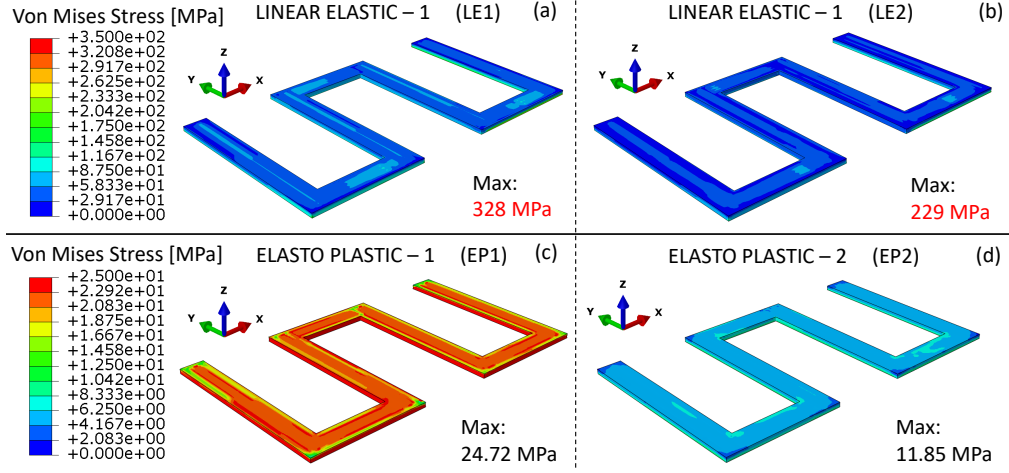


Figure 7.16: Von Mises stress at the end of the printing process obtained varying the constitutive model. (a, b): yielding surface is not defined. (c): yielding surface is not dependent on the temperature. (d): yielding surface is dependent on the temperature. More details about the constitutive models are specified in Table 6

In Fig. 7.16 we show the Von Mises stress fields obtained at the end of the printing process. Since the cooling process has not yet taken place, building plate and chamber temperature are defined as in Tab. 7.3.

As discussed in Section 7.0.3 (see Fig. 7.6), for a given temperature the Von Mises stress must not exceed the corresponding yield stress. The results of the analyses confirm that the constitutive models LE1 (a), LE2 (b) and EP1 (c) do not allow to obtain physically acceptable values of the residual stresses. The only constitutive model that allows to achieve physically acceptable residual stresses is the elasto plastic model EP2 with the yielding stress dependent on the temperature (d).

### 7.1.2 Validation

In the present section we compare the displacements, obtained with our simulation scheme, with the displacements obtained trough experimental tests. The samples have been measured with a high precision laser scanner (Julight S.r.l.), with spatial and vertical resolution of 200 nm.

According to the results shown in Section 7.1.1, we have adopted a thermo-elasto-plastic constitutive law for both models, but different meshing strategies and time steps. The planar spring, compared to the filament dimensions, is a relatively small model in which the local effects can significantly affect the final results, therefore we have adopted meshing strategy M-4 and time step  $\Delta t_6$ . Compared to the filament dimensions, the bridge is a relatively large model and the local effects are negligible, therefore we have adopted meshing strategy M-2 with time step  $\Delta t_3$ .

### 7.1.3 Planar spring

Figure 7.17 shows a samples of the planar spring after the detachment from the building plate; in particular we notice the warpage effect at the corners of the structure. Figure 7.18 shows



the vertical displacements of the upper surface of the four samples, obtained through the experimental measurements.

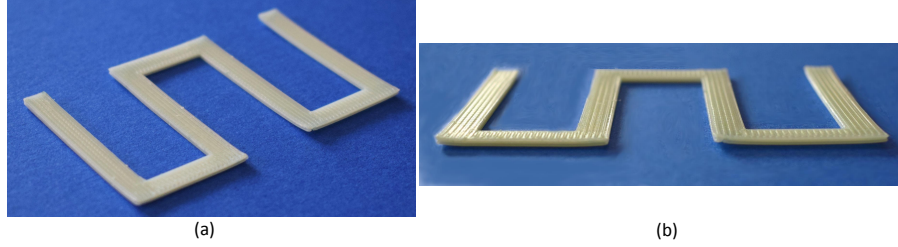


Figure 7.17: Planar spring model after the detachment from the building plate. Warpage effect is appreciable at the corners of the component

We observe how the deformed shapes of the four samples are similar; in particular the highest displacements are found in correspondence of corner A where the printing process starts. Furthermore on the sides along X direction the samples show a very similar displacements path.

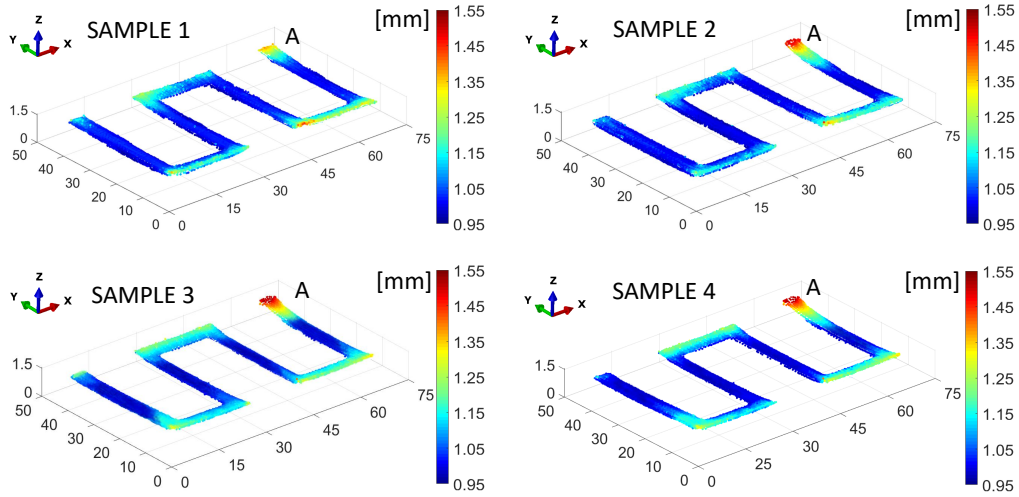


Figure 7.18: Experimental measurements of the vertical displacements of the upper surface of the planar spring. Four different samples have been considered

Since the part has been printed without raft, in order to simulate the part detachment from the building plate, we need to identify the points of the samples which remain attached at the building plate at the end of the cooling process. Knowing that the samples height is equal to 0.95 mm (see Fig. 7.7(a)), it is sufficient to find the points of the upper surface with Z coordinate equal to 0.95 mm.

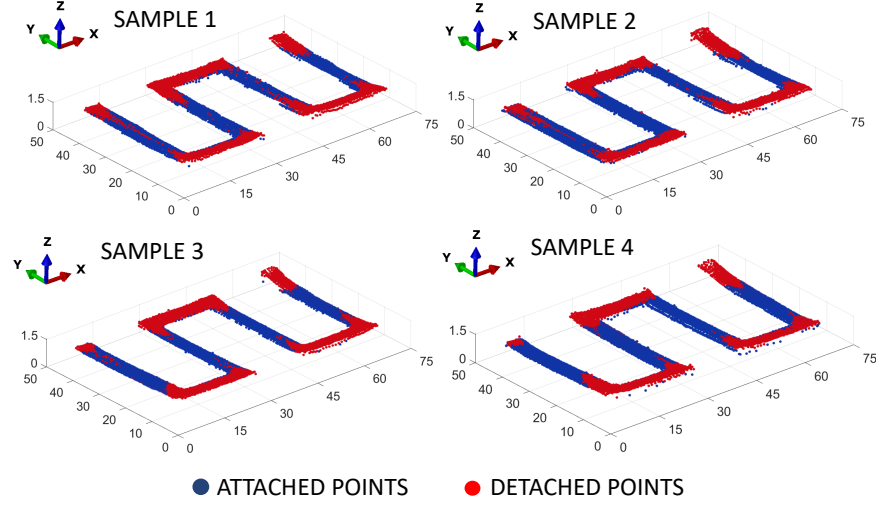


Figure 7.19: In blue, the points that remain attached to the building plate at the end of the cooling process. In red, the points detached from the building plate at the end of the cooling process

Figure 7.19 shows the points that remain attached to the building plate (blue points) and the points which are detached from the building plate (red points). We notice that the distributions are very similar for the four samples.

During the simulation of the printing process, we impose Dirichlet boundary conditions setting all the displacements components to zero on the bottom nodes of the planar spring; then, according with the results shown in Fig. 7.19, to simulate the part detachment after the cooling process, we remove the constraints on the bottom nodes in correspondence to the (experimentally observed) detached points. Since the detached points are not precisely the same among the four samples, we assume a point to be detached if it is detached at least twice on the four samples.

We underline that, in general, the physical points do not match the mesh nodes, so in order to state which nodes have to be detached at the end of the cooling process, we need to interpolate the measured points with the mesh nodes. We consider for each node a square influence area with size equal to  $l_y$  (i.e., the base size of the element) and centered in the node. Then, we consider the points that belong to the influence area: if the number of the detached points is greater than the number of the attached ones, the node is assumed to be detached.

In Fig. 7.20 we show the simulation results in terms of residual stresses at the end of the printing process (a), at the end of the cooling process (b) and after the part detachment from the building plate (c).

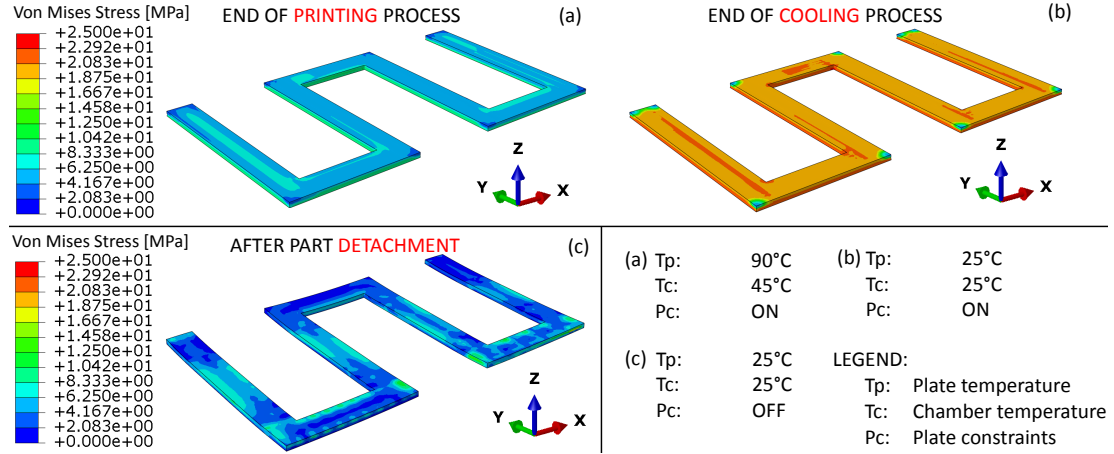


Figure 7.20: Von Mises stress at significant time instants of the simulation. Residual stresses increase during the cooling process due to the shrinking effect. Residual stresses are, finally, relaxed after the constraints removal

We observe a consistent increase of the residual stresses between the end of the printing process and the end of the cooling process. This effect arises due to the constraints applied on the bottom of the model that does not allow the planar shrinking of the part. After removing the constraints corresponding to the detached nodes, we can appreciate the relaxation of the residual stresses due to the release of the elastic strain energy.

Figure 7.21 shows the simulated Z axis displacements at the end of the printing process (a), at the end of the cooling process (b) and after the part detachment from the building plate (c), respectively. We appreciate how the model exhibits a shrinking effect during the cooling process and how, after part detachment, the deformed shape is qualitatively similar to the experimental results proposed in Fig. 7.18. In particular we can observe that the maximum displacement is in correspondence of corner A; furthermore we appreciate the same displacement path on the sides along X direction.

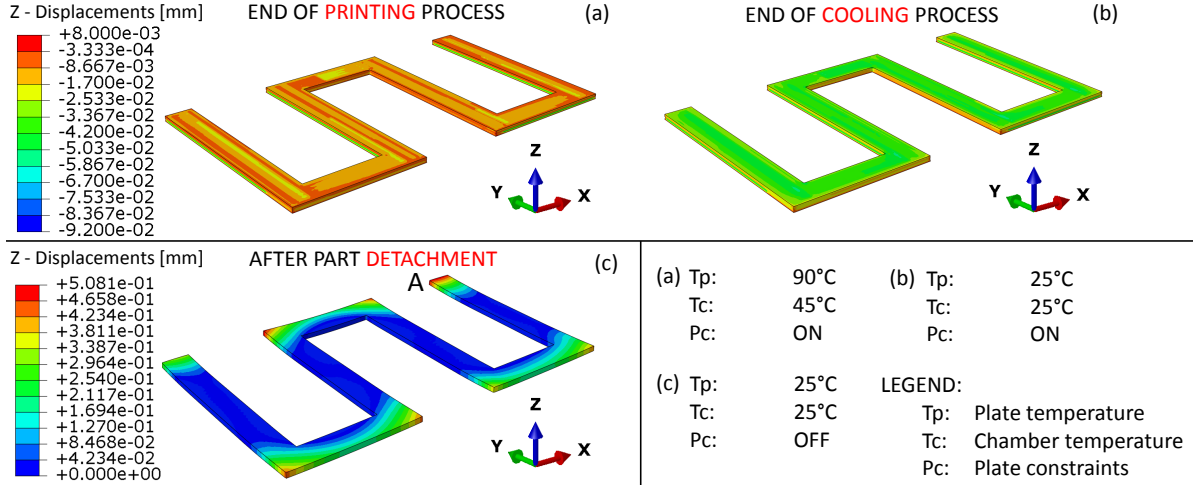


Figure 7.21: Z axis displacements at significant time instants of the simulation. Displacements at the end of both printing and cooling process are of an order of magnitude lower than the displacements after part detachment

Finally, we observe that the displacements after constraints removal are of an order of magnitude greater than the displacements during printing and cooling process.

Test Point	$u_z^1$	$u_z^2$	$u_z^3$	$u_z^4$	$u_z^m$	$u_z^h$	$u_z^m - u_z^h$	$\frac{(u_z^m - u_z^h)}{u_z^m}$
	$[\mu m]$	$[\mu m]$	$[\mu m]$	$[\mu m]$	$[\mu m]$	$[\mu m]$	$[\mu m]$	$[\%]$
S-1	315	254	331	397	324	376	-52	-16.0
S-2	226	219	245	231	230	269	-39	-16.8
S-3	305	251	329	243	282	382	-100	-35.5
S-4	412	353	337	393	374	348	26	6.9
S-5	323	273	302	293	298	268	30	10.0
S-6	341	263	412	387	351	372	-21	-6.1
S-7	242	201	315	145	226	296	-70	-31.1
S-8	351	248	298	367	316	412	-96	-30.4
S-9	214	227	302	295	260	256	4	1.3
S-10	234	241	206	332	253	422	-169	-66.5
S-11	424	553	622	578	544	508	36	6.7

Table 7.7: Experimental and numerical values of Z axis displacements on the planar spring test points. The errors are calculated between the average of the experimental results  $u_z^m$  and simulation results  $u_z^h$  (measured in  $\mu m$ )

In Tab. 7.7 we report the Z axis displacements of the four samples in the test points. We compare the experimental displacements with the numerical ones and we evaluate the point-wise errors.

We can observe that the highest point-wise error is found in correspondence of point S-10 (see Fig. 7.9) where the simulation overestimate the experimental displacement of about 66.5%. In test points S-3, S-7, and S-8 the error is around 30%, while in the other test points

is always below 20%.

Finally, from the results of Tab. 7.7, we obtain the following coefficient of variation:

$$CV = 23.5\%$$

Looking at the point-wise errors we notice that the larger errors are caused by an overestimation of the displacements. The source of this error must be sought in the adopted detachment procedure (see Section 7.0.4). The real detaching process occurs when the stresses exceed the adhesion force, thus part of the strain energy is spent to *break* the constraint generated by the adhesion force. In the simulated detachment process, instead, no dissipation of strain energy occurs since constraints are simply removed in correspondence of the detached points and, therefore, the numerical displacements exceed the experimental ones. Finally, another possible source of error may consist in a non-perfect matching between the physical detached points and the finite element detached nodes.

#### 7.1.4 Bridge model

The bridge model is significantly different from the planar spring, since, even if the base sizes are comparable, the height of the bridge is an order of magnitude larger than the planar spring height. The bridge has been printed using rafts; furthermore the printing process involves two important issues:

- o The *infill path* of the model is 30%, meaning that not all the elements will be activated during the simulation;
- o The printing process needs *support structures* among the pillars. In the proposed framework we assume that, during the printing and the cooling process, the component is perfectly attached to the supports; as a consequence we do not simulate the printing process of the support structures, but we, simply, replace them with perfect clamps in correspondence of the bottom parts of the deck among the pillars (which would be in contact with the support structures). Besides leading to a much faster simulation, this approach is consistent with the physical process because the last layers of the supports are larger than the underlying layers and larger than the bridge deck; moreover in these layers the adopted filament dimensions are larger than in the other layers. This solution increases the stiffness of the supports, favoring the clamping of the bridge deck with the support structures.

Figure 7.22 shows the sample before and after the supports removal. At the end of the cooling process the bridge is perfectly attached to the support structures; after support removal, the bridge shows a remarkable warpage. Furthermore, we observe an anomalous indentation between the top of the external pillars and the deck of the bridge. The physical supports removal can be considered an instantaneous process, therefore our simulated detaching procedure (Section 7.0.4) is fully consistent with the physics of the problem.

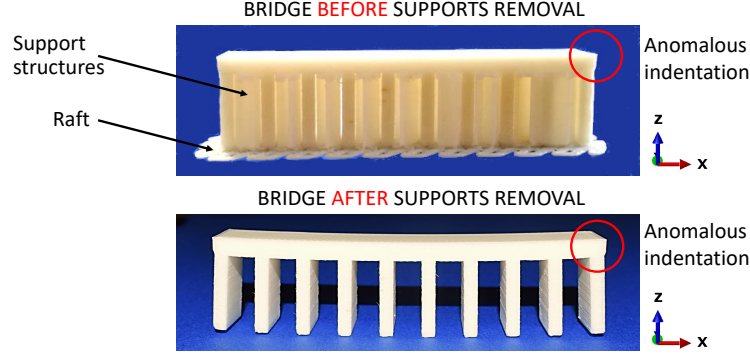


Figure 7.22: Bridge model before and after the supports removal. A warpage effect is clearly evident on the upper surface of the model after support removal

We observe that the deformed structure is symmetric with respect to both X-Z and Y-Z plane; moreover, when the bridge is positioned on a horizontal planar surface, only the two central pillars touch the planar surface, while the other pillars result detached. During the simulation of the printing process, we impose Dirichlet boundary conditions setting all the displacements components to zero on the bottom nodes; then, during the detachment simulation we have removed all the constraints except on the two central pillars. We remark that this assumption does not affect in any way the final deformed shape of the model, which could also be obtained with other constraint configurations and imposing a rigid motion. In Figure 7.23 we show the results of the experimental measurements of the bridge.

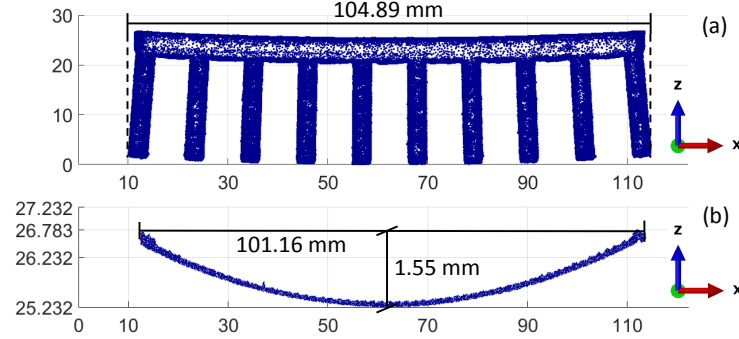


Figure 7.23: Experimental measurements of the bridge model. (a): XZ surface of the model; (b) detail of the upper surface of the model

We present the XZ surface (a) and a detail of X-axis and Z-axis displacements of the upper surface of the bridge (b). In Fig. 7.24 we show the simulation results in terms of residual stresses at the end of the printing process (a), at the end of the cooling process (b), and after the supports removal (c). During the cooling process residual stresses significantly increase due to the shrinking effect and the presence of the constraints. After support removal from the building plate, the residual stresses partially relax and part deformation takes place. Furthermore, we can appreciate how the highest stresses are located in correspondence of the interface between the pillars and the deck.

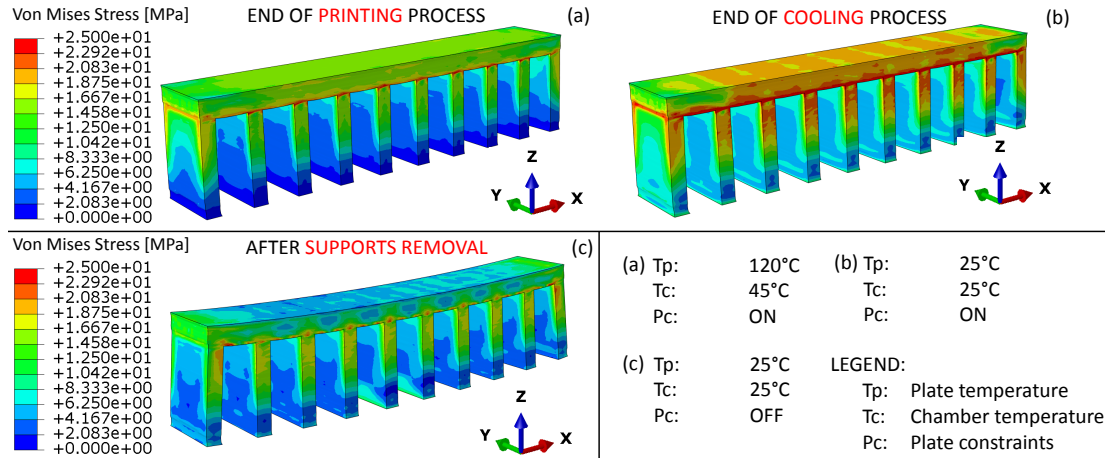


Figure 7.24: Von Mises stress at significant time instants of the simulation. Residual stresses increase during the cooling process due to the shrinking effect. Residual stresses are, finally, relaxed after the constraints removal

Figure 7.25 shows the numerical Z axis displacements at the end of the printing process (a), at the end of the cooling process (b), and after the supports removal (c). Looking at the displacements, we appreciate a slight shrinking effect after the cooling process and we notice that the deformed shape after support removal is qualitatively similar to the experimental one. Furthermore, we observe that the simulation is able to predict also the anomalous indentation between the external pillars and the deck.

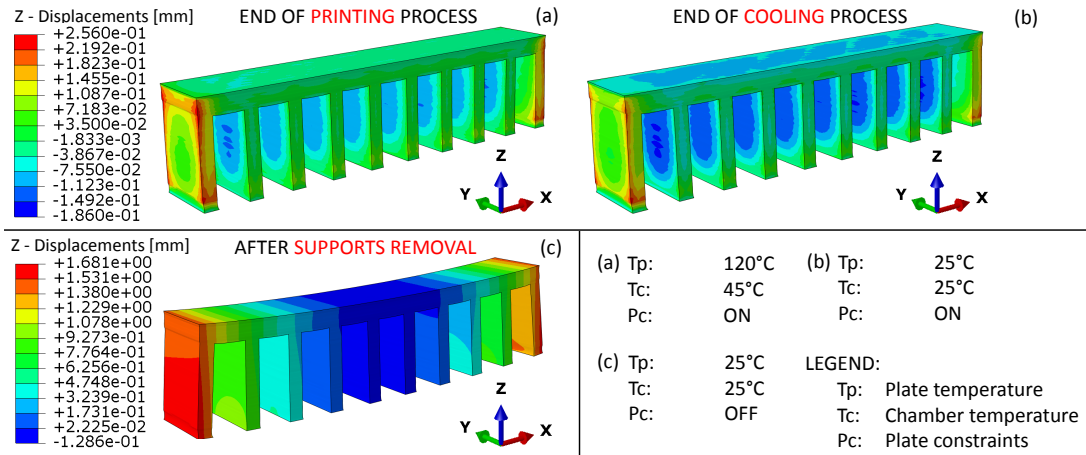


Figure 7.25: Z axis displacements at significant time instants of the simulation. A shrinking effect is detected during the cooling process and the indentation between the external pillars and the deck of the bridge is evident in the simulation

Fig. 7.26 shows the anomalous indentation in correspondence of the interface between the external pillars and the deck of the bridge.

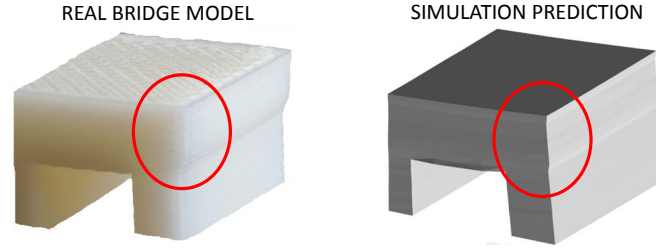


Figure 7.26: Detail of the indentation between the top of the external pillars and the deck of the bridge. The simulation is able to predict this anomalous effect

As first quantitative comparison between simulation and experimental results, we study the characteristics of the upper surface of the bridge after support removal. In Fig. 7.27 we show the X-axis (a) and the Z-axis (b) displacements of XZ surface of the bridge. To analyze the upper surface of the part, we consider the Z-axis displacements in correspondence of the center and the X-axis shortening.

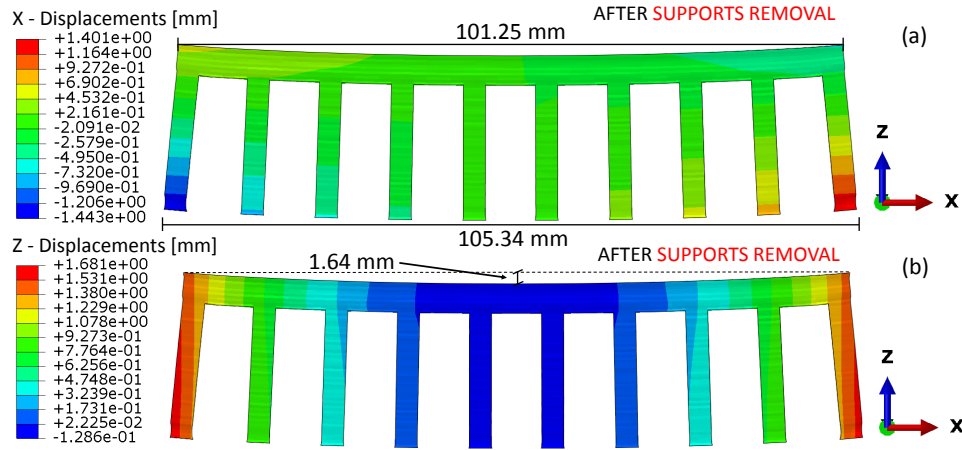


Figure 7.27: X axis and Z axis displacements of the XZ surface of the bridge

The relative displacement error between numerical and experimental measurements is equal to 5.9%. X-axis shortening is calculated starting from the nominal length of the bridge which is equal to 102.5 mm (see Fig. 7.7b)). The relative shortening error between numerical and experimental measurements is equal to 6.7%. An analogous procedure is adopted to evaluate the X-axis elongation of the bottom surface of the bridge. In this case, the relative error between numerical and experimental measurements is equal to 18.8%.

In Table 7.8 we report the Z axis displacements of the considered the test points. The experimental displacements are compared with the numerical ones and the point-wise errors are calculated. All the errors are below 20% and in all the points the simulation overestimate the numerical displacements. Furthermore it is interesting to notice that the errors of the bottom surface test points B-1:B-6 (see Fig. 7.9) are higher than 10%, while the errors of the top surface test points B-7:B12 are lower than 10%.



Test Point	$u_z$ [ $\mu m$ ]	$u_z^h$ [ $\mu m$ ]	$u_z - u_z^h$ [ $\mu m$ ]	$\frac{(u_z - u_z^h)}{u_z}$ [%]
B-1	1824	2074	-250	-13.7
B-2	961	1143	-182	-18.9
B-3	553	650	-97	-17.5
B-4	548	639	-91	-16.6
B-5	984	1136	-152	-15.4
B-6	1831	2023	-192	-10.5
B-7	1417	1469	-52	-3.7
B-8	851	874	-23	-2.7
B-9	409	437	-28	-6.8
B-10	413	427	-14	-3.4
B-11	841	855	14	-1.7
B-12	1402	1444	-42	-3.0

Table 7.8: Experimental and numerical measurements of Z axis displacements on bridge model test points. The errors are calculated between the experimental results  $u_z$  and simulation results  $u_z^h$  (measured in  $\mu m$ )

Finally, we obtain the following coefficient of variation:

$$CV = 12.2\%$$

The global simulation error is lower than the one obtained for the planar spring. This result was expected considering that the detaching procedure, in this case, is more repeatable and thus, more consistent with the physical one.

## 7.2 Conclusions

In this work, using the commercial software Abaqus, we have developed a FEA framework to simulate the Fused Deposition Modeling process. The simulation framework has been analyzed in detail, with a particular focus on the sequential element activation scheme; furthermore, we have investigated the influence of the simulation parameters on the results of the analysis. We concluded that:

- o The *time step* has a large influence on the the local temperature distribution during the printing process, while it has a minor influence on the mechanical analysis results;
- o The *meshing strategy* is important to reproduce the real printing process. A finer meshing strategy is suggested in case of *small* models to investigate local effects, while a coarser meshing strategy is recommended in case of *large* models in which the local effects are negligible, where *small* and *large* refers to the dimensions of the models in comparison with the filament dimensions;
- o The *constitutive model* must be calibrated with accuracy. In particular, temperature dependency of Young's modulus and yield stress limit must be taken into account in order to obtain physically acceptable results.

With the proposed framework we have simulated two case studies: a planar spring and a bridge model, studying and adopting, for the simulation parameters, a suitable trade-off between computational time and results accuracy. According to the real printing process, two different detachment procedures have been considered and the limitations of each model have been discussed in detail. We have validated the simulation outcomes through a comparison with experimental tests. We are able to capture correctly the deformed shape of the models, furthermore, 23% and 12% vertical displacement errors have been detected for the planar spring and the bridge model, respectively. These errors can be justified by the adopted simplified modeling assumptions but also by measurement errors. We showed that the temperature dependency of some physical properties of the extruded filament, as the yielding stress and Young's modulus, must be considered to obtain physically acceptable results and cannot be neglected when performing FDM process simulations.

### 7.3 Limitations

The major limitation of this study lies in the execution of numerical simulations without considering any type of adhesion model between the first layer and the building plate. The introduction of any type of adhesion model requires the execution of complex experimental tests, carried out at different temperatures, to measure the adhesion force between the plate and the filament. The procedure proposed in the present work is able to capture the deformed shape of the printed component and obtain an acceptable agreement with experimental data.

## Chapter 8

# Final remarks

In this thesis we have faced the simulation of two widely diffused 3D printing technologies: Powder Bed Fusion (PBF) and Fused Deposition Modeling (FDM).

The first part of this work is dedicated to PBF. We have analyzed the physical aspects involved within this very complex technology; in particular we have focused on phase-change modeling and thermo-fluid dynamic evolution of the melt pool which influence shape and mechanical properties of the final part. From a literature review it merged that there are two levels to simulate PBF process: the powder level and the continuum level; advantages and disadvantages of each technology has been discussed in detail. In this thesis we have investigated both the simulation approaches.

Powder level simulations aim to predict melt pool evolution and stability during the printing process. The only method which has revealed able to simulate such complex process is the lattice Boltzmann method (LBM). Starting from the kinetic theory of gases we have derived the Boltzmann equation and, finally, the lattice Boltzmann scheme; moreover we have proved that LBM mathematically represents a *non conventional* method to solve Navier-Stokes and Advection-Diffusion equations. We have adopted the lattice Boltzmann method to solve some interesting thermo fluid dynamic problems, including droplet wetting at variable temperatures and solid-liquid phase change. The next step of our work will be to include the phase change within the thermo-fluid dynamic models so to reproduce the entire melting process.

Continuum level simulations are used to predict temperature distributions, residual stresses and deformations on the final part. In this work we have set up a finite element scheme based on sequential element activation in which the laser scan path is accurately taken into account as well as the laser power distribution. We have used the developed scheme to simulate the heat source interaction with a domain constituted of two layers of powder. In particular we have studied the influence of several process parameters on temperature and residual stress distributions, showing that these distributions are dependent on laser energy density. Finally, using a coarsest meshing strategy, we have simulated an entire part produced with SLM and we have evaluated the displacements after detaching from the building plate.

The second part of this thesis is dedicated to Fused Deposition Modeling (FDM). We have analyzed the physical aspects involved within this technology with particular attention to the bonding between the filaments and the adhesion force between the plastic filaments and the building plate. Like for PBF, also in case of FDM, the process can be simulated at the filament/fiber level and at the component level. In this work we have developed an

uncoupled thermo-mechanical finite element method, based on sequential element activation, to reproduce with high fidelity FDM printing process starting from the informations contained in the G-Code file. The simulations have been validated through a comparison between the numerical displacements and the ones obtained through experimental tests. Next step of our work will be to include the adhesion force in our framework.

In conclusion in this thesis we have studied in detail the critical aspects of PBF and FDM; moreover we have set up a practical, even if approximated framework, to predict residual stress and displacement fields in 3D printed parts. In case of SLM the predicted displacements revealed to be consistent with the order of magnitude of literature results. In case of FDM, instead, the comparison with the experimental data revealed the method to be able to predict the displacements with good accuracy. The authors hope that this thesis could be a good instrument to have a better comprehension of AM processes and to set up a practical and efficient simulation framework.

# Bibliography

- M. Cotteleer and J. Joyce. 3d opportunity: Additive manufacturing paths to performance, innovation, and growth. *Deloitte Review*, 14:5–19, 2014.
- Wohlers Associates. *Wohlers Report 2017 3D Printing and Additive Manufacturing State of the Industry*. Wohlers Associates, 2017.
- S. Siddique, M. Imran, E. Wycisk, C. Emmelmann, and F. Walther. Influence of process-induced microstructure and imperfections on mechanical properties of alSi12 processed by selective laser melting. *Journal of Materials Processing Technology*, 221:205–213, 2015.
- K. Prashanth, S. Scudino, H. Klauss, K. Surreddi, L. Löber, Z. Wang, A. Chaubey, U. Kühn, and J. Eckert. Microstructure and mechanical properties of al–12Si produced by selective laser melting: Effect of heat treatment. *Materials Science and Engineering: A*, 590:153–160, 2014.
- C. Song, Y. Yang, Y. Wang, D. Wang, and J. Yu. Research on rapid manufacturing of CoCrMo alloy femoral component based on selective laser melting. *The International Journal of Advanced Manufacturing Technology*, 75(1-4):445–453, 2014.
- A. Takaichi, T. Nakamoto, N. Joko, N. Nomura, Y. Tsutsumi, S. Migita, H. Doi, S. Kurosu, A. Chiba, and N. Wakabayashi. Microstructures and mechanical properties of Co–29Cr–6Mo alloy fabricated by selective laser melting process for dental applications. *Journal of the mechanical behavior of biomedical materials*, 21:67–76, 2013.
- B. Vrancken, L. Thijs, J. Kruth, and J. Van Humbeeck. Heat treatment of Ti6Al4v produced by Selective Laser Melting: Microstructure and mechanical properties. *Journal of Alloys and Compounds*, 541:177–185, 2012.
- M. Simonelli, Y. Tse, and C. Tuck. Effect of the build orientation on the mechanical properties and fracture modes of SLM Ti–6Al–4V. *Materials Science and Engineering: A*, 616:1–11, 2014.
- Q. Jia and D. Gu. Selective laser melting additive manufacturing of Inconel 718 superalloy parts: Densification, microstructure and properties. *Journal of Alloys and Compounds*, 585: 713–721, 2014.
- D. Zhang, W. Niu, X. Cao, and Z. Liu. Effect of standard heat treatment on the microstructure and mechanical properties of selective laser melting manufactured Inconel 718 superalloy. *Materials Science and Engineering: A*, 644:32–40, 2015.

- AM. Prokhorov. *Laser Heating of Metals*. CRC Press, 2018.
- I. Sani. *Selective Laser Melting process simulation: advancements towards a cost-effective model*. PhD thesis, 2017.
- Y. Shi and Y. Zhang. Simulation of random packing of spherical particles with different size distributions. In *ASME 2006 International Mechanical Engineering Congress and Exposition*, pages 539–544, 2006.
- T. Scharowsky, A. Bauereiß, R. Singer, and C. Körner. Observation and numerical simulation of melt pool dynamic and beam powder interaction during selective electron beam melting. In *Proceedings of the Solid Freeform Fabrication Symposium*, pages 815–820, 2012.
- E. Attar and C. Körner. Lattice boltzmann method for dynamic wetting problems. *Journal of colloid and interface science*, 335(1):84–93, 2009.
- A. Block-Bolten and TW. Eagar. Metal vaporization from weld pools. *Metallurgical Transactions*, 15(3):461–469, 1984.
- N. Aboulkhair, N. Everitt, T. Ashcroft, and C. Tuck. Reducing porosity in alsil0mg parts processed by selective laser melting. *Additive Manufacturing*, 1:77–86, 2014.
- G. Strano, L. Hao, R. Everson, and K. Evans. Surface roughness analysis, modelling and prediction in selective laser melting. *Journal of Materials Processing Technology*, 213(4): 589–597, 2013.
- M. Jamshidinia and R. Kovacevic. The influence of heat accumulation on the surface roughness in additive manufacturing by electron beam melting (ebm). In *Proceedings-ASPE 2014 Spring Topical Meeting: Dimensional Accuracy and Surface Finish in Additive Manufacturing*, pages 45–50, 2014.
- L. Papadakis, A. Loizou, J. Risse, and J. Schrage. Numerical computation of component shape distortion manufactured by selective laser melting. *Procedia CIRP*, 18:90–95, 2014.
- S. Afazov, W. Denmark, B. Toralles, A. Holloway, and A. Yaghi. Distortion prediction and compensation in selective laser melting. *Additive Manufacturing*, 17:15–22, 2017.
- C. Körner, A. Bauereiß, and E. Attar. Fundamental consolidation mechanisms during selective beam melting of powders. *Modelling and Simulation in Materials Science and Engineering*, 21(8):085011, 2013.
- R. Ammer, M. Markl, U. Ljungblad, C. Körner, and U. Råde. Simulating fast electron beam melting with a parallel thermal free surface Lattice Boltzmann method. *Computers and Mathematics with Applications*, 67(2):318–330, 2014a.
- M. Markl, A. Bauereiß, A. Rai, and C. Körner. Numerical investigations of selective electron beam melting on the powder scale. In *Proceedings of the Fraunhofer Direct Digital Manufacturing Conference*, 2016.

- W. King, A. Anderson, R. Ferencz, N. Hodge, C. Kamath, and S. Khairallah. Overview of modelling and simulation of metal powder bed fusion process at Lawrence Livermore National Laboratory. *Materials Science and Technology*, 31(8):957–968, 2015.
- A. Hussein, L. Hao, C. Yan, and R. Everson. Finite element simulation of the temperature and stress fields in single layers built without-support in selective laser melting. *Materials & Design (1980-2015)*, 52:638–647, 2013.
- C. Li, J. Liu, X. Fang, and Y. Guo. Efficient predictive model of part distortion and residual stress in selective laser melting. *Additive Manufacturing*, 17:157–168, 2017.
- C. Li, C. Fu, Y. Guo, and F. Fang. A multiscale modeling approach for fast prediction of part distortion in selective laser melting. *Journal of Materials Processing Technology*, 229:703–712, 2016a.
- C. Li, Y. Guo, X. Fang, and F. Fang. A scalable predictive model and validation for residual stress and distortion in selective laser melting. *CIRP Annals*, 2018.
- Q. Zou and X. He. On pressure and velocity boundary conditions for the Lattice Boltzmann BGK model. *Physics of Fluids*, 9(6):1591–1598, 1997.
- U. Ghia, K. Ghia, and C. Shin. High Re solutions for incompressible flow using the Navier-Stokes equations and a multigrid method. *Journal of Computational Physics*, 48(3):387–411, 1982.
- C. Liu, K. Lin, C. Mai, and C. Lin. Thermal boundary conditions for thermal Lattice Boltzmann simulations. *Computers and Mathematics with Applications*, 59(7):2178–2193, 2010.
- R. Clever and F. Busse. Transition to time-dependent convection. *Journal of Fluid Mechanics*, 65(4):625–645, 1974.
- X. Shan and H. Chen. Lattice boltzmann model for simulating flows with multiple phases and components. *Physical Review*, 47(3):1815, 1993.
- X. He and G. Doolen. Thermodynamic foundations of kinetic theory and Lattice Boltzmann models for multiphase flows. *Journal of Statistical Physics*, 107(1-2):309–328, 2002.
- N. Thürey, C. Körner, and U. Rude. Interactive free surface fluids with the lattice Boltzmann method. *Technical Report 05-4. University of Erlangen-Nuremberg, Germany*, 2005.
- J. Cantrell, S. Rohde, D. Damiani, R. Gurnani, L. DiSandro, J. Anton, A. Young, et al. Experimental characterization of the mechanical properties of 3d-printed ABS and polycarbonate parts. *Rapid Prototyping Journal*, 23(4):811–824, 2017.
- B. Rankouhi, S. Javadpour, F. Delfanian, and T. Letcher. Failure analysis and mechanical characterization of 3d printed ABS with respect to layer thickness and orientation. *Journal of Failure Analysis and Prevention*, 16(3):467–481, 2016.

- K. Weiss, N. Bagrets, C. Lange, W. Goldacker, and J. Wohlgemuth. Thermal and mechanical properties of selected 3D printed thermoplastics in the cryogenic temperature regime. In *IOP Conference Series: Materials Science and Engineering*, volume 102, page 012022. IOP Publishing, 2015.
- A. Bagsik, V. Schöppner, and E. Klemp. FDM part quality manufactured with Ultem\* 9085. In *14th international scientific conference on polymeric materials*, volume 15, pages 307–315, 2010.
- P. Gurralla and S. Regalla. Part strength evolution with bonding between filaments in fused deposition modelling: This paper studies how coalescence of filaments contributes to the strength of final FDM part. *Virtual and Physical Prototyping*, 9(3):141–149, 2014.
- C. Bellehumeur, L. Li, Q. Sun, and P. Gu. Modeling of bond formation between polymer filaments in the fused deposition modeling process. *Journal of Manufacturing Processes*, 6(2):170–178, 2004.
- R. Sanatgar, C. Campagne, and V. Nierstrasz. Investigation of the adhesion properties of direct 3d printing of polymers and nanocomposites on textiles: Effect of FDM printing process parameters. *Applied Surface Science*, 403:551–563, 2017.
- H. Xia, J. Lu, S. Dabiri, and G. Tryggvason. Fully Resolved Numerical Simulations of Fused Deposition Modeling. Part I-Fluid Flow. *arXiv preprint arXiv:1711.05940*, 2017.
- Y. Zhang and K. Chou. A parametric study of part distortions in fused deposition modelling using three-dimensional finite element analysis. *Proceedings of the Institution of Mechanical Engineers, Part B: Journal of Engineering Manufacture*, 222(8):959–968, 2008.
- Gammadot Rheology Testing And Consultancy. Acrylonitrile Butadiene Styrene thermal properties, 2004. URL <http://gammadot.com/Techzone/nexus/ABS/ABSsp.htm>.
- P. Song, Z. Cao, Q. Meng, S. Fu, Z. Fang, Q. Wu, and J. Ye. Effect of lignin incorporation and reactive compatibilization on the morphological, rheological, and mechanical properties of ABS resin. *Journal of Macromolecular Science, Part B*, 51(4):720–735, 2012.
- J. Richeton, S. Ahzi, K. Vecchio, F. Jiang, and R. Adharapurapu. Influence of temperature and strain rate on the mechanical behavior of three amorphous polymers: characterization and modeling of the compressive yield stress. *International journal of solids and structures*, 43(7-8):2318–2335, 2006.
- A. Armillotta, M. Bellotti, and M. Cavallaro. Warpage of FDM parts: Experimental tests and analytic model. *Robotics and Computer-Integrated Manufacturing*, 50:140–152, 2018.
- ASTM. Standard terminology for additive manufacturing technologies. *ASTM International*, 2012.
- H. Lipson and M. Kurman. *Fabricated: The new world of 3D printing*. John Wiley & Sons, 2013.



- The Economist. Mastering the Fourth Industrial Revolution. *The Economist Newspaper Limited*, 2016.
- B. Mueller. Additive manufacturing technologies—Rapid prototyping to direct digital manufacturing. *Assembly Automation*, 32(2), 2012.
- E. Atzeni and A. Salmi. Economics of additive manufacturing for end-usable metal parts. *The International Journal of Advanced Manufacturing Technology*, 62(9):1147–1155, 2012.
- S. Ahn, D. Chun, and W. Chu. Perspective to green manufacturing and applications. *International Journal of Precision Engineering and Manufacturing*, 14(6):873–874, 2013.
- F. Auricchio and S. Marconi. 3D printing: clinical applications in orthopaedics and traumatology. *EFORT open reviews*, 1(5):121–127, 2016.
- The Economist. A printed smile - 3D printing is coming of age as a manufacturing technique. <https://www.economist.com/science-and-technology/2016/04/28/a-printed-smile>, 2016. [Online; accessed 31-July-2018].
- M. Rombouts. *Selective Laser Sintering/Melting of Iron-Based Powders*. PhD thesis, 2006.
- S. Bremen, W. Meiners, and A. Diatlov. Selective laser melting. *Laser Technik Journal*, 9(2): 33–38, 2012.
- L. Murr, S. Gaytan, D. Ramirez, E. Martinez, J. Hernandez, K. Amato, P. Shindo, F. Medina, and R. Wicker. Metal fabrication by additive manufacturing using laser and electron beam melting technologies. *Journal of Materials Science & Technology*, 28(1):1–14, 2012.
- M. Agarwala, D. Bourell, J. Beaman, H. Marcus, and J. Barlow. Direct selective laser sintering of metals. *Rapid Prototyping Journal*, 1(1):26–36, 1995.
- Z. Wang, K. Guan, M. Gao, X. Li, X. Chen, and X. Zeng. The microstructure and mechanical properties of deposited-IN718 by selective laser melting. *Journal of Alloys and Compounds*, 513:518–523, 2012.
- J. Kruth, G. Levy, F. Klocke, and T. Childs. Consolidation phenomena in laser and powder-bed based layered manufacturing. *CIRP annals*, 56(2):730–759, 2007.
- I. Yadroitsev, A. Gusarov, I. Yadroitsava, and I. Smurov. Single track formation in selective laser melting of metal powders. *Journal of Materials Processing Technology*, 210(12):1624–1631, 2010.
- L. Thijs, F. Verhaeghe, T. Craeghs, J. Van Humbeeck, and J-P. Kruth. A study of the microstructural evolution during selective laser melting of Ti6Al4V. *Acta Materialia*, 58(9):3303–3312, 2010.
- P. Mercelis and J-P. Kruth. Residual stresses in selective laser sintering and selective laser melting. *Rapid Prototyping Journal*, 12(5):254–265, 2006.
- L. Andrews and R. Phillips. *Laser beam propagation through random media*, volume 152. SPIE press Bellingham, WA, 2005.

- M. Markl and C. Körner. Multiscale modeling of powder bed-based additive manufacturing. *Annual Review of Materials Research*, 46:93–123, 2016.
- D. Rosenthal. Mathematical theory of heat distribution during welding and cutting. *Welding Journal*, 46:20, 1941.
- D. Rosenthal. The theory of moving sources of heat and its application to metal treatments. *Transactions of the ASME*, 46:852, 1946.
- H. Cline and T. Anthony. Heat treating and melting material with a scanning laser or electron beam. *Journal of Applied Physics*, 48(9):3895–3900, 1977.
- R. Brockmann, K. Dickmann, P. Geshev, and K. Matthes. Calculation of laser-induced temperature field on moving thin metal foils in consideration of Stefan problem. *Optics & Laser Technology*, 35(2):115–122, 2003.
- S. Kou, S. Hsu, and R. Mehrabian. Rapid melting and solidification of a surface due to a moving heat flux. *Metallurgical Transactions*, 12(1):33–45, 1981.
- P. Cheng and S. Lin. An analytical model for the temperature field in the laser forming of sheet metal. *Journal of Materials Processing Technology*, 101(1-3):260–267, 2000.
- A. Pinkerton and L. Li. Modelling the geometry of a moving laser melt pool and deposition track via energy and mass balances. *Journal of Physics*, 37(14):1885, 2004.
- T. Debroy and S. David. Physical processes in fusion welding. *Reviews of modern physics*, 67(1):85, 1995.
- T. Bergman, F. Incropera, D. DeWitt, and A. Lavine. *Fundamentals of heat and mass transfer*. John Wiley & Sons, 2011.
- S. Bland and N. Aboulkhair. Reducing porosity in additive manufacturing. *Metal Powder Report*, 70(2):79–81, 2015.
- K. Vafai. *Handbook of porous media*. Crc Press, 2015.
- J. Maxwell. *Electricity and Magnetism* Clarendon Press, 1873.
- A. Luikov, A. Shashkov, L. Vasiliev, and Y. Fraiman. Thermal conductivity of porous systems. *International Journal of Heat and Mass Transfer*, 11(2):117–140, 1968.
- Y. Chiew and E. Glandt. The effect of structure on the conductivity of a dispersion. *Journal of Colloid and Interface Science*, 94(1):90–104, 1983.
- Z. Yinping and L. Xingang. Numerical analysis of effective thermal conductivity of mixed solid materials. *Materials & Design*, 16(2):91–95, 1995.
- H. Kou, K. Lu, and C. Yu. Effective thermal conductivity of composite material with spherical inclusions in orthorhombic structure. *Computers & structures*, 53(3):569–577, 1994.

- N. Tolochko, M. Arshinov, A. Gusarov, V. Titov, T. Laoui, and I. Froyen. Mechanisms of selective laser sintering and heat transfer in ti powder. *Rapid prototyping journal*, 9(5): 314–326, 2003.
- Y. Zeldovich and Y. Raizer. *Physics of shock waves and high-temperature hydrodynamic phenomena*. Courier Corporation, 2012.
- A. Klassen, A. Bauereiß, and C. Körner. Modelling of electron beam absorption in complex geometries. *Journal of Physics*, 47(6):065307, 2014.
- D. Swinehart. The beer-lambert law. *Journal of chemical education*, 39(7):333, 1962.
- N. Tolochko, Y. Khlopkov, S. Mozzharov, M. Ignatiev, T. Laoui, and V. Titov. Absorptance of powder materials suitable for laser sintering. *Rapid Prototyping Journal*, 6(3):155–161, 2000.
- A. Gusarov and J. Kruth. Modelling of radiation transfer in metallic powders at laser treatment. *International Journal of Heat and Mass Transfer*, 48(16):3423–3434, 2005.
- X. Wang, T. Laoui, J. Bonse, J. Kruth, B. Lauwers, and L. Froyen. Direct selective laser sintering of hard metal powders: experimental study and simulation. *The International Journal of Advanced Manufacturing Technology*, 19(5):351–357, 2002.
- A. Gusarov and I. Smurov. Modeling the interaction of laser radiation with powder bed at selective laser melting. *Physics Procedia*, 5:381–394, 2010.
- D. Drouin, A. Couture, J. Réal, D. Dany, X. Tastet, V. Aimez, and R. Gauvin. CASINO V2. 42—A Fast and Easy-to-use Modeling Tool for Scanning Electron Microscopy and Microanalysis Users. *Scanning*, 29(3):92–101, 2007.
- G. Comini, S. Del Guidice, R. Lewis, and O. Zienkiewicz. Finite element solution of non-linear heat conduction problems with special reference to phase change. *International Journal for Numerical Methods in Engineering*, 8(3):613–624, 1974.
- D. Chatterjee and S. Chakraborty. An enthalpy based Lattice Boltzmann model for diffusion dominated solid liquid phase transformation. *Physics Letters*, 341(1-4):320–330, 2005.
- M. Eshraghi and S. Felicelli. An implicit Lattice Boltzmann model for heat conduction with phase change. *International Journal of Heat and Mass Transfer*, 55(9-10):2420–2428, 2012.
- Y. Cao, A. Faghri, and W. Chang. A numerical analysis of Stefan problems for generalized multi-dimensional phase-change structures using the enthalpy transforming model. *International journal of heat and mass transfer*, 32(7):1289–1298, 1989.
- D. Celentano, E. Oñate, and S. Oller. A temperature-based formulation for finite element analysis of generalized phase-change problems. *International Journal for Numerical Methods in Engineering*, 37(20):3441–3465, 1994.
- T. Chen and Y. Zhang. Thermal modeling of metal powder-based selective laser sintering. *Proc. Solid Freeform Fabrication*, pages 356–69, 2005.

- P. Meakin and R. Jullien. Restructuring effects in the rain model for random deposition. *Journal de Physique*, 48(10):1651–1662, 1987.
- TI Zohdi. Additive particle deposition and selective laser processing-a computational manufacturing framework. *Computational Mechanics*, 54(1):171–191, 2014.
- F. Fowkes. *Contact angle, wettability, and adhesion*. ACS Publications, 1964.
- M. Schrader. Young-dupre revisited. *Langmuir*, 11(9):3585–3589, 1995.
- E. Bormashenko, R. Pogreb, G. Whyman, Y. Bormashenko, and M. Erlich. Vibration-induced Cassie-Wenzel wetting transition on rough surfaces. *Applied physics letters*, 90(20):201917, 2007.
- R. Hoffman. A study of the advancing interface. I. Interface shape in liquid—gas systems. *Journal of colloid and interface science*, 50(2):228–241, 1975.
- S. Schiaffino and A. Sonin. Molten droplet deposition and solidification at low weber numbers. *Physics of Fluids*, 9(11):3172–3187, 1997a.
- R. German. Supersolidus liquid phase sintering. I: Process review. *International journal of powder metallurgy*, 26(1):23–34, 1990.
- R. German. Powder metallurgy science. *Metal Powder Industries Federation*, 1984.
- M. Pasandideh-Fard, Y. Qiao, S. Chandra, and J. Mostaghimi. Capillary effects during droplet impact on a solid surface. *Physics of fluids*, 8(3):650–659, 1996.
- P. Raiskinmäki, A. Koponen, J. Merikoski, and J. Timonen. Spreading dynamics of three-dimensional droplets by the lattice-boltzmann method. *Computational Materials Science*, 18(1):7–12, 2000.
- H. Huang, J. Thorne, M. Schaap, and M. Sukop. Proposed approximation for contact angles in shan-and-chen-type multicomponent multiphase lattice boltzmann models. *Physical Review E*, 76(6):066701, 2007.
- E. Attar and C. Körner. Lattice boltzmann model for thermal free surface flows with liquid–solid phase transition. *International Journal of Heat and Fluid Flow*, 32(1):156–163, 2011.
- S. Coriell, S. Hardy, and Cordes. Stability of liquid zones. *Journal of Colloid and Interface Science*, 60(1):126–136, 1977.
- N. Bezdeneynykh, J. Meseguer, and Perales. An experimental analysis of the instability of nonaxisymmetric liquid bridges in a gravitational field. *Physics of Fluids*, 11(10):3181–3185, 1999.
- L. Rayleigh. Xvi. on the instability of a cylinder of viscous liquid under capillary force. *The London, Edinburgh, and Dublin Philosophical Magazine and Journal of Science*, 34(207):145–154, 1892.
- S. Chandrasekar. *Hydrodynamic and hydromagnetic stability*. Claredron Press, 1970.

- S. Schiaffino and A. Sonin. Formation and stability of liquid and molten beads on a solid surface. *Journal of fluid mechanics*, 343:95–110, 1997b.
- R. Roy and L. Schwartz. On the stability of liquid ridges. *Journal of Fluid Mechanics*, 391:293–318, 1999.
- T. Baer, R. Cairncross, P. Schunk, R. Randall, R. Rao, and P. Sackinger. A finite element method for free surface flows of incompressible fluids in three dimensions. part ii. dynamic wetting lines. *International Journal for Numerical Methods in Fluids*, 33(3):405–427, 2000.
- P. Raiskinmäki, A. Shakib-Manesh, A. Jäsberg, A. Koponen, J. Merikoski, and J. Timonen. Lattice-boltzmann simulation of capillary rise dynamics. *Journal of statistical physics*, 107(1-2):143–158, 2002.
- B. Ahrenholz, J. Tölke, P. Lehmann, A. Peters, A. Kaestner, M. Krafczyk, and W. Durner. Prediction of capillary hysteresis in a porous material using lattice-boltzmann methods and comparison to experimental data and a morphological pore network model. *Advances in Water Resources*, 31(9):1151–1173, 2008.
- A. Gusarov, I. Yadroitsev, P. Bertrand, and I. Smurov. Heat transfer modelling and stability analysis of selective laser melting. *Applied Surface Science*, 254(4):975–979, 2007.
- M. Zäh and S. Lutzmann. Modelling and simulation of electron beam melting. *Production Engineering*, 4(1):15–23, 2010.
- B. Cheng and K. Chou. Melt pool geometry simulations for powder-based electron beam additive manufacturing. In *24th Annual International Solid Freeform Fabrication Symposium-An Additive Manufacturing Conference, Austin, TX, USA*, pages 644–654, 2013.
- B. Keene. Review of data for the surface tension of iron and its binary alloys. *International Materials Reviews*, 33(1):1–37, 1988.
- C. Chan, J. Mazumder, and M. Chen. Three-dimensional axisymmetric model for convection in laser-melted pools. *Material Science and Technology*, 33(1):306–3011, 1987.
- C. Chan, J. Mazumder, and M. Chen. Effect of surface tension gradient driven convection in a laser melt pool: Three-dimensional perturbation model. *Journal of applied physics*, 64(11):6166–6174, 1988.
- A. Robert and T. Debroy. Geometry of laser spot welds from dimensionless numbers. *Metallurgical and materials transactions*, 32(5):941–947, 2001.
- C. Qiu, C. Panwisawas, M. Ward, H. Basoalto, J. Brooks, and M. Attallah. On the role of melt flow into the surface structure and porosity development during selective laser melting. *Acta Materialia*, 96:72–79, 2015.
- M. Jamshidinia, F. Kong, and R. Kovacevic. Numerical modeling of heat distribution in the electron beam melting® of Ti-6Al-4V. *Journal of Manufacturing Science and Engineering*, 135(6):061010, 2013.

- T. Boublik, V. Fried, and E. Hála. *The Vapour Pressures of Pure Substances: Selected Values of the Temperature Dependence of the Vapour Presses of Some Pure Substances in the Normal and Low Pressure Region*. 1973.
- D. Geiger and Poirier. Transport phenomena in materials processing, the minerals. *Metals and Materials Society*, 1994.
- SI Anisimov. Vaporization of metal absorbing laser radiation. In *30 Years Of The Landau Institute—Selected Papers*, pages 14–15. World Scientific, 1996.
- C. Knight. Theoretical modeling of rapid surface vaporization with back pressure. *AIAA journal*, 17(5):519–523, 1979.
- M. Von Allmen and A. Blatter. *Laser-beam interactions with materials: physical principles and applications*, volume 2. Springer Science & Business Media, 2013.
- F. Gürtler, M. Karg, K. Leitz, and M. Schmidt. Simulation of laser beam melting of steel powders using the three-dimensional volume of fluid method. *Physics Procedia*, 41:881–886, 2013.
- X. Shan and H. Chen. Simulation of nonideal gases and liquid-gas phase transitions by the lattice boltzmann equation. *Physical Review E*, 49(4):2941, 1994.
- S. Gong and P. Cheng. A lattice boltzmann method for simulation of liquid–vapor phase-change heat transfer. *International Journal of Heat and Mass Transfer*, 55(17-18):4923–4927, 2012.
- L. Loh, C. Chua, W. Yeong, J. Song, M. Mapar, S. Sing, Z. Liu, and D. Zhang. Numerical investigation and an effective modelling on the Selective Laser Melting (SLM) process with aluminium alloy 6061. *International Journal of Heat and Mass Transfer*, 80:288–300, 2015.
- E. Louvis, P. Fox, and C. Sutcliffe. Selective laser melting of aluminium components. *Journal of Materials Processing Technology*, 211(2):275–284, 2011.
- K. Osakada and M. Shiomi. Flexible manufacturing of metallic products by selective laser melting of powder. *International Journal of Machine Tools and Manufacture*, 46(11):1188–1193, 2006.
- A. Bauereiß, T. Scharowsky, and C. Körner. Defect generation and propagation mechanism during additive manufacturing by selective beam melting. *Journal of Materials Processing Technology*, 214(11):2522–2528, 2014.
- O. Cansizoglu, O. Harrysson, D. Cormier, H. West, and T. Mahale. Properties of ti–6al–4v non-stochastic lattice structures fabricated via electron beam melting. *Materials Science and Engineering*, 492(1-2):468–474, 2008.
- M. Rombouts, L. Froyen, A. Gusarov, E. Bentefour, and C. Glorieux. Photopyroelectric measurement of thermal conductivity of metallic powders. *Journal of Applied physics*, 97(2):024905, 2005.

- F. Gürtler, M. Karg, M. Dobler, S. Kohl, I. Tzivilsky, and M. Schmidt. Influence of powder distribution on process stability in laser beam melting: analysis of melt pool dynamics by numerical simulations. In *Solid freeform fabrication symposium. SFF, Austin*, pages 1099–1117, 2014.
- J. Li, L. Li, and F. Stott. Thermal stresses and their implication on cracking during laser melting of ceramic materials. *Acta Materialia*, 52(14):4385–4398, 2004.
- K. Dai and L. L. Shaw. Parametric studies of multi-material laser densification. *Materials Science and Engineering*, 430(1-2):221–229, 2006.
- T. Krol, C. Seidel, J. Schilp, M. Hofmann, W. Gan, and M. Zaeh. Verification of structural simulation results of metal-based additive manufacturing by means of neutron diffraction. *Physics Procedia*, 41:849–857, 2013.
- M. Zaeh and G. Branner. Investigations on residual stresses and deformations in selective laser melting. *Production Engineering*, 4(1):35–45, 2010.
- N. Keller, F. Neugebauer, H. Xu, and V. Ploshikhin. Thermo-mechanical simulation of additive layer manufacturing of titanium aerospace structures. In *LightMAT Conference*, volume 3, 2013.
- C. Seidel, M. Zaeh, M. Wunderer, J. Weirather, T. Krol, and M. Ott. Simulation of the Laser Beam Melting Process—Approaches for an Efficient Modelling of the Beam-material Interaction. *Procedia CIRP*, 25:146–153, 2014.
- C. Weisman. *Welding handbook 1. Fundamentals of Welding*, volume 1. Macmillan, 1976.
- M.J. Cieslak. *Fundamentals of welding - Cracking phenomena associated with welding*, volume 6. ASM Handbook, 2002.
- J.C. Borland. Hot cracks in Welds. *British Welding Journal*, 7:558–559, 1960.
- L. Carter, C. Martin, P. Withers, and M. Attallah. The influence of the laser scan strategy on grain structure and cracking behaviour in SLM powder-bed fabricated nickel superalloy. *Journal of Alloys and Compounds*, 615:338–347, 2014.
- KF Walker, Q Liu, and M Brandt. Evaluation of fatigue crack propagation behaviour in ti-6al-4v manufactured by selective laser melting. *International Journal of Fatigue*, 104: 302–308, 2017.
- S. Siddique, M. Imran, and F. Walther. Very high cycle fatigue and fatigue crack propagation behavior of selective laser melted alSi12 alloy. *International Journal of Fatigue*, 94:246–254, 2017.
- X. He, S. Chen, and G. Doolen. A novel thermal model for the lattice boltzmann method in incompressible limit. *Journal of Computational Physics*, 146(1):282–300, 1998.
- R. Ammer, U. Rüde, M. Markl, V. Jüchter, and C. Körner. Validation experiments for LBM simulations of electron beam melting. *International Journal of Modern Physics*, 25(12): 1441009, 2014b.

- V. Juechter, T. Scharowsky, R. Singer, and C. Körner. Processing window and evaporation phenomena for Ti-6Al-4V produced by selective electron beam melting. *Acta Materialia*, 76:252–258, 2014.
- M. Markl, R. Ammer, U. Råde, and C. Körner. Numerical investigations on hatching process strategies for powder-bed-based additive manufacturing using an electron beam. *The International Journal of Advanced Manufacturing Technology*, 78(1-4):239–247, 2015.
- M. Matsumoto, M. Shiomi, K. Osakada, and F. Abe. Finite element analysis of single layer forming on metallic powder bed in rapid prototyping by selective laser processing. *International Journal of Machine Tools and Manufacture*, 42(1):61–67, 2002.
- A. Foroozmehr, M. Badrossamay, and E. Foroozmehr. Finite element simulation of selective laser melting process considering optical penetration depth of laser in powder bed. *Materials & Design*, 89:255–263, 2016.
- C. Li, J. Liu, and Y. Guo. Prediction of residual stress and part distortion in selective laser melting. *Procedia CIRP*, 45:171–174, 2016b.
- W. Yan, J. Smith, W. Ge, F. Lin, and W. Liu. Multiscale modeling of electron beam and substrate interaction: a new heat source model. *Computational Mechanics*, 56(2):265–276, 2015.
- C. Seidel and M. Zaeh. Multi-scale Modelling Approach for Contributing to Reduced Distortion in Parts Made by Laser-based Powder Bed Fusion. *Procedia CIRP*, 67:197–202, 2018.
- E. Borel. *Introduction géométrique à quelques théories physiques*. Gauthier-Villars Paris, 1914.
- C. Cercignani. *Mathematical methods in kinetic theory*. Springer, 1969.
- C. Cercignani. On the Boltzmann equation for rigid spheres. *Transport Theory and Statistical Physics*, 2(3):211–225, 1972.
- C. Cercignani. *Ludwig Boltzmann e la meccanica statistica*, volume 4. La goliardica pavese, 1997.
- H. Tang. Gauss Lemma. *Proceedings of the American Mathematical Society*, 35(2):372–376, 1972.
- C. Cercignani, R. Illner, and M. Pulvirenti. *The mathematical theory of dilute gases*, volume 106. Springer Science & Business Media, 2013.
- N. Bogoliubov. *Problemy dinamicheskoi teorii v statisticheskoi fizike*. Gostekhizdat, 1946.
- H. Spohn. Boltzmann hierarchy and Boltzmann equation. In *Kinetic Theories and the Boltzmann Equation*, pages 207–220. Springer, 1984.
- C. Cercignani. *Theory and application of the Boltzmann equation*. Scottish Academic Press, 1975.



- C. Cercignani. The Boltzmann equation. In *The Boltzmann Equation and Its Applications*, pages 40–103. Springer, 1988.
- H. Grad. The many faces of entropy. *Communications on Pure and Applied Mathematics*, 14(3):323–354, 1961.
- T. Carleman. *Problèmes mathématiques dans la théorie cinétique de gaz*, volume 2. Almqvist & Wiksell, 1957.
- C. Cercignani. Are there more than five linearly-independent collision invariants for the Boltzmann equation? *Journal of Statistical Physics*, 58(5):817–823, 1990.
- L. Boltzmann. Weitere studien über das wärme Gleichgewicht unter gasmolekülen. In *Kinetische Theorie II*, pages 115–225. Springer, 1870.
- T. Carleman. Sur la théorie de l'équation intégrodifférentielle de Boltzmann. *Acta Mathematica*, 60(1):91–146, 1933.
- M. Gurtin and O. Williams. On the clausius-duhem inequality. *Zeitschrift für Angewandte Mathematik und Physik (ZAMP)*, 17(5):626–633, 1966.
- D. Hilbert. Grundzüge einer allgemeinen Theorie der linearen integralgleichungen. Vierte Mitteilung. *Nachrichten von der Gesellschaft der Wissenschaften zu Göttingen, Mathematisch-Physikalische Klasse*, 1906:157–228, 1906.
- C. Cercignani. *Rarefied gas dynamics: from basic concepts to actual calculations*, volume 21. Cambridge University Press, 2000.
- S. Chapman and T. Cowling. *The mathematical theory of non-uniform gases: an account of the kinetic theory of viscosity, thermal conduction and diffusion in gases*. Cambridge university press, 1970.
- R. Agarwal, K. Yun, and R. Balakrishnan. Beyond Navier–Stokes: Burnett equations for flows in the continuum–transition regime. *Physics of Fluids*, 13(10):3061–3085, 2001.
- H. Struchtrup. Failures of the Burnett and super-Burnett equations in steady state processes. *Continuum Mechanics and Thermodynamics*, 17(1):43–50, 2005.
- G. McNamara and G. Zanetti. Use of the Boltzmann equation to simulate lattice gas automata. *Physical Review Letters*, 61(20):2332, 1988.
- U. Frisch, D. D’Humières, B. Hasslacher, P. Lallemand, Y. Pomeau, and J-P. Rivet. Lattice gas hydrodynamics in two and three dimensions. Technical report, Los Alamos National Lab., NM (USA); Observatoire de Nice, 06 (France); Ecole Normale Supérieure, 75-Paris (France), 1986.
- D. Wolf-Gladrow. *Lattice-gas cellular automata and lattice Boltzmann models: an introduction*. Springer, 2004.
- X. He and L. Luo. Theory of the Lattice boltzmann method: From the Boltzmann equation to the Lattice Boltzmann equation. *Physical Review*, 56(6):6811, 1997a.

- A. Ladd and R. Verberg. Lattice Boltzmann simulations of particle-fluid suspensions. *Journal of Statistical Physics*, 104(5-6):1191–1251, 2001.
- Z. Guo and T. Zhao. Lattice Boltzmann model for incompressible flows through porous media. *Physical Review*, 66(3):036304, 2002.
- C. Teixeira, H. Chen, and D. Freed. Multi speed thermal Lattice Boltzmann method stabilization via equilibrium under relaxation. *Computer Physics Communications*, 129(1-3):207–226, 2000.
- B. Palmer and D. Rector. Lattice Boltzmann algorithm for simulating thermal flow in compressible fluids. *Journal of Computational Physics*, 161(1):1–20, 2000.
- D. Yu, R. Mei, L. Luo, and W. Shyy. Viscous flow computations with the method of Lattice Boltzmann equation. *Progress in Aerospace Sciences*, 39(5):329–367, 2003.
- C. Körner, M. Thies, T. Hofmann, N. Thürey, and U. Rüde. Lattice Boltzmann model for free surface flow for modeling foaming. *Journal of Statistical Physics*, 121(1-2):179–196, 2005.
- S. Geller, M. Krafczyk, J. Tölke, S. Turek, and J. Hron. Benchmark computations based on Lattice Boltzmann, finite element and finite volume methods for laminar flows. *Computers & Fluids*, 35(8-9):888–897, 2006.
- H. Zheng, C. Shu, and Y. Chew. A Lattice Boltzmann model for multiphase flows with large density ratio. *Journal of Computational Physics*, 218(1):353–371, 2006.
- R. Huang, H. Wu, and P. Cheng. A new Lattice Boltzmann model for solid liquid phase change. *International Journal of Heat and Mass Transfer*, 59:295–301, 2013.
- X. He and L. Luo. A priori derivation of the Lattice Boltzmann equation. *Physical Review*, 55(6):R6333, 1997b.
- E. Coddington. *An introduction to ordinary differential equations*. Courier Corporation, 2012.
- A. Kuzmin. *Multiphase simulations with lattice Boltzmann scheme*. 2010.
- Z. Guo, C. Zheng, and B. Shi. Discrete Lattice effects on the forcing term in the Lattice Boltzmann method. *Physical Review*, 65(4):046308, 2002a.
- N. Martys, X. Shan, and H. Chen. Evaluation of the external force term in the discrete Boltzmann equation. *Physical Review*, 58(5):6855, 1998.
- O. Burggraf. Analytical and numerical studies of the structure of steady separated flows. *Journal of Fluid Mechanics*, 24(1):113–151, 1966.
- T. Krüger, H. Kusumaatmaja, A. Kuzmin, O. Shardt, G. Silva, and E. Viggien. *The Lattice Boltzmann Method*. Springer, 2017.
- G. McNamara, A. Garcia, and B. Alder. Stabilization of thermal Lattice Boltzmann models. *Journal of Statistical Physics*, 81(1-2):395–408, 1995.

- Z. Guo, B. Shi, and C. Zheng. A coupled Lattice BGK model for the Boussinesq equations. *International Journal for Numerical Methods in Fluids*, 39(4):325–342, 2002b.
- J. Boussinesq. *Théorie analytique de la chaleur: mise en harmonie avec la thermodynamique et avec la théorie mécanique de la lumière*, volume 2. Gauthier-Villars, 1903.
- J. Latt. Choice of units in lattice Boltzmann simulations. *Freely available online at [http://lbmethod.org/\\_media/howtos:lbunits.pdf](http://lbmethod.org/_media/howtos:lbunits.pdf)*, 2008.
- P. Kao and R. Yang. Simulating oscillatory flows in Rayleigh Benard convection using the Lattice Boltzmann method. *International Journal of Heat and Mass Transfer*, 50(17-18):3315–3328, 2007.
- M. Fyta, S. Melchionna, E. Kaxiras, and S. Succi. Multiscale coupling of molecular dynamics and hydrodynamics: application to DNA translocation through a nanopore. *Multiscale Modeling & Simulation*, 5(4):1156–1173, 2006.
- H. Huang, Z. Li, S. Liu, and X. Lu. Shan-and-Chen type multiphase Lattice Boltzmann study of viscous coupling effects for two-phase flow in porous media. *International Journal for Numerical Methods in Fluids*, 61(3):341–354, 2009.
- R. Benzi, L. Biferale, M. Sbragaglia, S. Succi, and F. Toschi. Mesoscopic modeling of a two phase flow in the presence of boundaries: the contact angle. *Physical Review*, 74(2):021509, 2006.
- P. Yuan and L. Schaefer. Equations of state in a lattice boltzmann model. *PF*, 18(4):042101, 2006.
- J. D. Van der Waals. *Over de Continuïteit van den Gas en Vloeistoestand*, volume 1. Sijthoff, 1873.
- O. Redlich and J. Kwong. On the thermodynamics of solutions. An equation of state. Fugacities of gaseous solutions. *Chemical Reviews*, 44(1):233–244, 1949.
- N. Carnahan and K. Starling. Equation of state for nonattracting rigid spheres. *The Journal of Chemical Physics*, 51(2):635–636, 1969.
- M. De Ruijter, P. Kölsch, M. Voué, J. De Coninck, and JP. Rabe. Effect of temperature on the dynamic contact angle. *Colloids and Surfaces A: Physicochemical and Engineering Aspects*, 144(1-3):235–243, 1998.
- C. Körner. Lattice Boltzmann model for free surface flow. In *Integral Foam Molding of Light Metals*, pages 163–170. Springer, 2008.
- M. Thies. *Lattice Boltzmann modeling with free surfaces applied to in-situ gas generated foam formation*. PhD thesis, PhD-Thesis, University of Erlangen-Nürnberg, 2005.
- W. Miller and S. Succi. A Lattice Boltzmann model for anisotropic crystal growth from melt. *Journal of Statistical Physics*, 107(1-2):173–186, 2002.

- S. Chakraborty and D. Chatterjee. An enthalpy based hybrid Lattice Boltzmann method for modelling solid liquid phase transition in the presence of convective transport. *Journal of Fluid Mechanics*, 592:155–175, 2007.
- D. Chatterjee. An enthalpy based thermal Lattice Boltzmann model for non isothermal systems. *Europhysics Letters*, 86(1):14004, 2009.
- V. Alexiades. *Mathematical modeling of melting and freezing processes*. CRC Press, 1992.
- D. Noble and J. Torczynski. A Lattice Boltzmann method for partially saturated computational cells. *International Journal of Modern Physics*, 9(08):1189–1201, 1998.
- O. Strack and B. Cook. Three dimensional immersed boundary conditions for moving solids in the Lattice Boltzmann method. *Journal for Numerical Methods in Fluids*, 55(2):103–125, 2007.
- G. Zhao-Li, Z. Chu-Guang, and S. Bao-Chang. Non equilibrium extrapolation method for velocity and pressure boundary conditions in the Lattice Boltzmann method. *Chinese Physics*, 11(4):366, 2002.
- G. Tang, W. Tao, and Y. He. Thermal boundary condition for the thermal Lattice Boltzmann equation. *Physical Review*, 72(1):016703, 2005.
- B. Schoinochoritis, D. Chantzis, and K. Salonitis. Simulation of metallic powder bed additive manufacturing processes with the finite element method: A critical review. *Proceedings of the Institution of Mechanical Engineers, Part B: Journal of Engineering Manufacture*, 231(1):96–117, 2017.
- K. Dai and L. Shaw. Finite element analysis of the effect of volume shrinkage during laser densification. *Acta materialia*, 53(18):4743–4754, 2005.
- I. Roberts. Investigation of residual stresses in the laser melting of metal powders in additive layer manufacturing. 2012.
- J. Goldak, A. Chakravarti, and M. Bibby. A new finite element model for welding heat sources. *Metallurgical transactions B*, 15(2):299–305, 1984.
- C. Fu and Y. Guo. Three-dimensional temperature gradient mechanism in selective laser melting of Ti-6Al-4V. *Journal of Manufacturing Science and Engineering*, 136(6):061004, 2014.
- K. Mills. *Recommended values of thermophysical properties for selected commercial alloys*. Woodhead Publishing, 2002.
- P. Hagqvist, F. Sikström, and A. Christiansso. Emissivity estimation for high temperature radiation pyrometry on Ti-6Al-4V. *Measurement*, 46(2):871–880, 2013.
- C. Ziemian, m. Sharma, and S. Ziemiana. Anisotropic mechanical properties of abs parts fabricated by fused deposition modelling. In *Mechanical engineering*. InTech, 2012.

- T. Letcher and M. Waytashek. Material property testing of 3d-printed specimen in pla on an entry-level 3D printer. In *ASME 2014 international mechanical engineering congress and exposition*, pages V02AT02A014–V02AT02A014. American Society of Mechanical Engineers, 2014.
- K. Rahman, T. Letcher, and R. Reese. Mechanical properties of additively manufactured PEEK components using fused filament fabrication. In *ASME 2015 International Mechanical Engineering Congress and Exposition*, pages V02AT02A009–V02AT02A009. American Society of Mechanical Engineers, 2015.
- I. Zein, D. Hutmacher, K. Tan, and S. Teoh. Fused deposition modeling of novel scaffold architectures for tissue engineering applications. *Biomaterials*, 23(4):1169–1185, 2002.
- B. Wittbrodt and J. Pearce. The effects of PLA color on material properties of 3-d printed components. *Additive Manufacturing*, 8:110–116, 2015.
- T. Lieneke, V. Denzer, G. Adam, and D. Zimmer. Dimensional tolerances for additive manufacturing: Experimental investigation for Fused Deposition Modeling. *Procedia CIRP*, 43: 286–291, 2016.
- G. Alaimo, S. Marconi, L. Costato, and F. Auricchio. Influence of meso-structure and chemical composition on FDM 3D-printed parts. *Composites Part B: Engineering*, 113:371–380, 2017.
- H. Tadokoro. *Structure of crystalline polymers*. Krieger Pub Co, 1979.
- E. Pei, J. Shen, and J. Watling. Direct 3D printing of polymers onto textiles: experimental studies and applications. *Rapid Prototyping Journal*, 21(5):556–571, 2015.
- L. Sabantina, F. Kinzel, A. Ehrmann, and K. Finsterbusch. Combining 3D printed forms with textile structures-mechanical and geometrical properties of multi-material systems. In *IOP Conference Series: Materials Science and Engineering*, volume 87, page 012005. IOP Publishing, 2015.
- T. Coogan and D. Kazmer. Healing simulation for bond strength prediction of FDM. *Rapid Prototyping Journal*, 23(3):551–561, 2017.
- Y. Zhang and Y. Chou. Three-dimensional finite element analysis simulations of the fused deposition modelling process. *Proceedings of the Institution of Mechanical Engineers, Part B: Journal of Engineering Manufacture*, 220(10):1663–1671, 2006.
- B. Courter, V. Savane, J. Bi, S. Dev, and C. Hansen. Finite Element Simulation of the Fused Deposition Modelling Process. In *Proceedings of the NAFEMS World Congress*, pages 11–14, 2017.
- B. Tiganis, LS. Burn, P. Davis, and AJ. Hill. Thermal degradation of acrylonitrile–butadiene–styrene (ABS) blends. *Polymer degradation and stability*, 76(3):425–434, 2002.
- J. Richeton, S. Ahzi, L. Daridon, and Y. Rémond. A formulation of the cooperative model for the yield stress of amorphous polymers for a wide range of strain rates and temperatures. *Polymer*, 46(16):6035–6043, 2005.

- J. Rault. Yielding in amorphous and semi-crystalline polymers: the compensation law. *Journal of non-crystalline solids*, 235:737–741, 1998.
- J. Rodríguez, J. Thomas, and J. Renaud. Mechanical behavior of acrylonitrile butadiene styrene fused deposition materials modeling. *Rapid Prototyping Journal*, 9(4):219–230, 2003.
- F. Ning, W. Cong, Y. Hu, and H. Wang. Additive manufacturing of carbon fiber-reinforced plastic composites using fused deposition modeling: Effects of process parameters on tensile properties. *Journal of Composite Materials*, 51(4):451–462, 2017.
- G. Liao, Z. Li, Y. Cheng, D. Xu, D. Zhu, S. Jiang, J. Guo, X. Chen, G. Xu, and Y. Zhu. Properties of oriented carbon fiber/polyamide 12 composite parts fabricated by fused deposition modeling. *Materials & Design*, 139:283–292, 2018.
- M. Ryder, D. Lados, G. Iannacchione, and A. Peterson. Fabrication and properties of novel polymer-metal composites using fused deposition modeling. *Composites Science and Technology*, 158:43–50, 2018.
- 3ntr, Additive Manufacturing Systems. <http://www.3ntr.eu/>. Accessed: 2018-09-19.